Precision Predictions of Exclusive Jet Cross Sections at the LHC

Dissertation

zur Erlangung des Doktorgrades
an der Fakultät für Mathematik,
Informatik und Naturwissenschaften
Fachbereich Physik
der Universität Hamburg

vorgelegt von

SHIREEN GANGAL

aus

Mumbai, INDIEN

Hamburg
2015

Gutachter/in der Dissertation:	Dr. Frank Tackmann. Prof. Dr. Gudrid Moortgat-Pick.
Gutachter/in der Disputation:	Dr. Frank Tackmann. Prof. Dr. Gudrid Moortgat-Pick. Dr. Markus Diehl. Prof. Dr. Peter Schleper.
Datum der Disputation:	14 Oktober 2015.
Vorsitzender des Prüfungsausschusses:	Prof. Dr. Günter Sigl
Vorsitzender des Promotionsausschusses:	Prof. Dr. Jan Louis.
Leiter des Fachbereichs Physik:	Prof. Dr. Peter Hauschildt.
Dekan der Fakultät für Mathematik, Informatik und Naturwissenschaften:	Prof. Dr. Heinrich Graener.

Abstract

With the discovery of the Higgs boson, a central objective of the LHC Higgs program is to study its properties in detail by exploring different production and decay channels. This requires precise theoretical predictions of inclusive cross sections as well as differential and exclusive cross sections. In this thesis, we study perturbative uncertainties in the fixed-order (FO) predictions of exclusive jet cross sections and obtain resummed predictions for a new class of rapidity-dependent jet veto observables, focusing on Higgs production via gluon gluon fusion (ggF) at the LHC. Experimental analyses at the LHC often use jet binning and jet selection cuts to distinguish between different Higgs production mechanisms and to separate signal from backgrounds. Such jet vetoes and jet selection cuts induce Sudakov logarithms of the ratio of the veto scale and the hard scale in the process. In the limit of very tight jet vetoes, these logarithms can become large and introduce large uncertainties in the FO predictions of cross sections. By resumming these large logarithms to all orders, the perturbative uncertainties can be considerably reduced. Whether in FO or resummed predictions, a consistent treatment of uncertainties in different jet bins is required. In the first part of the thesis, we studied in detail the perturbative uncertainties in the NLO predictions for $pp \to H$+2-jets via ggF for the vector boson fusion (VBF) selection cuts used by ATLAS and CMS in their $H \to \gamma\gamma$ analyses. Our study shows that, while applying strong restrictions on additional emissions is expected to increase the sensitivity to the VBF signal and reduce the ggF contribution, it is not necessarily beneficial for distinguishing the VBF and ggF production modes because of the quickly increasing ggF uncertainties. In the second part of the thesis, we introduce rapidity-dependent jet veto observables for which the transverse momentum of a jet is weighted by a smooth function of the jet rapidity. These jet-based observables provide natural and clean ways to veto central jets and can yield valuable complementary information in the exclusive jet bins. Using Soft Collinear Effective Theory (SCET), we study the factorization and resummation properties of these rapidity-dependent observables and obtain predictions for the resummed H+0-jet cross section at NLL$'$ with a veto on these observables. Because the experimentally relevant region is an intermediate one, where both the resummed and the FO contributions are important, we calculate the FO corrections at NLO and combine them with our resummed predictions to obtain the full NLL$'$+NLO result for the H+0-jet cross section. We compare our numerical predictions with the differential cross section measurement by ATLAS in the $H \to \gamma\gamma$ channel and find good agreement. At $O(\alpha_s^2)$, these jet-based observables have a non trivial dependence on the jet-algorithm due to clustering effects. In the final part, we consider the corrections due to clustering of two collinear or soft particles into a single jet which are an important input for predicting the cross section at NNLL$'$+NNLO. These corrections are numerically significant for the jet radii currently used in experiments.

Zusammenfassung

Nach der Entdeckung des Higgs-Bosons liegt das Hauptaugenmerk des LHC Higgs Programms auf der exakten Vermessung seiner Eigenschaften durch Untersuchung der verschiedenen Produktions- und Zerfallskanäle. Dies verlangt präzise theoretische Vorhersagen von inklusiven als auch differentiellen und exklusiven Wirkungsquerschnitten (WQ). In dieser Arbeit untersuchen wir störungstheoretische (ST) Unsicherheiten in den Vorhersagen von exklusiven Jet-WQ in fester Ordnung der ST Reihe (FO). Wir erhalten resummierte Vorhersagen für eine neue Klasse von Rapiditäts-abhängigen Jet-Veto Observablen, wobei unser Fokus auf Higgsproduktion durch Gluonfusion (ggF) am LHC liegt. Experimentelle Analysen beruhen häufig auf Jet-Binning in Kombination mit gewissen kinematischen Schnitten, um die verschiedenen Produktionsmechanismen zu unterscheiden und das Signal vom Untergrund zu separieren. Solche Jet-Vetoes und Jet-Selektionsschnitte generieren Sudakov-Logarithmen abhängig vom Verhältnis der Skala des Jet-Vetoes zur harten Skala des Prozesses. Im Grenzfall sehr kleiner Jet-Vetoes werden diese Logarithmen sehr groß und bedingen große Unsicherheiten in der FO Vorhersage der WQ. Durch Resummierung dieser großen Logarithmen zu allen Ordnungen der ST Reihe werden die Unsicherheiten deutlich reduziert. Eine konsistente Behandlung der Unsicherheiten in den unterschiedlichen Jet-Bins ist unabdingbar, sowohl für FO wie auch resummierte Vorhersagen. Im ersten Teil dieser Arbeit untersuchen wir im Detail die ST Unsicherheiten in der Vorhersage von $pp \to H$+2-Jets durch ggF in nächstführender Ordnung (NLO) ST bei Anwendung von Auswahlschnitten für Vektorbosonfusion (VBF), wie sie von ATLAS und CMS in ihren $H \to \gamma\gamma$ Analysen zum Einsatz kommen. Während starke Einschränkungen auf die Emission weiterer Teilchen die Sensitivität auf das VBF Signal erhöhen und auf den ggF Anteil reduzieren sollten, zeigt unsere Studie, dass ebensolche Einschränkungen nicht zwangsläufig vorteilhaft für die Unterscheidung der VBF und ggF Produktionsmechanismen sind, eben gerade aufgrund der stark ansteigenden ggF Unsicherheiten. Im zweiten Teil der Arbeit führen wir Rapiditäts-abhängige Jet-Veto Observablen ein, für die der Transversalimpuls eines Jet mit einer glatten Funktion der Jet-Rapidität gewichtet wird. Diese Jet-basierten Observablen erlauben zentrale Jets zu verbieten und bieten dennoch komplementäre Informationen in den exklusiven Jet-Bins. Mit der Hilfe von "Soft Collinear Effective Theory" (SCET) untersuchen wir die Faktorisierungs- und Resummierungseigenschaften dieser Rapiditäts-abhängigen Observablen und erhalten so Vorhersagen für den resummierten $H + 0$-Jet WQ in Ordnung NLL$'$ bei entsprechendem Veto auf diese Observablen kombiniert mit dem FO WQ auf NLO. Wir vergleichen unsere numerische Vorhersage mit den Messungen des differentiellen WQ von ATLAS im $H \to \gamma\gamma$ Kanal und finden gute Übereinstimmung. In $O(\alpha_s^2)$ haben die Jet-basierten Observablen eine nichttriviale Abhängigkeit vom Jet-Algorithmus aufgrund von “Clustering”. Zuletzt betrachten wir Korrekturen aufgrund des “Clustering” von zwei kollinearen oder weichen Teilchen in einen Jet, die einen wichtigen Beitrag zur Vorhersage von WQ in der Ordnung NNLL$'$+NNLO liefern und numerisch von Relevanz für die experimentell genutzten Jet-Radien sind.

Acknowledgements

I would like to express my appreciation and gratitude to my advisor Dr. Frank Tackmann for his patient guidance right from the time I joined the PhD program through to the completion of this degree. I would like to thank him for his expertise and knowledge in the field, for the useful discussions and for his good and helping nature. Many thanks to Dr. Maximilian Stahlhofen for the plenty of discussions, for his willingness to spend hours carefully going through my calculations and for being supportive and encouraging. I would also like to thank Dr. Jonathan Gaunt for patiently answering my trivial questions, for discussing the basics of QCD and SCET during the first years of my PhD and for his guidance and active collaboration in the 2-loop calculation. I would also thank Prof. Gudrid Moortgart-Pick for her willingness to be a co-referee of my work.

The theory group of building 1b have been an enjoyable place to work, and I would like to take this opportunity to thank the many friends I made during this period of three years. My special thanks to Dr. Kazuki Sakurai for always being there to answer my trivial questions and for the fun-filled coffees and dinners together talking about physics and life! A big thanks to Dr. Stefan Liebler for his kindness, helpfulness and for being a great friend. Thanks to my office mates, Dr. Marco Tonini, Peter Drechsel, Shruti Patel and Christian Weiss for their funny discussions which kept the positive spirit and made the atmosphere lively at work. Then the other group members, Dr. Markus Diehl, Dr. Piotr Pietrulewicz, Dr. Andrew Papanastasiou, Dr. Florian Domingo, So Young Shim, Markus Ebert, Simone Lionetti for their friendship, physics discussions, lunches, coffees and cakes together. I would also like to thank my Indian friends Anand Kamlapure and Amul Shinde for the fun times with delicious Indian food.

I would not have made it to DESY, without the support and sacrifice of my family members in India. This thesis is dedicated to my mother who has always been very kind, loving and understanding. I thank my father for supporting me in all my decisions right from the time I decided to do physics. I would like to thank my sister for being a friend I always relied on and my relatives in India for their good wishes and blessings. I will always be grateful to Prof. Amol Dighe, TIFR, India for believing in me and guiding me. I would also like to thank Prof. Ashutosh Kumar Alok, IIT Jodhpur, India for his guidance and friendship all these years. A heartfelt thanks goes to my boyfriend Girish Sharma for all his love, support and patience when I was only thinking about strange calculations and for making my life beautiful and complete.

List of publications

This thesis is based on the following publications:

[1] S. Gangal, M. Stahlhofen, F.J. Tackmann, *Rapidity dependent jet vetoes*, Phys. Rev. D 91 (2015), 054023, [arxiv:1412.4792].

[2] F.U. Bernlochner, S. Gangal, D. Gillberg, F.J. Tackmann, *contribution to Handbook of LHC Higgs Cross sections 3*, [arxiv:1307.1347].

[3] S. Gangal, F.J. Tackmann, *Next-to-leading-order uncertainties in Higgs+2 jets from gluon fusion*, Phys. Rev. D 87 (2013) 093008, [arxiv: 1302.5437].

Declaration on oath

I hereby declare, on oath, that I have written the present dissertation by my own and have not used other than the acknowledged resources and aids.

Hamburg, the 2nd September 2015 Shireen Gangal.

Eidesstattliche Erklärung

Hiermit erkläre ich an Eides statt, dass ich die vorliegende Dissertationsschrift selbst verfasst und keine anderen als die angegebenen Quellen und Hilfsmittel benutzt habe.

Hamburg, den 2. September 2015 Shireen Gangal.

Contents

1 Introduction **1**

2 QCD and Higgs Physics **7**

2.1 Introduction 7

2.2 Deep inelastic scattering and the parton model 8

2.3 $e^+e^- \to$ Jets 10

2.4 Resummation of large logarithms 16

2.5 Spontaneous Symmetry breaking 20

2.6 Higgs Mechanism in the Standard Model 22

2.7 Higgs boson discovery 24

3 NLO Uncertainties in Higgs + 2 jets **29**

3.1 Introduction 29

3.2 Jet Binning Uncertainties 30

3.3 Application to $gg \to H + 2$ Jets 34

3.3.1 Variables 36

3.3.2 Inclusive Scale Uncertainties 37

3.3.3 Exclusive Uncertainty 39

3.4 Results 43

3.4.1 $gg \to H + 2$ Jets Cross Section 43

3.4.2 Combination of Exclusive Cuts . . . 45
3.4.3 Uncertainties in ggF-VBF Separation . . . 46
3.4.4 Generalization to arbitrary cuts and application to MVAs . . . 49
3.5 Conclusions . . . 53

4 Rapidity-dependent jet vetoes. 55

4.1 Introduction . . . 55
4.2 Rapidity-dependent observables: $\mathcal{T}_B^{\rm jet}$ and $\mathcal{T}_C^{\rm jet}$ . . . 58
4.3 $pp \to HX$ process at NLO . . . 61
4.3.1 Higgs Production matrix elements . . . 65
4.3.2 Cross section differential in $\mathcal{T}_{B\rm cm}$ . . . 66
4.4 Introduction to SCET . . . 68
4.5 Ingredients and SCET Lagrangian . . . 70
4.6 Factorization in SCET . . . 75
4.6.1 Ultrasoft collinear factorization . . . 75
4.6.2 Factorization formula for Drell-Yan like processes . . . 76
4.6.3 Application to jet-based observables . . . 82
4.7 Resummation of large logarithms in SCET . . . 85
4.8 Ingredients at NLL′ . . . 89
4.9 NLO Nonsingular with subtraction method . . . 90
4.10 Scale choices . . . 92
4.10.1 Fixed-order and resummation uncertainties . . . 96
4.11 Results . . . 100
4.12 Conclusions . . . 104

5 Clustering corrections in the beam and soft functions 107

5.1 Introduction . . . 107

5.2 Clustering corrections in the Soft function . . . 109

5.2.1 Clustering for $\mathcal{T}_B^{\text{jet}}$ . . . 111

5.2.2 Clustering for $\mathcal{T}_C^{\text{jet}}$ . . . 116

5.3 Clustering corrections in the Beam function . . . 120

5.4 Conclusions and Outlook . . . 124

6 Conclusions **127**

A Hard, beam and soft functions **131**

A.1 Hard Function . . . 131

A.2 Beam function . . . 132

A.3 Soft functions . . . 133

A.3.1 Soft function for $\mathcal{T}_{B(\text{cm})}^{\text{jet}}$ . . . 133

A.3.2 Soft function for $\mathcal{T}_{C(\text{cm})}^{\text{jet}}$ . . . 133

B NLO H+0-jet crosss section **135**

B.1 H+0-jet cross section differential in $\mathcal{T}_B^{\text{jet}}$ . . . 135

B.2 Differential cross section for $\mathcal{T}_C^{\text{jet}}$ . . . 136

B.3 Differential cross section for $\mathcal{T}_{C\text{cm}}^{\text{jet}}$ . . . 138

Bibliography **139**

Chapter 1

Introduction

The observation of a Higgs-like boson at the LHC is a huge success of science and in particular of the Standard Model (SM) of particle physics – a theory used to understand matter and forces in the universe and which predicted the existence of the Higgs boson. The insight into the basic structure of matter reveals that everything in the universe is made up of a few building blocks called the fundamental particles and is governed by four basic forces – strong, electromagnetic, weak and gravitational. The SM provides a successful theory of the strong, the electromagnetic and the weak interactions. Electromagnetic interactions are mediated by photons, the strong interactions by massless spin-1 gluons (discovered at DESY in 1979) and the weak interactions by spin-1 W^+, W^- and Z bosons (discovered at CERN in 1983).

The formulation of the SM is based on Quantum Field Theory (QFT) which is a mathematical and conceptual framework describing the creation and destruction of particles and their interactions. In a rather informal sense, QFT is the extension of quantum mechanics (QM), which deals with systems having an infinite number of degrees of freedom. The motivation behind developing QFT was to put together QM and Special Theory of Relativity (STR) for the proper quantum treatment of electromagnetic field. There is a long and impressive history of theoretical and experimental advances in the field of QFT and particle physics owing to the efforts of many scientists in the 20th century. QFT was introduced by De Broglie, Heisenberg in 1920s and by Paul Dirac with the theory of quantum electrodynamics (QED), which is an abelian gauge theory with the symmetry group U(1). In the 1930s, the basic physical quantities in QED, such as the self-energy of the electron gave infinite, divergent contributions when computed using perturbative techniques. This "divergence problem" was solved for QED by Hans Bethe, Tomonaga, Schwinger, Feynman and Dyson, through the procedure known as renormalization. The concepts of 'charge' and 'mass' were understood with the idea that the 'bare' masses and

charges of particles that appear in free field (non-interacting) equations are not experimentally measured quantities and that 'vacuum' is populated by creation and annihilation of virtual particles. The quantities that are measured in experiments are 'renormalized' masses and charges. Another important development was due to Feynman, who found a representative way to study scattering of particles through "diagrams" and set of rules to compute scattering matrices, amplitudes, decay widths and cross sections.

The theory for the strong interaction, which binds the protons and neutrons inside the nucleus, was formulated as Quantum Chromodynamics (QCD). QCD is a non-abelian gauge theory based on a local gauge symmetry SU(3). Yang and Mills formulated the first example of a non-Abelian gauge theory, called the Yang-Mills theory to provide an explanation for strong interaction. Following this in the early 1960s, the electromagnetic and weak interactions were unified into the electroweak interaction in the Glashow-Weinberg-Salam (GWS) model described by an SU(2) $\times$ U(1) group. The GWS model was shown to be renormalisable by t' Hooft and Veltman. In 1973, Gross, Wilczek and Politzer showed that the attraction between quarks grows weaker as the quarks approach one another, and correspondingly the attraction grows stronger as the quarks are separated. This discovery, known as "asymptotic freedom" allows us to use perturbaion theory to predict QCD cross sections at large energies.

In the 1960s, the concept of particles acquiring mass through symmetry breaking in massless theories was put forward by Jeffrey Goldstone, Yoichiro Nambu and Giovanni Jona-Lasinio. A theory able to finally explain mass generation for particles without breaking gauge theory was published almost simultaneously by three independent groups in 1964: by Robert Brout and Francois Englert [1], by Peter Higgs and by Gerald Guralnik [2, 3], C. R. Hagen, and Tom Kibble [4]. The so-called "Brout-Englert-Higgs (BEH) Mechanism" explains how massless bosons from the electroweak theory mix to produce three massive weak bosons, and the massless photon field. The SM is thus a theory which combines the strong interaction with the unified electroweak interaction through the symmetry group SU(2) $\times$ U(1)$\times$ SU(3).

On July 4 2012 [5, 6], scientists at the LHC announced that they had found the Higgs boson, a particle that is responsible for generation of mass, as proposed in 1964. In this concept of mass generation, after the Big Bang, an energy field, now dubbed the Higgs field, emerged that imparts mass to the subatomic particles. Pictorially, particles that travel through this field slow down more while traversing the field and become heavier. Because subatomic particles are either matter carriers called fermions or force-carrying particles called bosons, the existence of the Higgs field implied an associated force-carrying particle, called the Higgs boson, which is like a ripple in that field. The 2012 discovery at the LHC left little doubt that the Higgs boson exists, and Higgs and his colleague, Fracois

Englert, won the Nobel Prize in 2013 for the their theory of electroweak symmetry breaking or the BEH mechanism.

After 2012, there have been several measurements of the properties of the discovered Higgs boson, by exploring different production and decay channels as well as new physics searches at the LHC. The LHC, being a proton-proton collision environment, a good understanding of QCD is important for achieving the best possible predictions and description of any events. Every interesting measurement at the LHC requires a certain number of selection cuts on the QCD radiation (that is jets) to maximize the signal sensitivity, reduce QCD background and to study specific Higgs production and decay modes. For example, in the $H \to WW$ analyses, with leptonic W decays, experiments distinguish events according to the number of jets in the final state. In particular, selecting events with zero jets by imposing a jet veto, which defines what is called the "exclusive" 0-jet cross section, significantly reduces the background. Such restrictions introduce additional theoretical uncertainties in the cross section predictions that need to be understood. The transverse momentum threshold for identifying jets, $p_T^{\text{cut}} \sim 25 - 30\,\text{GeV}$, is substantially smaller than the hard scale Q of the process. As a result, perturbative calculations of the cross section with the jet veto involve terms enhanced by up to two powers of $\log\left(m_H/p_T^{\text{cut}}\right)$ (called Sudakov logarithms) for each power of α_s beyond the leading-order cross section. When p_T is relatively unconstrained and $p_T^{\text{cut}} \sim Q$, then these logarithms are of order unity, and fixed-order QCD perturbation theory can be applied to predict the distribution. However one needs to carefully take into account the uncertainties introduced in the fixed-order predictions of exclusive cross sections due to such jet vetoes. However for tighter jet vetoes, when $p_T^{\text{cut}} \ll Q$, the logarithms overwhelm the α_s suppression, and the perturbative expansion must be resummed to all orders in α_s to ensure that the distribution does not diverge as $p_T^{\text{cut}} \to 0$. Techniques exist to perform resummation for such exclusive cross sections in QCD and in effective field theories (EFTs).

Generically in QCD a separation of scales is important for determining what parts of a process are perturbative with the strong coupling constant $\alpha_s \ll 1$ and what parts are nonperturbative with $\alpha_s \sim 1$. A typical cross section for any process is "factorized" into parton distribution functions describing the density of partons inside the proton (non-perturbative) and the hard interaction (perturbative). Any process at the LHC, involves widely separated energy scales; for example the energy scale of the non-perturbative physics, intermediate scales like the transverse momentum of jets and the mass of the particles produced like the Higgs or W/Z bosons. The EFT approach allows us to study the low-energy dynamics, independently of the details of the high-energy interactions. To build an EFT describing physics at a given energy scale E, one makes an expansion in powers of E_i/Q, where E_i are the various scales involved in the problem which are smaller than the hard scale Q. To ensure that the physics for the full theory and the effective theory is the same at the

boundary, there are matching conditions. First the heavy degrees of freedom are identified and integrated out of the action which results in an effective action that describes non-local interactions between lighter degrees of freedom. To obtain a local action, the effective action is expanded in a set of local operators. In a "top-bottom" approach, one starts with a full theory at a high energy and large renormalization scale μ, and evolves to lower energy through renormalization group evolution (RGE) which results in a logarithmic dependence on the ratio of the scales. In this thesis, we will compute cross sections in Soft- Collinear effective theory (SCET) which is an EFT of QCD that describes the interaction of soft particles with momentum p_{soft} such that $Q \gg p_{\text{soft}}$ and collinear energetic particles in the presence of a hard interaction. It provides a systematic way to factorize cross sections of different processes at the LHC and allows to resum logarithms using RGE.

The success of LHC Run 1 strongly relied upon advanced QCD simulation tools to guide experimental analyses, calculations in perturbative QCD upto the next-to-next-to-leading order in different Higgs production and decay channels and sophisticated Monte Carlo tools. There is, however, still a lot of work to be done in order to confirm that what has been observed is indeed the SM Higgs boson responsible for the electroweak symmetry breaking and not a close resemblance. Run 2 of the LHC with higher center-of-mass energy $\sqrt{s} = 13,14\,\text{TeV}$ is the beginning of the precision phase which means that a detailed understanding of experimental and theoretical uncertainties in each of the channels is of prime importance. This thesis aims at improving the evaluation of perturbative uncertainties in the exclusive jet cross sections at the LHC, introducing more efficient observables to veto central jets and providing resummed predictions for those jet veto observables in the framework of SCET [7–10]

Structure of the thesis:
In **chapter** 2, we will briefly discuss the basics of perturbative QCD which includes the parton model, running of the strong coupling constant α_s, infrared and ultraviolet divergences, DGLAP evolution and the origin and summation of large logarithms for exclusive jet cross sections. In the second part we will discuss briefly the main features of the Higgs Mechanism in the SM, the Higgs production and decay modes at the LHC and some recent results by the ATLAS and CMS experiments. In **chapter** 3 we will estimate the uncertainties in the exclusive jet cross sections induced by jet selection cuts and nontrivial jet binning used in experiments. In particular, we will explain in detail and generalize the so-called "Stewart-Tackmann" method to estimate such fixed-order uncertainties and obtain perturbative uncertainties in the NLO predictions for $pp \to H + 2$ jets via gluon gluon fusion (ggF) with the selection cuts used by ATLAS and CMS experiments in the vector boson fusion (VBF) analyses. These results have been published in [11]. In **Chapter** 4 we will introduce a new class of rapidity dependent jet vetoes and discuss their factorization and resummation properties in SCET. We will obtain resummed predictions at NLL$'$+

NLO order for gluon fusion $H + 0$-jet cross section with a veto on these observables. For one of these observables, we also compare our numerical predictions with the recent differential cross section measurement by the ATLAS experiment in the $H \to \gamma\gamma$ channel. This work is published in [12]. For more than one emissions (i.e. beyond NLL$'$) such jet-based observables have a dependence on the jet-algorithm (and the jet radius R) due to the clustering of two collinear or soft emissions into a single jet and due to soft-collinear mixing. The corrections due soft-collinear mixing are $O(R^2)$ while those due to clustering of correlated emissions within the collinear or soft sectors give rise to logarithms of R. In **chapter** 5, we will consider these clustering logarithms in the beam and soft functions at $O(\alpha_s^2)$ which are important for $R \ll 1$ currently used in experiments. A summary of the results and future work of implementing the clustering corrections to obtain the full NNLL$'$+ NNLO cross section is finally discussed in **chapter** 6.

Chapter 2

QCD and Higgs Physics

The first part of this chapter is an introduction to perturbative QCD, in particular the soft and collinear divergences encountered in higher-order calculations, the origin of large logarithms and the idea of resummation. The second part briefly explains the Higgs Mechanism in the Standard Model, the Higgs production and decay channels and the recent Higgs measurements at the LHC.

2.1 Introduction

Quantum Chromodynamics (QCD) is the SU(3) gauge field theory that describes the strong interaction of colored quarks and gluons. The QCD Lagrangian is given by

$$\mathcal{L} = \sum_q \bar{\psi}_{q,a}(i\gamma^\mu \partial_\mu \delta_{ab} - g_s \gamma^\mu t^C_{ab} \mathcal{A}^C_\mu - m_q \delta_{ab})\psi_{q,b} - \frac{1}{4} F^A_{\mu\nu} F^{A\mu\nu} \,. \tag{2.1}$$

The $\psi_{q,a}$ are quark field spinors for a quark of flavor q and mass m_q, with a color index 'a' that runs from $a = 1$ to $N_C = 3$, i.e. quarks come in 3 colors. Quarks are said to be in the fundamental representation of the SU(3) color group. The $\mathcal{A}^C_\mu$ correspond to the gluon fields with C running from 1 to $N_c^2 - 1 = 8$, i.e. there are 8 kinds of gluons. Gluons are in the adjoint representation of the SU(3) color group. The t^C_{ab} correspond to eight 3×3 matrices and are the generators of the SU(3) group. The quantity g_s is the QCD coupling constant. The field tensor $F^A_{\mu\nu}$ is given by

$$F^A_{\mu\nu} = \partial_\mu \mathcal{A}^A_\nu - \partial_\nu \mathcal{A}^A_\mu - g_s f_{ABC} \mathcal{A}^B_\mu \mathcal{A}^C_\nu \quad , \quad [t^A, t^B] = i f_{ABC} t^C \,, \tag{2.2}$$

where f_{ABC} are the structure constants of the $SU(3)$ group.

The fundamental parameters of QCD are the coupling g_s or $\alpha_s = g_s^2/4\pi$ and the quark masses. In perturbative QCD, predictions of observables are expressed in terms of the renormalized coupling $\alpha_s(\mu_R^2)$, a function of a renormalization scale μ_R. The coupling satisfies the following renormalization group equation (RGE)

$$\frac{d\alpha_s}{d\tau} = \beta(\alpha_s(\tau)) = -(b_0\alpha_s^2(\tau) + b_1\alpha_s^3(\tau) + b_2\alpha_s^4(\tau) + ...)\,, \tag{2.3}$$

where $\tau = \log(Q^2/\mu^2)$, $b_0 = (33-2n_f)/(12\pi)$ is the 1-loop beta function coefficient and b_1, b_2 are the 2-loop and 3-loop coefficients respectively. At leading order, Eq. (2.3) becomes

$$\int_{\alpha_s(\mu^2)}^{\alpha_s(Q^2)} \frac{d\alpha_s}{\alpha_s^2} = -\frac{\beta_0}{4\pi}\int_0^{\tau} d\tau_1 \tag{2.4}$$

yielding

$$\alpha_s(Q^2) = \frac{\alpha_s(\mu^2)}{1 + \alpha_s(\mu^2)\frac{\beta_0}{4\pi}\log(Q^2/\mu^2)}\,. \tag{2.5}$$

This equation expresses the effective QCD coupling in terms of the experimental observable $\alpha_s(\mu^2)$. The renormalization point μ is arbitrary. The minus sign in Eq. (2.3) indicates that the strong coupling is large at small Q^2 (that is large distance), where confinement occurs but decreases to zero at large Q^2, which is the origin of the asymptotic freedom. In QED it is easy to define the charge of an electron as it is related to the large distance behavior of the electric potential. This is not possible in QCD since the $Q^2 \to 0$ limit of $\alpha_s(Q^2)$ is not calculable in perturbation theory. So one has to choose an arbitraty point μ and measure the effective coupling at that point. The conventional choice is to define the coupling at $\mu^2 = m_Z^2$. The deep inelastic scattering experiment designed to detect point-like structure in the nucleon was the first to signal the need for asymptotic freedom, so we will discuss it shortly next.

2.2 Deep inelastic scattering and the parton model

Quarks and gluons, the fundamental dynamic entities of QCD, are not observed as free particles but confined inside the hadrons. Since the coupling constant of the strong interaction decreases with increasing energy, perturbative QCD calculations with expansion parameter α_s can only provide accurate descriptions of high energy scattering processes but they cannot explain the properties of low energy bound states i.e parton densities inside the hadrons. The solution is "factorization" of different energy scales which allows us to predict cross sections by separating the long-distance physics into functions describing the distributions of partons in hadrons (with parton distribution functions PDFs) and short

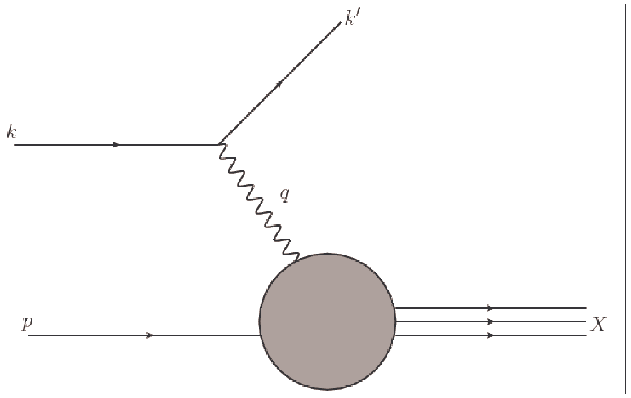

Figure 2.1: *Deep Inelastic Scattering at tree level.*

distance behaviour which describes the hard scattering process. Roughly, any cross section can be expressed as a convolution between the PDFs f and the pertubative hard matrix element H, that is, $\sigma = f \otimes H$. Deep inelastic scattering (DIS) was the first experiment where factorization was studied in detail and proved.

In DIS, a massive hadronic state X is produced by the scattering of a lepton (an electron) on a nucleon, $e(k) + N(p) \to e(k') + X_{\text{hadronic}}$. This process is shown in Fig. 2.1. Because the lepton interacts with the nucleon only through the exchange of a photon, W or Z boson, the cross section for this process factors into leptonic and hadronic tensors,

$$d\sigma = \frac{d^3k'}{2s|k'|}\frac{1}{q^4}L^{\mu\nu}(k,q)W_{\mu\nu}(p,q)\,. \tag{2.6}$$

where q is the four momentum of the exchanged photon. The leptonic tensor is known and the hadronic tensor $W_{\mu\nu}$ can be parameterized after imposing the parity and current conservation as follows

$$W_{\mu\nu} = -\Big(g_{\mu\nu} - \frac{q_\mu q_\nu}{q^2}\Big)W_1(x,q^2) + \Big(p_\mu + q_\mu\frac{1}{2x}\Big)\Big(p_\nu + q_\nu\frac{1}{2x}\Big)W_2(x,q^2)\,. \tag{2.7}$$

The W's are functions of $Q^2 = -q^2$ and the dimensionless ratio,

$$x = \frac{-q^2}{2p\cdot q} \equiv \frac{Q^2}{2p\cdot q}\,. \tag{2.8}$$

It is convenient to introduce dimensionless structure functions,

$$F_1 \equiv W_1\ , \quad F_2 \equiv (p\cdot q)W_2\,. \tag{2.9}$$

An important observation first made in the DIS experiments at SLAC was that for $Q^2 \geq 1\,\text{GeV}^2$, the structure functions $F(x,Q^2)$ become functions of x only, nearly independent of Q^2. Infact the experiments observed that the structure functions obey the relation

$F_2(x, Q^2) = 2xF_1(x, Q^2)$ known as the Callan-Gross relation. These features in the data can be explained by assuming that the DIS experiment is dominated by the scattering of a single virtual photon from point-like spin-half constituents of the proton called the partons. This is beacuse if electric charges were uniformly distributed within the nucleon then the wide-angle scattering would be very rare giving rise to structure functions that decrease rapidly with Q^2. The fundamental relation of the parton model for DIS is given by

$$d\sigma(p, q) = \sum_i \int_0^1 d\xi \, d\sigma_B \left(\xi p, q\right) f_{i/N}(\xi) \,, \tag{2.10}$$

where $d\sigma$ is the inclusive cross section for nucleon-electron scattering, $d\sigma_B$ is the lowest-order (Born) elastic parton-electron cross section where the parton's momentum p is given by a fraction ξ of the proton's momentum, ξp with ξ between zero and one. The function $f_{i/N}$ are parton distributions which describe the probability of finding a parton (of flavor i) in the hadron N. These parton distribution functions are universal and process-independent in the sense that they are the same for all inclusive scattering processes.

2.3 $e^+e^- \to$ Jets

Higher-order QCD calculations are plagued by infrared (IR) divergences. To study these IR divergences, we will compute the cross section for an example process of electron positron annihilation into quark antiquark pair at next-to-leading order (NLO). Such a 1-loop calculation will give us an idea of the origin of IR divergences and Sudakov logarithms in QCD and will help us build our understanding of higher-order calculations in SCET which reproduce exactly the same IR divergences as QCD.

This process contains no color charge in the initial state, and it is convenient to visualize this process as an e^+e^- annihilating into a virtual photon, which then decays into either a muon pair or a quark-antiquark pair. According to the Kinoshita, Lee and Nauenberg (KLN) theorem, at any order in perturbation theory, if we sum over all quark and gluon final states the resulting cross section should be finite even for massless quarks and gluons. However the total cross section for the emission of a single real gluon, $e^+e^- \to q\bar{q}g$, is infinite. The divergence in the real emission process comes from the energy of the gluon going to zero or when the outgoing gluon and quark become parallel, referred to as the (infrared) soft singgularity and collinear singularity respectively. This divergence is cancelled by the virtual gluon correction to the quark-vector-boson vertex. The virtual corrections are UV-finite after renormalization but are IR-divergent. A regularization procedure is required that will control the IR divergences in the individual real and virtual contributions such

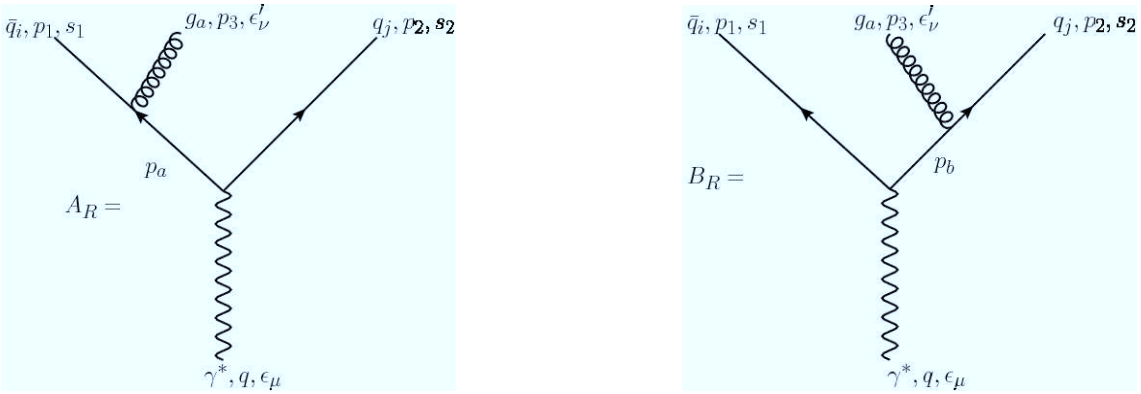

Figure 2.2: *Feynman diagrams for the decay of a virtual photon into a quark-antiquark pair and a gluon.*

that the sum is finite.

The Born cross section for the process $e^+e^- \to q\bar{q}$ is fairly straightforward to compute and is the same as $e^+e^- \to \mu^+\mu^-$ with an additional color factor. The two-body differential decay rate for $\gamma^* \to q\bar{q}$ is given by

$$\begin{aligned} d\Gamma &= \frac{1}{2E_{\text{cm}}}|\overline{M}|^2 d^6\phi_2 \,, \\ d^6\phi_2 &= \frac{d^3p_1}{(2\pi)^3(2E_1)}\frac{d^3p_2}{(2\pi)^3(2E_2)}(2\pi)^4\delta^4(q-p_1-p_2)\,. \end{aligned} \tag{2.11}$$

The leading order (LO) cross section for $\gamma^* \to q\bar{q}$ is given by (where for massless particles $E_1 = E_2 = Q/2$)

$$\Gamma(\gamma^* \to q\bar{q}) = \sigma_0 = 3\alpha e_q^2 Q\,, \tag{2.12}$$

where e_q is the charge of the quark.

We will now consider the decay of a virtual photon γ^* into a quark-antiquark pair and a real gluon as shown in Fig. 2.2. The 3-body differential decay rate is given by

$$d\Gamma = \frac{1}{2E_{\text{cm}}}|\overline{M}|^2 d\phi_3\,, \tag{2.13}$$

where the three-body phase space factor is

$$d\phi_3 = \frac{d^3p_1}{(2\pi)^3 2E_1}\frac{d^3p_2}{(2\pi)^3 2E_2}\frac{d^3p_3}{(2\pi)^3 2E_3}(2\pi)^4\delta(q-p_1-p_2-p_3)\,. \tag{2.14}$$

Integrating over the three-momentum of particle 3 using the delta function, the phase space

factor simplifies to

$$d\phi_3 = \frac{(2\pi)^4}{8(2\pi)^9}\frac{d^3p_1 d^3p_2}{E_1E_2E_3}\,\delta(E_1+E_2+E_3-Q) \quad \text{and}$$
$$\int \frac{d^3p_1 d^3p_2}{2E_1 2E_2} = \int 2\pi^2 E_1 dE_1 E_2 dE_2 \int_{-1}^{1} dz\,, \tag{2.15}$$

where $z = \cos\theta_{12}$ is the angle between particle 1 and 2. Further simplification yields

$$d\phi_3 = \frac{1}{4(2\pi)^3} dE_1\, dE_2\, dE_3\, \delta(E_1+E_2+E_3-Q) = \frac{Q^2 dx_1 dx_2}{16(2\pi)^3}\,, \tag{2.16}$$

where we define

$$x_i = \frac{2E_i}{Q} \quad \text{and} \quad p_i \cdot p_j = \frac{1}{2}Q^2(1-x_k)\,. \tag{2.17}$$

The differential cross section then becomes

$$\frac{d\sigma}{dx_1 dx_2} = \frac{Q}{32(2\pi)^3}|\overline{M}|^2\,. \tag{2.18}$$

The amplitudes for this process from the Feynman diagrams given in Fig. 2.2 are

$$A_R = \bar{u}(p_2,s_2)\,(-ig_s\gamma^\rho T^a_{ij})\,\epsilon_\rho \left(\frac{i\not{p}_a}{p_a^2}\right)(-iee_q\gamma^\mu)\,v(p_1,s_1)\,,$$
$$B_R = \bar{u}(p_2,s_2)\,(-iee_q\gamma^\mu)\left(\frac{i\not{p}_b}{p_b^2}\right)(-ig_s\gamma^\rho T^a_{ij})\,\epsilon_\rho\, v(p_1,s_1)\,, \tag{2.19}$$

where $p_a = p_2 + p$ and $p_b = p_1 + p$. The spin averaged matrix element squared is given by

$$|\overline{M}|^2 = |A_R|^2 + |B_R|^2 + 2A_R B_R = 32 g_s^2 e^2 e_q^2 \frac{(x_1^2+x_2^2)}{(1-x_1)(1-x_2)}\,. \tag{2.20}$$

Combining Eq. (2.20), Eq. (2.18) and using the definition of σ_0 from Eq. (2.12), the differential cross section becomes

$$\frac{1}{\sigma_0}\frac{d\sigma}{dx_1 dx_2} = \frac{2\alpha_s}{3\pi}\frac{x_1^2+x_2^2}{(1-x_1)(1-x_2)}\,. \tag{2.21}$$

The α_s correction to the Born cross section due to the emission of a real gluon is arrived at by integrating the above differential cross section over the allowed region of x_1 and x_2. The allowed phase space region for massless quarks and gluons is the triangular region: $0 \le x_1 \le 1$ and $1 - x_1 \le x_2 \le 1$. The integral thus becomes

$$\sigma(\text{real}) = \frac{2\alpha_s}{3\pi}\sigma_0 \int_0^1 dx_1 \int_{1-x_1}^1 dx_2 \frac{x_1^2+x_2^2}{(1-x_1)(1-x_2)}\,. \tag{2.22}$$

We can see clearly that the integrand diverges as x_1 or x_2 goes to 1. The origin of the

divergence can be seen by considering

$$(1 - x_1) \sim p_2 \cdot p_3 = E_2\omega(1 - \cos\theta_{23})\,, \tag{2.23}$$

where E_2 and ω are the energies of outgoing quark and gluon respectively. The divergence occurs when either the gluon becomes soft, that is, the energy of the gluon goes to zero ($\omega \to 0$), referred to as the soft divergence, or the gluon becomes collinear to the quark direction ($\cos\theta_{23} \to 1$), called the collinear divergence, or both.

We need to decide some way of regularizing these IR divergences so that they can cancel between the real and virtual corrections and give a finite cross section. Dimensional regularization can be used to regularize both the divergences. Calculations are performed in $N = 4-2\epsilon$ dimensions and in the end after adding together the real and virtual corrections one sets $N = 4$.

We need to recompute the Born term ($\gamma^* \to q\bar{q}$) in N dimensions. The two body differential decay rate in N dimensions is

$$d\Gamma = \frac{1}{2E_{\rm cm}}|\overline{M}|^2 d^{2N-2}\phi_2\,, \tag{2.24}$$

where the 2-body phase space factor is given by

$$d^{2N-2}\phi_2 = \frac{d^{N-1}p_1}{(2\pi)^{N-1}(2E_1)}\frac{d^{N-1}p_2}{(2\pi)^{N-1}(2E_2)}(2\pi)^N\delta^N(q - p_1 - p_2)\,. \tag{2.25}$$

In N dimensions the matrix element squared is given by

$$|\overline{M}|^2 = 32(N-2)e_q^2e^2Q \tag{2.26}$$

The Born cross section in N dimensions is

$$\sigma_{0,N} = 3\alpha e_q^2 Q\frac{\Gamma[2-\epsilon]}{\Gamma[2-2\epsilon]}\Big(\frac{Q^2}{4\pi}\Big)^{-\epsilon}\,. \tag{2.27}$$

We now need to compute the decay rate of a virtual photon into a quark antiquark pair and a gluon in N dimensions. The three body decay rate in N dimensions is

$$d\Gamma = \frac{1}{2E_{\rm cm}}|\overline{M}|^2 d^{3N-3}\phi_3\,, \tag{2.28}$$

where the 3-body phase space is given by

$$d^{3N-3}\phi_3 = (2\pi)^N \delta^N(Q-p_1-p_2-p)\frac{d^{N-1}k_1}{(2\pi)^{N-1}2E_1}\frac{d^{N-1}k_2}{(2\pi)^{N-1}2E_2}\frac{d^{N-1}k_3}{(2\pi)^{N-1}2E_3},$$
$$\int\int \frac{d^{N-1}p_1}{2E_1}\frac{d^{N-1}p_2}{2E_2} = \frac{2^{N-3}\pi^{N-2}}{\Gamma[N-2]}E_1^{N-3}dE_1 E_2^{N-3}dE_2\int_{-1}^{1}dz(1-z^2)^{N/2-2}. \tag{2.29}$$

Here the 3-body phase space in 4 dimensions given in Eq. (2.15) can be generalized to N dimesions. The amplitude squared in N dimensions is given by

$$|\overline{M}|^2 = 32 g_N^2 e^2 e_q^2\Big[(1-\epsilon)\Big(\frac{x_1^2+x_2^2}{(1-x_1)(1-x_2)}\Big) - 2\epsilon(1-\epsilon)\Big(\frac{2-2x_1-2x_2+x_1x_2}{(1-x_1)(1-x_2)}\Big)\Big], \tag{2.30}$$

where $g_N = g_s/\mu^{-\epsilon}$ is the N dimensional coupling.

Combining the phase space factor and the matrix element one arrives at

$$\sigma_{DR}(\text{real}) = \frac{2\alpha_s}{3\pi}\sigma_{0,N}\Big(\frac{Q^2}{4\pi\mu^2}\Big)^{-\epsilon}\frac{1}{\Gamma[2-\epsilon]}\int_0^1 dx_1 x_1^{-2\epsilon}\int_{1-x_1}^1 dx_2 x_2^{-2\epsilon}\Big(\frac{1-z^2}{4}\Big)^{-\epsilon}|\overline{M}|^2. \tag{2.31}$$

This differential cross section has a similar divergence structure for $\epsilon \to 0$ as in the case of 4 dimensions. The total cross section after integrating over the allowed region of x_1 and x_2 is

$$\sigma_{DR}(\text{real}) = \frac{2\alpha_s}{3\pi}\sigma_{0,N}\Big[\frac{2}{\epsilon^2} + \frac{3-2\gamma_E+2\log(4\pi)-2\log(Q^2/\mu^2)}{\epsilon} + \frac{19}{2} - 3\gamma_E + \gamma_E^2 - \frac{7\pi^2}{6}$$
$$+ (3-2\gamma_E)\log 4\pi + \log(4\pi)^2 + (-3+2\gamma_E-2\log 4\pi)\log\Big(\frac{Q^2}{\mu^2}\Big) + \log^2\Big(\frac{Q^2}{\mu^2}\Big)\Big]. \tag{2.32}$$

The $1/\epsilon^2$ is a double singularity coming from soft and collinear divergences, while $1/\epsilon$ is a single pole when the gluon is either soft or collinear. We expect to get the same divergences from the virtual corrections so that the cross section is finite. The logarithms of Q^2/μ^2 here are called the Sudakov logarithms. Note that a similar calculation in SCET will reproduce the same IR divergences and logarithms and matching QCD to SCET will result in matching coefficients that are independent of the IR divergences.

Virtual gluon corrections: The virtual gluon corrections come from two sources, the vertex correction and the self energy graphs. The self energy graph vanishes in dimensional regularization, so for simplicity we only calculate the diagram shown in Fig. 2.3. Since the final state is the same as the Born term and we are interested in the correction to the graph given by A_0, we need to compute $\text{Re}(A_0 A_v)$. The amplitudes for the Feynman digrams

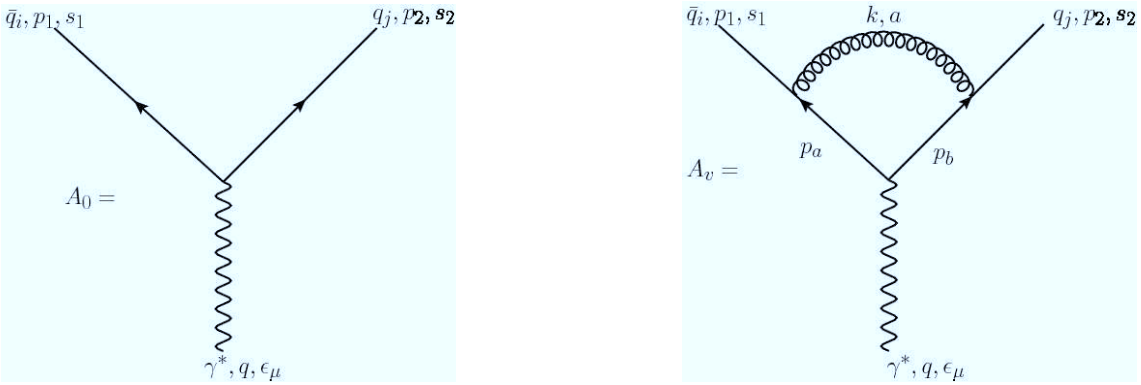

Figure 2.3: *Left: Feynman diagram for the Born cross section $\gamma^* \to q\bar{q}$, Right: Feynman diagram for the virtual corrections to the Born cross section.*

given in Fig. 2.3 are

$$A_v = \bar{u}(p_2)\,(-ig\gamma_\beta T^e_{il})\,\frac{i\not{p}_b}{p_b^2}\,(-iee_q\gamma_\mu)\left(\frac{i\not{p}_a}{p_a^2}\right)(-ig\gamma_\alpha T^e_{ji})\left(\frac{-ig_{\beta\alpha}}{k^2}\right)v(p_1)\epsilon^\mu(q)\,,$$
$$A_0 = -iee_q\,\bar{u}(p_2)\,\gamma_\mu\,v(p_1)\,\epsilon^\mu(q)\,, \tag{2.33}$$

and the cross section is

$$\sigma_v = \frac{1}{16\pi Q}\int\frac{d^4k}{(2\pi)^4}(2A_0A_v^*) = \frac{8}{3}\sigma_0 g_s^2(-i)\int\frac{d^4k}{(2\pi)^4}\frac{N(p_1,p_2,k,q)}{(p_1-k)^2(p_2+k)^2k^2}\,, \tag{2.34}$$

where

$$\frac{N(p_1,p_2,k,q)}{k^2} = \frac{q^2}{k^2}\Big[-2+8\frac{(p_1\cdot k)(p_2\cdot k)}{q^4}+4\frac{p_2\cdot k - p_1\cdot k}{q^2}\Big] = \frac{q^2}{k^2}N_1(p_1,p_2,k,q)\,. \tag{2.35}$$

Here we have considered Feynman gauge. Using the Feynman parameterization given by

$$\frac{1}{ab} = \int_0^1 dy\frac{1}{(ay+b(1-y))^2}\,, \tag{2.36}$$

the cross section can be reexpressed as

$$\sigma_v = \frac{8}{3}\sigma_0 g_s^2(-i)\int\frac{d^4k}{(2\pi)^4}\frac{N(p_1,p_2,k,q)}{(k^2-2p_y\cdot k)^2k^2}\,, \tag{2.37}$$

where $p_y = yp_1 - (1-y)p_2$. Simplifying further using

$$\frac{1}{c^2d^2} = \int_0^1 dx\frac{2x}{(cx+d(1-x))^3}\,, \tag{2.38}$$

In N dimensions the cross section has the form

$$\sigma(\text{virtual}) = \frac{8}{3} g_N^2 (-i) \int \frac{d^N K}{(2\pi)^N} \int_0^1 dy \int_0^1 \frac{2xq^2 N_1(k \to K + xp_y)}{(K^2 - C)^3} \,, \tag{2.39}$$

where

$$N_1(k \to K + xp_y) = -2 - 2x^2 y(1-y) + 2x + (1-2\epsilon)\frac{4}{N}\frac{K^2}{q^2} \,. \tag{2.40}$$

The integrals over K, x and y yield

$$\begin{aligned}\sigma(\text{virtual}) = \frac{2\alpha_s}{3\pi}\sigma_{0,N}\Big[\frac{-2}{\epsilon^2} + \frac{-3 + 2\gamma_E - 2\log(4\pi) + 2\log(Q^2/\mu^2)}{\epsilon} - 8 + 3\gamma_E - \gamma_E^2 + \frac{7\pi^2}{6} \\ + (-3 + 2\gamma_E)\log 4\pi - \log(4\pi)^2 - (-3 + 2\gamma_E - 2\log 4\pi)\log\Big(\frac{Q^2}{\mu^2}\Big) - \log^2\Big(\frac{Q^2}{\mu^2}\Big)\Big] \,.\end{aligned} \tag{2.41}$$

Comparing this virtual contribution with the real in Eq. (2.32), we see that both have exactly the same divergences and logarithms. Combining the real and virtual corrections, the NLO correction to the Born cross section is

$$\sigma_{DR}(\text{real}) + \sigma_{DR}(\text{virtual}) = \frac{2\alpha_s}{3\pi}\sigma_0 \frac{3}{2} = \frac{\alpha_s}{\pi}\sigma_0 \tag{2.42}$$

The main point of this calculation is to explicitly see that the virtual correction has the same IR divergences as the real one, and hence adding the two results in a finite cross section for $e^+e^- \to q\bar{q}$ at next-to-leading order (NLO). This calculation also gives a basic understanding of soft and collinear divergences which are a universal property of any QCD process.

2.4 Resummation of large logarithms

Consider that the partons are now in the initial state for e.g. Drell Yan ($q\bar{q} \to l^+l^-X$) or Higgs production process ($gg \to HX$). Consider the emission of a gluon in the collinear limit as shown in the Fig. 2.4. For this case, we can write down the Sudakov decomposition of the four momentum as

$$k = zp + \xi n + k_T \;,\; k' = (1-z)p - \xi n - k_T \;,\; k^2 = \frac{-k_T^2}{1-z} \;,\; \xi = \frac{-k_T^2}{2(1-z)} \,. \tag{2.43}$$

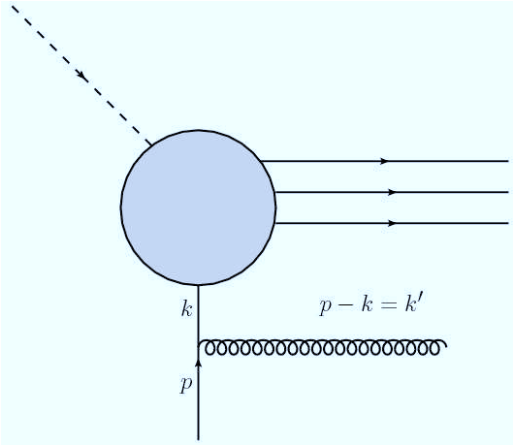

Figure 2.4: *Emission of a gluon (in the collinear limit) from an initial state parton.*

The amplitude for this process is

$$M_1 = (-ig_s)[M(k)\frac{i}{\not k}\gamma^\mu t^a u(p,s)\epsilon^*_\mu(k',\lambda)] = \frac{-g_s}{k_T^2}(1-z)[M(k)\not k\gamma^\mu u(p,s)\epsilon\mu^*(k',\lambda)]\,. \tag{2.44}$$

The matrix element squared for this process is given by

$$|\overline{M}|^2 = \frac{4\pi\alpha_s}{k_T^2}C_F\frac{1}{2}Tr[M(k)\not pM^\dagger(k)](1+z^2)\,. \tag{2.45}$$

The phase space factor is

$$d\phi_3 \sim \frac{d^3k'}{(2\pi)^3 2k'_0} \sim \frac{1}{(4\pi)^2}\frac{dz}{1-z}\frac{d^2k_T}{\pi}\,. \tag{2.46}$$

Combining the phase space factor and the amplitude we get

$$\sigma_1^R(p) = \int\frac{dk_T^2}{k_T^2}\int_0^1 dz\frac{\alpha_s C_F}{2\pi}\frac{1+z^2}{1-z}\frac{1}{\Phi(p)}|\overline{M}_0(zp)|^2 = \int\frac{dk_T^2}{k_T^2}\int_0^1 dz\frac{\alpha_s C_F}{2\pi}P(z)\sigma_0(zp)\,, \tag{2.47}$$

where $P(z)$ is the splitting function defined by

$$P(z) = C_F\frac{1+z^2}{1-z}\,. \tag{2.48}$$

$\sigma_1^R(p)$ contains a soft singularity ($z \to 1$) and a collinear singularity ($k_T \to 0$). The soft singularity is cancelled by the virtual correction. Adding the real and virtual corrections,

the total 1-loop cross section is given by

$$\sigma_1^R(p) = \int \frac{dk_T^2}{k_T^2} \int_0^1 dz \frac{\alpha_s C_F}{2\pi} P(z)(\sigma_0(zp) - \sigma_0(p)) = \int \frac{dk_T^2}{k_T^2} \int_0^1 dz \frac{\alpha_s}{2\pi} P_+(z)\sigma_0(zp)\,. \tag{2.49}$$

Here we introduce the plus prescription $P_+(z)$ such that

$$\int dz g_+(z) f(z) = \int dz g(z)[f(z) - f(1)] \quad \text{implies}$$
$$P_+(z) = C_F\Big[\frac{1+z^2}{(1-z)_+} + \frac{3}{2}\delta(1-z)\Big]\,. \tag{2.50}$$

For $k_T \to 0$, the cross section diverges and thus is not collinear safe. This can be regularized by a cut-off μ_0. Then we can introduce a factorizations scale μ which separates the small and large k_T regions. The small k_T region which diverges for $\mu_0 \to 0$ is absorbed in the parton distribution functions. In this way the 1-loop cross section can be rewritten as

$$\sigma_1^R(p) = \int_{\mu_0^2}^{\mu^2} \frac{dk_T^2}{k_T^2} \int_0^1 dz \frac{\alpha_s}{2\pi} P_+(z)\sigma_0(yzp) + \sigma_1^R(yzp,\mu)\,. \tag{2.51}$$

The 1-loop cross section $\sigma_1^R(yzp,\mu)$ is now finite due to the infrared cutoff μ. The density of a quark inside a quark is given by

$$f_{q/q} = \delta(1-z) + \int_{\mu_0^2}^{\mu^2} \frac{dk_T^2}{k_T^2} \int_0^1 dz \frac{\alpha_s}{2\pi} P_+(z)\,. \tag{2.52}$$

The hadronic cross section in terms of $f_{q/H}(x,\mu)$ is then defined as

$$\sigma_H(P) = \int_0^1 dx f_{q/H}(x,\mu)\sigma_1(xp,\mu)\,, \tag{2.53}$$

where $f_{q/H}(x,\mu) = f_{q/q} \otimes f_{q/H}$ that is

$$f_{q/H}(x,\mu) = \int_x^1 \frac{dz}{z}\Big[\delta(1-z) + \int_{\mu_0^2}^{\mu^2} \frac{dk_T^2}{k_T^2}\frac{\alpha_s C_F}{2\pi} P_+(z)\Big] f_{q/H}\Big(\frac{x}{z}\Big)\,. \tag{2.54}$$

Taking a derivative with respect to μ we obtain

$$\mu^2 \frac{\partial f_{q/H}(x,\mu)}{\partial \mu^2} = \int_x^1 \frac{dz}{z}\frac{\alpha_s C_F}{2\pi} P_+(z) f_{q/H}\Big(\frac{x}{z}\Big)\,. \tag{2.55}$$

This is the leading order form of the Dokshitzer-Gribov-Lipatov-Altarelli-Parisi (DGLAP) equation [13] for the parton distribution $f_{q/H}(x,\mu)$. The above formula is however incomplete, because it only sums up the leading logarithmic contributions from a single type of splitting process – emission of a gluon from a quark line. There are other QCD branching processes that can also contribute at the leading logarithmic level- quark-antiquark, or

gluon pair production from a gluon, or gluon production from a quark. Including all of these effects, the DGLAP equation becomes a matrix equation. The important thing here to note is that the parton distributions now depend logarithmically on the scale Q. At each higher-order in perturbation series, there is an additional logarithm arising from the k_T integration and this equation resums logarithms of the form $\alpha_s^k \log^k(\mu/\mu_0)$ arising from multiple emissions of a gluon from a quark line where the successive emissions are strongly ordered in transverse momentum.

The hadronic production cross section for the Drell-Yan process or Higgs production and other LHC processes, now including both scales, reads

$$\sigma_{tot}(\mu_F, \mu_R) = \int_0^1 dx_1 \int_0^1 dx_2 \sum_{ij} f_i(x_1, \mu_F) f_j(x_2, \mu_F) \hat{\sigma}_{ij}(x_1 x_2 S, \alpha_s(\mu_R^2), \mu_R, \mu_F)\,. \quad (2.56)$$

where i, j are the incoming partons with momentum fractions $x_{i,j}$ and the partonic energy of the process is $s = x_i x_j S$ with S being the total energy. This is the collinear approximation where all partons are assumed to travel in the same direction as the incoming particle, i.e. they don't have a transverse momentum.

The cross section differential in transverse momentum q_T of the boson V has terms of the form $(\alpha_s C_F/k_T^2)\ln(Q^2/k_T^2)$. In the kinematic region where $q_T \ll Q$, large logarithms arise to all orders in the perturbative expansion and an all-order ressumation is needed to make sensible predictions. Consider the approximation such that the soft and collinear gluons are strongly ordered in k_T as $k_{T\,i,1}^2 \ll k_{T\,i,2}^2 \ll ... \ll k_{T\,i,N}^2 \leq q_T^2 \ll Q^2$. The resummed cross section in this approximation has the dominant contribution given by [14]

$$\begin{aligned}\frac{1}{\sigma_0}\frac{d\sigma}{dq_T^2} &= \frac{1}{q_T^2}\Big[\frac{\alpha_s C_F}{2\pi}\ln\Big(\frac{Q^2}{q_T^2}\Big) - \frac{\alpha_s^2 C_F^2}{8\pi^2}\ln^3\Big(\frac{Q^2}{q_T^2}\Big) + ... + \frac{-1^{N-1}}{2^{2N-2}}\frac{\alpha_s^N C_F^N}{\pi^N}\ln^{2N-1}\Big(\frac{Q^2}{q_T^2}\Big)\Big] \\ &= \frac{\alpha_s C_F}{2\pi q_T^2}\ln\Big(\frac{Q^2}{q_T^2}\Big)\exp\Big[\frac{-\alpha_s C_F}{4\pi}\ln^2\Big(\frac{Q^2}{q_T^2}\Big)\Big]\,. \end{aligned} \quad (2.57)$$

Due to the structure of the logs here, this approximation is called leading logarithmic (LL) approximation. However the strongly-ordered case is not the only dominant one in the small q_T limit. There are equally important non-strongly ordered contributions coming from the soft gluons whose transverse momentum vectorially add to give the overall q_T. To take into account such sub-leading logarithms, the resummation is performed in fourier conjugated b-space imposing transverse momentum conservation. Following the q_T resummation in [14] , a method to systematically resum the logarithmically enhanced contributions at small q_T was set up by Collins, Soper and Sterman in [15, 16] called the CSS formalism.

The phenomenological significance of transverse momentum resummation ranges from

Drell-Yan pair production to Higgs production at the LHC. At the LHC, besides the total cross section and the invariant mass distribution, the fundamental measurable used is the transverse momentum of the boson or of the jets. The Higgs analyses at the LHC use jet vetoes to minimize QCD background and to obtain cross sections with a fixed number of jets in the final state. The default jet variable by which jets are currently classified and vetoed is the transverse momentum p_T of a jet. To obtain an exclusive 0-jet cross section, the experiments put a cut on the maximum p_T of the jets, that is, allow only soft jets with $p_T^{\rm jet} < p_T^{\rm cut}$. For tight jet vetoes, $p_T^{\rm cut} \ll m_H$, large Sudakov logarithms of the form $\alpha_s^n \ln^m (p_T^{\rm cut}/m_H)$ with $m \leq 2n$ appear in the perturbative series and must be resummed. The leading 0-jet Higgs production cross section with such a veto has the following structure

$$\sigma_0(p_T^{\rm cut}) = \sigma_B\Big(1 - \frac{2\alpha_s C_A}{\pi} \ln^2 \frac{p_T^{\rm cut}}{m_H} + ...\Big) \tag{2.58}$$

where σ_B is the lowest-order cross section. Such large logarithms can be resummed in SCET, where the cross section is factorized into calculable pieces and the resummation is performed by renormalization group evolution (RGE). Schematically, a factorized cross section in SCET has the structure,

$$\sigma(p_T^{\rm cut}) \sim H_{gg} \times B_a \times B_b \times S\,, \tag{2.59}$$

where H_{gg} is the hard function which is determined by matching QCD onto the operators in SCET. B_a and B_b are the so-called beam functions which describe the initial state radiation in the n_a and n_b light-cone directions. The beam functions are defined as $B_i = \mathcal{I}_{ij} \otimes f_j$, where $\mathcal{I}_{ij}$ is the perturbatively calculable matching coefficient and f are the PDFs. S is the soft function which describes the soft-radiation. The way the evolution works roughly is as follows: One has the standard DGLAP evolution for PDFs from μ_Λ to μ_B, where μ_B is the beam scale. Each of the beam, soft and hard functions are evaluated at their natural scales (μ_B, μ_S, μ_H), and then evolved to a common scale μ which sums logarithms of the ratio of the scales using RGE. We will discuss in detail the structure of the factorized cross sections and resummation in the framework of SCET in chapter 4.

2.5 Spontaneous Symmetry breaking

Having discussed some of the basics of perturbative QCD calculations, and the origin and summation of large logarithms in any differential cross section predictions, we will now give a brief introduction of the Higgs Mechanism in the SM and the current status of the Higgs measurements at the LHC.

In the SM, the Brout-Englert-Higgs mechanism is essential to explain the generation of mass for the gauge bosons. The electroweak interactions of fermions exhibit a symmetry under the group $SU(2)_W \times U(1)_Y$. On contrast to the gauge bosons of the electromagnetic and strong interactions, the $W^{\pm}$, Z bosons of the electroweak interaction are found to have larger masses. Because pure gauge theory requires all gauge fields to be massless, adding an explicit mass term to the Lagrangian violates gauge invariance. Therefore, the formulation of a gauge theory for the electroweak interaction requires a concept of spontaneous symmetry breaking in which gauge fields are coupled with additional scalar fields, which owing to their self interactions, acquire non-vanishing vaccum expectation values (vevs).

To define spontaneous symmetry breaking , consider a Lagrangian that is invariant under a group of transformations G. There are two possibilities for the ground state $|0\rangle$: only a single ground state which is invariant under transformation or multiple degenerate ground states which transform into one another under the group G. For multiple ground states, choosing one of them causes the G symmetry to be spontaneously broken. Consider now the spontaneous breaking of a global symmetry as an example. Consider a Lagrangian describing the self-interaction of a complex scalar field $\phi(x) = 1/\sqrt{2}(\phi_1 + i\phi_2)$ given by

$$\mathcal{L} = (\partial^{\mu}\phi)^{\dagger}\partial_{\mu}\phi - V(\phi)\,, \tag{2.60}$$

where

$$V(\phi) = \frac{\lambda}{4}\Big(|\phi|^2 - \frac{\mu^2}{\lambda}\Big)^2 = \frac{\lambda}{4}|\phi|^4 - \frac{\mu^2}{2}|\phi^2| + \frac{\mu^4}{4\lambda} \tag{2.61}$$

is invariant under global phase transformations. The coupling λ is positive so that the energy is bounded from below. There are two possibilities for the sign of μ^2. For $\mu^2 < 0$, the field ϕ has a mass $M^2 = -\mu^2$ and the potential $V(\phi)$ has a unique vaccum $\phi_0(x) = 0$. When $\mu^2 > 0$, there are an infinite number of vacua that satisfy

$$\sqrt{\phi_1^2 + \phi_2^2} = \sqrt{\frac{-\mu^2}{\lambda}} = v\,. \tag{2.62}$$

From these we choose the ground state ϕ_0 as $\phi_1 = v$ and $\phi_2 = 0$. The perturbation around this vaccum is described as

$$\phi(x) = \frac{1}{\sqrt{2}}\Big(v + \eta(x) + i\xi(x)\Big)\,. \tag{2.63}$$

Here $\eta(x)$ and $\xi(x)$ are real fields describing small deviations around v and the phase of the field ϕ from the ground state. Inserting the above defined field into the Lagrangian

yields

$$\mathcal{L} = \frac{1}{2}(\partial_\mu \xi)(\partial^\mu \xi) + \frac{1}{2}(\partial_\mu \eta)(\partial^\mu \eta) - \lambda v^2 \eta^2 + \text{higher order terms}\,. \tag{2.64}$$

Here $\eta(x)$ is a scalar field with mass $\sqrt{2\lambda v^2} = \sqrt{-2\mu^2}$ while $\xi(x)$ is a massless scalar field known as the Goldstone field. The excitations of $\xi(x)$ results in the appearance of new massless scalar particles called Goldstone boson. There is one scalar particle, called a Nambu-Goldstone boson, for each generator of the symmetry that is broken. Goldstone theorem says that for each broken generator of the original symmetry group, i.e. for each generator that connects the vacuum states one massless spin-zero particle will appear. Spontaneously breaking a continuous global symmetry gives rise to a massless (Goldstone) boson. When a local gauge symmetry is broken, something special will happen and the Goldstone boson will disappear and will be "eaten up" by the gauge bosons which become massive.

2.6 Higgs Mechanism in the Standard Model

Among the electroweak gauge bosons only the photon is masless, while the other gauge bosons are massive, so the $SU(2)_L \otimes U(1)_Y$ gauge symmetry must be broken down to $U(1)_{\text{em}}$. The breaking is accomplished via the Higgs mechanism which is also responsible for the generation of fermion masses. To obtain gauge boson masses additional terms are added to the Lagrangian of a scalar field

$$\mathcal{L}_{\text{scalar}} = (D^\mu \phi)^\dagger (D_\mu \phi) - V(\phi)\,, \tag{2.65}$$

where

$$V(\phi) = \mu^2(\phi^\dagger \phi) + \lambda(\phi^\dagger \phi)^2 \;\text{ and }\; D_\mu = \partial_\mu + ig\frac{1}{2}\bar{\tau}\cdot\bar{W}_\mu + ig'\frac{1}{2}YB_\mu\,. \tag{2.66}$$

Since the Lagrangian should retain all symmetries only the $SU(2)_L \otimes U(1)_Y$ multiplets can be added. We add an isospin doublet given by

$$\phi = \begin{pmatrix} \phi^+ \\ \phi^0 \end{pmatrix} = \begin{pmatrix} \phi_1 + i\phi_2 \\ \phi_3 + i\phi_4 \end{pmatrix}. \tag{2.67}$$

Any choice of vaccum that breaks a symmetry will generate a mass for the corresponding gauge boson. The vacuum we choose has $\phi_1 = \phi_2 = \phi_4 = 0$ and $\phi_3 = v$

$$\phi_0 = \frac{1}{\sqrt{2}}\begin{pmatrix} 0 \\ v \end{pmatrix}. \tag{2.68}$$

The perturbation around this vaccum state is given by

$$\phi(x) = \exp\left(\frac{i\vec{\xi}(x)\cdot\vec{\tau}}{v}\right)\begin{pmatrix}0\\ v+h(x)\end{pmatrix}. \tag{2.69}$$

Here $h(x)$ is the real field. To eliminate the unphysical (would be Goldstone boson) fields ξ, we make a gauge transformation in the form

$$\phi'(x) = U(\xi(x))\phi(x) = \begin{pmatrix}0\\ v+h(x)\end{pmatrix} \tag{2.70}$$

where $U(\xi) = \exp\left(\frac{-i\vec{\xi}(x)\cdot\vec{\tau}}{v}\right)$. This is called the unitary gauge. For simplicity, in what follows we will continue to use the notation $\phi(x)$ for the field $\phi'(x)$ in the unitary gauge. Plugging in the definition of $\phi(x)$ in the Lagrangina, the kinetic term becomes

$$(D^\mu\phi)^\dagger D_\mu\phi = \frac{1}{8}v^2[g^2(W_1^2+W_2^2)+(-gW_3^\mu+g'YB_\mu)^2]+\frac{1}{2}(\partial_\mu h)^2+\dots. \tag{2.71}$$

The first term is the mass term $M_W^2 W_\mu^+ W^{-\mu}$ for the charged gauge boson field

$$W^\pm = \frac{1}{\sqrt{2}}(W_\mu^1 \mp iW_\mu^2) \quad \text{with} \quad M_W = \frac{1}{2}vg \tag{2.72}$$

The second term mixes two neutral components of the gauge fields W_3^μ and B^μ but after diagonalization in the form

$$Z_\mu = \frac{gW_\mu^3 - g'B_\mu}{\sqrt{g^2+g'^2}} \quad , \quad A_\mu = \frac{gW_\mu^3+g'B_\mu}{\sqrt{g^2+g'^2}} \tag{2.73}$$

The Z boson acquires a mass $1/2M_Z^2 Z_\mu Z^\mu$ where $M_Z = (1/2)v\sqrt{g^2+g'^2}$. Thus by spontaneous breaking of $SU(2)_L \times U(1)_Y \to U(1)_Q$, three goldstone bosons have been absorbed by W^+, W^- and Z bosons to form their longitudinal component and get their masses. Since the $U(1)$ symmetry is unbroken, the photon remains massless.

The kinetic part of the Higgs field comes from the covariant derivate term shown before, while the Higgs mass and self-interaction parts come from the scalar potential. The SM Higgs Lagrangian is given by

$$\mathcal{L}_H = \frac{1}{2}(\partial_\mu h)^2 - \frac{2\lambda v^2}{2}h^2 - \lambda v h^3 - \frac{\lambda}{4}h^4 + \frac{\lambda v^4}{4}. \tag{2.74}$$

From this we know that the Higgs boson mass is $M_H^2 = 2\lambda v^2$.

Fermion masses: The fermions in the SM consist of leptons and quarks. Fermion masses can be generated by the Yukawa coupling λ_f of the Higgs field to the fermion field. Such

a term is given by

$$\mathcal{L}_{\text{Yukawa}} = -[\bar{l}_L \lambda_l \phi e_R + \bar{q}_L \lambda_d \phi d_R + \bar{q}_L \lambda_u \bar{\phi} u_R + h.c.] \,. \tag{2.75}$$

Note that the first two terms give masses only to the down-type fermions. The charge-conjugated Higgs field $\bar{\phi} = -i\sigma_2 \phi^*$ is needed to give masses to the up-type fermions. The mass of the leptons is $m_L = \lambda_l v/\sqrt{2}$. The mass eigenstates of quarks are obtained by unitary transformation of the quark fields, the diagonalised mass matrix for up and down type quarks is given by

$$m_u = \frac{v}{\sqrt{2}} (U_L^U)^\dagger \lambda_u U_R^U \;\; , \;\; \mu = \frac{v}{\sqrt{2}} (U_L^D)^\dagger \lambda_D U_R^D \,, \tag{2.76}$$

where $V_{CKM} = U_L^{U\dagger} U_L^D$ is the 'Cabibbo-Kobayashi-Maskawa (CKM)' quark mixing matrix.

2.7 Higgs boson discovery

At the LHC, the relevant Higgs boson production modes are gluon-gluon fusion (ggF), vector boson fusion (VBF), production in association with a vector boson (V) and in association with top quarks (ttH). The five most sensitive Higgs boson decay channels at the LHC are the modes $H \to \gamma\gamma$, $H \to ZZ \to 4l$, $H \to WW$, $H \to \tau\tau$ and $H \to b\bar{b}$. At lower Higgs masses, the dominant decay channels are $\tau\tau$ and $b\bar{b}$ while the decay to bottom pairs and W pairs become equal for Higgs masses of about 130 GeV. In July 2012, the ATLAS experiment with proton-proton energies of 7 TeV and 8 TeV observed a peak with an invariant $\gamma\gamma$ or 4l mass of 126 GeV and a combined significance of 5.9σ [5]. The channels which contributed to the statistical discovery are Higgs decays $H \to ZZ \to 4l$, $H \to \gamma\gamma$ and $H \to W^+W^- \to 2l2\nu$. The CMS experiment observed a similar excess at a mass of 125 GeV with a local significance of 5σ [6].

Fig. 2.5 shows the tree level diagrams of the four main Higgs production channels in pp collision. The ggF is the dominant process over the whole mass spectrum followed by the VBF which is an order of magnitude lower than ggF for a large range of the Higgs masses. The remaining production processes have a very small cross section, much smaller than those of ggF and VBF. We will now consider in detail the two most relevant production mechanisms – ggF and VBF here.

Gluon gluon fusion: At tree level the Higgs hardly couples to light-flavor quarks and has no coupling to gluons. The ggF process $gg \to H + X$, shown by the top left Feynman diagram in Fig. 2.5, is mediated by a virtual top quark loop and contributions from lighter quarks in the loop are suppressed proportional to m_q^2. The channel $gg \to H \to b\bar{b}$ has

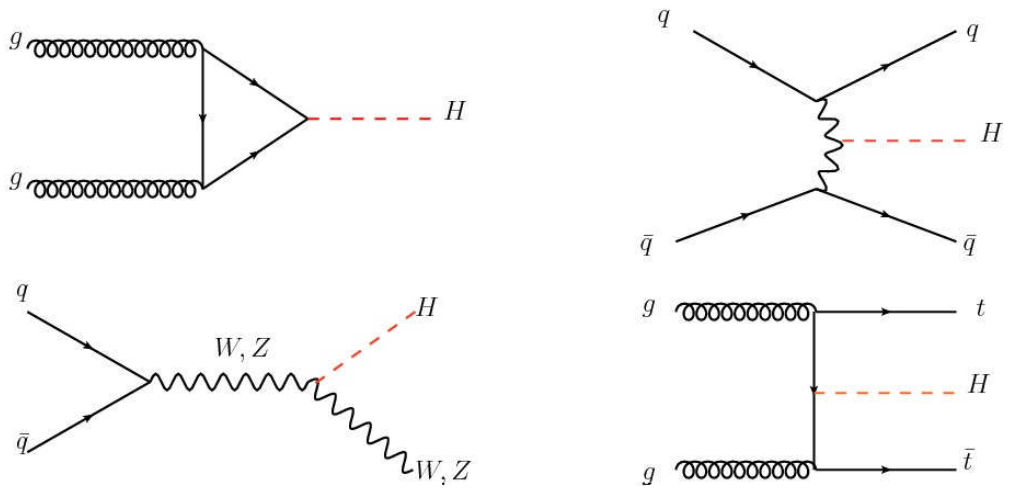

Figure 2.5: *Feynman diagrams for the Higgs boson production. Top panel: gluon gluon fusion (left) and vector boson fusion (right). Bottom panel: Higgs-strahlung or associated production with a gauge boson (left) and associated production with top quarks (right).*

a large branching ratio but is very hard to measure due to the dominating $gg \to b\bar{b}$ background. $H \to \gamma\gamma$ is, in spite of the small rate, one of the main Higgs discovery channel because $m_{\gamma\gamma}$ can be reconstructed to $O(1\%)$. $H \to ZZ \to 4l$, works great, in particular for muons, because of the fully reconstructed m_{4l} and is called the 'golden channel' at the LHC. $H \to W^+W^-$ has a large rate but a dominant background is $t\bar{t}$ production. $H \to \tau\tau$ is problematic because if taus decay leptonically we can identify them in the detector, but there will appear one or two neutrinos in the decay so reconstructing the τ momentum is not possible.

Including the full dependence on the quark and Higgs boson masses, the cross section has been calculated at the next-to-leading order (NLO) [17,18]. To a very good approximation, the leading top-quark contribution can be evaluated in the limit $m_t \to \infty$ by matching the Standard Model to an effective theory. In this approximation the cross section is known at next-to-next-to-leading order (NNLO) [19,20] and recently N^{3}LO has also been computed [21,22]. The NLO QCD corrections increase the leading-order prediction for the cross section by about 80%, and the NNLO corrections further enhance the cross section by approximately 20%. Besides considering the inclusive Higgs boson production cross section at the LHC, it is important to study differential distributions in order to probe the properties of the Higgs boson in a detailed way. A more exclusive account of Higgs production is required because the experimental analyses often impose cuts in order to improve the signal-to-background ratio and to distinguish between different production and decay channels depending on the number of jets. By vetoing jets, one restricts the phase space for additional emissions. This makes the cross section sensitive to soft and collinear radiation, which induces Sudakov double logarithms of the jet-veto observable that need to be resummed as explained in Sec. 2.4. Efforts have been made to obtain

resummed predictions for the Higgs production cross section with a jet-veto for "H+0-jet" upto NNLL′+ NNLO order in [23–25]. There has been activity in computing the Higgs cross section in association with jets e.g. H+1-jet [26] at NNLL accuracy and in [27] at NNLO. The $gg \to H$+2-jets cross section is computed in [28] at NLO and the NLO predictions have been matched to parton showers in [29,30] which provide leading-log (LL) resummation. An all order resummation of soft gluon emissions in the presence of a central jet veto is performed in [31,32].

Vector boson fusion: Higgs boson production via VBF $qq \to qqH$, as shown in the top-right of Fig. 2.5, proceeds by the scattering of two (anti-)quarks, mediated by t- or u-channel exchange of a W or Z boson, with the Higgs boson radiated off the weak-boson propagator. It has a very clear experimental signal due to the presence of two spectator jets in the forward region. These characteristic features of VBF processes can be exploited to distinguish them from overwhelming QCD backgrounds as well as from including gluon-fusion induced H+2-jet production. The total cross section and differential distributions for Higgs production via VBF has been computed upto NNLO in [33], the parton shower effects have been studied in [34] and the NLO QCD result has been matched to parton shower in [35,36]. After the application of specific selection cuts to enhance the VBF signal over the ggF background, the VBF channel provides a clean environment not only for the Higgs searches but also for the determination of the Higgs boson couplings at the LHC.

Current Higgs results: Both ATLAS and CMS have published in [37] a measured value of the mass of the Higgs boson using the high precision $H \to \gamma\gamma$ and $H \to ZZ^* \to 4l$ channels, coresponding at $\sqrt{s} = 7, 8\,\text{TeV}$. The two collaborations joined forces to combine these measurements and they obtained the Higgs mass, $m_H = 125.09 \pm 0.24\,(0.21\,\text{stat} \pm 0.11\,\text{syst.})\,\text{GeV}$, the most precise measured value to date.

Distributions of the differential $pp \to H$ cross sections have been measured by ATLAS [38,39] as a function of the jet multiplicity N_{jet}, the Higgs boson transverse momentum p_T^H, the transverse momentum of the leading jet p_{Tj1} and beam-thrust like observables $\mathcal{T}_C^{\text{jet}}(\mathcal{T}_1)$. The p_{Tj1} and N_{jet} measurements have been compared to theoretical predictions as shown in the first two plots of Fig. 2.6. The last plot shows the measurement of cross section in the $H \to \gamma\gamma$ channel in bins of $\mathcal{T}_C^{\text{jet}}$ for which theoretical predictions didn't exist. We have obtained the resummed predictions for $\mathcal{T}_C^{\text{jet}}$ and we will present a comparison with this measurement in chapter 4.

The signal strength which allows one to compare the measured cross sections (σ) of each decay channel, to that predicted by the SM, (σ_{SM}) is defined as

$$\mu_i^f = \frac{\sigma_i \times BR_f}{(\sigma_i \times BR)_{SM}} \equiv \mu_i \times \mu_f \tag{2.77}$$

where $\mu_i = \sigma_i/(\sigma_i)_{SM}$ and $\mu_f = BR_f/(BR_f)_{SM}$ denote the signal strength for production and decay respectively. Studies of the production and decay properties of the Higgs boson where the Higgs boson decays into vector bosons, $(\gamma\gamma, ZZ, WW, Z\gamma)$ and into fermions $(\tau\tau, bb, \mu\mu)$ were found to be compatible with $\mu = 1$, corresponding to Standard Model predictions. The new combination of all production and decay channels gives $\mu = 1.0 \pm 0.13$ for CMS and 1.18 ± 0.10 for ATLAS.

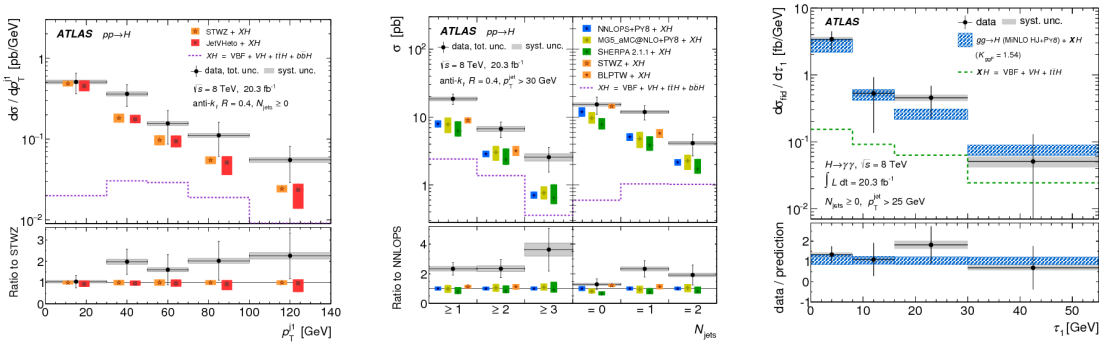

Figure 2.6: *Left: Differential cross section for inclusive Higgs production combining the $H \to \gamma\gamma$ and $H \to ZZ^*$ channels, compared to theoretical predictions for p_{Tj1}. Middle: Measured Higgs boson production cross sections in inclusive and exclusive jet multiplicity bins compared to different theoretical predictions. Right: Differential cross section in $H \to \gamma\gamma$ channel as a function of $\mathcal{T}_C^{\text{jet}}(\mathcal{T}_1)$. Figs. taken from Ref. [38, 39]*

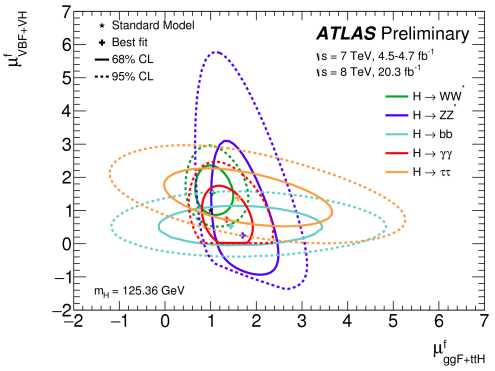

Figure 2.7: *Likelihood contours measured for $H \to \{\gamma\gamma, ZZ, WW, b\bar{b}, \tau\tau\}$ indicating the best-fit value to the data (+), 68% (full) and 95% (dashed) CL contours and the SM expectation. Fig. taken from Ref. [40]*

To measure the Higgs couplings to gauge bosons and fermions, the Higgs boson production modes are probed with four signal strength parameters μ_{VBF}, μ_{VH}, μ_{ggF} and μ_{ttH} for each production mode assuming SM value for the decay branching ratio ($\mu_f = 1$) in Eq. (2.77). The production processes can be categorised into two groups according to the Higgs boson couplings to fermions (ggF and ttH) or vector bosons (VBF and VH). For each decay channel f, the potential deviations from the SM can be tested with two signal strengths:

the coupling to vector bosons $\mu^{f}_{VBF+VH} \equiv (\mu_{VBF} = \mu_{VH})$ and the coupling to fermions $\mu^{f}_{ggF+ttH} \equiv (\mu_{ggF} = \mu_{ttH})$, assuming SM values for the ratio of ggF and ttH cross sections and the ratio of VBF and VH cross sections. Recent measurement of the couplings by ATLAS in [40] is shown in Fig. 2.7. The SM expectation of $\mu^{f} = 1$ is within 65% CL contour of most of these measurements.

For such coupling measurements, it is crucial to distinguish between ggF and VBF production mechanisms and for that as we will discuss in the next chapter it is important to have precise theory predictions for cross sections with a fixed number of jets in the final state. The focus of the next chapter will be to estimate uncertainties in the fixed-order predictions of exclusive jet cross sections in particular considering the H+2-jet cross section via ggF which is important for separating ggF and VBF.

Chapter 3

NLO Uncertainties in Higgs + 2 jets

This chapter reviews and extends the procedure of estimating jet binning uncertainties and is based on my work in [11]. In this, we present results for the NLO uncertainty in the H+2-jet cross section after implementing the VBF selection cuts used in the $H \to \gamma\gamma$ analyses of ATLAS and CMS. Typical VBF selections include indirect restrictions or explicit vetoes on additional jet activity, primarily to reduce non-Higgs backgrounds. We find that such restrictions have to be chosen carefully and are not necessarily beneficial for the purpose of distinguishing between the VBF and ggF production modes, since a modest reduction in the relative ggF contamination can be easily overwhelmed by its quickly increasing perturbative uncertainties.

3.1 Introduction

As discussed in the previous chapter, a central ingredient in measuring the properties of the Higgs boson is to separate out the different production mechanisms via gluon-gluon fusion (ggF) and vector boson fusion (VBF). To distinguish between different production processes and to maximize the signal sensitivity, ATLAS and CMS in their analyses separate the data into various exclusive selection categories, based on the number of jets ("jet bins"). In particular, in their VBF analyses the experiments apply different kinematic selection cuts to enhance the VBF signal and reduce the non-Higgs backgrounds as well as the sizable contamination from ggF production. One selection category, designed to isolate a clean VBF signal, is also the production in connection with two jets that are widely separated in rapidity. A characteristic feature of the VBF process is that it is accompanied by few extra gluon emissions, because of its color structure and incoming quarks. The same is not the case for ggF production or generic non-Higgs backgrounds, so the VBF signal tends to be

most significant in the exclusive 2-jet region of phase space with two forward jets and little additional radiation. Therefore, when optimizing its significance, whether in a cut-based approach or via multivariate techniques, one dominantly selects events from this region.

In general, placing a restriction on additional real emissions induces Sudakov logarithms at each order in the perturbative series as discussed in the previous chapter. In the limit of very tight restrictions, the logarithms become large and must be resummed to all orders in the strong coupling constant α_s to obtain a meaningful perturbative prediction. Often, the experimentally relevant region is an intermediate one, where the logarithmic corrections are already sizable but their resummation is not yet strictly necessary and a fixed-order expansion can still be applied. In this case, however, it is important that the possible sizable effects of higher-order logarithms are reflected in the perturbative uncertainty estimate for the fixed-order prediction.

Due to the incoming gluons in ggF and the associated large color factor, the logarithmic corrections in this intermediate region are indeed sizable. A numerically important ggF contribution to the VBF-like 2-jet selection is the partonic $gg \to Hgg$ process, where both incoming and outgoing gluons generate additional radiation. When restricting that radiation by forcing the kinematics into the exclusive 2-jet region, the logarithmic corrections can be expected to be large hence the perturbative uncertainties have to estimated carefully.

In Ref. [41] a simple method was devised that explicitly takes into account the size of the logarithmic corrections in the fixed-order uncertainty estimate (for which a simple scale variation in the exclusive jet cross section is insufficient). It has been adopted in Refs. [42, 43], and is being employed in various exclusive analyses at the LHC and the Tevatron. It is sometimes referred to as the "ST method." We applied this method to provide robust uncertainty estimates for the NLO calculation [28, 44] in the exclusive 2-jet bin in ggF production that was used in the ATLAS and CMS $7 - 8\,\text{TeV}$ Higgs analyses. We also discuss the application to more general cuts restricting to the exclusive 2-jet region. The next section gives a discussion of uncertainties associated with jet-binning and generalizes the basic procedure given in [41].

3.2 Jet Binning Uncertainties

Consider the *inclusive* N-jet cross section, $\sigma_{\geq N}$, for some process containing at least N jets. We will assume that $\sigma_{\geq N}$ is a sufficiently inclusive quantity such that it can be computed in fixed-order perturbation theory. We are interested in the case where $\sigma_{\geq N}$ is divided up

into a corresponding *exclusive* N-jet cross section, σ_N, and a remainder $\sigma_{\geq N+1}$,

$$\sigma_{\geq N} = \sigma_N(\text{excl. cut}) + \sigma_{\geq N+1}(\text{inverse excl. cut})\,. \tag{3.1}$$

All three cross sections here have the *same* selection cuts applied that identify the leading N signal jets. What defines σ_N to be "exclusive" is that the additional exclusive cut applied to it restricts the phase space of additional emissions in such a way that σ_N is dominated by configurations close to the N-parton Born kinematics. In particular, at leading order (LO) in perturbation theory $\sigma^{\text{LO}}_{\geq N} = \sigma^{\text{LO}}_N$, while relative to these, $\sigma_{\geq N+1}$ is suppressed by $O(\alpha_s)$. In other words, $\sigma_{\geq N+1}$ requires at least one additional emission to be nonvanishing. Hence, we can consider it an inclusive $(N+1)$-jet cross section with at least $N+1$ jets.

In the simplest case, $\sigma_{\geq N}$ is divided into the two jet bins σ_N and $\sigma_{\geq N+1}$ by using a cut on some kinematic variable, p_{N+1}, which characterizes additional emissions, with $p_{N+1} = 0$ for a tree-level N-parton state. Typical examples would be the p_T of the $N+1$st jet or the total $|\vec{p}_T|$ of the underlying N-jet system. The two jet bins then correspond to the integrals of the differential spectrum $\mathrm{d}\sigma/\mathrm{d}p_{N+1}$ above and below some cut,

$$\begin{aligned}\sigma_{\geq N} &= \int_0^{p^{\text{cut}}} \mathrm{d}p_{N+1}\,\frac{\mathrm{d}\sigma_{\geq N}}{\mathrm{d}p_{N+1}} + \int_{p^{\text{cut}}} \mathrm{d}p_{N+1}\,\frac{\mathrm{d}\sigma_{\geq N}}{\mathrm{d}p_{N+1}} \\ &\equiv \sigma_N(p^{\text{cut}}) + \sigma_{\geq N+1}(p^{\text{cut}})\,.\end{aligned} \tag{3.2}$$

In general, the jet bin boundary could be a much more complicated function of phase space, for example in a multivariate analysis.

We are interested in the uncertainties involved in the binning. The covariance matrix for $\{\sigma_N, \sigma_{\geq N+1}\}$ is a symmetric 2×2 matrix with three independent parameters. A convenient and general parametrization is to write it in terms of two components,

$$C = \begin{pmatrix} (\Delta^{\text{y}}_N)^2 & \Delta^{\text{y}}_N\,\Delta^{\text{y}}_{\geq N+1} \\ \Delta^{\text{y}}_N\,\Delta^{\text{y}}_{\geq N+1} & (\Delta^{\text{y}}_{\geq N+1})^2 \end{pmatrix} + \begin{pmatrix} \Delta^2_{\text{cut}} & -\Delta^2_{\text{cut}} \\ -\Delta^2_{\text{cut}} & \Delta^2_{\text{cut}} \end{pmatrix}. \tag{3.3}$$

Here, the first term is an absolute "yield" uncertainty, denoted with a superscript "y," which (by definition) is 100% correlated between the two bins σ_N and $\sigma_{\geq N+1}$. The second term is a "migration" uncertainty between the bins and corresponds to the uncertainty introduced by the binning cut. It has the same absolute size, Δ_{cut}, for both bins and is 100% anticorrelated between them, such that it drops out when the two bins are added. Hence, the total uncertainty for each bin is given by

$$\begin{aligned}\Delta^2_N &= (\Delta^{\text{y}}_N)^2 + \Delta^2_{\text{cut}} \\ \Delta^2_{\geq N+1} &= (\Delta^{\text{y}}_{\geq N+1})^2 + \Delta^2_{\text{cut}}\,,\end{aligned} \tag{3.4}$$

while the total uncertainty on their sum, i.e., on $\sigma_{\geq N}$, is given by the total yield uncertainty,

$$\Delta_{\geq N} = \Delta^{\mathrm{y}}_{\geq N} = \Delta^{\mathrm{y}}_{N} + \Delta^{\mathrm{y}}_{\geq N+1}\,. \tag{3.5}$$

Considering the perturbative uncertainties, the basic question is how each of the uncertainties in Eq. (3.3) can be evaluated. The fixed-order prediction provides us with two independent pieces of information, namely the variations obtained by the standard scale variations, which we denote as $\Delta^{\mu}_{\geq N}$, Δ^{μ}_{N}, $\Delta^{\mu}_{\geq N+1}$, and which satisfy $\Delta^{\mu}_{\geq N} = \Delta^{\mu}_{N} + \Delta^{\mu}_{\geq N+1}$. Following Ref. [41], we start by assuming that the standard fixed-order scale variations can be used to obtain a reliable estimate of the total uncertainties in the *inclusive* cross sections (which is of course the common assumption underlying any inclusive fixed-order calculation). Hence, we impose the two well-motivated boundary conditions,

$$\Delta_{\geq N} = \Delta^{\mu}_{\geq N}\,, \qquad \Delta_{\geq N+1} = \Delta^{\mu}_{\geq N+1}\,. \tag{3.6}$$

Together with Eqs. (3.4) and (3.5), these lead to

$$\begin{aligned} &\text{(i)} && \Delta^{\mu}_{\geq N} = \Delta^{\mathrm{y}}_{N} + \Delta^{\mathrm{y}}_{\geq N+1}\,, \\ &\text{(ii)} && (\Delta^{\mu}_{\geq N+1})^2 = (\Delta^{\mathrm{y}}_{\geq N+1})^2 + \Delta^2_{\mathrm{cut}}\,. \end{aligned} \tag{3.7}$$

Thus, the question is how to divide up $\Delta^{\mu}_{\geq N+1}$ between $\Delta^{\mathrm{y}}_{\geq N+1}$ and Δ_{cut} in order to satisfy condition (ii). Condition (i) then determines Δ^{y}_{N}. The nontrivial effect Δ_{cut} can have is on the size of Δ_N as well as on the off-diagonal entries in Eq. (3.3), which determine the correlation between Δ_N and $\Delta_{\geq N+1}$.

Clearly, the simplest is to neglect the effect of Δ_{cut} altogether and to directly use common scale variations to estimate the uncertainties, i.e., to take

$$\begin{aligned} &\Delta^{\mathrm{y}}_{N} = \Delta^{\mu}_{\geq N} - \Delta^{\mu}_{\geq N+1} \equiv \Delta^{\mu}_{N}\,, \quad \Delta^{\mathrm{y}}_{\geq N+1} = \Delta^{\mu}_{\geq N+1}\,, \\ &\Delta_{\mathrm{cut}} = 0\,, \end{aligned} \tag{3.8}$$

which leads to

$$\text{direct:} \qquad C = \begin{pmatrix} (\Delta^{\mu}_{N})^2 & \Delta^{\mu}_{N}\,\Delta^{\mu}_{\geq N+1} \\ \Delta^{\mu}_{N}\,\Delta^{\mu}_{\geq N+1} & (\Delta^{\mu}_{\geq N+1})^2 \end{pmatrix}. \tag{3.9}$$

The direct scale variation choice is reasonable as long as the effect of Δ_{cut} is indeed negligible. It is certainly justified if numerically $\Delta^{\mu}_{\geq N} \gg \Delta^{\mu}_{\geq N+1}$, since any uncertainty due to migration effects can be, at most as large as $\Delta^{\mu}_{\geq N+1}$ [by virtue of condition (ii)]. This can happen, for example, when $\Delta^{\mu}_{\geq N}$ is sizable due to large perturbative corrections in $\sigma_{\geq N}$ and/or the binning cut is very loose (i.e., is cutting out only a small fraction of phase

space) such that $\sigma_{\geq N+1}$ is numerically small to begin with.

In perturbation theory, the effect of the binning cut is to introduce Sudakov double logarithms in the perturbative series of σ_N and $\sigma_{\geq N+1}$, which have opposite sign and cancel in the sum of the two bins, schematically,

$$\begin{aligned}
\sigma_{\geq N} &\simeq \sigma_B[1 + \alpha_s + \alpha_s^2 + \mathrm{O}(\alpha_s^3)]\,, \\
\sigma_{\geq N+1} &\simeq \sigma_B\big[\alpha_s(L^2 + L + 1) + \alpha_s^2(L^4 + L^3 + L^2 + L + 1) + \mathrm{O}(\alpha_s^3 L^6)\big]\,, \\
\sigma_N &= \sigma_{\geq N} - \sigma_{\geq N+1}\,,
\end{aligned} \tag{3.10}$$

where σ_B denotes the Born cross section and L is a Sudakov logarithm, e.g., for Eq. (3.2), $L = \ln(p^{\mathrm{cut}}/Q)$, where $Q \sim m_H$ is a typical hard scale. As the binning cut becomes tighter (p^{cut} becomes smaller) the logarithms grow in size. Once the logarithms are $\mathrm{O}(1)$ numbers, one is in the transition region and the logarithms will start to dominate the perturbative series of $\sigma_{\geq N+1}$, and there will be sizable cancellations in σ_N between the perturbative series for $\sigma_{\geq N}$ and the logarithmic series in $\sigma_{\geq N+1}$. Eventually, the logarithms will grow large enough to overcome the α_s suppression and σ_N becomes negative, at which point one is in the resummation region and the fixed-order expansion has broken down.

The perturbative migration uncertainty Δ_{cut} can be directly associated with the perturbative uncertainty in the logarithmic series induced by the binning, and so should not be neglected once the logarithms have a noticeable effect. In particular, as demonstrated in Ref. [41], the simple choice in Eqs. (3.8) and (3.9) can easily lead to an underestimate of Δ_N in the region where there are sizable numerical cancellations between the two series in $\sigma_{\geq N}$ and $\sigma_{\geq N+1}$. Since in this region the dominant contribution to $\sigma_{\geq N+1}$ comes from the logarithmic series, varying the scales in $\sigma_{\geq N+1}$ directly tracks the size of the logarithms, which means we can use $\Delta_{\mathrm{cut}} = \Delta^{\mu}_{\geq N+1}$ as an estimate for the binning uncertainty, which is the basic idea of Ref. [41]. From Eq. (3.7), we then find

$$\begin{aligned}
\Delta^{\mathrm{y}}_N &= \Delta^{\mu}_{\geq N}\,, \qquad \Delta^{\mathrm{y}}_{\geq N+1} = 0\,, \\
\Delta_{\mathrm{cut}} &= \Delta^{\mu}_{\geq N+1}\,,
\end{aligned} \tag{3.11}$$

such that

$$\text{ST:} \quad C = \begin{pmatrix} (\Delta^{\mu}_{\geq N})^2 + (\Delta^{\mu}_{\geq N+1})^2 & -(\Delta^{\mu}_{\geq N+1})^2 \\ -(\Delta^{\mu}_{\geq N+1})^2 & (\Delta^{\mu}_{\geq N+1})^2 \end{pmatrix}. \tag{3.12}$$

Since $\Delta^{\mu}_{\geq N+1}$ is now used as Δ_{cut}, the effective outcome is that one treats $\Delta^{\mu}_{\geq N}$ and $\Delta^{\mu}_{\geq N+1}$ as uncorrelated.

More generally, we can introduce a parameter $0 \leq \rho \leq 1$, which controls the fraction of

	ATLAS	CMS loose	CMS tight
2-jet selection	anti-k_T $R = 0.4$ $p_{Tj} > 25\,\text{GeV}$ for $\lvert\eta_j\rvert < 2.5$ $p_{Tj} > 30\,\text{GeV}$ for $2.5 < \lvert\eta_j\rvert < 4.5$	anti-k_T $R = 0.5$ jet 1: $p_{Tj} > 30\,\text{GeV}$, $\lvert\eta_j\rvert < 4.7$ jet 2: $p_{Tj} > 20\,\text{GeV}$, $\lvert\eta_j\rvert < 4.7$	anti-k_T $R = 0.5$ $p_{Tj} > 30\,\text{GeV}$, $\lvert\eta_j\rvert < 4.7$
$\Delta\eta_{jj} = \lvert\eta_{j1} - \eta_{j2}\rvert$	> 2.8	> 3.0	> 3.0
m_{jj}	$> 400\,\text{GeV}$	$> 250\,\text{GeV}$	$> 500\,\text{GeV}$
$\lvert\eta_H - (\eta_{j1} + \eta_{j2})/2\rvert$	-	< 2.5	< 2.5
$\Delta\phi_{H-jj}$	> 2.6	> 2.6	> 2.6

Table 3.1: *VBF selection cuts we use, corresponding to the $H \to \gamma\gamma$ analyses by ATLAS [5, 45] and CMS [6]. CMS loose excludes events that pass CMS tight. The cut on $\Delta\phi_{H-jj}$ in the last row is treated specially as an exclusive binning cut.*

$\Delta^{\mu}_{\geq N+1}$ assigned to $\Delta^{\text{y}}_{\geq N+1}$, such that

$$\begin{aligned} \Delta^{\text{y}}_{N} &= \Delta^{\mu}_{\geq N} - \rho\,\Delta^{\mu}_{\geq N+1}\,, \quad \Delta^{\text{y}}_{\geq N+1} = \rho\,\Delta^{\mu}_{\geq N+1}\,, \\ \Delta_{\text{cut}} &= \sqrt{1-\rho^2}\,\Delta^{\mu}_{\geq N+1}\,, \end{aligned} \tag{3.13}$$

which leads to

$$\text{ST } (\rho): \qquad C = \begin{pmatrix} (\Delta^{\mu}_{\geq N})^2 + (\Delta^{\mu}_{\geq N+1})^2 - 2\rho\,\Delta^{\mu}_{\geq N}\Delta^{\mu}_{\geq N+1} & (\rho\,\Delta^{\mu}_{\geq N} - \Delta^{\mu}_{\geq N+1})\Delta^{\mu}_{\geq N+1} \\ (\rho\,\Delta^{\mu}_{\geq N} - \Delta^{\mu}_{\geq N+1})\Delta^{\mu}_{\geq N+1} & (\Delta^{\mu}_{\geq N+1})^2 \end{pmatrix}. \tag{3.14}$$

From this one can easily see that ρ corresponds to the correlation between $\Delta^{\mu}_{\geq N}$ and $\Delta^{\mu}_{\geq N+1}$. The choice $\rho = 1$ would be equivalent to the case in Eq. (3.9), while $\rho = 0$ reproduces Eqs. (3.11) and (3.12). Hence, from the above arguments one should take ρ to be small. In the next section, we will explore the dependence on ρ in the ST method. We will see that all choices $\rho \lesssim 0.4$ give very similar results, so we will use the default choice $\rho = 0$ for our applications to H + 2−jets.

As a final comment, note that in general one could also take ρ to be a function of the binning cut. For example, at large p^{cut} the logarithms become small, in which case one might want to reproduce the direct scale variation uncertainties in Eq. (3.9). However, in this limit, typically $\Delta^{\mu}_{\geq N+1}$ becomes much smaller than $\Delta^{\mu}_{\geq N}$, which makes the precise choice of ρ irrelevant there, and so it is consistent to use a fixed $\rho = 0$ everywhere.

3.3 Application to $gg \to H + 2$ Jets

We now discuss the application of our method to the case of $pp \to H + 2$ jet production via gluon fusion (which for simplicity we denote as $gg \to H + 2j$, where a sum over all possible partonic channels is implied). We will study the uncertainties in the exclusive $H + 2$ jet

cross section as a function of two kinematic variables, p_{THjj} and $\Delta\phi_{H-jj}$.

We take $\sqrt{s} = 8\,\text{TeV}$ and $m_H = 125\,\text{GeV}$. We use MCFM [28, 44, 46] to compute the NLO cross section, with the ggH effective vertex in the infinite top mass limit. We then rescale the cross section with the exact m_t dependence of the total Born cross section, $\sigma_B(m_t)/\sigma_B(\infty) = 1.0668$. We use the MSTW2008 [47] NLO PDFs with their corresponding value of $\alpha_s(m_Z) = 0.12018$. For all our central value predictions we use $\mu_r = \mu_f = m_H$, which was also used in Refs. [28, 44]. In our analysis we implement the 2-jet selection and VBF selection cuts summarized in Table 3.1, which are taken from the 7-8 TeV ATLAS and CMS $H \to \gamma\gamma$ analyses in [5, 6, 45]. However, note that we consider the cross section for the production of an on-shell Higgs boson, without including any branching ratios or cuts on the Higgs decay product, as the perturbative corrections are independent of the Higgs decay modes.

The main inputs for MCFM are : the process definition (in our case $gg \to H + 2$-jets), order (NLO), E_{cm}, m_H, mass of top quark, the factorization scale μ_F and renormalization scale μ_R scales, PDF type, jet radius (ATLAS $R = 0.4$ and CMS $R = 0.5$) and jet algorithm (anti-kT). Other options which MCFM provides and are important for us in this analyses are a minimum p_T to identify the two jets and maximum rapidity η for the two jets, the rapidity separation and invariant mass of the dijet system. We define a momentum four vector for each jet and events with two jets ordered in their p_T are preselected which further go through a set of selection criteria defined by the ATLAS and CMS VBF category. An event is selected if each of the two jets have a minimum p_T and a maximum rapidity η_j and the two jets are separated with a rapidity gap as defined in Table 3.1. The two jets should also fulfill the condition on their invariant mass which is defined as $\Delta m_{jj} = \sqrt{(E_{j1} + E_{j2})^2 - |\vec{p}_{j1} + \vec{p}_{j2}|^2}$. An additional selection based on the variable $\Delta\phi_{H-jj}$ defined in the next section also applies. We obtain from MCFM a list of histograms, with the differential 2-jet cross section in bins of the jet-veto observables like $\Delta\phi_{H-jj}$ or p_{THjj} and the cumulant cross sections we plot are given by

$$\sigma_2(p_{THjj} < p_T^{\text{cut}}) = \int_0^{p_T^{\text{cut}}} \frac{d\sigma}{dp_{THjj}}(p_{Tj1}, p_{Tj2} > p_T^{\text{cut}}, ...) \tag{3.15}$$

where the dots refer to the additional selection criteria we impose depending on ATLAS and CMS VBF selection. We have to be careful while specifying the selection cuts in order to obtain reliable predictions from MCFM in the exclusive limit $p_{THjj} \to 0$ and $\Delta\phi_{H-jj} \to \pi$, where the NLO predictions break down.

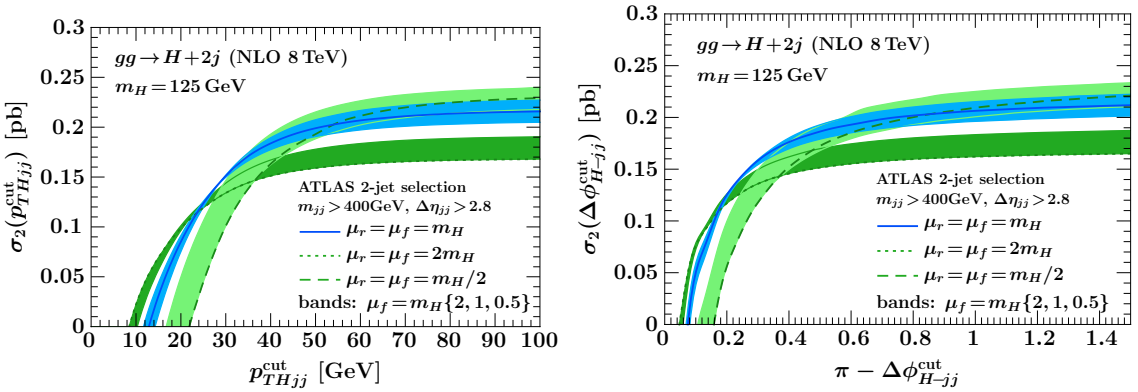

Figure 3.1: *Exclusive 2-jet cross section using the ATLAS VBF selection for various scale choices as a function of $p_{THjj}^{\rm cut}$ (left panel) and $\pi - \Delta\phi_{H-jj}^{\rm cut}$ (right panel).*

3.3.1 Variables

p_{THjj}: We define p_{THjj} as the magnitude of the total transverse momentum of the Higgs-dijet system,

$$p_{THjj} = |\vec{p}_{Tj1} + \vec{p}_{Tj2} + \vec{p}_{TH}| \,. \tag{3.16}$$

At Born level, $p_{THjj} = 0$ and so applying a cut $p_{THjj} < p_{THjj}^{\rm cut}$ restricts the phase space to the exclusive 2-jet region. At NLO p_{THjj} is equivalent to the p_T of the third jet, so it is a useful reference variable for a p_T-veto on additional emissions, such as the central jet vetoes applied in the $H \to WW$ and $H \to \tau\tau$ VBF analyses (see e.g. Refs. [48–51]).It is also considered directly, for example, in the 7-8 TeV $H \to \tau\tau$ analysis [49].

The exclusive 2-jet cross section $\sigma_2(p_{THjj} < p_{THjj}^{\rm cut})$ is shown in the left panel of Fig. 3.1 as a function of $p_{THjj}^{\rm cut}$ and using three different combinations of the factorization and renormalization scales, μ_r and μ_f. The solid line and blue band correspond to $\mu_r = m_H$ and varying $\mu_f = \{2, 1, 1/2\}m_H$. Similarly, we vary μ_f while keeping $\mu_r = m_H/2$ for the dark green band and $\mu_r = 2m_H$ for the light green band. One can see that the biggest variation is due to the μ_r variation, while the μ_f variation only has a subdominant effect, which was already noticed in Ref. [28]. Therefore, for simplicity we will take $\mu_r = \mu_f = \mu$ and vary $\mu = \{2, 1, 1/2\}m_H$ when showing the direct scale variations as reference in the following.

We write the exclusive 2-jet bin defined by this cut in terms of the inclusive 2-jet cross section, $\sigma_{\geq 2}$, and the inclusive 3-jet cross section with the cut inverted as,

$$\sigma_2(p_{THjj} < p_{THjj}^{\rm cut}) = \sigma_{\geq 2} - \sigma_{\geq 3}(p_{THjj} > p_{THjj}^{\rm cut}) \,, \tag{3.17}$$

where in all cases the remaining VBF selection cuts in Table 3.1 are applied (excluding the cut on $\Delta\phi_{H-jj}$ in this case).

The restriction on p_{THjj} is infrared sensitive and induces Sudakov logarithms of the form $L = \ln(p^{\text{cut}}_{THjj}/m_H)$ in the perturbative series of σ_2 and $\sigma_{\geq 3}$. In Fig. 3.1 we see that the veto starts to have a noticeable effect below $p_{THjj} \lesssim 50\,\text{GeV}$, where the different scale variations start crossing and we start to see cancellations between $\sigma_{\geq 2}$ and $\sigma_{\geq 3}$. In the region below $p_{THjj} \lesssim 20\,\text{GeV}$, the logarithms have grown large enough for the NLO cross section to go negative and the fixed-order perturbative expansion to break down. In the intermediate region in between, the fixed-order prediction can still be used, but the direct scale variation does not provide a reliable uncertainty estimate as it does not properly take into account the effect of the binning cut.

$\Delta\phi_{H-jj}$: As shown in Table 3.1, the VBF category in the $H \to \gamma\gamma$ analyses by ATLAS and CMS includes a cut $\Delta\phi_{H-jj} > 2.6$ radians (150 deg) (where the Higgs momentum is represented by the total momentum of the diphoton system). Taking the beam direction along the z-axes, $\Delta\phi_{H-jj}$ is defined as

$$\cos\Delta\phi_{H-jj} = \frac{(\vec{p}_{Tj1} + \vec{p}_{Tj2}) \cdot \vec{p}_{TH}}{|\vec{p}_{Tj1} + \vec{p}_{Tj2}||\vec{p}_{TH}|}\,. \tag{3.18}$$

Momentum conservation in the transverse plane implies that events with only two jets always have $\Delta\phi_{H-jj} \approx \pi$, so the constraint $\Delta\phi_{H-jj} > \Delta\phi^{\text{cut}}_{H-jj}$ forces the kinematics into the exclusive 2-jet region and restricts additional emissions. Hence, it behaves similar to p^{cut}_{THjj} and for $\pi - \Delta\phi^{\text{cut}}_{H-jj} \to 0$ induces large logarithms in the perturbative series. The exclusive 2-jet cross section in terms of $\Delta\phi^{\text{cut}}_{H-jj}$ is written as

$$\sigma_2(\Delta\phi_{H-jj} > \Delta\phi^{\text{cut}}_{H-jj}) = \sigma_{\geq 2} - \sigma_{\geq 3}(\Delta\phi_{H-jj} < \Delta\phi^{\text{cut}}_{H-jj})\,, \tag{3.19}$$

with the remaining VBF cuts applied in all three cross sections. The right panel of Fig. 3.1 shows $\sigma_2(\Delta\phi_{H-jj} > \Delta\phi^{\text{cut}}_{H-jj})$ plotted as a function of $\pi - \Delta\phi^{\text{cut}}_{H-jj}$, where one can clearly see the very similar behavior to the p^{cut}_{THjj} case in the left panel. Here, the exclusive cut on $\Delta\phi_{H-jj}$ starts having a noticeable effect below $\pi - \Delta\phi_{H-jj} \lesssim 0.6$, and the fixed-order perturbative expansion breaks down below around $\pi - \Delta\phi \lesssim 0.2$. In the transition region in between, the direct scale variations again do not provide a meaningful uncertainty estimate, because they neglect the effect of Δ_{cut}.

3.3.2 Inclusive Scale Uncertainties

The two fixed-order scale variation uncertainties we require as inputs are $\Delta^{\mu}_{\geq 2}$ and $\Delta^{\mu}_{\geq 3}$. In Fig. 3.1, one can already see that the scale variation is asymmetric at large values of p^{cut}_{THjj} and $\pi - \Delta\phi^{\text{cut}}_{H-jj}$. In Fig. 3.2, we show the scale dependence of the inclusive 2-jet cross section, $\sigma_{\geq 2}$, where we plot it over a range of $1/4 < \mu_r/m_H < 4$ for three different

values of μ_f. We take $\mu_f = \mu_r = m_H$, corresponding to the $\mu_r/m_H = 1$ point on the blue solid line, as our central value for $\sigma_{\geq 2}$, and consider the range $0.5 \leq \mu_r/m_H \leq 2$ to estimate the inclusive scale uncertainty. The maximum deviation from the central value is given by the green dotted curve for $\mu_f = \mu_r = 2m_H$. We use this maximum variation to construct a symmetric uncertainty $\Delta^{\mu}_{\geq 2}$, as shown by the uncertainty bar in the figure. It corresponds to a relative uncertainty at NLO of 21%, which is similar to what was found in earlier studies [28,44] where a somewhat looser VBF selection was used. The corresponding uncertainty at LO is +76% and −40%.

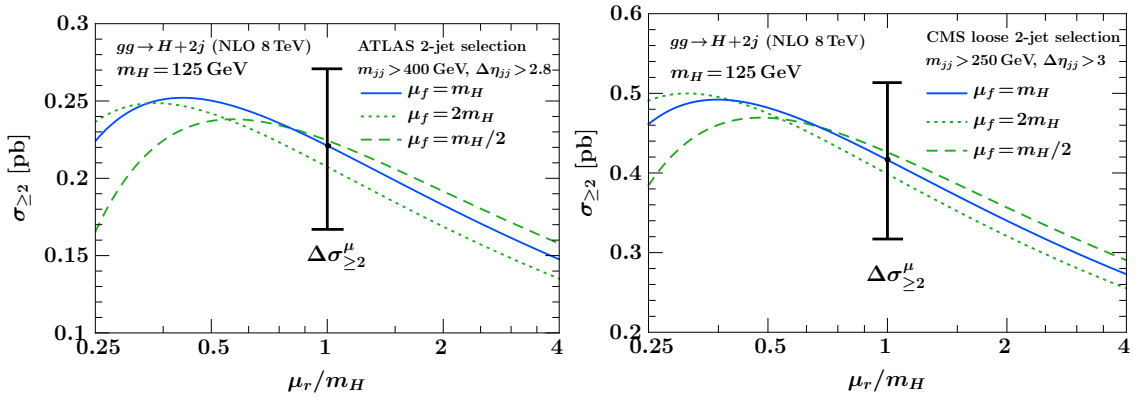

Figure 3.2: *Inclusive 2-jet cross section over a range of μ_r/m_H for ATLAS VBF selection (left panel) and CMS loose selection (right panel). The three curves show different values of μ_f. The blue solid, green dotted, and green dashed curves correspond to $\mu_f = m_H$, $\mu_f = 2m_H$, and $\mu_f = m_H/2$, respectively. The uncertainty bars show the inclusive 2-jet scale variation uncertainty.*

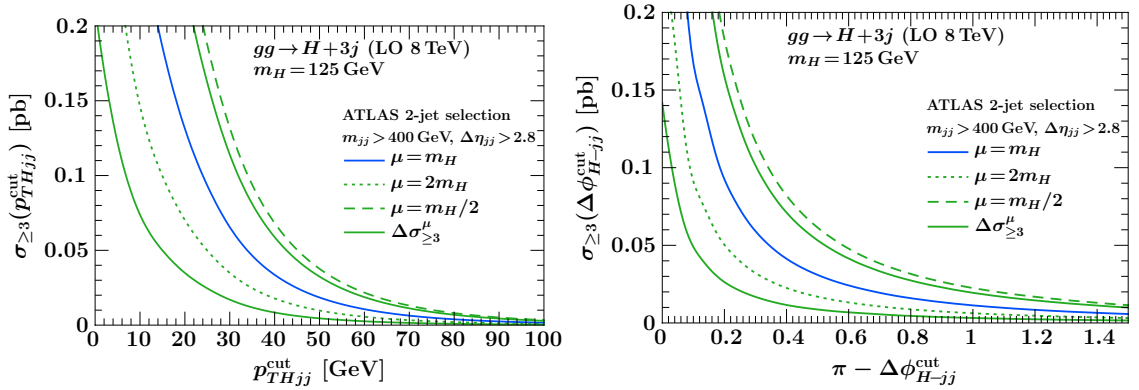

Figure 3.3: *Inclusive 3-jet cross section as a function of $p^{\rm cut}_{THjj}$ (left panel) and $\pi - \Delta\phi^{\rm cut}_{H-jj}$ (right panel) for the ATLAS VBF selection. The outer solid green lines show the inclusive 3-jet scale variation uncertainty after symmetrization.*

In Fig. 3.3, we illustrate the scale variation uncertainties for the inclusive 3-jet cross section, $\sigma_{\geq 3}$, for both $p^{\rm cut}_{THjj}$ and $\Delta\phi^{\rm cut}_{H-jj}$, and using the ATLAS selection as example. (The results for $\sigma_{\geq 3}$ with the CMS selections look very similar except for the different overall scale.) The blue solid line shows the cross section for $\mu_r = \mu_f = m_H$, which we take as the central value for $\sigma_{\geq 3}$. The green dashed and dotted lines show the scale variations $\mu_r = \mu_f = m_H/2$ and $\mu_r = \mu_f = 2m_H$, respectively. For simplicity, we symmetrize the uncertainty by taking half of the difference between the up and down variations as the inclusive 3-jet scale uncertainty

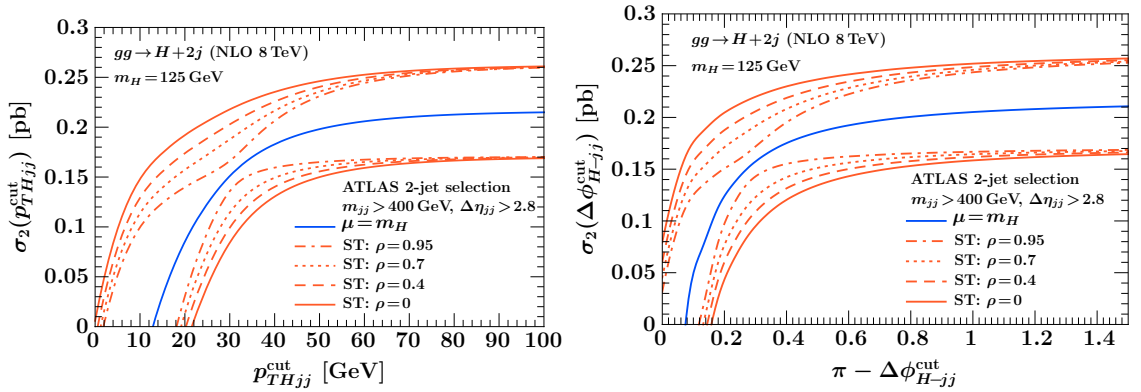

Figure 3.4: *Perturbative uncertainties in the exclusive 2-jet cross section with the ATLAS VBF selection as a function of $p_{THjj}^{\rm cut}$ (left panel) and $\pi - \Delta\phi_{H-jj}^{\rm cut}$ (right panel) for different choices of the correlation parameter ρ. Our default choice is $\rho = 0$.*

$\Delta_{\geq 3}^{\mu}$, i.e., we keep the size of the band and move it to be symmetric about the central blue line, which is shown by the outer solid green lines. The relative uncertainty is of $O(70\%)$ and almost independent of $p_{THjj}^{\rm cut}$ and $\Delta\phi_{H-jj}^{\rm cut}$. This rather large uncertainty is not too surprising, since this is a leading-order $H + 3j$ cross section, which starts at $O(\alpha_s^5)$.

3.3.3 Exclusive Uncertainty

Having obtained the perturbative uncertainties $\Delta_{\geq 2}^{\mu}$ and $\Delta_{\geq 3}^{\mu}$ in the inclusive cross sections from the usual scale variation, we now study the resulting uncertainty Δ_2 in the exclusive 2-jet cross section according to the discussion in secjetbinreview. From Eq. (3.14) we have in general

$$\Delta_2^2 = (\Delta_{\geq 2}^{\mu})^2 + (\Delta_{\geq 3}^{\mu})^2 - 2\rho\, \Delta_{\geq 2}^{\mu} \Delta_{\geq 3}^{\mu}\,, \tag{3.20}$$

where ρ is the assumed correlation between $\Delta_{\geq 2}^{\mu}$ and $\Delta_{\geq 3}^{\mu}$.

Dependence on ρ

We first investigate the dependence on the choice of ρ. In Fig. 3.4 we show the uncertainty in the exclusive 2-jet cross section as a function of $p_{THjj}^{\rm cut}$ and $\Delta\phi_{H-jj}^{\rm cut}$ for different values of ρ from 0 to 0.95. The outermost solid curves show the uncertainty obtained with our default choice $\rho = 0$, which effectively assumes that $\Delta_{\geq 2}^{\mu}$ and $\Delta_{\geq 3}^{\mu}$ are uncorrelated. For $\rho \lesssim 0.4$ the results are not very sensitive to the precise value of ρ, which is reassuring and shows that $\rho = 0$ is in fact a safe choice on the conservative side.

As ρ increases further, the uncertainty bands in the transition region keep shrinking, and

for $\rho = 0.95$, shown by the innermost dot-dashed lines, pinch near $p_{THjj}^{\text{cut}} \simeq 30\,\text{GeV}$ and $\pi - \Delta\phi_{H-jj}^{\text{cut}} \simeq 0.3$. (For $\rho = 1$ the uncertainty goes exactly to zero around these points.) This is because for $\rho \to 1$, $\Delta_{\geq 3}^{\mu}$ and $\Delta_{\geq 2}^{\mu}$ become 100% correlated, which is equivalent to the case of direct scale variation. (The only difference compared to the direct scale variations we saw in Fig. 3.1 is that here we symmetrized the scale variations.)

One can also see that for large cut values, where the veto is not relevant and we approach the inclusive 2-jet cross section, the choice of ρ becomes irrelevant, because the absolute size of $\Delta_{\geq 3}^{\mu}$ becomes numerically negligible compared to $\Delta_{\geq 2}^{\mu}$.

Comparison to Efficiency Method

Another prescription to obtain fixed-order uncertainty estimates for exclusive jet cross section, which is based on using veto efficiencies, was applied in Ref. [24] to the 0-jet case at NNLO. We will refer to it as "efficiency method". In Ref. [52] it was shown that for the case of $H + 0$ jets at NNLO the ST method and efficiency method yield very similar uncertainties, providing a good cross check on both methods.

The starting point in the efficiency method is to write the exclusive jet cross section in terms of the corresponding inclusive jet cross section times the corresponding exclusive efficiency, i.e., applied to our 2-jet case,

$$\begin{aligned} \sigma_2 &= \sigma_{\geq 2}\left(1 - \frac{\sigma_{\geq 3}}{\sigma_{\geq 2}}\right) \equiv \sigma_{\geq 2} \times \epsilon_2\,, \\ \sigma_{\geq 3} &= \sigma_{\geq 2}\,(1 - \epsilon_2)\,, \end{aligned} \tag{3.21}$$

where the logarithmic series induced by the jet binning now only affects the efficiency. The basic assumption [24] one then makes is to treat the perturbative uncertainties in $\sigma_{\geq 2}$ and ϵ_2 as uncorrelated (which one can think of as a multiplicative version of the ST approach). One should be aware that this method does not satisfy one of our starting conditions, namely the total uncertainty $\Delta_{\geq 3}$ for $\sigma_{\geq 3}$ will not be given by its standard scale variation $\Delta_{\geq 3}^{\mu}$ anymore. Nevertheless, it is a useful way to gain additional insights into the size of higher-order corrections.

The 2-jet efficiency $\epsilon_2 = 1 - \sigma_{\geq 3}/\sigma_{\geq 2}$ is still an exclusive quantity. Similar cancellations between the two perturbative series for $\sigma_{\geq 2}$ and $\sigma_{\geq 3}$ can happen in their ratio than in their difference, so the direct scale variation for ϵ_2 might not provide a reliable uncertainty estimate. To circumvent this, in Ref. [24] the perturbative uncertainty in ϵ is instead estimated by using three different schemes for how to write the perturbative result for ϵ, which are all equivalent up to the desired order in α_s, but differ in the higher-order terms

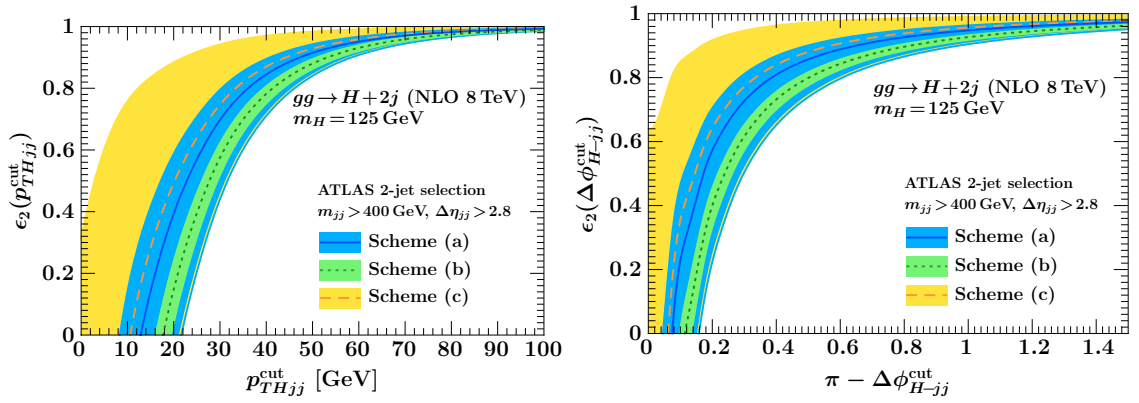

Figure 3.5: *Exclusive 2-jet efficiency for different schemes in the efficiency method for $p^{\rm cut}_{THjj}$ (left panel) and $\pi - \Delta\phi^{\rm cut}_{H-jj}$ (right panel) using the ATLAS VBF selection.*

that are retained or not.

The inclusive 2-jet and 3-jet cross sections have the following perturbative structure

$$\begin{aligned}\sigma_{\geq 2} &= \alpha_s^2\left[\sigma^{(0)}_{\geq 2} + \alpha_s\,\sigma^{(1)}_{\geq 2} + \alpha_s^2\,\sigma^{(2)}_{\geq 2} + \mathrm{O}(\alpha_s^3)\right],\\ \sigma_{\geq 3} &= \alpha_s^2\left[\alpha_s\sigma^{(0)}_{\geq 3} + \alpha_s^2\,\sigma^{(1)}_{\geq 3} + \mathrm{O}(\alpha_s^3)\right].\end{aligned} \tag{3.22}$$

At NLO, the pieces we have available are $\sigma^{(0)}_{\geq 2}$, $\sigma^{(1)}_{\geq 2}$, and $\sigma^{(0)}_{\geq 3}$. In scheme (a) one defines the efficiency by keeping the full expressions in numerator and denominator, which at NLO gives

$$\epsilon_2^{(a)} = 1 - \frac{\sigma_{\geq 3}}{\sigma_{\geq 2}} = 1 - \frac{\alpha_s\sigma^{(0)}_{\geq 3}}{\sigma^{(0)}_{\geq 2} + \alpha_s\sigma^{(1)}_{\geq 2}} + \mathrm{O}(\alpha_s^2)\,. \tag{3.23}$$

In scheme (b) one keeps the same number of terms in the perturbative series in the denominator as in the numerator, which in our case amounts to dropping the $\sigma^{(1)}_{\geq 2}$ term in the denominator,

$$\epsilon_2^{(b)} = 1 - \alpha_s\,\frac{\sigma^{(0)}_{\geq 3}}{\sigma^{(0)}_{\geq 2}} + \mathrm{O}(\alpha_s^2)\,. \tag{3.24}$$

Finally, in scheme (c) one strictly re-expands the ratio to a given order in α_s, which to $\mathrm{O}(\alpha_s)$ unfortunately yields the same result as scheme (b). To produce another expression with differing higher-order terms, the closest scheme (c) analog we can do is to keep the $\mathrm{O}(\alpha_s^2)$ cross term that comes from expanding the denominator, so

$$\epsilon_2^{(c)} = 1 - \alpha_s\,\frac{\sigma^{(0)}_{\geq 3}}{\sigma^{(0)}_{\geq 2}}\left(1 - \alpha_s\,\frac{\sigma^{(1)}_{\geq 2}}{\sigma^{(0)}_{\geq 2}}\right) + \mathrm{O}(\alpha_s^2)\,. \tag{3.25}$$

In Fig. 3.5 we show the result for ϵ_2 in the three schemes for both $p^{\rm cut}_{THjj}$ and $\Delta\phi^{\rm cut}_{H-jj}$ using

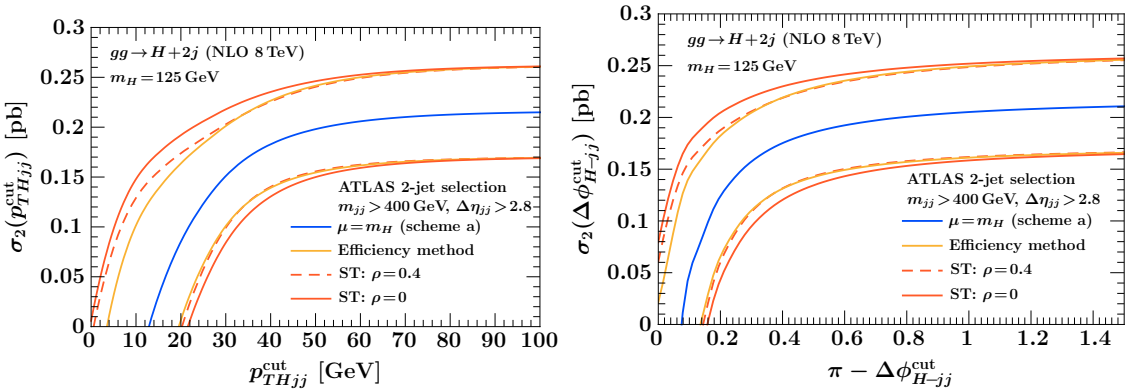

Figure 3.6: *Comparison of the ST method with the efficiency method for p_{THjj}^{cut} (left panel) and $\pi - \Delta\phi_{H-jj}^{\text{cut}}$ (right panel) using the ATLAS VBF selection. The exclusive scale uncertainties from both methods are consistent with each other. The uncertainties from the efficiency method are very close to those from the ST method with $\rho = 0.4$.*

the ATLAS VBF selection. The central lines show the results for $\mu_r = \mu_f = \mu = m_H$, while the bands are obtained from varying $\mu = \{2, 1/2\}m_H$ in each scheme. At NLO the central values from the three schemes are quite close and still lie within the direct scale variation of scheme (a), so their difference does not provide a useful uncertainty estimate here. The direct scale variation in scheme (b) is very small and in scheme (c) abnormally large (which is very similar to what was seen in Ref. [24]). Hence, in the end the most reasonable choice to get an uncertainty estimate for ϵ_2 is to just use the direct scale variation in scheme (a).

In Fig. 3.6 we compare the results of the ST and efficiency methods for the exclusive 2-jet cross section σ_2 for both p_{THjj}^{cut} and $\Delta\phi_{H-jj}^{\text{cut}}$ using the ATLAS VBF selection. The blue solid curve shows our usual NLO central value, which is equivalent to the central value from scheme (a). The light orange solid curves are the uncertainties obtained in the efficiency method by combining the scale uncertainties $\Delta_{\geq 2}^{\mu}$ with the direct scale variations in $\epsilon_2^{(a)}$ treating both as uncorrelated. The dark orange solid curves show the default ST uncertainties for $\rho = 0$, which are somewhat larger. The dashed lines show the ST uncertainties for $\rho = 0.4$, which agree almost perfectly with the efficiency method. This result is not surprising. Basically, to obtain the ϵ_2 scale uncertainty we vary the scales correlated in $\sigma_{\geq 2}$ and $\sigma_{\geq 3}$, which has the effect of reintroducing a certain amount of correlation between $\Delta_{\geq 2}^{\mu}$ and $\Delta_{\geq 3}^{\mu}$ when considering σ_2, which is also what a nonzero value of ρ does. Overall, the good consistency between the various methods gives us confidence in the reliability of our uncertainty estimates.

3.4 Results

3.4.1 $gg \to H + 2$ Jets Cross Section

In this section, we present our results for the exclusive $pp \to H + 2$ jet cross section via ggF at NLO, taking ST with $\rho = 0$ as our method of choice to estimate the perturbative uncertainties. All our inputs are summarized at the beginning of Sec. 3.3. The ATLAS, CMS loose, and CMS tight VBF selection cuts we apply are summarized in Table 3.1.

p_{THjj} and $\Delta\phi_{H-jj}$: In Fig. 3.7 we plot the result for the exclusive 2-jet cross section as a function of p_{THjj}^{cut} and $\Delta\phi_{H-jj}^{\text{cut}}$ for the 7-8 TeV ATLAS, CMS loose, and CMS tight VBF selections. In all our cross section plots the solid blue central line shows the central-value prediction obtained from $\mu = m_H$, while the outer orange solid lines show our uncertainty estimate. For reference, the green dashed and dotted curves show the direct scale variation for $\mu = m_H/2$ and $\mu = 2m_H$, respectively.

The overall picture is very similar for all three VBF selections and both binning variables. For large values of p_{THjj}^{cut} or $\pi - \Delta\phi_{H-jj}^{\text{cut}}$, the cross section $\sigma_{\geq 3}$ that is cut away becomes small and so the effect of Δ^{cut} is negligible. In this limit the uncertainties reproduce those in the inclusive 2-jet cross section, which here are determined by the $\mu = 2m_H$ variation. On the other hand, in the transition region, once the exclusive cut starts to impact the cross section, the direct scale variations cannot be used any longer to estimate uncertainties, which is exhibited by the crossing of the lines. As explained in detail in the previous two sections, the reason is that the direct scale variation only gives an estimate of the yield uncertainties, which effectively assumes the scale variations in the inclusive cross sections to be 100% correlated (corresponding to $\rho = 1$). At the same time it neglects the migration uncertainty in the binning, which becomes important as the exclusive cut gets tighter. In the ST procedure, this effect is taken into account explicitly, which thus gives more robust uncertainties for all values of p_{THjj}^{cut} or $\Delta\phi_{H-jj}^{\text{cut}}$.

In Table 3.2 we quote results for the cross sections and their percentage uncertainties for specific cuts. For $\Delta\phi_{H-jj}$ we use the current experimental value $\Delta\phi_{H-jj} > 2.6$. Compared to the 21% in the inclusive 2-jet cross section with VBF cuts ($\sigma_{\geq 2}$), we see a moderate increase in the uncertainty in $\sigma_2(\Delta\phi_{H-jj} > 2.6)$ to 26% for ATLAS and CMS tight, and 24% for CMS loose. For p_{THjj} we use a representative value of $p_{THjj} < 30\,\text{GeV}$, for which the uncertainties increase substantially to 44% and 49% for ATLAS and CMS tight, and moderately to 28% for CMS loose. Note that for a fixed cut the uncertainties increase with a tighter VBF selection. This is also clearly visible in Fig. 3.7, where the region where the cross section drops and the uncertainties grow large moves to larger values of p_{THjj} or

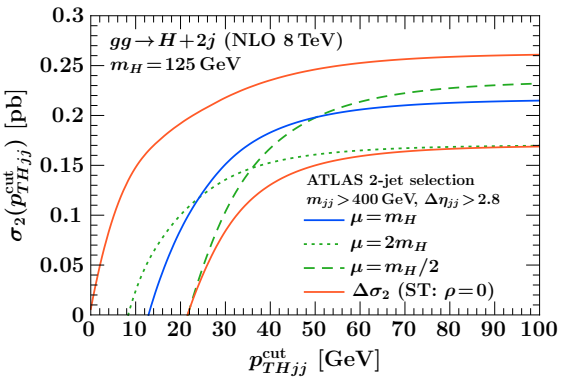

(a) ATLAS VBF selection

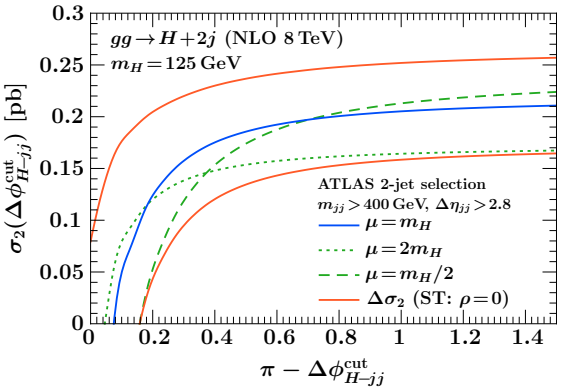

(b) ATLAS VBF selection

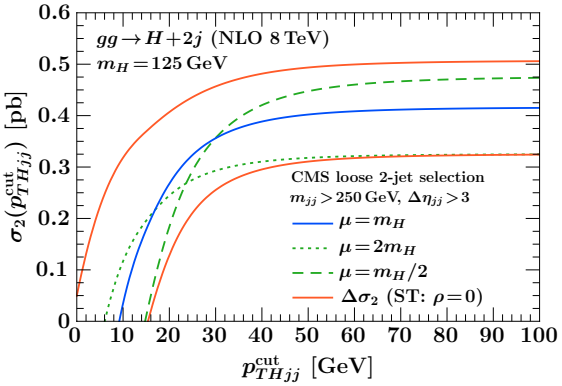

(c) CMS loose VBF selection

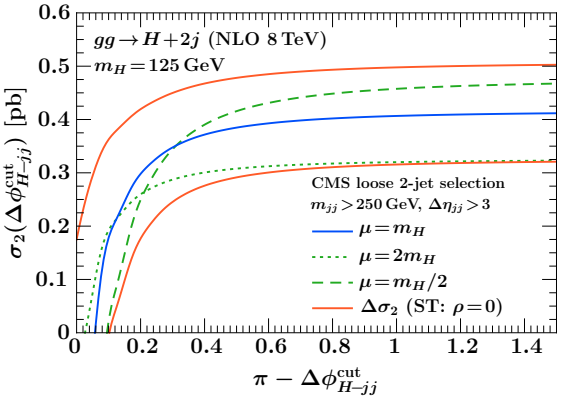

(d) CMS loose VBF selection

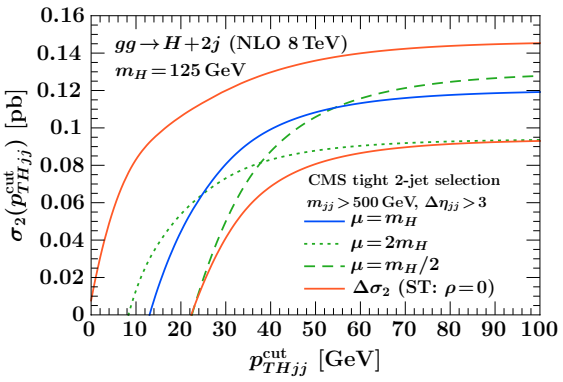

(e) CMS tight VBF selection

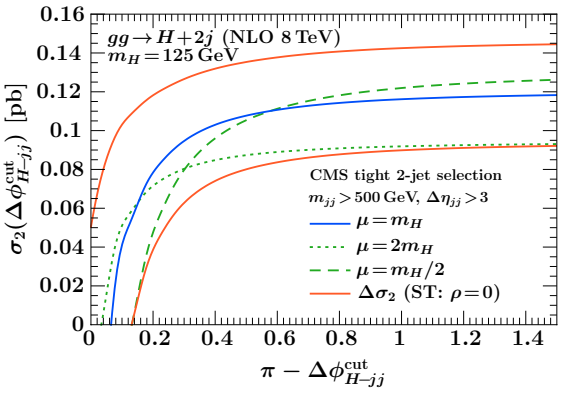

(f) CMS tight VBF selection

Figure 3.7: *Exclusive $pp \to H + 2$ jet cross section via ggF at NLO for as function of $p_{THjj}^{\rm cut}$ (left panels) and $\pi - \Delta\phi_{H-jj}^{\rm cut}$ (right panels) for both ATLAS and CMS VBF selections.*

$\pi - \Delta\phi_{H-jj}$, going from CMS loose to ATLAS to CMS tight.

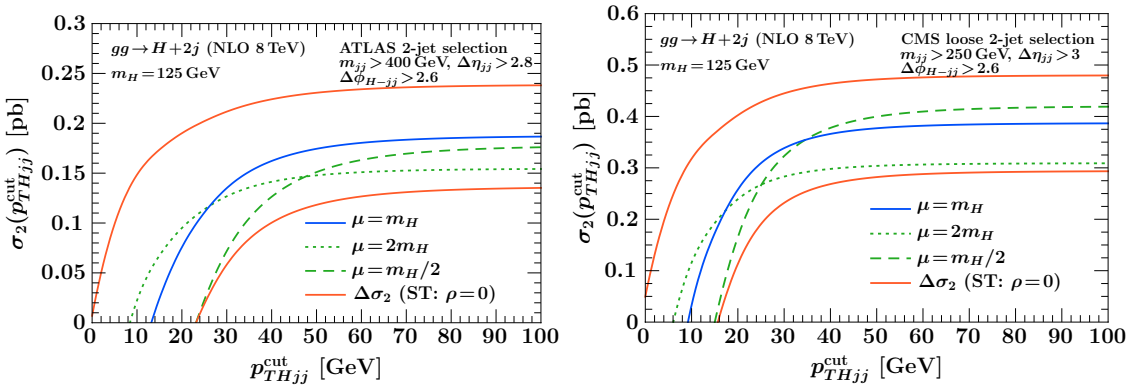

Figure 3.8: *Exclusive 2-jet cross section as a function of* $p_{THjj}^{\rm cut}$ *with an additional cut* $\Delta\phi_{H-jj} > 2.6$ *using the ATLAS (left panel) and CMS loose (right panel) VBF selections.*

3.4.2 Combination of Exclusive Cuts

As the cases of $\Delta\phi_{H-jj}$ and p_{THjj} already show, one has to be careful when cutting on variables which effectively force the kinematics in the exclusive 2-jet region and induce large logarithms in the perturbative series. Whether implementing a cut-based approach or in multivariate analysis (MVA), it is important to take into account the uncertainties induced by the exclusive restriction. As an illustration of the application of the ST method to a more general case, we now consider the case where we combine cuts on both p_{THjj} and $\Delta\phi_{H-jj}$. Later in Subsec. 3.4.4, we will discuss how to propagate uncertainties into MVAs.

Specifically, we study the exclusive 2-jet cross section as a function of $p_{THjj}^{\rm cut}$ with an additional constraint that we select only events which already have $\Delta\phi_{H-jj} > 2.6$. Following Eq. (3.1), the corresponding exclusive 2-jet cross section can be expressed as

$$\sigma_2(\Delta\phi_{H-jj} > 2.6,\, p_{THjj} < p_{THjj}^{\rm cut}) = \sigma_{\geq 2} - \sigma_{\geq 3}(\Delta\phi_{H-jj} < 2.6 \text{ or } p_{THjj} > p_{THjj}^{\rm cut})\,. \quad (3.26)$$

Taking $\rho = 0$ for simplicity, the corresponding exclusive uncertainty is now given in terms of the uncertainties obtained by scale variation in the inclusive cross sections as

$$\Delta_2^2(\Delta\phi_{H-jj} > 2.6,\, p_{THjj} < p_{THjj}^{\rm cut}) = \Delta_{\geq 2}^{\mu\,2} + \Delta_{\geq 3}^{\mu\,2}(\Delta\phi_{H-jj} < 2.6 \text{ or } p_{THjj} > p_{THjj}^{\rm cut})\,. \quad (3.27)$$

In Fig. 3.8, we show σ_2 as a function of the $p_{THjj}^{\rm cut}$ with fixed $\Delta\phi_{H-jj} > 2.6$ for the ATLAS and CMS loose VBF selections. As before, the cross section for $\mu = m_H$ is the central solid blue curve and the green dashed and dotted curves show the result of direct scale variation by a factor of two, while the outer solid orange lines show the uncertainties obtained from Eq. (3.27). As shown in Table 3.2, for $p_{THjj}^{\rm cut} = 30\,\text{GeV}$ we now get 56%, 31%, and 53% uncertainty for ATLAS, CMS loose, and CMS tight, which is slightly increased compared

Selection	σ [pb] $\mu = m_H$	Direct scale variation $\mu = 2m_H$	$\mu = m_H/2$	Combined incl. uncertainties ST ($\rho = 0$)
ATLAS				
$\sigma_{\geq 2}$	0.21			$\pm 21\%$
$\sigma_2(p_{THjj} < 30\,\text{GeV})$	0.15	-8%	-29%	$\pm 44\%$
$\sigma_2(\Delta\phi_{H-jj} > 2.6)$	0.19	-17%	-4%	$\pm 26\%$
$\sigma_2(p_{THjj} < 30\,\text{GeV}, \Delta\phi_{H-jj} > 2.6)$	0.14	-5%	-45%	$\pm 56\%$
CMS loose				
$\sigma_{\geq 2}$	0.41			$\pm 21\%$
$\sigma_2(p_{THjj} < 30\,\text{GeV})$	0.35	-18%	0%	$\pm 28\%$
$\sigma_2(\Delta\phi_{H-jj} > 2.6)$	0.39	-20%	$+9\%$	$\pm 24\%$
$\sigma_2(p_{THjj} < 30\,\text{GeV}, \Delta\phi_{H-jj} > 2.6)$	0.34	-16%	-4%	$\pm 31\%$
CMS tight				
$\sigma_{\geq 2}$	0.12			$\pm 21\%$
$\sigma_2(p_{THjj} < 30\,\text{GeV})$	0.08	-8%	-35%	$\pm 49\%$
$\sigma_2(\Delta\phi_{H-jj} > 2.6)$	0.10	-19%	-1%	$\pm 26\%$
$\sigma_2(p_{THjj} < 30\,\text{GeV}, \Delta\phi_{H-jj} > 2.6)$	0.07	-7%	-46%	$\pm 53\%$

Table 3.2: *Perturbative uncertainties at NLO in the exclusive $pp \to H + 2$ jet cross section via gluon fusion for cuts on p_{THjj} and $\Delta\phi_{H-jj}$ for both ATLAS and CMS VBF selections.*

to not having the additional cut on $\Delta\phi_{H-jj}$. For large values of p_{THjj}^{cut} the uncertainties in Fig. 3.8 correctly reproduce the exclusive uncertainties for $\Delta_2(\Delta\phi_{H-jj} > 2.6)$ without the cut on p_{THjj}.

3.4.3 Uncertainties in ggF-VBF Separation

The VBF production process is characterized by two forward jets with large rapidity separation and large dijet invariant mass. The VBF selection cuts used by the ATLAS and CMS experiments enhance the VBF contribution, but a significant $\sim 25\%$ ggF contribution remains. Since the VBF cross section is known rather precisely, an important source of theoretical uncertainty in the extraction of the VBF signal is the large perturbative uncertainty in the ggF contribution. After subtracting the non-Higgs backgrounds (which are of course another source of uncertainty), the measured cross section for Higgs production after implementing the VBF selection is given by

$$\sigma_2^{\text{measured}}(\Delta\phi_{H-jj}^{\text{cut}}) = \sigma_2^{\text{VBF}}(\Delta\phi_{H-jj}^{\text{cut}}) + \sigma_2^{\text{ggF}}(\Delta\phi_{H-jj}^{\text{cut}})\,. \tag{3.28}$$

For the purpose of extracting the VBF cross section, we effectively have to subtract the theory prediction for $\sigma_2^{\text{ggF}}(\Delta\phi_{H-jj}^{\text{cut}})$ from $\sigma_2^{\text{measured}}(\Delta\phi_{H-jj}^{\text{cut}})$. Therefore, the relevant figure of merit is $\Delta\sigma_2^{\text{ggF}}(\Delta\phi_{H-jj}^{\text{cut}})/\sigma_2^{\text{VBF}}(\Delta\phi_{H-jj}^{\text{cut}})$, i.e., the theory uncertainty in σ_2^{ggF} measured relative to the expected VBF cross section, σ_2^{VBF}. In Fig. 3.9 we show the ggF uncertainty relative to the VBF signal cross section over a range of p_{THjj}^{cut} and $\Delta\phi_{H-jj}^{\text{cut}}$ using the ATLAS

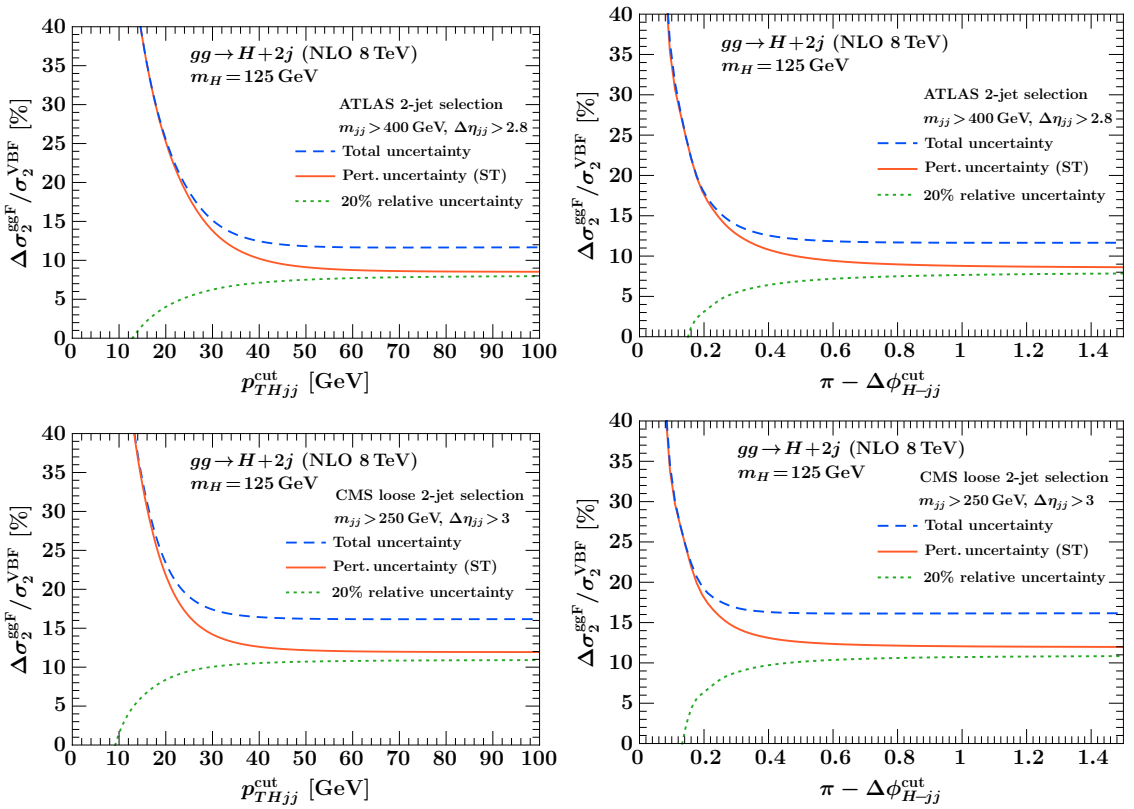

Figure 3.9: *Theoretical uncertainties of the ggF contribution relative to the VBF cross section as function of p_{THjj}^{cut} (left panels) and $\Delta\phi_{H-jj}^{\text{cut}}$ (right panels) for the ATLAS VBF selection (top panels) and CMS loose VBF selection (bottom panels). The solid orange lines show the perturbative uncertainties in σ_2^{ggF}, the green dotted lines a flat 20% parametric uncertainty in σ_2^{ggF}, and the dashed blue lines both contributions added in quadrature.*

and CMS loose VBF selections. In these plots, the solid orange curve shows our results for the NLO perturbative uncertainties (corresponding to the orange lines in Fig. 3.7). For comparison, the green dotted curve shows a fixed 20% uncertainty in the ggF cross section, i.e., taking $\Delta\sigma_2^{\text{ggF}} = 0.2\,\sigma_2^{\text{ggF}}$, which for example could be due to PDF and α_s parametric uncertainties. Hence, the green dotted lines effectively track the size of the ggF cross section relative to the VBF cross section (multiplied by 0.2). In the dashed blue lines, both uncertainty contributions are added in quadrature.

In the region of low p_{THjj}^{cut} or $\pi - \Delta\phi_{H-jj}^{\text{cut}}$, the relative uncertainty coming from the ggF contribution quickly increases below $p_{THjj} \lesssim 30\,\text{GeV}$ and $\pi - \Delta\phi_{H-jj} \lesssim 0.4$. This is despite the fact that the relative ggF cross section quickly decreases there, as can be inferred from the decrease in the dotted green lines. In this region, the total uncertainty shown by the blue dashed curve becomes completely dominated by the perturbative ggF uncertainty. Hence, one should be careful when implementing and optimizing either indirect restrictions on additional radiation, like $\Delta\phi_{H-jj}$, or explicit p_T-vetoes like p_{THjj}, since the gain in sensitivity in the Higgs signal from reduced non-Higgs backgrounds must be weighed against

the increased theoretical uncertainty in separating the ggF and VBF contributions.

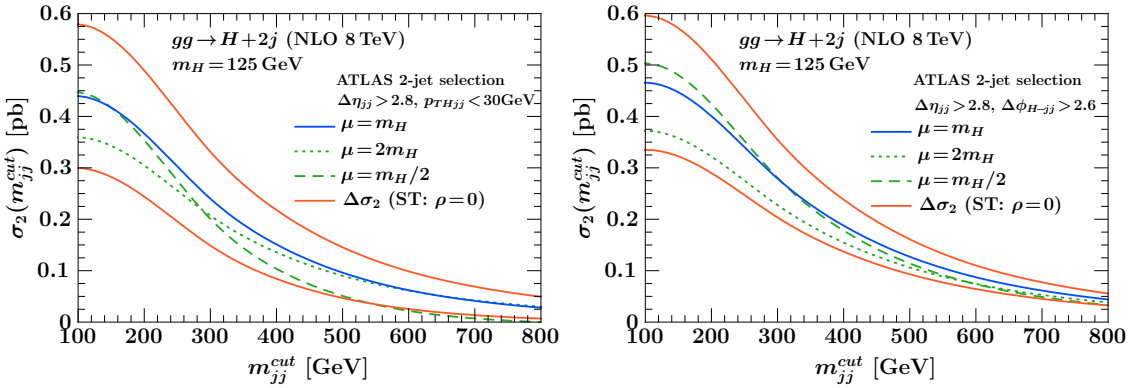

Figure 3.10: *Exclusive 2-jet cross section over a range of m_{jj}^{cut} for fixed $p_{THjj} < 30\,\text{GeV}$ (left panel) and fixed $\Delta\phi_{H-jj} > 2.6$ (right panel) for the ATLAS VBF selection.*

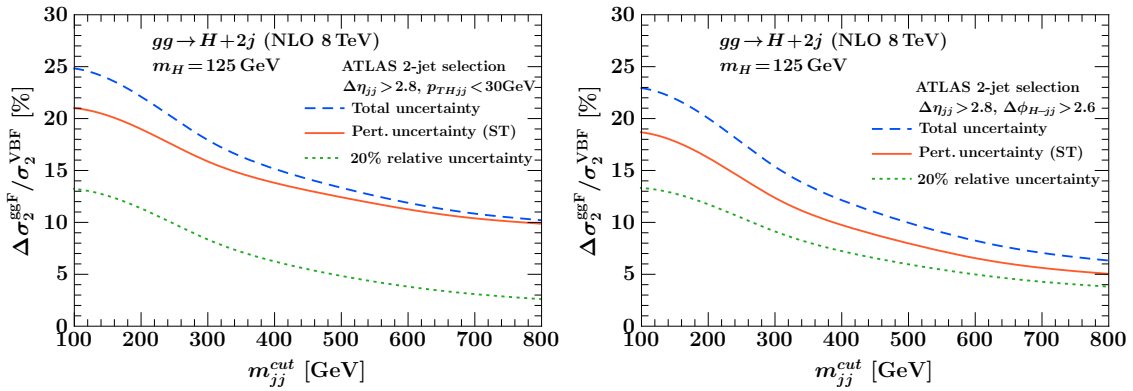

Figure 3.11: *Perturbative uncertainties of the ggF contribution relative to the VBF cross section over a range of m_{jj}^{cut} for fixed $p_{THjj} < 30\,\text{GeV}$ (left panel) and fixed $\Delta\phi_{H-jj} > 2.6$ (right panel) for the ATLAS VBF selection.*

The perturbative uncertainties in the exclusive 2-jet cross section also depend on the chosen VBF cuts and increase with a higher cut on the dijet invariant mass, m_{jj}. The reason for this effect is that at higher m_{jj} the effective hard scale in the process is also pushed higher causing the logarithmic corrections at a given value of p_{THjj}^{cut} to increase. This is seen explicitly in Fig. 3.10, which shows the exclusive 2-jet cross section over a range of m_{jj}^{cut} using the ATLAS VBF selection for a fixed cut $p_{THjj} < 30\,\text{GeV}$ or $\Delta\phi_{H-jj} > 2.6$, where the curves have the same meaning as in Figs. 3.7 and 3.8. As expected, with a cut on $p_{THjj} < 30\,\text{GeV}$, we see that the relative uncertainty in the ggF cross section grows for larger m_{jj} values, and reaches almost 100% for $m_{jj} \gtrsim 800\,\text{GeV}$. Note however that for such large m_{jj} cuts one might have to reevaluate whether $\mu = m_H$ is still an appropriate scale choice for this process. With a cut on $\Delta\phi_{H-jj} > 2.6$, the relative uncertainty in the ggF cross section stays roughly constant for larger m_{jj} presumably because this cut is somewhat milder, which we also saw in the results in Table 3.2.

In Fig. 3.11 we show the ggF uncertainty relative to the VBF cross section analogous to

Fig. 3.9. We can clearly see that in this case tightening the cut on m_{jj} does improve the separation of the ggF and VBF contributions, as the perturbative ggF uncertainty relative to the VBF cross section, shown by the orange curves, decreases. In this case, the overall reduction of the ggF contamination relative to the VBF cross section is stronger than the increase in the perturbative uncertainties of the ggF contribution. Hence, care must be taken when implementing and optimizing either indirect restrictions on additional radiation, like $\Delta\phi_{H-jj}$, or explicit p_T-vetoes like p_{THjj} or a central jet veto, and also in applying more general cuts which restrict to the exclusive 2-jet region as in the case of multivariate analysis.

3.4.4 Generalization to arbitrary cuts and application to MVAs

In this subsection, we will discuss a simple method to propagate the theory uncertainties into multivariate analysis (MVA). This work was done in collaboration with the ATLAS experimentalists Dag Gillberg and Florian Bernlochner and appeared in Ref. [53].

To apply our procedure of estimating uncertainties in jet-binning to MVAs, we need to generalize our method to include arbitrary number of cuts. For this, the formalism of Eq. (3.2) can be extended to further divide $\sigma_{\geq N+1}$ into an arbitrary number of bins,

$$\begin{aligned}\sigma_{\geq N} &= \int_0^{p^{\text{cut}\,1}} \mathrm{d}p_{N+1}\,\frac{\mathrm{d}\sigma_{\geq N}}{\mathrm{d}p_{N+1}} + \int_{p^{\text{cut}\,1}}^{p^{\text{cut}\,2}} \mathrm{d}p_{N+1}\,\frac{\mathrm{d}\sigma_{\geq N}}{\mathrm{d}p_{N+1}} + \cdots + \int_{p^{\text{cut}\,n-1}}^{p^{\text{cut}\,n}} \mathrm{d}p_{N+1}\,\frac{\mathrm{d}\sigma_{\geq N}}{\mathrm{d}p_{N+1}} \\ &\equiv \sigma_N(p^{\text{cut}\,1}) + \sigma_{\geq N+1}(p^{\text{cut}\,1}, p^{\text{cut}\,2}) + \cdots + \sigma_{\geq N+1}(p^{\text{cut}\,n-1}, p^{\text{cut}\,n})\,. \end{aligned} \tag{3.29}$$

This splitting divides the inclusive N-jet cross section, $\sigma_{\geq N}$, into n bins, whose uncertainties and correlations can be described by a symmetric $n \times n$ covariance matrix with $n(n+1)/2$ independent parameters. To construct this covariance matrix we use the boundary conditions that the inclusive cross sections $\sigma_{\geq N}$ and $\sigma_{\geq N+1}(p^{\text{cut}}, \infty)$ are uncorrelated, which implements the ST procedure for a given p^{cut}. This is not sufficient to determine the complete matrix. For the remaining entries, a simple linear correlation model is used, where the correlation κ_{ij} between $\sigma_{\geq N+1}(p^{\text{cut}\,i}, \infty)$ and $\sigma_{\geq N+1}(p^{\text{cut}\,j}, \infty)$ is given by

$$\kappa_{ij} = 1 - (1-\rho)\frac{|p^{\text{cut}\,i} - p^{\text{cut}\,j}|}{p^{\text{cut}\,n} - p^{\text{cut}\,1}}. \tag{3.30}$$

The parameter ρ determines the strength of the correlations between the inclusive $N+1$-jet cross sections for different p^{cut}. The dependence on this underlying correlation model is tested below by using the three different values $\rho = \{50\%, 90\%, 99\%\}$. As we will see, the obtained uncertainty estimates are very insensitive to the precise choice of ρ.

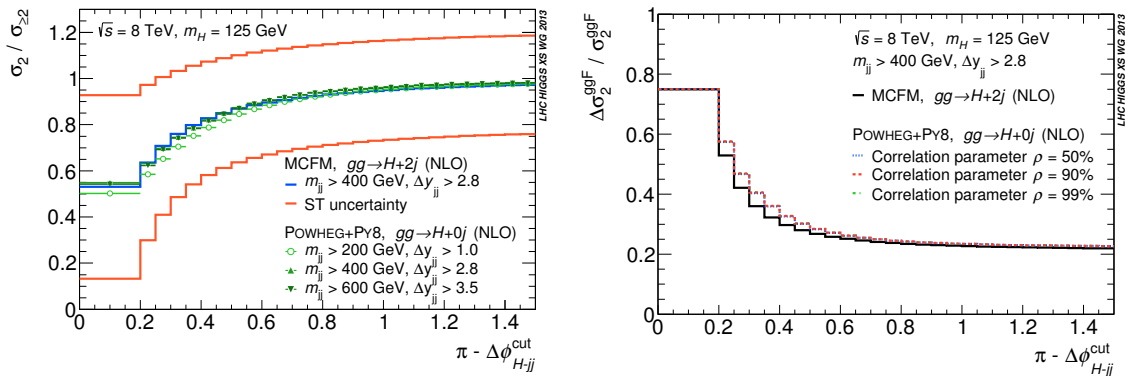

Figure 3.12: *Comparison of the exclusive $pp \to H + 2$ jet cross section via ggF from MCFM and* POWHEG+PYTHIA8 *$H+0$ jets as a function of $\pi - \Delta\phi^{\text{cut}}_{H-jj}$ (where the cut value is given by the upper bin edges). Left: The normalized cumulant $\sigma_2/\sigma_{\geq 2}$. The histograms show the fixed-order results from MCFM, corresponding to Fig. 3.7(b). The data points show* POWHEG+PYTHIA8 *results for different VBF selections, which only depend weakly on the precise VBF selection and agree well with MCFM. Right: The relative ST uncertainties from MCFM (black solid histogram) are compared to the resulting uncertainties (dotted histograms) after propagation to the* POWHEG+PYTHIA8 *prediction using Eq. (3.31). The resulting uncertainties closely agree with the MCFM input uncertainties and do not depend on the correlation model assumed in the propagation. Figs. taken from Ref. [53].*

ATLAS and CMS used POWHEG $gg \to H + 0$ jets at NLO [54–56] to model the hard scattering process, interfaced with PYTHIA8 [57] for modelling of underlying event, parton showering, and hadronization. In the left panel of 3.12 we compare the normalized cumulative cross section for different values of $\Delta\phi^{\text{cut}}_{H-jj}$ between POWHEG+PYTHIA8 and MCFM. For both generators, the anti-k_T algorithm with $R = 0.4$ is used to reconstruct the jets, excluding the Higgs decay products, and a typical VBF phase space selection is applied. Here, the first bin, which encloses the IR sensitive region, must be chosen large enough to ensure that MCFM can still be used to estimate its uncertainties using the ST procedure. Based on 3.7(b) and 3.7(f) we choose the first bin as $(\pi - \Delta\phi_{H-jj}) \in [0, 0.2]$. The cumulant shapes are in good agreement, also when the POWHEG+PYTHIA8 VBF selection is varied. When applying an exclusive 2-jet selection based on $\Delta\phi_{H-jj}$, the uncertainty of the event yield N_2 from POWHEG+PYTHIA8 can be estimated from

$$(\Delta N_2)^2 = \sum_{i,j} \widehat{C}_{ij}\, n_i\, n_j\,, \qquad \widehat{C}_{ij} = \frac{1}{\sigma_i \sigma_j} C_{ij}\,, \qquad N_2 = \sum_i n_i\,, \tag{3.31}$$

where C_{ij} denotes the covariance matrix, σ_i the predicted cross section in the interval of the i^{th} bin, n_i denotes the event yield of the Monte Carlo prediction in the i^{th} bin, and the sum runs over all bins that define the exclusive 2-jet phase space one is interested in. To construct C_{ij}, we use the MCFM uncertainties of Fig. 3.7(b) as inputs to the procedure described above. The right panel of Fig. 3.12 compares the relative uncertainties calculated from Eq. (3.31) for POWHEG+PYTHIA8 for different correlation models, showing a good agreement with the input MCFM uncertainties. Note in particular that the 2-jet inclusive cross section uncertainty is recovered when calculating the cumulant over the full range of

$\Delta\phi_{H-jj}$. Eq. (3.31) is used in the following two sections to derive uncertainties for nonlinear cuts on $\Delta\phi_{H-jj}$ due to resolution effects and for selections based on a multivariate classifier.

In the context of a multivariate analysis, the effective cuts on $\Delta\phi_{H-jj}$ and p_{THjj} introduced by the nonlinear selection of phase space have to be studied carefully. In particular, if either of the variables are used directly as learning input for the multivariate classifier, one has to make sure that the final classification does not cut arbitrarily close into the infrared sensitive regions, i.e. $\Delta\phi_{H-jj} \to \pi$ and $p_{THjj} \to 0$. This can be prevented by transforming either variable into an infrared safe form,

$$\Delta\phi'_{H-jj} = \begin{cases} \Delta\phi_{H-jj} & \text{if } \Delta\phi_{H-jj} < \Delta\phi^{\text{cut}}_{H-jj}, \\ \Delta\phi^{\text{cut}}_{H-jj} & \text{if } \Delta\phi_{H-jj} \geq \Delta\phi^{\text{cut}}_{H-jj}, \end{cases} \qquad p'_{THjj} = \begin{cases} p_{THjj} & \text{if } p_{THjj} < p^{\text{cut}}_{THjj}, \\ p^{\text{cut}}_{THjj} & \text{if } p_{THjj} \geq p^{\text{cut}}_{THjj}, \end{cases} \tag{3.32}$$

allowing the multivariate algorithm only to exploit the normalization difference in the infrared sensitive region of phase space.

The procedure of deriving the exclusive 2-jet cross section uncertainties using a multivariate selection based on a boosted decision tree was mainly done by the ATLAS experimentalists. In this, the decision tree was trained to distinguish VBF like events in $H \to \gamma\gamma$ and to reject prompt diphoton background. As input for background, simulated prompt diphoton decays by Sherpa are used. The signal was simulated using Powheg+Pythia8 for VBF and ggF decays, both simulated at NLO. To all samples resolution effects were added using the same simple normal resolution model as above. Six typical variables often used in VBF analyses were chosen to train the decision tree.

Fig. 3.13(a) shows the distribution in $\Delta\phi_{H-jj}$ for the simulated background and signal decays. VBF events produce a topology which causes the Higgs and dijet system to be more back-to-back than background and ggF events. The multivariate method will make use of this to select a signal enriched region of phase space, and cut into this distribution. Fig. 3.13(b) depicts the $m_{\gamma\gamma}$ invariant mass distribution before and after a cut on the multivariate classifier, illustrating the effect of the smearing model. Fig. 3.13(c) shows the classifier $\mathcal{O}_{\text{MVA}}$: VBF signal peaks near the positive values, and background and ggF accumulates near negative values. Finally, Fig. 3.13(d) depicts the ggF $\Delta\phi_{H-jj}$ spectrum for a progression of cuts on the classifier. The curves were normalized to have the same number of events in the region of $0 - 0.2$, which corresponds to the cutoff value used in Eq. (3.32).

Cutting on the classifier separates the inclusive 2-jet cross section into an exclusive 2-jet and an inclusive 3-jet part, similar as with a rectangular cut on $\Delta\phi_{H-jj}$ or p_{THjj}. In Tab. 3.3 we list the uncertainties calculated from Eq. (3.31) for a progression of cuts and different

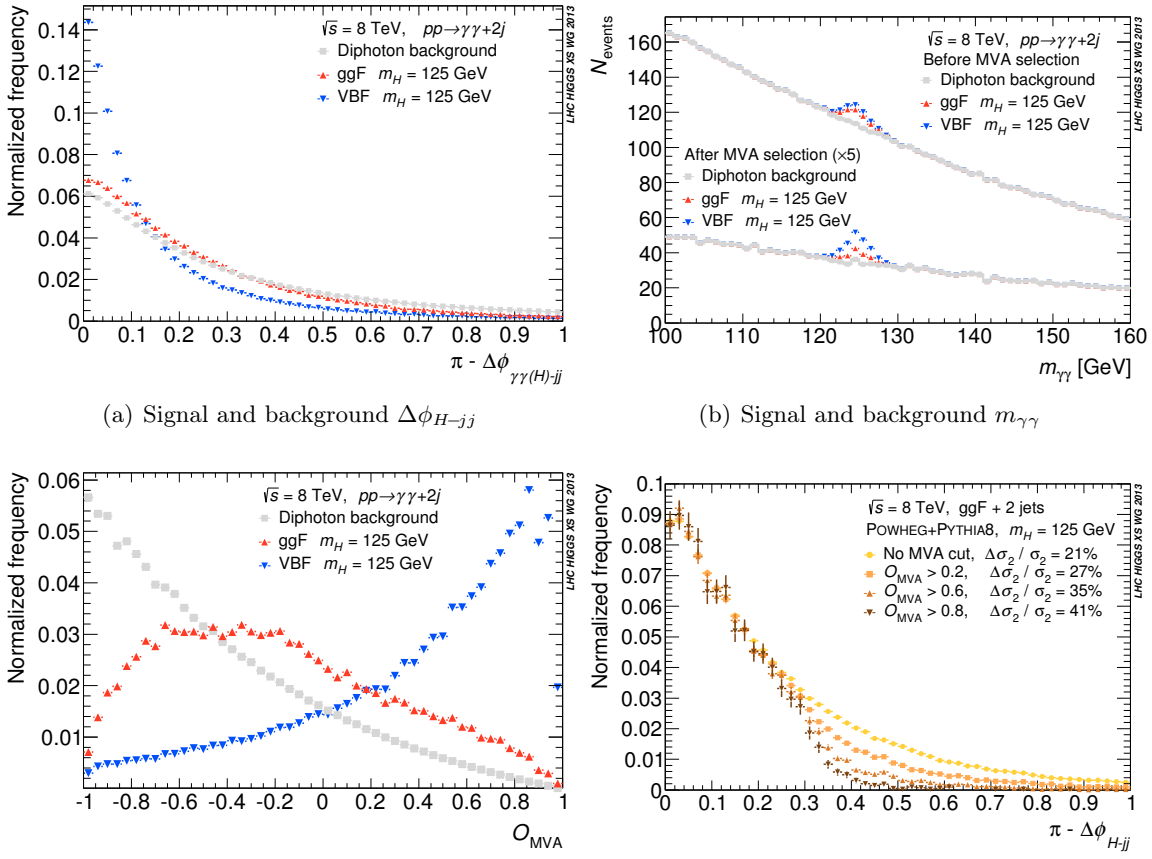

(a) Signal and background $\Delta\phi_{H-jj}$

(b) Signal and background $m_{\gamma\gamma}$

(c) Multivariate classifier

(d) ggF $\Delta\phi_{H-jj}$ for a progression of cuts

Figure 3.13: *Signal and Background distributions of the multivariate selection: 3.13(a) shows $\Delta\phi_{H-jj}$ for background and VBF signal; 3.13(b) depicts the invariant diphoton mass spectrum for diphoton background (grey), ggF (red), and VBF (blue) before and after an arbitrary cut on the multivariate classifier. 3.13(c) depicts the multivariate classifier constructed from the six input variables for background, ggF, and VBF following the same color code. 3.13(d) shows the $\Delta\phi_{H-jj}$ distribution without any cut, and a progression of cuts on the multivariate classifier, also quoting the uncertainties on the integral obtained using Eq. (3.31). Figs. taken from Ref. [53]*

slopes for the linear correlation model: Harder cuts on the classifier translate into a tighter nonlinear selection in $\Delta\phi_{H-jj}$ phase space. As expected, this increases the exclusive 2-jet cross section uncertainty. The progressive harder cuts have a flat efficiency in $\Delta\phi_{H-jj}$ above the threshold of 0.2 (i.e. cut into this region without changing its shape), which is important to obtain reliable uncertainties from Eq. (3.31). The dependence on the actual details on the linear correlation model is small: Changing the bin-by-bin correlations of the inclusive 3-jet cross section phase space by varying ρ from 50% to 99% has a practically negligible effect on the estimated uncertainty.

The method described here was used in the ATLAS $H \to \gamma\gamma$ measurement [58], to determine the uncertainties for the two used VBF MVA selections. The uncertainties found there were 28.3% and 48.4% for the loose and tight MVA category, respectively. The same

Table 3.3: *Relative perturbative uncertainties at NLO for $gg \to H + 2$ jets after applying a selection on the multivariate classifier $\mathcal{O}_{MVA}$. The uncertainty is calculated using generator level $\Delta\phi_{H-jj}$.*

Cut	$\Delta\sigma_2/\sigma_2$ ($\rho = 50\%$)	$\Delta\sigma_2/\sigma_2$ ($\rho = 90\%$)	$\Delta\sigma_2/\sigma_2$ ($\rho = 99\%$)
no cut	21.0%	21.0%	20.9%
$\mathcal{O}_{\text{MVA}} > 0.2$	26.6%	26.8%	26.9%
$\mathcal{O}_{\text{MVA}} > 0.6$	34.3%	34.6%	34.7%
$\mathcal{O}_{\text{MVA}} > 0.8$	40.8%	41.1%	41.1%

approach applied to the CMS MVA analysis [59] at reconstruction level gives an uncertainty for the tight category of about 40%, which is similar to the ATLAS result. Our procedure of estimating theory uncertainties was used in the ATLAS VBF analyses in $H \to ZZ \to l^+l^-q\bar{q}$ in [60] and $H \to \gamma\gamma$ in [61–63].

3.5 Conclusions

The exclusive H+2-jet cross section for Higgs production via VBF is a key ingredient in determining the Higgs coupling to gauge bosons. The typical VBF selection cuts used by the ATLAS and CMS experiments include either indirect or direct restrictions on additional emissions in order to enhance the VBF signal over non-Higgs background and ggF contribution. Such restrictions introduce a nontrivial jet binning, where the inclusive 2-jet cross section ($\sigma_{\geq 2}$) is effectively divided into an exclusive 2-jet bin (σ_2) and a remaining inclusive 3-jet bin ($\sigma_{\geq 3}$). With such a jet binning one has to account for two sources of perturbative uncertainties. In addition to the absolute yield uncertainty which is correlated between the jet bins, there is also a migration uncertainty which is anticorrelated and drops out in the sum of the bins. This migration uncertainty is associated with the perturbative uncertainty in the logarithmic series that is introduced by the exclusive binning cut. As the binning cut becomes tighter, the logarithms grow large and eventually lead to a breakdown of fixed-order perturbation theory, at which point a logarithmic resummation becomes necessary. In practice, the experimentally relevant region typically lies inside the transition region between the fully inclusive region (no binning) and the extreme exclusive region (very tight binning). In this region, fixed-order perturbation theory can still be applied. However, since the logarithms are already sizeable, one has to explicitly take into account the migration uncertainty. This can be achieved using the ST method.

In this chapter, we studied in detail the application of the ST method for estimating NLO perturbative uncertainties in $pp \to H + 2$ jets via ggF, including its generalization and validation against alternative prescriptions. We find that the perturbative uncertainties are very sensitive to the exclusive cut and can quickly become sizeable. While applying

a strong restriction on additional emissions is expected to increase the sensitivity to the VBF signal, it is not necessarily beneficial for distinguishing the VBF and ggF production modes because of the quickly increasing ggF uncertainties. Hence, it would be important to include the perturbative uncertainties as a function of the binning cut when optimizing the experimental selections.

We also considered the extension of the ST procedure to arbitrary number of cuts, where to construct the covariance matrix, we assumed a set of correlation relations between the N+1-th jet cross sections for different values of the binning cut. We compared the exclusive $pp \to H + 2$-jet cross section via ggF from MCFM with POWHEG+PYTHIA8 H+0 jet cross section as a function of $\pi - \Delta\phi_{H-jj}$ cut and found good agreement. We also found agreement between our uncertainty estimates from MCFM and from applying our covariance matrix to POWHEG+PYTHIA8. As an application to MVAs, we studied the relative perturbative uncertainties at NLO for $gg \to H + 2$ jets after applying a selection on the multivariate classifier and found that tighter selection cuts result in an increase in the exclusive 2-jet cross section uncertainty.

In principle, by performing a higher-order logarithmic resummation, one can gain additional information, which allows for refined perturbative predictions and uncertainty estimates, however it is technically more demanding for the exclusive $H + 2-$jet cross section. Our analysis of NLO uncertainties provides an important baseline for future studies and can be extended to estimate uncertainties in fixed-order cross sections as well as resummed predictions for different exclusive Higgs production processes.

For any exclusive jet cross section measurements at the LHC, jet vetoes play a crucial part of the signal selection. In the following chapter we will discuss in detail the different jet veto observables in particular rapidity dependent jet vetoes and the factorization and resummation properties of such observables in the framework of SCET.

Chapter 4

Rapidity dependent jet vetoes.

This chapter is based on my work in [12]. In this chapter I will introduce rapidity dependent jet vetoes and discuss their factorization and resummation properties in SCET. I will obtain resummed predictions at NLL′+ NLO for the gluon fusion H+0-jet cross section with these type of jet vetoes. For one of the jet-veto observables, we also compare our numerical predictions with the differential cross section measurement by ATLAS in the $H \to \gamma\gamma$ channel and find good agreement.

4.1 Introduction

The jet-like characteristics of hadronic final states in an event can be described using 'shape variables'. The idea is to define a quantity which describes the shape of an event, for example whether the distribution of hadrons in the final state is pencil-like, planar, spherical etc. The procedure is to define a kinematic observable X which measures a particular aspect of the shape of the hadronic final state and to theoretically predict the differential distribution $\mathrm{d}\sigma/\mathrm{d}X$ and compare with the measurements. Some examples of event shape observables are

$$\begin{aligned}
&\text{Thrust} : T = \max_n \frac{\sum_i |p_i \cdot n|}{\sum_i |p_i|} \,. \\
&\text{C-parameter} : C = \frac{3}{Q} \sum_i \frac{|\vec{p}_{Ti}|}{2\cosh\eta_i} \,. \\
&\text{N-jettiness} : \tau_N = \frac{2}{Q^2} \sum_i \min\{q_a \cdot p_i, q_b \cdot p_i, q_1 \cdot p_i, q_2 \cdot p_i ...\} \,. \\
&\text{beam thrust} : \tau_B = \frac{1}{Q} \sum_i \min\{q_a \cdot p_i, q_b \cdot p_i\} \,.
\end{aligned} \tag{4.1}$$

Here q_a, q_b and $q_1 ... q_n$ are a fixed set of massless reference momenta for the two beams and the N signal jets. For almost collinear energetic jets, p_i lies along the direction of q_i. For the case of $e^+e^- \to q\bar{q}$, $T = 1$ for two pencil-like jets and $T < 1$ for events with additional jets (>2) in the final state. The kinematic range for C parameter is $0 \leq C \leq 1$, with $C = 0$ for a perfectly two-jet-like final state and $C = 1$ for an isotropic distribution of final-state momenta. For an event with at least N energetic jets, N-jettiness τ_N [64, 65] provides an inclusive measure of how N-jet-like the event looks. In the limit $\tau_N \to 0$ the event contains exactly N infinitely narrow jets and for $\tau_N \sim 1$, the event has hard radiation between the signal jets. Requiring $\tau_N \ll 1$ constrains the radiation outside the signal and beam jets providing an inclusive way to veto additional central jets. Beam thrust τ_B is the limit of τ_N for processes where there is initial state radiation (ISR) from incoming partons but no final state jets $N = 0$ (eg: Drell Yan, Higgs+0-jet). Thus beam thrust provides a continuous measure of the zero-jettiness of an event.

Jet veto observables can in general be distinguished into two classes, inclusive and jet-based. Inclusive variables, such as the ones defined above, do not depend on a specific jet algorithm or jet size. Instead, they sum over all hadrons in the final state, and provide a global view of the event, effectively measuring the sum of all emissions. For such inclusive obseravables, the resummation has been performed upto NNLL and there are no issues for extending to higher orders. However, experimentally it is challenging to measure or contrain such inclusive observables due to pileup, underlying event and other issues. The solution is to use jet-based observables which are more straightforward because they are based on clustering final state hadrons into jets $J(R)$ of radius R using jet-algorithms like k_T [66, 67] or anti-k_T [68]. They provide a local view of the event and measure emissions locally with an effective "resolution" size set by R. A common choice in current experiments is p_T^{jet} with jets constructed using anti-k_T algorithm. On the theory side, however, the jet-algorithm dependence renders the resummation structure of jet-based observables more involved at higher orders. Depending on the size of R, there are competing effects due to clustering starting at $O(\alpha_s^2)$ which can spoil the logarithmic resummation but we will discuss more about such effects in Sec. 4.6 and compute them in chapter 5. We will mainly focus on the jet-based observables from now on.

While a veto on additional jets can be desirable in many contexts, the application of a tight jet veto is usually subject to both theoretical and experimental limitations. Theoretically, applying a tight jet veto leads to Sudakov double logarithms of the jet-veto variable in perturbation theory, which as the veto gets tighter (smaller veto cuts) become larger and dominate the perturbative series, leading to increased theoretical uncertainties in the fixed-order (FO) predictions [41]. This can be remedied by resumming the jet-veto logarithms to all orders [23–25, 64, 65, 69–75]. This of course requires the considered jet-veto variable to be resummable and under good enough theoretical control.

Experimentally, jets can only be robustly reconstructed down to some minimum p_T, which limits how low one can go in the jet veto cut, i.e., how tight one can make the jet veto. Furthermore, in harsh pile-up conditions low-p_T jets are particularly hard to identify at forward rapidities (beyond $|\eta| \geq 2.4$), when a large part or all of the jet area lies in a detector region where no tracking information is available.

In principle, one possibility would be to place a hard cut on the (pseudo)rapidity η_j of the classified jets, i.e., one only considers and possibly vetoes jets within a certain range of central rapidities, $\eta_j < |\eta^{\text{cut}}|$. Theoretically, such a hard rapidity cut represents a nonglobal measurement. This means that a priori it is not clear how to incorporate it into the jet-veto resummation at higher orders, and none of the present jet-veto resummations for p_{Tj} actually includes such a rapidity cut. Another option, which avoids a hard rapidity cut, is to raise the cut on p_{Tj}, and thus loosen the jet veto everywhere. Clearly, this may also not be ideal since one now looses the utility of a tight jet veto for central jets.

Here, we discuss a class of jet-veto variables which explicitly depend on the jet rapidity y_j,[1]

$$\mathcal{T}_{fj} = p_{Tj}\, f(y_j)\,, \tag{4.2}$$

where $f(y)$ is some weighting function of the jet rapidity. By classifying jets according to $\mathcal{T}_{fj}$ and only allowing jets with $\mathcal{T}_{fj} < \mathcal{T}^{\text{cut}}$, we effectively have a rapidity-dependent veto on p_{Tj},

$$p_{Tj} < \frac{\mathcal{T}^{\text{cut}}}{f(y_j)}\,. \tag{4.3}$$

If the weighting function $f(y)$ is chosen as a decreasing function of $|y|$ this corresponds to a veto which gets tighter at central rapidities and looser at forward rapidities. Effectively, the contribution of forward jets is smoothly suppressed by the weighting function $f(y_j)$. At the same time, $f(y_j)$ can be chosen such that explicit theoretical control is maintained. In fact, all the variables we discuss can be resummed to a similar (and possibly higher) level of precision as p_{Tj}. In this way, one can largely avoid the theoretical and experimental limitations discussed above. (Of course, the lowest $\mathcal{T}_{fj}$ values that can be measured are ultimately still limited by how well central jets can be measured.)

Apart from such practical considerations, given the usefulness of jet binning, it is clearly beneficial to have several alternative and complementary ways to perform it, as this gives the experiments a wider range of options for optimizing their analyses. One could even optimize the form of $f(y)$ to the needs of a given analysis. On the theoretical side, it allows one to test jet-veto resummations in different and as of now unexplored regimes. Note that

[1] We consider the exact jet rapidity y_j in the following, though the difference between η_j and y_j due to a nonzero jet mass is not important to our discussion, and in principle either could be used.

two special cases we have already discussed above are no weighting, $f(y) \equiv 1$, for which $\mathcal{T}_{fj} \equiv p_{Tj}$, while $f(y) = \theta(|y| < y^{\text{cut}})$ is equivalent to a hard cut on the jet rapidity.

This chapter is organized as follows: in Sec. 4.2 we will define the weighting functions for the four different rapidity dependent jet veto observables, $\mathcal{T}_B^{\text{jet}}$, $\mathcal{T}_{B\text{cm}}^{\text{jet}}$, $\mathcal{T}_C^{\text{jet}}$ and $\mathcal{T}_{C\text{cm}}^{\text{jet}}$. In the next Sec. 4.3, we will compute the NLO cross section for $pp \to HX$ differential in the rapidity-dependent observables using fixed-order perturbation theory. In Sec. 4.4, we will review the basic structure of SCET including the ingredients and the Lagrangian. We will then derive the factorization formula for the generic process $pp \to LX$ differential in inclusive beam thrust and discuss the factorization for H+0-jet cross section with a veto $\mathcal{T}_f^{\text{jet}} < \mathcal{T}^{\text{cut}}$ in Sec. 4.6,. In Sec. 4.7, we will discuss the scale hierarchy between the factorized components, RG evolution and the structure of the resummed cross section. We will then provide the various inputs required to compute the NLL$'$ resummed cross section in Sec. 4.8. Having obtained the resummed results, in Sec. 4.9 we will compute the nonsingular corrections to the resummed cross sections using the NLO differential cross section computed in Sec. 4.3. These corrections are important to match our resummed cross section to the full fixed-order result. In Sec. 4.10, we will discuss how to estimate the perturbative uncertainties in our resummed cross section predictions extending the ST procedure discussed in chapter 3. And in Sec. 4.11, we provide numerical results at NLL$'$+NLO for the H+0-jet cross section with $\mathcal{T}_B$ and $\mathcal{T}_C$-type vetoes and compare our theory predictions with ATLAS measurements. We conclude in Sec. 4.12.

4.2 Rapidity-dependent observables: $\mathcal{T}_B^{\text{jet}}$ and $\mathcal{T}_C^{\text{jet}}$

Given the set of jets, $J(R)$, identified by some jet clustering algorithm, we define

$$p_T^{\text{jet}} = \max_{j \in J(R)} p_{Tj} \tag{4.4}$$

as the largest p_{Tj} of any jet. Requiring $p_T^{\text{jet}} < p_T^{\text{cut}}$ vetoes any event having at least one jet with $p_{Tj} > p_T^{\text{cut}}$. The so-defined 0-jet cross section then consists of events where all jets have $p_{Tj} < p_T^{\text{cut}}$. It is important to note that despite that fact, this does not actually require one to reconstruct jets with $p_{Tj} < p_T^{\text{cut}}$. Rather, one only has to be able to reconstruct jets with $p_{Tj} > p_T^{\text{cut}}$ which are to be vetoed. The resummation for a veto on p_T^{jet} is known to NNLL and partially beyond [24, 25, 69–71, 74].

For simplicity, we explicitly consider the 0-jet bin in the following. The extension to an N-jet bin is obtained by simply removing from the set $J(R)$ the N identified jets that have been selected as the "signal" jets. p_T^{jet} is then defined as the largest p_{Tj} of any additional

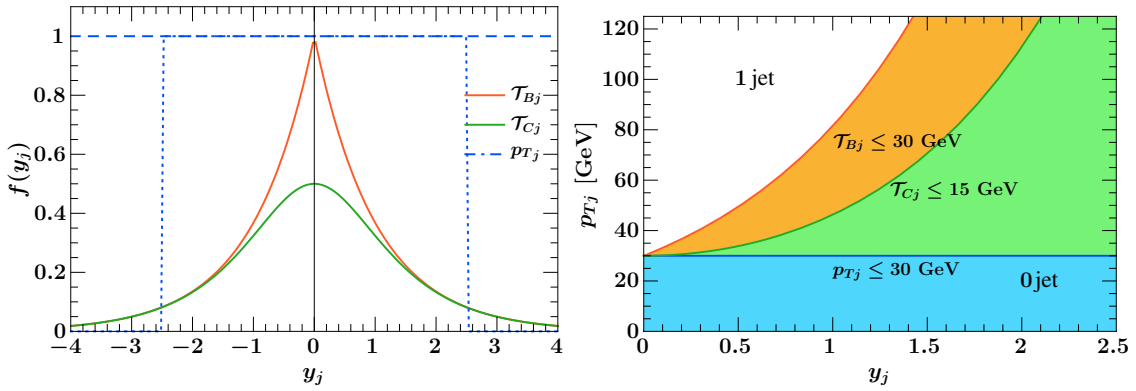

Figure 4.1: *Left: Illustration of rapidity weighting functions for $\mathcal{T}_{Bj}$ (orange), $\mathcal{T}_{Cj}$ (green), and p_{Tj} (blue dashed). The blue dotted lines show a fixed cut on the jet rapidity. Right: Phase-space region in the $p_{Tj} - y_j$ plane selected by the different jet-veto variables. (Here we take $Y = 0$, so $\mathcal{T}_{Bj} = \mathcal{T}_{B\text{cm}j}$.)*

unwanted jet (i.e. from additional initial-state or final-state radiation), which are to be vetoed by requiring $p_T^{\text{jet}} < p_T^{\text{cut}}$.

We can generalize this to $\mathcal{T}_{fj}$ by defining

$$\mathcal{T}_f^{\text{jet}} = \max_{j \in J(R)} \mathcal{T}_{fj} = \max_{j \in J(R)} |\vec{p}_{Tj}|\, f(y_j)\,. \tag{4.5}$$

We now distinguish between the $\mathcal{T}_{fj}$ value of any given jet j and $\mathcal{T}_f^{\text{jet}}$, which is the maximum $\mathcal{T}_{fj}$ of all jets (or all additional jets for the case of N selected signal jets). In particular, the "leading" jet is now determined by $\mathcal{T}_{fj}$ and not by p_{Tj}.[2] We can then classify events into jet bins according to $\mathcal{T}_f^{\text{jet}}$ and define a 0-jet cross section by requiring

$$\mathcal{T}_f^{\text{jet}} < \mathcal{T}^{\text{cut}}\,, \tag{4.6}$$

which consists of events where all jets have $\mathcal{T}_{fj} < \mathcal{T}^{\text{cut}}$. The corresponding inclusive 1-jet cross section defined by requiring $\mathcal{T}_f^{\text{jet}} > \mathcal{T}^{\text{cut}}$ consists of all remaining events that have at least one jet with $\mathcal{T}_{fj} > \mathcal{T}^{\text{cut}}$. Similar to the p_T^{jet} case, this $\mathcal{T}_f^{\text{jet}}$ binning now requires one to be able to reconstruct jets down to $\mathcal{T}_{fj} > \mathcal{T}^{\text{cut}}$, while jets below $\mathcal{T}^{\text{cut}}$ do not have to be reconstructed.

The four jet-veto variables we consider in the following are defined with their respective

[2] In principle, one could also measure the $\mathcal{T}_{fj}$ of the leading-p_T jet. However, using this as a jet veto would make things much more involved and we will not consider such mixed cases.

weighting functions as follows:

$$\mathcal{T}_B: \quad f(y) = e^{-|y-Y|}\,, \tag{4.7}$$

$$\mathcal{T}_{B\text{cm}}: \quad f(y) = e^{-|y|}\,, \tag{4.8}$$

$$\mathcal{T}_C: \quad f(y) = \frac{1}{2\cosh(y-Y)}\,, \tag{4.9}$$

$$\mathcal{T}_{C\text{cm}}: \quad f(y) = \frac{1}{2\cosh y} \tag{4.10}$$

Here, Y denotes the rapidity of the hard system. For the 0-jet case, this is equivalent to the nonhadronic final state, i.e. Y is the vector-boson rapidity for Drell-Yan or the Higgs-boson rapidity in gluon-fusion Higgs production. By including Y in $\mathcal{T}_B$ and $\mathcal{T}_C$, the variables become longitudinally boost-invariant.[3] On the other hand, $\mathcal{T}_{B\text{cm}}$ and $\mathcal{T}_{C\text{cm}}$ are explicitly defined in the hadronic center-of-mass (cm) frame, i.e. the lab frame, which has the advantage that one does not have to reconstruct Y.

The different rapidity weighting functions are illustrated in the left panel of Fig. 4.1 by the orange ($\mathcal{T}_{Bj}$) and green ($\mathcal{T}_{Cj}$) lines. For comparison, the blue dashed line shows the case of p_{Tj} ($f(y) = 1$) and the blue dotted line a hard rapidity cut. The weighting $\sim e^{-|y|}$ for $\mathcal{T}_{Bj}$ is the same as that for inclusive beam thrust, so we can think of $\mathcal{T}_{Bj}$ as the beam thrust of a single jet and $\mathcal{T}_B^{\text{jet}}$ as the maximum jet beam thrust (which was first discussed in Ref. [70]). The rapidity weighting for $\mathcal{T}_{Cj}$ is the same as that for the C-parameter event-shape in $e^+e^- \to$ dijets. It becomes equal to $\mathcal{T}_{Bj}$ at forward rapidities, while at central rapidities it is much flatter and approaches $p_{Tj}/2$ for $y_j = 0$. Experimentally, this has the advantage that $\mathcal{T}_C^{\text{jet}}$ can be measured to much smaller values. The region in the $p_{Tj} - y_j$ phase space selected by the different variables is illustrated in Fig. 4.1 on the right. The lines correspond to the given fixed value of $\mathcal{T}_{fj}$. They separate the "0-jet" region (colored), where the jet would be allowed by the corresponding jet-veto cut, and the "1-jet" region (uncolored), where the jet would be vetoed.

The strict exponential weighting for $\mathcal{T}_{Bj}$ is distinguished by the fact that $\mathcal{T}_{Bj}$ is related to the small light-cone component with respect to the beam axis of the total jet momentum. More precisely, including the nonzero mass of the jet, m_j, we have

$$\begin{aligned} p_{Tj}\, e^{-|\eta_j|} &= |\vec{p}_j| - |p_{zj}|\,, \\ m_{Tj}\, e^{-|y_j|} &\equiv \sqrt{p_{Tj}^2 + m_j^2}\, e^{-|y_j|} = E_j - |p_{zj}|\,. \end{aligned} \tag{4.11}$$

Either of these variants can be used as alternative definitions of $\mathcal{T}_{B\text{cm}}$ (and analogously

[3] They can be thought of as being defined in the frame where $Y = 0$, and in all other frames by boosting from that frame.

for $\mathcal{T}_B$), if this is desired or turns out to be advantageous for their experimental measurement. Theoretically, all of these are distinct variables which however have a very similar logarithmic structure at small $\mathcal{T}_B^{\text{jet}}$. The different treatment of the jet mass amounts to having different jet clustering corrections for each variable and can be taken into account systematically. They start entering at $O(\alpha_s^2)$, which is beyond the order we are currently working at. We will compute them in the next chapter.

The analogous discussion holds for $\mathcal{T}_{C(\text{cm})}$, which including nonzero m_j can be defined in terms of either combination of p_{Tj} or m_{Tj} and η_j or y_j. Explicitly,

$$\begin{aligned} \frac{p_{Tj}}{2\cosh\eta_j} &= \frac{p_{Tj}^2}{2|\vec{p}_j|}\,, \\ \frac{m_{Tj}}{2\cosh y_j} &= \frac{p_{Tj}^2 + m_j^2}{2E_j}\,. \end{aligned} \tag{4.12}$$

Again, either of these variants could be used as alternative definitions of $\mathcal{T}_{Cj}$. The ATLAS measurement [38] uses the last variant above in the $Y = 0$ frame, i.e., $\mathcal{T}_{Cj} \equiv m_{Tj}/[2\cosh(y_j - Y)]$.

Note that $1/(2\cosh x) = 1/(e^x + e^{-x}) \to e^{-|x|}$ for large $|x|$, such that at forward rapidities $\mathcal{T}_{Cj}$ has the same behavior as $\mathcal{T}_{Bj}$, as seen in Fig. 4.1. For this reason, its logarithmic structure is closely related to that of $\mathcal{T}_{Bj}$, and in particular the same technology can be used to resum it to the same level of accuracy.[4] The same reasoning also applies more generally to any (continuous) weighting function $f(y)$ that approaches $e^{-|y|}$ at large rapidities. This gives considerable freedom in choosing other alternative rapidity weighting functions yielding resummable jet-veto variables.

4.3 $pp \to HX$ process at NLO

The full H + 0-jet cross section differential in the Higgs rapidity Y and with a cut on $\mathcal{T}_f^{\text{jet}} < \mathcal{T}^{\text{cut}}$ can be written as

$$\frac{\mathrm{d}\sigma_0}{\mathrm{d}Y}(\mathcal{T}_f^{\text{jet}} < \mathcal{T}^{\text{cut}}) = \frac{\mathrm{d}\sigma_0^{\text{resum}}}{\mathrm{d}Y}(\mathcal{T}_f^{\text{jet}} < \mathcal{T}^{\text{cut}}) + \frac{\mathrm{d}\sigma_0^{\text{nons}}}{\mathrm{d}Y}(\mathcal{T}_f^{\text{jet}} < \mathcal{T}^{\text{cut}})\,, \tag{4.13}$$

where the first term contains the resummed logarithmic contributions, which dominate at small $\mathcal{T}^{\text{cut}}$, and the second term contains the "nonsingular" corrections, which are suppressed relative to the leading terms by $O(\mathcal{T}^{\text{cut}}/m_H)$ and vanish in the limit $\mathcal{T}^{\text{cut}} \to 0$.

[4] Analogously, in the context of $e^+e^- \to$ jets, the C-parameter event shape is closely related to thrust, which makes it comparably easy to resum to the same high order as for thrust [76].

The cross sections also depend on the jet algorithm and jet radius R, which we suppress here to keep the notation simple.

In this section, we will compute the NLO $pp \to HX$ cross section differential in rapidity Y and the above defined $\mathcal{T}_B$ and $\mathcal{T}_C$-type jet veto observables. This fixed-order result is required as an input to extract the nonsingular contributions, which are important at large $\mathcal{T}^{\rm cut}$ to reproduce the right inclusive cross section. The nonsingular corrections will be computed using subtraction method in Sec. 4.9.

Let us consider a process where a pair of hadrons of momenta P_a and P_b collide producing a Higgs boson H with a momentum q and a number of other particles with a total momentum p_X. Momentum conservation then reads

$$P_a + P_b = q + p_X \,. \tag{4.14}$$

A factorization formula relates this hadronic process $h_a h_b \to HX$ to the partonic process $ab \to HX'$ as discussed in Sec. 2.2. Here a and b are partons of momenta $p_a = \xi_a P_a$ and $p_b = \xi_b P_b$ and X' stands for the final state particles except for the Higgs boson. The momentum conservation for the partonic process is

$$p_a + p_b = q + p'_X \,. \tag{4.15}$$

where

$$p'_X = P_a + P_b - q - (1-\xi_a)P_a - (1-\xi_b)P_b \,. \tag{4.16}$$

The total energy in the center-of-mass system of the two colliding partons is

$$\hat{s} = (p_a + p_b)^2 = \xi_a \xi_b E_{\rm cm}^2 \,, \tag{4.17}$$

where $E_{\rm cm}^2 = (P_a + P_b)^2$.

Light Cone Coordinates and Kinematics : The natural coordinates for particles whose energy is much larger than their mass are the light-cone coordinates. The light-cone basis vectors n and $\bar{n}$ satisfy the properties

$$n^2 = 0 \,, \;\; \bar{n}^2 = 0 \,, \;\; n \cdot \bar{n} = 2 \,. \tag{4.18}$$

The natural choice is to take $\bar{n}$ in the opposite direction to n and have

$$n^\mu = (1,0,0,1) \,, \;\; \bar{n}^\mu = (1,0,0,-1) \,. \tag{4.19}$$

A standard 4-vector in the light-cone basis is represented as

$$p^\mu = \frac{n^\mu}{2}\bar{n}\cdot p + \frac{\bar{n}^\mu}{2} n\cdot p + p_\perp^\mu \,. \tag{4.20}$$

A momentum in these coordinates is represented by

$$p^\mu = (p^+, p^-, p_\perp)\,, \tag{4.21}$$

where the last entry is two-dimensional and the Minkowski $p_\perp^2$ is the negative of the Euclidean $\vec{p}_\perp^{\,2}$. We define

$$p^+ = n\cdot p \;,\;\; p^- = \bar{n}\cdot p\,. \tag{4.22}$$

Assuming that the mass of the incoming protons is negligible compared to $E_{\rm cm}$, and n_a and n_b are the light-cone vectors aligned with the beam directions, we can define the momenta of the incoming protons as

$$P_a^\mu = \frac{E_{\rm cm}}{2} n_a^\mu \;,\; P_b^\mu = \frac{E_{\rm cm}}{2} n_b^\mu\,. \tag{4.23}$$

The boson momentum can be written as

$$q^\mu = q^- \frac{n_a^\mu}{2} + q^+ \frac{n_b^\mu}{2} + q_{\perp\mu} = q_a^\mu + q_b^\mu + q_{\perp\mu}\,. \tag{4.24}$$

In the hadronic center-of-mass frame where $P_a + P_b = 0$ we can define

$$\begin{aligned} &P_a = E_{\rm cm}(0,1,0)\;, && P_b = E_{\rm cm}(1,0,0)\;, && q = (q^+, q^-, \bar{q}_\perp)\,, \\ &p_a = (0, p_a^-, 0) = (0, \xi_a E_{\rm cm}, 0)\;, && p_b = (p_b^+, 0, 0) = (\xi_b E_{\rm cm}, 0, 0)\,. \end{aligned} \tag{4.25}$$

where the components of q satisfy $Q^2 = q^+q^- - |\vec{q}_\perp^{\,2}|$.

The factorization formula for such a process is given by

$$\sigma_{h_a h_b \to HX} = \sum_{ab} \int d\xi_a d\xi_b f_{(a/H)}(\xi_a) f_{(b/H)}(\xi_b) d\hat{\sigma}_{ab\to HX}(\xi_a, \xi_b)\,, \tag{4.26}$$

where $f_k^{(h)}$ is the renormalized PDF of the parton k in the hadron H evaluated at the scale μ^2. The partonic cross section for this process is given by

$$\hat{\sigma}_{ab} = \frac{1}{2\hat{s}} |\overline{M}_{ab}|^2 d\phi_2\,, \tag{4.27}$$

where $|\overline{M}_{ab}|^2$ is the matrix element squared, $\hat{s}$ is the flux factor and $d\phi_2$ is the phase space

factor. The phase space factor for $ab \to Bk$ where k is a massless particle, is

$$d\phi_2 = \frac{d^4p}{(2\pi)^4}\frac{d^4q}{(2\pi)^4}(2\pi)^4\delta^4[(p_a+p_b)-(q+p)](2\pi)\delta(q^2-Q^2)(2\pi)\delta(p^2)\,. \tag{4.28}$$

Writing the above expression in terms of the light-cone coordinates

$$\begin{aligned} d\phi_2 =& \frac{1}{2(2\pi)^2}\delta(p_a^- - q^- - p^-)\delta(p_b^+ - q^+ - p^+)\delta^2(\vec{p}_\perp - \vec{q}_\perp)\delta(q^2-Q^2)\delta(p^2)dp^+dp^- \\ & d^2\vec{p}_\perp dq^+dq^-d^2\vec{q}_\perp\,, \\ =& \frac{1}{2(2\pi)^2}\delta(p_a^- - q^- - p^-)\delta(p_b^+ - q^+ - p^+)\delta(q^+q^- - p^+p^- - Q^2)\delta(p^+p^- - |\vec{p}_\perp|^2) \\ & dp^+dp^-|\vec{p}_\perp|d|\vec{p}_\perp|d\Omega_2 dq^-dq^+\,, \\ =& \frac{1}{4(2\pi)}\delta(p_a^- - q^- - p^-)\delta(p_b^+ - q^+ - p^+)\delta(q^+q^- - p^+p^- - Q^2)dp^+dp^-dq^-dq^+\,. \end{aligned} \tag{4.29}$$

Inserting the above phase space factor in Eq. (4.27) yields

$$\begin{aligned} \hat{\sigma}_{ab} &= \frac{1}{16\pi}\frac{1}{\xi_a\xi_b E_{\rm cm}^2}|\overline{M}_{ab}|^2\delta\big(p_b^+ - q^+ - p^+\big)\delta\big(p_a^- - q^- - p^-\big)\delta\Big(q^+q^- - q_\perp^2 - m_H^2\Big)dq^+dq^-dp^+dp^-\,, \\ &= \frac{1}{16\pi}\frac{1}{\xi_a\xi_b E_{\rm cm}^2}|\overline{M}_{ab}|^2\delta\big(\xi_b - \tilde{x}_b - \hat{p}^+\big)\delta\big(\xi_a - \tilde{x}_a - \hat{p}^-\big)\delta\Big(\tilde{x}_b\tilde{x}_a - \hat{p}^+\hat{p}^- - \frac{m_H^2}{E_{\rm cm}^2}\Big)d\tilde{x}_a d\tilde{x}_b d\hat{p}^- d\hat{p}^+\,. \end{aligned} \tag{4.30}$$

Here

$$\tilde{x}_{a,b} = \frac{q^{-,+}}{E_{\rm cm}}\,, \qquad \hat{p}^{+,-} = \frac{p^{+,-}}{E_{\rm cm}}\,, \qquad z_{a,b} = \frac{\tilde{x}_{a,b}}{\xi_{a,b}}\,. \tag{4.31}$$

Inserting this in the factorization formula, the differential cross section can be written as

$$\begin{aligned} \frac{d^4\sigma}{d\tilde{x}_a d\tilde{x}_b d\hat{p}^+ d\hat{p}^-} =& \frac{1}{16\pi E_{cm}^2}\int\frac{d\xi_a}{\xi_a}\frac{d\xi_b}{\xi_b}f_a(\xi_a)f_b(\xi_b)|\overline{M}_{ab}|^2\delta\big(\xi_b - \tilde{x}_b - \hat{p}^+\big)\delta\big(\xi_a - \tilde{x}_a - \hat{p}^-\big) \\ & \delta\Big(\tilde{x}_b\tilde{x}_a - \hat{p}^+\hat{p}^- - \frac{m_H^2}{E_{\rm cm}^2}\Big)\,. \end{aligned} \tag{4.32}$$

The rapidity Y of the Higgs boson is defined as

$$\begin{aligned} Y = \frac{1}{2}\log\frac{q^-}{q^+} = \frac{1}{2}\log\frac{\tilde{x}_a}{\tilde{x}_b} \qquad \text{then} \\ \tilde{x}_a E_{\rm cm} = q^- = Qe^Y\ ,\ \tilde{x}_b E_{\rm cm} = q^+ = Qe^{-Y} \end{aligned} \tag{4.33}$$

Using the definition of $q_{a,b}^\mu$ and p_i in Eq. (4.24), Eq. (4.33) and Eq. (4.20) , the beam thrust

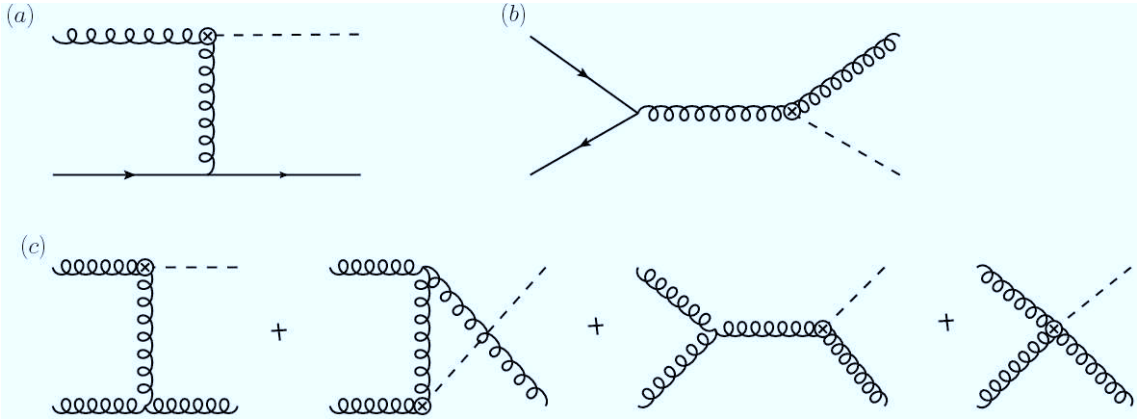

Figure 4.2: *Feyman diagrams for* $pp \to H$ *at NLO. Diagram (a) is* $gq \to Hq$ *or* $g\bar{q} \to Hg$ *channel, Diagram (b) is* $q\bar{q} \to Hg$ *channel and (c) has four possible diagrams for* $gg \to Hg$.

observable in Eq. (4.1) can be expressed as

$$\tau_B = \frac{1}{Q}\sum_k |\bar{p}_{kT}| \min\{e^{Y-y}, e^{-Y+y}\} = \frac{1}{Q}\sum_k \min\{p_k^+ e^Y, p_k^- e^{-Y}\}\,. \tag{4.34}$$

Note that $\mathcal{T}_B = Q\tau_B$. The first equality rightly reproduces the $f(y_j)$ defined for $\mathcal{T}_B$ in Eq. (4.7).

To get the cross section differential in $\mathcal{T}_B$ and $\mathcal{T}_{B\mathrm{cm}}$ we insert a measurement function of the form

$$\begin{aligned} 1 &= \int d\mathcal{T}_{B\mathrm{cm}}[\delta(\mathcal{T}_{B\mathrm{cm}} - p^+)\theta(p^- - p^+) + \delta(\mathcal{T}_{B\mathrm{cm}} - p^-)\theta(p^+ - p^-)]\,, \\ 1 &= \int d\mathcal{T}_B[\delta(\mathcal{T}_B - e^Y p^+)\theta(e^{-Y}p^- - e^Y p^+) + \delta(\mathcal{T}_B - e^{-Y}p^-)\theta(e^Y p^+ - e^{-Y}p^-)]\,. \end{aligned} \tag{4.35}$$

4.3.1 Higgs Production matrix elements

We obtain the tree level matrix elements for $H+1-$jet cross section, $ab \to Hk$, where a, b and k are either quarks, antiquarks or gluons, from the tree level hard function in [26]. The partonic channels for the Higgs production are $gq \to Hq$, $g\bar{q} \to H\bar{q}$, $q\bar{q} \to Hg$ and $gg \to Hg$ as shown in Fig. 4.2. Considering a and b as the initial state partons we introduce the notation,

$$\begin{aligned} s_{ab} &= 2p_a.p_b = 2\xi_a\xi_b E_{\mathrm{cm}}^2 = \hat{s}\,, \\ s_{ak} &= 2p_a.p_k = 2p_a.(p_a + p_b - q) = 2p_a.p_b + 2p_a.q = \hat{s} - \hat{s}z_b\,, \\ s_{bk} &= 2p_b.p_k = 2p_b.(p_a + p_b - q) = 2p_b.p_a + 2p_b.q = \hat{s} - \hat{s}z_a\,. \end{aligned} \tag{4.36}$$

The amplitudes for different production channels are
$gq \to Hq$ or $g\bar{q} \to H\bar{q}$

$$|\overline{M_{gq}}|^2 = \frac{8\alpha_s(\mu)^3 C_A C_F}{9\pi} \frac{\sqrt{2}G_f}{4N_c(N_c^2-1)} \Big(\Big| \frac{s_{ab}}{\sqrt{2|s_{bk}|}} \Big|^2 + \Big| \frac{s_{ak}}{\sqrt{2|s_{bk}|}} \Big|^2 \Big) ,$$
$$= \frac{\sqrt{2}G_f \alpha_s(\mu)^3 C_F}{36\pi} \frac{2 - 2z_b + z_b^2}{2(-1+z_a)(-1+z_a+z_b)} . \tag{4.37}$$

$qg \to Hq$ or $\bar{q}g \to H\bar{q}$

$$|\overline{M_{qg}}|^2 = \frac{8\alpha_s(\mu)^3 C_A C_F}{9\pi} \frac{\sqrt{2}G_f}{4N_c(N_c^2-1)} \Big(\Big| \frac{s_{ba}}{\sqrt{2|s_{ak}|}} \Big|^2 + \Big| \frac{s_{bk}}{\sqrt{2|s_{ak}|}} \Big|^2 \Big) ,$$
$$= \frac{\sqrt{2}G_f \alpha_S(\mu)^3 C_F}{36\pi} \frac{2 - 2z_a + z_a^2}{2(-1+z_b)(-1+z_a+z_b)} . \tag{4.38}$$

$q\bar{q} \to Hg$

$$|\overline{M_{qq}}|^2 = \frac{8\alpha_s(\mu)^3 C_A C_F}{9\pi} \frac{\sqrt{2}G_f}{(2N_c)^2} \Big(\Big| \frac{s_{kb}}{\sqrt{2|s_{ba}|}} \Big|^2 + \Big| \frac{s_{ka}}{\sqrt{2|s_{ba}|}} \Big|^2 \Big) ,$$
$$= \frac{\sqrt{2}G_f \alpha_s(\mu)^3 C_F}{36\pi} \frac{(2 - 2z_a + z_a^2 - 2z_b + z_b^2)}{-1 + z_a + z_b} . \tag{4.39}$$

$gg \to Hg$

$$|\overline{M_{gg}}|^2 = \frac{16\alpha_s(\mu)^3 C_A^2 C_F}{9\pi} \frac{\sqrt{2}G_f}{4(N_c^2-1)^2} \Big(\Big| \frac{m_H^4}{\sqrt{2|s_{ab}s_{ak}s_{bk}}} \Big|^2 + \Big| \frac{s_{ab}^2}{\sqrt{2|s_{ab}s_{ak}s_{bk}}} \Big|^2 + \Big| \frac{s_{ak}^2}{\sqrt{2|s_{ak}s_{ab}s_{kb}}} \Big|^2 ,$$
$$+ \Big| \frac{s_{kb}^2}{\sqrt{2|s_{kb}s_{ka}s_{ba}}} \Big|^2 \Big)$$
$$= \frac{\sqrt{2}G_f \alpha_s(\mu)^3}{36\pi} \frac{1}{(-1+z_a)(-1+z_b)(-1+z_a+z_b)} \Big[2 + z_a^4 - 4z_b + 6z_b^2 - 4z_b^3 + z_b^4$$
$$z_a^3(-4+2z_b) z_a^2(6 - 6z_b + 3z_b^2) + z_a(-4 + 6z_b - 6z_b^2 + 2z_b^3) \Big] . \tag{4.40}$$

4.3.2 Cross section differential in $\mathcal{T}_{B\mathrm{cm}}$

Inserting the measurement function for $\mathcal{T}_{B\mathrm{cm}}$ in Eq. (4.32) we get

$$\frac{d^3\sigma}{d\tilde{x}_a d\tilde{x}_b d\mathcal{T}_{B\mathrm{cm}}} = \frac{1}{16\pi E_{cm}^2} \Big\{ \Big[\int \frac{dz_a}{z_a} \frac{dz_b}{z_b} f_a\Big(\frac{\tilde{x}_a}{z_a}\Big) f_b\Big(\frac{\tilde{x}_b}{z_b}\Big) \int dp^- \frac{|\overline{M_{ab}}|^2}{E_{\mathrm{cm}}^2} \delta\Big(\frac{\tilde{x}_b}{z_b} - \tilde{x}_b - \frac{\mathcal{T}_{B\mathrm{cm}}}{E_{\mathrm{cm}}}\Big)$$
$$\delta\Big(\frac{\tilde{x}_a}{z_a} - \tilde{x}_a - \frac{p^-}{E_{\mathrm{cm}}}\Big) \delta\Big(\tilde{x}_b\tilde{x}_a - \frac{\mathcal{T}_{B\mathrm{cm}} p^-}{E_{\mathrm{cm}}^2} - \frac{m_H^2}{E_{\mathrm{cm}}^2}\Big) \theta\Big(p^- - \mathcal{T}_{B\mathrm{cm}}\Big)\Big] +$$
$$\Big[\int \frac{dz_a}{z_a} \frac{dz_b}{z_b} f_a\Big(\frac{\tilde{x}_b}{z_b}\Big) f_b\Big(\frac{\tilde{x}_a}{z_a}\Big) \int dp^+ \frac{|\overline{M_{ab}}|^2}{E_{\mathrm{cm}}^2} \delta\Big(\frac{\tilde{x}_b}{z_b} - \tilde{x}_b - \frac{p^+}{E_{\mathrm{cm}}}\Big)$$
$$\delta\Big(\frac{\tilde{x}_a}{z_a} - \tilde{x}_a - \frac{\mathcal{T}_{B\mathrm{cm}}}{E_{\mathrm{cm}}}\Big) \delta\Big(\tilde{x}_b\tilde{x}_a - \frac{\mathcal{T}_{B\mathrm{cm}} p^+}{E_{\mathrm{cm}}^2} - \frac{m_H^2}{E_{\mathrm{cm}}^2}\Big) \theta\Big(p^+ - \mathcal{T}_{B\mathrm{cm}}\Big)\Big] \Big\} . \tag{4.41}$$

Changing variables to dQ^2 and dY and performing the dp^- integral using the delta function (the result for the dp^+ integral is similar with a and b exchanged) we get

$$\frac{d^3\sigma}{dQ^2 dY d\mathcal{T}_{B\mathrm{cm}}} = \frac{1}{16\pi E_{cm}^2}\Big[\int \frac{dz_a}{z_a}\frac{dz_b}{z_b} f_a\Big(\frac{\tilde{x}_a}{z_a}\Big) f_b\Big(\frac{\tilde{x}_b}{z_b}\Big)\Big\{\frac{|\overline{M_{ab}}|^2}{E_{\mathrm{cm}}^3}\delta\Big(1 - z_b - \frac{\mathcal{T}_{B\mathrm{cm}} z_b}{E_{\mathrm{cm}}\tilde{x}_b}\Big) \frac{z_b}{\tilde{x}_a\tilde{x}_b^2}\delta\Big(1 - \frac{\mathcal{T}_{cm}}{E_{\mathrm{cm}}}\frac{(1-z_a)}{\tilde{x}_b z_a} - \frac{m_H^2}{Q^2}\Big)\theta\Big(1 - z_a - \frac{\mathcal{T}_{B\mathrm{cm}}}{E_{\mathrm{cm}}}\frac{z_a}{\tilde{x}_a}\Big) + a \leftrightarrow b\Big\}\Big]. \tag{4.42}$$

Performing the z_a (or z_b) integrals we have

$$\begin{aligned}\frac{d^3\sigma}{dQ^2 dY d\mathcal{T}_{B\mathrm{cm}}} = {} & \frac{1}{16\pi E_{cm}^2}\int \frac{dz_a}{z_a} f_a\Big(\frac{\tilde{x}_a}{z_a}\Big) f_b\Big(\frac{E_{\mathrm{cm}}\tilde{x}_b + \mathcal{T}_{B\mathrm{cm}}}{E_{\mathrm{cm}}}\Big)|\overline{M_{ab}}|^2 \frac{1}{E_{\mathrm{cm}}^2\tilde{x}_a\tilde{x}_b^2} \\ & \frac{\tilde{x}_b}{\mathcal{T}_{B\mathrm{cm}} + E_{\mathrm{cm}}\tilde{x}_b}\delta\Big(1 - \frac{\mathcal{T}_{B\mathrm{cm}}}{E_{\mathrm{cm}}}\frac{(1-z_a)}{\tilde{x}_b z_a} - \frac{m_H^2}{Q^2}\Big)\theta\Big(1 - z_a - \frac{\mathcal{T}_{B\mathrm{cm}} z_a}{E_{\mathrm{cm}}\tilde{x}_a}\Big) + \\ & \int \frac{dz_b}{z_b} f_a\Big(\frac{E_{\mathrm{cm}}\tilde{x}_a + \mathcal{T}_{B\mathrm{cm}}}{E_{\mathrm{cm}}}\Big) f_b\Big(\frac{\tilde{x}_b}{z_b}\Big)|\overline{M_{ab}}|^2 \frac{\tilde{x}_a}{\mathcal{T}_{B\mathrm{cm}} + E_{\mathrm{cm}}\tilde{x}_a}\frac{1}{E_{\mathrm{cm}}^2\tilde{x}_a\tilde{x}_b^2} \\ & \delta\Big(1 - \frac{\mathcal{T}_{B\mathrm{cm}}}{E_{\mathrm{cm}}}\frac{(1-z_b)}{\tilde{x}_a z_b} - \frac{m_H^2}{Q^2}\Big)\theta\Big(1 - z_b - \frac{\mathcal{T}_{B\mathrm{cm}} z_b}{E_{\mathrm{cm}}\tilde{x}_b}\Big).\end{aligned} \tag{4.43}$$

Now we perform the Q^2 integral

$$\begin{aligned}\frac{d^2\sigma}{dY d\mathcal{T}_{B\mathrm{cm}}} = {} & \frac{1}{16\pi E_{cm}^2}\int \frac{dz_a}{z_a} f_a\Big(\frac{\tilde{x}_a}{z_a}\Big) f_b\Big(\frac{E_{\mathrm{cm}}x_b + \mathcal{T}_{B\mathrm{cm}}}{E_{\mathrm{cm}}}\Big)\frac{1}{\mathcal{T}_{B\mathrm{cm}} + E_{\mathrm{cm}}\tilde{x}_b}\theta\Big(1 - z_a - \frac{\mathcal{T}_{B\mathrm{cm}} z_a}{E_{\mathrm{cm}}\tilde{x}_a}\Big) \\ & |\overline{M_{ab}}|^2\Big(\frac{2z_a Q_i}{2z_a Q_i - \mathcal{T}_{B\mathrm{cm}}(1-z_a)e^Y E_{\mathrm{cm}}}\Big) + \int \frac{dz_b}{z_b} f_a\Big(\frac{E_{\mathrm{cm}}\tilde{x}_a + \mathcal{T}^{Bcm}}{E_{\mathrm{cm}}}\Big) f_b\Big(\frac{\tilde{x}_b}{z_b}\Big) \\ & \frac{1}{\mathcal{T}_{B\mathrm{cm}} + E_{\mathrm{cm}}\tilde{x}_a}|\overline{M_{ab}}|^2\theta\Big(1 - z_b - \frac{\mathcal{T}_{B\mathrm{cm}} z_b}{E_{\mathrm{cm}}\tilde{x}_b}\Big)\Big(\frac{2z_b Q_j}{2z_b Q_j - \mathcal{T}_{B\mathrm{cm}}(1-z_b)e^{-Y}E_{\mathrm{cm}}}\Big)\end{aligned} \tag{4.44}$$

where

$$\begin{aligned} Q_i &= \frac{\mathcal{T}_{B\mathrm{cm}}(1-z_a)e^Y}{2z_a} + \frac{1}{2}\sqrt{\Big(\frac{\mathcal{T}_{B\mathrm{cm}}(1-z_a)e^Y}{z_a}\Big)^2 + 4m_H^2}, \\ Q_j &= \frac{\mathcal{T}_{B\mathrm{cm}}(1-z_b)e^{-Y}}{2z_b} + \frac{1}{2}\sqrt{\Big(\frac{\mathcal{T}_{B\mathrm{cm}}(1-z_b)e^{-Y}}{z_b}\Big)^2 + 4m_H^2}. \end{aligned} \tag{4.45}$$

After expressing $\tilde{x}_a$ and $\tilde{x}_b$ in terms of Q and Y as $\tilde{x}_a = Qe^Y$ and $\tilde{x}_b = Qe^{-Y}$, the left over z integral can be performed numerically over the PDFs (using LHAPDF) and the resulting H+0-jet cross section differential in rapidity Y and $\mathcal{T}_{B\mathrm{cm}}$ is obtained.

The steps that lead to the cross section differential in rapidity Y and each of the $\mathcal{T}_B^{\mathrm{jet}}$, $\mathcal{T}_C^{\mathrm{jet}}$ and $\mathcal{T}_{C\mathrm{cm}}^{\mathrm{jet}}$ observables are analogous and the calculation is shown in App. B.1, App. B.2 and App. B.3 respectively.

4.4 Introduction to SCET

We will now review the basic structure of SCET and the general structure of the factorization formulae and resummation in this framework.

A typical proton proton collision process at the LHC involves physics from very large energy scales down to very low energy scales and in such cases Effective Field Theories (EFT) can be used to describe physics at different scales. Broadly, in any collision process at the LHC, there are two scales involved, the momentum scale of the hard interaction Q and the scale of hadronization and non-pertubative physics, $\Lambda_{\rm QCD} \ll Q$. There are other intermediate scales involved like the jet mass m_J or the p_T of the jets. To eliminate huge QCD backgrounds, experiments often impose stringent jet vetoes to measure exclusive jet cross sections where a fixed number of jets with $p_T^{\rm jet} < p_T^{\rm cut}$ are allowed. For small values of $p_T^{\rm cut}$, large Sudakov logarithms of the ratio of $p_T^{\rm cut}$ and the hard scale are introduced as we discussed in Sec. 2.4. Higher-order corrections to the cross section are enhanced by such large logarithms of the scale ratios and hence such logarithms need to be summed. This requires factorization of the cross sections into different components relevant at different energy scales. SCET is an EFT of QCD which allows to systematically derive factorization theorems and perform the resummation of large Sudakov logarithms. It reproduces the full infrared singularity structure of QCD.

The basic degrees of freedom of SCET are collinear and soft quarks and gluons. Soft degrees of freedom have momentum $p_{\rm soft} \ll Q$ and they have no preferred direction so each component of $p^\mu_{\rm soft}$ has an identical scaling. Collinear degrees of freedom describe particles having large energy and small invariant mass moving in some preferred direction. The most convenient coordinate system used to define the momenta and directions of particles in SCET is the light cone coordinates defined in Sec. 4.3. For example, for $pp \to HX$, we need two collinear sectors n_a and n_b along the directions of the two incoming proton beams and P_a and P_b their corresponding momenta (as defined in Sec. 4.3). If λ is the ratio of a small scale to the hard scale Q of the process, then the momentum of a proton moving along n_a direction scales as $p_a = Q(\lambda^2, 1, \lambda)$ where $p^- \sim Q$ corresponds to the large energy of the collinear parton, $p^\perp \sim \lambda Q$ is an intermediate momentum scale while $p^+ \sim \lambda^2 Q$ is a small residual momentum. There can be additional light cone directions n_j describing more collinear jets in the final state. The hard degrees of freedom are integrated out at $\mu \sim Q$, and below this scale only the soft and collinear modes are the relevant degrees of freedom. Depending on the scaling of the collinear and soft degrees of freedom, a given process or a measurement (of kinematic observables) fall into two categories SCET$_I$-like and SCET$_{II}$-like.

SCET I and SCET II : Consider an example process of proton-proton collisions at the

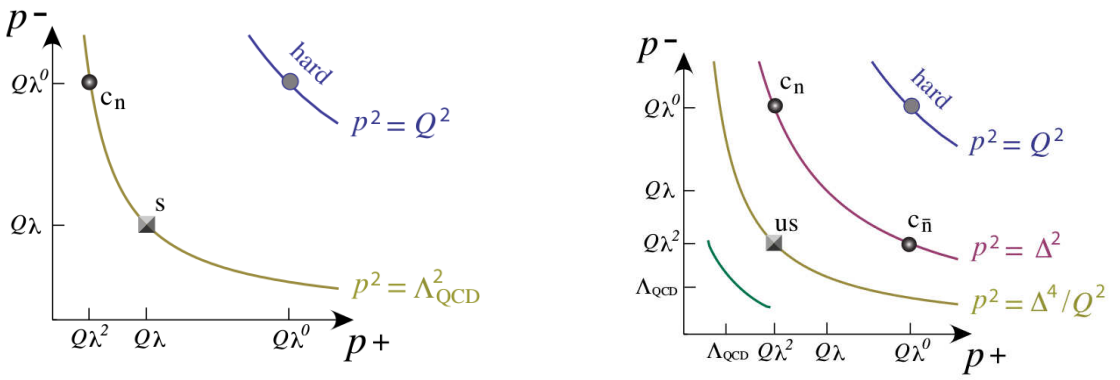

Figure 4.3: *Left: Degrees of freedom for $SCET_{II}$ type theories (e.g. pp collisions), Right: Degrees of freedom for $SCET_I$ type theories (e.g. $e^+e^- \to$ jets). Fig taken from [77].*

LHC. The partons inside the proton, in the rest frame of the proton, are non-perturbative with momentum scaling $p^\mu \sim (\Lambda_{\rm QCD}, \Lambda_{\rm QCD}, \Lambda_{\rm QCD})$. Boosting the parton along the $-z$ by an amount $\kappa = Q/\Lambda_{\rm QCD}$ causes the scaling to become

$$p_c^\mu = (\frac{\Lambda_{\rm QCD}^2}{Q}, Q, \Lambda_{\rm QCD})\,. \tag{4.46}$$

Here, the scaling $p_c^- \gg p_c^\perp \gg p_c^+$ is called the collinear scaling. Describing this scaling with a dimensionless parameter $\lambda = \Lambda_{\rm QCD}/Q$,

$$p_c^\mu \sim Q(\lambda^2, 1, \lambda)\,. \tag{4.47}$$

With this notation the scaling of the soft momenta is,

$$p_s^\mu \sim Q(\lambda, \lambda, \lambda)\,. \tag{4.48}$$

These soft and collinear degrees of freedom can be represented with a picture as shown in Fig. 4.3. The hyperbolas are lines of constant $p^2 \sim p^+p^-$. The hyperbola corresponding to $p^2 \sim Q^2$ denotes the hard region but these modes are integrated out when constructing SCET. On the $p^2 \sim \Lambda_{\rm QCD}$ hyperbola, there are collinear modes c_n (which are non-perturbative) and soft modes s. Since these modes live at the same invariant mass p^2 we need another variable namely p^-/p^+ which is the rapidity e^Y to distinguish them. This example where the soft and collinear modes in the theory have the same scaling for p^2 is known as $SCET_{II}$-type theory. This theory is fit for observables with measurements of $p_\perp$ like $p_T^{\rm jet}$ or p_T^H

Consider now an example process $e^+e^- \to q\bar{q}$. The collimated energetic constituents of the first jet will have a $\perp$-momentum parametrically smaller than their large-momentum,

$p_\perp \sim \Delta \ll p^- \sim Q$. The two jets aligned in the direction $(1, \pm\hat{z})$, will have the scaling

$$p_n^\mu = (\frac{\Delta^2}{Q}, Q, \Delta) = Q(\lambda^2, 1, \lambda) \ , \ p_{\bar{n}}^\mu = (Q, \frac{\Delta^2}{Q}, \Delta) = Q(1, \lambda^2, \lambda)\,. \tag{4.49}$$

In order to have a jet of hadrons and not a single hadron or a small number of hadrons we must have $\Delta \gg \Lambda_{\rm QCD}$. To derive the soft scaling consider two jets with jet masses $m_J^2 = (\sum_i p_i^\mu)^2 \sim p^+ p^- \sim \Delta^2$, then in one hemisphere we have

$$(p_n + p_{us})^2 = p_n^2 + 2p_n \cdot p_{us} + p_{us}^2 \sim \Delta^2\,. \tag{4.50}$$

From this, the ultrasoft mode should scale like

$$p_{us}^\mu \sim (\frac{\Delta^2}{Q}, \frac{\Delta^2}{Q}, \frac{\Delta^2}{Q}) = Q(\lambda^2, \lambda^2, \lambda^2)\,. \tag{4.51}$$

Fig. 4.3 shows the degrees of freedom in the p^+p^- plane and as before the hard modes with momenta $p^2 \sim Q^2$ are integrated out and the two types of collinear modes c_n and $c_{\bar{n}}$ live on the $p^2 \sim \Delta^2$ hyperbola. The ultrasoft modes live on a different hyperbola with $p^2 \sim \Delta^4/Q^2$. When the collinear and soft modes live on hyperbolas with parametrically different scaling, then the theory is SCET$_I$ type. This theory is used to measure observables that depend on the plus and minus components of momenta, like beam thrust $\mathcal{T}_B$ or $\mathcal{T}_B^{\rm jet}$ and $\mathcal{T}_C^{\rm jet}$ or N-jettiness τ_N.

4.5 Ingredients and SCET Lagrangian

Collinear Spinors: Consider the expansion of the Dirac spinors $u(p)$ and $v(p)$ with $p^\mu = (p^0, p^1, p^2, p^3)$, in the collinear limit. We have $p^- = p^0 + p^3 \gg p_\perp^{1,2} \gg p^+ = p^0 - p^3$ so

$$\frac{\sigma \cdot p}{p^0} = \sigma_3 + ... \tag{4.52}$$

Keeping only the leading terms gives us the spinors

$$u_n(p) = \sqrt{\frac{p^-}{2}} \begin{bmatrix} \mathcal{U} \\ \sigma^3 \mathcal{U} \end{bmatrix} \ , \ v_n(p) = \sqrt{\frac{p^-}{2}} \begin{bmatrix} \mathcal{V} \\ \sigma^3 \mathcal{V}\,, \end{bmatrix} \tag{4.53}$$

where $\mathcal{U} = \begin{bmatrix} 1 \\ 0 \end{bmatrix}$ and $\mathcal{V} = \begin{bmatrix} 0 \\ 1 \end{bmatrix}$. Note that $\not{n} u_n = 0$ and $\not{n} v_n = 0$. We also define the projection operators,

$$P_n = \frac{\not{n}\not{\bar{n}}}{4} \ , \ P_{\bar{n}} = \frac{\not{\bar{n}}\not{n}}{4} \tag{4.54}$$

such that $P_n + P_{\bar{n}} = 1$ and $P_n u_n = u_n$ and $P_n v_n = v_n$. The QCD Dirac field ψ can then be decomposed as

$$\psi = P_n\psi + P_{\bar{n}}\psi = \hat{\xi}_n + \phi_{\bar{n}}\,. \tag{4.55}$$

The fields satisfy the following relations

$$\begin{aligned} &\not{n}\hat{\xi}_n = 0\ ,\ P_n\hat{\xi}_n = \xi_n\ ,\ \bar{\not{n}}\phi_{\bar{n}} = 0\ ,\ P_{\bar{n}}\phi_{\bar{n}} = \phi_{\bar{n}}\ \text{ and} \\ &\bar{\hat{\xi}}_n\not{n} = 0\ ,\ \bar{\hat{\xi}}_n P_n = 0\ ,\ \bar{\hat{\xi}}_n P_{\bar{n}} = \bar{\hat{\xi}}_n\ \text{ where }\ \bar{\hat{\xi}}_n = \hat{\xi}_n^\dagger\gamma_0 \end{aligned} \tag{4.56}$$

Having defined $\hat{\xi}_n = P_n\psi$, the corresponding relations for the spinors $u_n = P_n u(p)$ and $v_n = P_n v(p)$ do not precisely reproduce the lowest order expanded results given in Eq. (4.53), instead we have,

$$u_n = \frac{1}{2}\begin{bmatrix} \mathbb{1} & \sigma_3 \\ \sigma_3 & \mathbb{1} \end{bmatrix}\sqrt{p^0}\begin{bmatrix} \mathcal{U} \\ \frac{\sigma\cdot p}{p^0}\mathcal{U} \end{bmatrix} = \frac{\sqrt{p^0}}{2}\begin{bmatrix} \left(1 + \frac{p_3}{p_0} - \frac{(i\bar{\sigma}\times\bar{p}_\perp)_3}{p^0}\right)\mathcal{U} \\ \sigma_3\left(1 + \frac{p_3}{p_0} - \frac{(i\bar{\sigma}\times\bar{p}_\perp)_3}{p^0}\right)\mathcal{U} \end{bmatrix} = \sqrt{\frac{p^-}{2}}\begin{bmatrix} \tilde{\mathcal{U}} \\ \sigma_3\tilde{\mathcal{U}} \end{bmatrix}, \tag{4.57}$$

where the two component spinor is

$$\tilde{\mathcal{U}} = \frac{\sqrt{p^0}}{2}\left[\left(1 + \frac{p_3}{p_0} - \frac{(i\bar{\sigma}\times\bar{p}_\perp)_3}{p^0}\right)\mathcal{U}\right]. \tag{4.58}$$

The same derivation holds for $\mathcal{V}$.

Collinear Fermion propagator: After considering the expansion of the spinors in the collinear limit, we will now consider the expansion of the fermion propagator. Here $p^2 + i0 = \bar{n}\cdot p\, n\cdot p + p_\perp^2$. Both the terms are $\propto \lambda^2$ and so there is no expansion in the denominator and we have,

$$\frac{i\not{p}}{p^2 + i0} = \frac{i\not{n}}{2}\frac{1}{n\cdot p + \frac{p_\perp^2}{\bar{n}\cdot p} \pm i0} \tag{4.59}$$

This leading collinear propagator should be obtained from the time-ordered product of the effective theory field, $\langle 0|\, T\hat{\xi}_n(x)\bar{\hat{\xi}}_{\bar{n}}(0)\,|0\rangle$. The λ power counting of the field ξ can be determined by dimensional analysis (knowing the power counting of the action from the propagator) and is given by $\xi_n \sim \lambda$.

Collinear gluons and ultrasoft fields: Consider the full theory covariant gauge gluon propagator and label the fields by A_n^μ to denote that these are the n-collinear momenta

$$\int d^4x e^{ik\cdot x}\,\langle 0|\, TA_n^\mu(x)A_n^\nu(0)\,|0\rangle = \frac{-i}{k^4}(k^2 g^{\mu\nu} - \tau k^\mu k^\nu)\,. \tag{4.60}$$

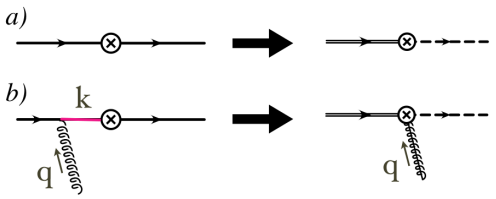

Figure 4.4: *Matching heavy to light ($b \to ue\bar{\nu}$) current at tree level and 1-loop.*

Here τ is the covariant gauge fixing parameter. By dimensional analysis, the power counting of A_n^μ is the same as the collinear momentum $A_n^\mu \sim k^\mu \sim (\lambda^2, 1, \lambda)$. The same logic used to derive the scaling of ultrasoft gluon fields gives $A_{us}^\mu \sim k_{us}^\mu \sim (\lambda^2, \lambda^2, \lambda^2)$.

Matching QCD onto SCET: Consider as an example the process $b \to ue\bar{\nu}$ where a heavy b quark decays to an energetic collinear u quark. This decay has the weak current $J_{QCD} = \bar{u}\Gamma b$. Without additional gluons we can match this QCD current onto a leading order current in SCET by considering the heavy b field to be the HQET field h_v and the lighter u field by the SCET field ξ_n : $\xi_n \Gamma h_v$. Next consider the case with an extra A_n^- gluon attached to the heavy quark. This process shown in Fig. 4.4 leads to an offshell propagator that must be integrated out. The full theory amplitude for this process is

$$\begin{aligned} A_n^\mu \bar{\xi}_n \Gamma \frac{i(\not{k} + m_b)}{k^2 - m_b^2} igT^A \gamma_\mu h_v &= -g(\frac{n^\mu}{2} \bar{n} \cdot A_n) \bar{\xi}_n \Gamma \frac{[m_b(1+\not{v}) + \not{q}]}{2m_b v \cdot q + q^2} T^A \gamma_\mu h_v \,, \\ &= \bar{\xi}_n \frac{-g\bar{n} \cdot A_n}{\bar{n} \cdot q} \Gamma h_v \,. \end{aligned} \tag{4.61}$$

Here the incoming b quark carries momentum $m_b v^\mu$ so $k = m_b v^\mu + q$. Also the gluon field can be written as

$$A_n^\mu = \frac{n^\mu}{2} \underbrace{\bar{n} \cdot A_n}_{O(\lambda)^0} + \frac{\bar{n}^\mu}{2} \underbrace{n \cdot A_n}_{O(\lambda^2)} + \underbrace{A_\perp^\mu}_{O(\lambda)} \tag{4.62}$$

where we can keep only the $O(1)$ term. The final simplified expression is obtained by expanding the numerator and denominator in λ. In summary, the propagator was offshell by Q^2 and so was integrated out leading to an operator for one collinear gloun coming out of the vertex. Let us now consider the situation of multiple gluon emissions from the heavy quark. We again have offshell propagators and the generalization to k gluons with momenta $q_1 ... q_n$ yields

$$\bar{\xi}_n \sum_{perm} \frac{(-g)^k}{k!} \left(\frac{\bar{n} \cdot A_{q1} ... \bar{n} \cdot A_{qk}}{[\bar{n} \cdot q_1][\bar{n} \cdot (q_1 + q_2)] ... [\bar{n} \cdot \sum_{i=1}^k q_i]} \right) . \tag{4.63}$$

Finally by summing over the number of possible gluon emissions, we can write the tree

level matching of the QCD current to the SCET current as $J_{SCET} = \bar{\xi}_n W_n \Gamma h_v$ where

$$W_n = \sum_k \bar{\xi}_n \sum_{perm} \frac{(-g)^k}{k!} \left(\frac{\bar{n} \cdot A_{q1} ... \bar{n} \cdot A_{qk}}{[\bar{n} \cdot q_1][\bar{n} \cdot (q_1 + q_2)] ... [\bar{n} \cdot \sum_{i=1}^{k} q_i]} \right). \tag{4.64}$$

Here W_n is the momentum space Wilson line built from collinear A_n gluon fields. In position space the corresponding Wilson line is

$$W(0, -\infty) = P \exp\left(ig \int_{-\infty}^{0} ds \bar{n} \cdot A_n(\bar{n}s) \right). \tag{4.65}$$

where P is the path ordered operator which puts fields with larger arguments to the left.

SCET Lagrangian: To construct the SCET lagrangian we begin with the standard QCD lagrangian for massless quarks and expanding ψ and the covariant derivative D in the collinear limit gives

$$\mathcal{L} = (\bar{\phi}_{\bar{n}} + \bar{\hat{\xi}}_n) \Big(\frac{\bar{\not{n}}}{2} in \cdot D + \frac{\not{n}}{2} i\bar{n} \cdot D + i\not{D}_\perp \Big) (\phi_{\bar{n}} + \hat{\xi}_n). \tag{4.66}$$

Simplifying using the projection matrix identities for collinear spinors,

$$\mathcal{L} = \bar{\hat{\xi}}_n \frac{\bar{\not{n}}}{2} in \cdot D \hat{\xi}_n + \bar{\phi}_{\bar{n}} i\not{D}_\perp \hat{\xi}_n + \bar{\hat{\xi}}_n i\not{D}_\perp \phi_{\bar{n}} + \bar{\phi}_{\bar{n}} \frac{\not{n}}{2} i\bar{n} \cdot D \phi_{\bar{n}}. \tag{4.67}$$

The field $\phi_{\bar{n}}$ corresponds to the spinor components subleading in the collinear limit. Therefore we will not consider a source term for $\phi_{\bar{n}}$ in the path integral. At tree level doing so gives

$$\frac{d\mathcal{L}}{d\phi_{\bar{n}}} = 0 \to \phi_{\bar{n}} = \frac{1}{i\bar{n} \cdot D} i\not{D}_\perp \frac{\bar{\not{n}}}{2} \hat{\xi}_n. \tag{4.68}$$

Plugging this into the Lagrangian

$$\mathcal{L} = \bar{\hat{\xi}}_n \Big(in \cdot D + i\not{D}_\perp \frac{1}{i\bar{n} \cdot D} i\not{D}_\perp \Big) \frac{\bar{\not{n}}}{2} \hat{\xi}_n. \tag{4.69}$$

We have to still separate the collinear and ultrasoft fields and the momentum components. In Heavy Quark Effective Theory (HQET), there are two relevant momentum scales, the mass of the heavy quark m and Λ_{QCD}. The scale m is separated from Λ_{QCD} by writing $p = mv + k$, where k is the residual momentum $k \ll m$. The variable v then becomes a label on the effective theory. Analogous to HQET, in our case the momentum p can be split as

$$p^\mu = p_l^\mu + p_r^\mu \tag{4.70}$$

where $p_l^\mu \sim Q(1,0,\lambda)$ and $p_r^\mu \sim Q(\lambda^2,\lambda^2,\lambda^2)$. This allows us to rewrite the hatted collinear field $\hat{\xi}_n(x)$ as

$$\begin{aligned}\hat{\xi}_n(x) &= \int \frac{d^4p}{(2\pi)^4} e^{-ip\cdot x}\tilde{\xi}_n(p) = \sum_{p_l\neq 0}\int \frac{d^4p_r}{(2\pi)^4} e^{-ip_l\cdot x}e^{-ip_r\cdot x}\tilde{\xi}_{n,p_l}(p_r)\\ &= \sum_{p_l\neq 0} e^{-ip_l\cdot x}\xi_{n,p_l}(x)\end{aligned} \tag{4.71}$$

where

$$\xi_{n,p_l}(x) = \int \frac{d^4p_r}{(2\pi)^4} e^{-ip_r\cdot x}\tilde{\xi}_{n,p_l}(p_r)\,. \tag{4.72}$$

We also define a label momentum operator such that

$$\mathcal{P}^\mu \xi_{n,p_l}(x) = p_l^\mu \xi_{n,p_l}(x)\,. \tag{4.73}$$

Note that $\mathcal{P}^\mu$ and p_l^μ only contain the components $\bar{\mathcal{P}} = \bar{n}\cdot\mathcal{P} \sim p_l^- \sim \lambda^0$ and $P_\perp \sim p_l^{\perp\mu} \sim \lambda$. The main advantage of the label operator is that it provides a definite power counting for derivatives. It can also remove the label sum as follows

$$\hat{\xi}_{n,p_l}(x) = \sum_{p_l\neq 0} e^{-ip_l\cdot x}\xi_{n,p_l}(x) = e^{-i\mathcal{P}\cdot x}\sum_{p_l\neq 0}\xi_{n,p_l}(x) = e^{-i\mathcal{P}\cdot x}\xi_n(x)\,. \tag{4.74}$$

Differentiating an arbitrary collinear field $\hat{\phi}_n(x)$ yields

$$\begin{aligned}i\partial^\mu\hat{\phi}_n(x) &= i\partial_\mu \sum_{p\neq 0} e^{-ip\cdot x}\phi_{n,p}(x)\\ &= \sum_{p\neq 0} e^{-ip\cdot x}(\mathcal{P}^\mu + i\partial^\mu)\phi_{n,p}(x) = e^{-i\mathcal{P}\cdot x}(\mathcal{P}^\mu + i\partial^\mu)\phi_n(x)\,.\end{aligned} \tag{4.75}$$

Changing $i\partial_\mu\hat{\phi}_n(x) \to (\mathcal{P}_\mu + i\partial_\mu)\phi_n(x)$ and $\hat{\xi}_n \to \xi_n$ and keeping the leading order terms in the covariant derivative, the lagrangian becomes

$$\mathcal{L}_{n\xi}^{(0)} = e^{-ix\cdot\mathcal{P}}\bar{\xi}_n\Big(in\cdot D + i\not{D}_{n,\perp}\frac{1}{i\bar{n}\cdot D_n}i\not{D}_{n\perp}\Big)\frac{\not{n}}{2}\xi_n\,, \tag{4.76}$$

where the collinear covariant derivatives are $iD_{n,\perp}^\mu = \mathcal{P}_\perp^\mu + gA_{n\perp}^\mu$ and $i\bar{n}\cdot D_n = \overline{\mathcal{P}} + g\bar{n}\cdot A_n$. The equation of motion for a Wilson line in position space, $i\bar{n}\cdot D_x W(x,-\infty) = 0$, can be transformed to momentum space

$$i\bar{n}\cdot D_n W_n = (\overline{\mathcal{P}} + g\bar{n}\cdot A_n)W_n = 0\,. \tag{4.77}$$

With this definition, the action of $i\bar{n}\cdot D_n$ on a product of W_n and some operator $\mathcal{O}$ is

$$i\bar{n}\cdot D_n(W_n\mathcal{O}) = [(\overline{\mathcal{P}} + g\bar{n}\cdot A_n)W_n]\mathcal{O} + W_n\overline{\mathcal{P}}\mathcal{O} = W_n\overline{\mathcal{P}}\mathcal{O}\,. \tag{4.78}$$

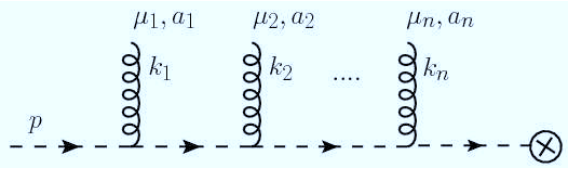

Figure 4.5: *The attachment of ultrasoft gluons to a collinear quark line.*

So we have the operator equation $i\bar{n}\cdot D_n W_n = W_n\bar{\mathcal{P}}$ and with $W^\dagger W = 1$ we have the identities,

$$i\bar{n}\cdot D_n = W_n^\dagger \frac{1}{\bar{\mathcal{P}}} W_n \quad , \quad \frac{1}{i\bar{n}\cdot D_n} = W_n^\dagger \frac{1}{\bar{\mathcal{P}}} W_n \,. \tag{4.79}$$

These identities allow us to rewrite the Lagrangian as

$$\mathcal{L}^{(0)}_{n\xi} = e^{-ix\cdot\mathcal{P}}\bar{\xi}_n\Big(in\cdot D + i\not{D}_{n,\perp} W_n^\dagger \frac{1}{\bar{\mathcal{P}}} W_n i\not{D}_{n\perp}\Big)\frac{\not{n}}{2}\xi_n \,. \tag{4.80}$$

The full leading order SCET$_I$ Lagrangian consists of a single set of quark and gluon collinear modes in the n direction, and quark and gluon ultrasoft modes give by

$$\mathcal{L}^{(0)} = \mathcal{L}^{(0)}_{n\xi} + \mathcal{L}^{(0)}_{ng} + \mathcal{L}^{(0)}_{us} \,, \tag{4.81}$$

where the collinear gluon Lagrangian can be found in [10] and the ultra soft Lagrangian is

$$\mathcal{L}^{(0)}_{us} = \bar{\psi}_{us} i\not{D}_{us}\psi_{us} - \frac{1}{2}Tr\{G^{\mu\nu}_{us}G^{us}_{\mu\nu}\} + \tau_{us}Tr\{(i\partial_\mu A^\mu_{us})^2\} + 2Tr\{\bar{c}_{us} i\partial_\mu i\mathcal{D}^\mu_{us} c_{us}\} \,. \tag{4.82}$$

where $iD^\mu_{us} = i\partial_\mu + A^\mu_{us}$.

4.6 Factorization in SCET

We will now explore the factorization between the collinear and soft modes.

4.6.1 Ultrasoft collinear factorization

At leading order in λ, only the ultra soft (usoft) gluons ($n\cdot A_{us}$) can couple to n-collinear quarks and gluons. Considering Fig. 4.5 with only one ultrasoft gluon, the collinear quark propagator is

$$\frac{\bar{n}\cdot p}{\bar{n}\cdot p\, n\cdot(p_r+k) + p_\perp^2 + i0} = \frac{\bar{n}\cdot p}{\bar{n}\cdot p\, n\cdot k + i0} \,. \tag{4.83}$$

Together with the n^μ from the vertex, this corresponds to the eikonal propagator for the coupling of ultrasoft gluons to an energetic particle. A graph with multiple usoft gluon emissions gives $\Gamma Y_n u_n$ where Γ is the structure at the vertex, u_n is the collinear quark and

$$Y_n = \sum_{m=0}^{\infty} \sum_{\text{perms}} \frac{(-g)^m n \cdot A^{a_1}(k_1) ... n \cdot A^{a_m}(k_m) T^{a_m} ... T^{a_1}}{n \cdot k_1 n \cdot (k_1 + k_2) ... n \cdot (\sum_i k_i)} \,. \tag{4.84}$$

corresponds to the momentum-space formula for an ultrasoft Wilson line Y_n. It is possible to show that all the leading order ultrasoft-collinear interactions within SCET$_I$ can be encoded through the non-local interactions contained in the Wilson line by considering the BPS field redefinitions given by

$$\xi_{n,p}(x) = Y_n(x) \xi^{(0)}_{n,p}(x) \quad , A^\mu_{n,p}(x) = Y_n(x) A^{(0)\mu}_{n,p}(x) Y^\dagger_n(x) \,. \tag{4.85}$$

Implementing this at the Lagrangian level, it can be shown that the collinear quark $\mathcal{L}^{(0)}_{n,\xi}$ and gluon Lagrangian $\mathcal{L}^{(0)}_{ng}$ completely decouples from the $n \cdot A_{us}$ usoft gluon field.

4.6.2 Factorization formula for Drell-Yan like processes

Consider the case of an inclusive process such as $pp \to XL$, where X is the hadronic final state and L is any color singlet final state e.g. H, V etc. In the soft and collinear limit the factorized cross section can be expressed as $d\sigma = H \otimes f \otimes f \otimes \mathcal{I} \otimes \mathcal{I} \otimes \Pi_i J_i \otimes S$. Here J_i denote the different jets in the final state, S describes the soft radiation and $B = \mathcal{I} \otimes f$ are the beam functions which describe the initial state radiation. In any QCD or SCET factorization, soft gluons decouple from the collinear particles through the eikonal approximation. However, the eikonal approximation is not applicable to soft gluons whose momenta p satisfy $|p^+ p^-| \ll p_\perp^2 \ll Q^2$, called the Glauber gluons. For the factorization to hold, the contribution from glauber modes should be power suppressed. Here, we derive the factorization formula in the absence of glauber gluons. However it was shown in [78,79] that the glauber gluons give rise to leading power corrections in the factorization. For the jet-based observables ($\mathcal{T}_B^{\text{jet}}$ and $\mathcal{T}_C^{\text{jet}}$) we are interested in, these corrections are $O(R^2)$ and hence power suppressed for the jet radii currently used in experiments. The steps here mainly sketch the matching of QCD onto SCET operators leading to the Wilson coefficients encoding the hard interaction, the beam functions which contain the PDF dependence and account for the collinear initial state radiation and the soft functions which describe the accompanying soft radiation. Let us now work through the steps that lead to such a factorization formula for this process with no additional hard jets in the central region. We closely follow the derivation in Ref. [64].

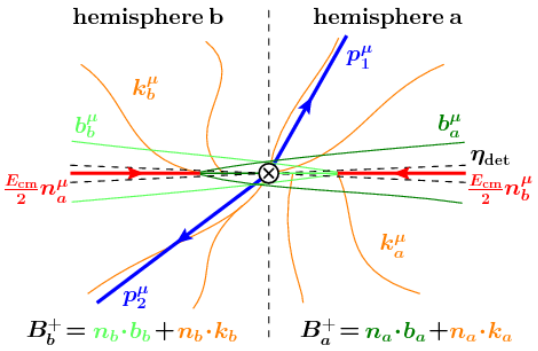

Figure 4.6: *Definition of hemispheres for $pp \to XL$ process (fig. taken from [64]).*

The full theory matrix element can be factorized into a leptonic and hadronic part,

$$M(pp \to XL) = \sum_J L_J \langle X| J |pp\rangle \,. \tag{4.86}$$

Here L_J contains the electroweak matrix element and the sum runs over all the color-singlet 2-particle QCD currents J. The cross section for this process differential in some observable O in the center-of-mass frame of the collision is

$$\begin{aligned}\frac{d\sigma}{dq^2 dY\, dO} &= \frac{1}{2E_{\rm cm}^2} \int \frac{d^2\vec{q}_T}{2(2\pi)^4} \int d\Phi_L (2\pi)^4 \delta^4(q - p_L) \frac{1}{4} \sum_{\rm spins} \sum_X |\overline{M}|^2 \delta(O - f_O(X)) \\ &\quad (2\pi)^4 \delta^4(P_a + P_b - q - p_X) \\ &= \frac{1}{2E_{\rm cm}^2} \sum L_{JJ'}(q^2, Y) W_{JJ'}(q^2, Y, O)\end{aligned} \tag{4.87}$$

where $P_{a,b}$ are the incoming proton momenta, p_X and p_L are the total hadronic and leptonic momenta. In the first equality, $d\Phi_L$ is the leptonic phase-space, the last delta function is the overall momentum conservation and the delta function with the observable O is the measurement function, similar to the one defined in Eq. (4.35). The delta function $\delta^4(q - p_L)$ defines the measured momentum q as the total leptonic momentum. The second equality follows from Eq. (4.86), where the leptonic tensor does not depend on $\vec{q}_T$ after expansion of the delta function for $\vec{q}_T = 0$, and is given by,

$$L_{JJ'}(q^2, Y) = \int d\Phi_L L_J^\dagger L_{J'} (2\pi)^4 \delta^4\Big(q^- \frac{n_a}{2} + q^+ \frac{n_b}{2} - p_L\Big) \,, \tag{4.88}$$

and the hadronic tensor is

$$\begin{aligned}W_{JJ'}(q^2, Y, O) = \int \frac{d^2\vec{q}_T}{2(2\pi)^4} \sum \langle pp| J^\dagger |X\rangle \langle X| J'(0) |pp\rangle (2\pi)^4 \delta^4(P_a + P_b - q - P_X) \\ \delta(O - f_O(X)) \,.\end{aligned} \tag{4.89}$$

We can divide the phase space into two hemispheres a and b as shown in the Fig. 4.6 and

then divide the total hadronic momentum as $p_X^\mu = B_a^\mu + B_b^\mu$ where B_a^μ and B_b^μ are the total hadronic momenta in hemispheres a and b respectively. B_a^μ and B_b^μ have collinear and soft momentum components and are given by

$$B_a^+ = n_a \cdot B_a = n_a \cdot b_a + n_a \cdot k_a \quad , \quad B_b^+ = n_b \cdot B_b = n_b \cdot b_b + n_b \cdot k_b \,, \tag{4.90}$$

where $k_s = k_a + k_b$ is the total soft momentum and b_a^μ (b_b^μ) is the total momentum of the energetic collinear particles in hemisphere a (b). We are interested in a cross section differential in beam thrust-type observables, because $\mathcal{T}_B^{\text{jet}}$ can be thought of as the beam thrust of a jet, while $\mathcal{T}_C^{\text{jet}}$ behaves exactly the same as $\mathcal{T}_B^{\text{jet}}$ in the collinear limit. We can define beam thrust in terms of the new variables as $\tau_B = (B_a^+ + B_b^+)/Q$, which is analogous to our definition of τ_B in Eq. (4.34) (with $Y = 0$). The hemisphere hadronic momenta is obtained from the states $|X\rangle$ using the momentum operators $\hat{p}_{a,b}^\mu$

$$\hat{p}_a^\mu \, |X\rangle = B_a^\mu(X) \, |X\rangle \quad , \quad \hat{p}_b^\mu \, |X\rangle = B_b^\mu(X) \, |X\rangle \,. \tag{4.91}$$

So considering $O = \{B_a^+, B_b^+\}$, the hadronic tensor is given by

$$\begin{aligned} W_{JJ'} = & \int \frac{d^2\vec{q}_T}{2(2\pi)^4} \int d^4x e^{-iq\cdot x} \sum_X \langle pp| \, J^\dagger(X) \, |X\rangle \, \langle X| \, J'(0) \, |pp\rangle \, \delta[B_a^+ - n_a \cdot B_a(X)] \\ & \delta[B_b^+ - n_b \cdot B_b(X)] \\ = & \int \frac{dx^+ dx^-}{(4\pi)^2} e^{-i(q^+x^- + q^-x^+)/2} \, \langle pp| \, J^\dagger\Big(x^- \frac{n_a}{2} + x^+ \frac{n_b}{2}\Big) \delta[B_a^+ - n_a \cdot \hat{p}_a] \\ & \delta[B_b^+ - n_b \cdot \hat{p}_b] J'(0) \, |pp\rangle \,. \end{aligned} \tag{4.92}$$

where in the second equality, the integration over q_T is performed and Eq. (4.91) is used to carry out the sum over X thus eliminating the dependence on X.

The next step is matching the QCD current J onto the SCET current by integrating out the hard modes at the scale Q. The matching takes the form

$$J(x) = \sum_{n_1, n_2} d\omega_1 d\omega_2 e^{-i(\tilde{b}_1 + \tilde{b}_2)\cdot x} \Big[\sum_q C_{Jq\bar{q}}^{\alpha\beta}(\tilde{b}_1, \tilde{b}_2) O_{q\bar{q}}^{\alpha\beta}(\tilde{b}_1, \tilde{b}_2, x) + C_{Jg\bar{g}}^{\mu\nu}(\tilde{b}_1, \tilde{b}_2) O_{gg\mu\nu}(\tilde{b}_1, \tilde{b}_2, x) \Big] \,, \tag{4.93}$$

where C_J are the Wilson coefficients which depend on

$$\tilde{b}_1^\mu = \frac{\omega_1 n_1^\mu}{2} \quad , \quad \tilde{b}_2^\mu = \frac{\omega_2 n_2^\mu}{2} \,, \tag{4.94}$$

where $\omega_{1,2}$ and $n_{1,2}$ are not specified but will be set to $\omega_{a,b} = x_{a,b} E_{\text{cm}}$ and $n_{a,b}^\mu$ respectively. α, β are the spinor indices and μ, ν are vector indices. The SCET operators $O_{q\bar{q}}^{\alpha\beta}$ and $O_{gg\mu\nu}$

contain the collinear quark and gluon fields and at leading order are given as

$$
\begin{aligned}
O_{q\bar{q}}^{\alpha\beta}(\tilde{b}_1,\tilde{b}_2;x) &= \bar{\chi}_{n_1,-\omega_1}^{(0)\alpha j}(x)T[\mathcal{Y}_{n_1}^\dagger(x)\mathcal{Y}_{n_2}(x)]^{jk}\chi_{n_2,-\omega_2}^{(0)\beta k}(x)\ , \\
O_{gg}^{\mu\nu}(\tilde{b}_1,\tilde{b}_2;x) &= \sqrt{\omega_1\omega_2}\mathcal{B}_{n_1,-\omega_1\perp}^{(0)\mu c}(x)T[\mathcal{Y}_{n_1}^\dagger(x)\mathcal{Y}_{n_2}(x)]^{cd}\mathcal{B}_{n_2,-\omega_2\perp}^{(0)\nu d}(x)\,,
\end{aligned}
\tag{4.95}
$$

where the fields are defined as

$$
\chi_{n,\omega} = \delta(\omega-\overline{\mathcal{P}}_n)W_n^\dagger\xi_n\ ,\ \ \mathcal{B}_{n,\omega\perp}^\mu = \frac{1}{g}[\delta(\omega+\overline{\mathcal{P}}_n)W_n^\dagger(y)i\mathcal{D}_{n\perp}^\mu W_n(y)]\,,
\tag{4.96}
$$

with $i\mathcal{D}_{n\perp}^\mu = \mathcal{P}_{n\perp}^\mu + gA_{n\perp}^\mu$, are the composite n-collinear quark and gluon fields. The soft Wilson lines are a result of the field redefinition, as given in subsec. 4.6.1. The matching coefficients can be obtained by computing the renormalised matrix elements on both sides of Eq. (4.93) and comparing the results.

Since the Lagrangian factorizes into independent collinear and soft sectors, the momentum operator can also be written as the sum of independent operators acting on each sector, $\hat{p}_a = \hat{p}_{a,n_a} + \hat{p}_{a,n_b} + \hat{p}_{a,s}$ and similarly for $\hat{p}_b$. The measurement function can also be factorized into measurement acting on collinear and soft sectors separately as follows

$$
\delta(B_a^+ - n_a\cdot\hat{p}_a) = \int db_a^+ dk_a^+ \delta(B_a^+ - b_a^+ - k_a^+)\delta(b_a^+ - n_a\cdot\hat{p}_{n_a})\delta(k_a^+ - n_a\cdot\hat{p}_{s_a})
\tag{4.97}
$$

and similarly for B_b^+. It is thus possible to factorize the matrix element into n_a-collinear, n_b-collinear and soft matrix elements.

Let us look at the contribution from the gluon operator O_{gg} (because we are interested in the Higgs production) for which the x integral takes the form

$$
\begin{aligned}
&\int \frac{dx^+dx^-}{(4\pi)^2} e^{-i(q^+x^-+q^-x^+)/2}e^{i(\tilde{b}_1+\tilde{b}_2)\cdot x}\,\langle P_{na}P_{nb}|\,O_{gg}^{\dagger\nu\mu}(x)\delta[B_a^+ - n_a\cdot\hat{p}_a]\delta[B_b^+ - n_b\cdot\hat{p}_b] \\
&O_{gg}^{\nu'\mu'}(0)\,|P_{na}P_{nb}\rangle = \int d\omega_a d\omega_b \delta(\omega_a - q^-)\delta(\omega_b - q^+)\int db_a^+ db_b^+ dk_a^+ dk_b^+ \delta(B_a^+ - b_a^+ - k_a^+) \\
&\delta(B_b^+ - b_b^+ - k_b^+)\Big[\delta_{n_1 n_a}\delta(\omega_1-\omega_a)\delta_{n_2 n_b}\delta(\omega_2-\omega_b) + a\leftrightarrow b\Big]\Big[\delta_{n_1' n_a}\delta(\omega_1'-\omega_a)\delta_{n_2' n_b}\delta(\omega_2'-\omega_b) \\
&+ a\leftrightarrow b\Big]\times\omega_a\theta(\omega_a)\,\langle p_{n_a}|\,\mathcal{B}_{n_a\perp}^{\mu c}(0)\delta(b_a^+ - n_a\cdot\hat{p}_{n_a})\delta(\omega-\overline{P}_{n_a})\mathcal{B}_{n_a\perp}^{\mu' c'}(0)\,|p_{n_a}\rangle\times\Big[a\to b\ ,\ c\to d\Big] \\
&\times\langle 0|\,\bar{T}[\mathcal{Y}_{n_a}^\dagger\mathcal{Y}_{n_b}(0)]^{cd}\delta(k_a^+ - n_a\cdot\hat{p}_{a,s})\delta(k_b^+ - n_b\cdot\hat{p}_{b,s})\bar{T}[\mathcal{Y}_{n_b}^\dagger\mathcal{Y}_{n_a}(0)]^{d'c'}\,|0\rangle\ ,
\end{aligned}
\tag{4.98}
$$

where in the second step, the x integral has been performed. For the x integral, the collinear and soft matrix elements in the last two lines are abbreviated as $M_{\omega_a}(x^-)$, $M_{\omega_b}(x^+)$ and $M_s(x^+,x^-)$ respectively. To perform the x integrals, we take the residual fourier transform

of the matrix elements,

$$M_{\omega_a}(x^-) = \int \frac{dk^+}{2\pi} e^{ik^+x^-/2} \tilde{M}_{\omega_a}(k^+) \ , \ \ M_{\omega_b}(x^+) = \int \frac{dk^-}{2\pi} e^{ik^-x^+/2} \tilde{M}_{\omega_b}(k^-) \, ,$$
$$M_s(x^-, x^+) = \int \frac{dk_s^+ dk_s^-}{(2\pi)^2} e^{i(k_s^+ x^- + k_s^- x^+)/2} \tilde{M}_s(k^+, k^-) \tag{4.99}$$

After defining the Fourier transformed variables, the x integrals can be performed,

$$\int \frac{dx^+ dx^-}{(4\pi)^2} e^{i(\omega_a - q^-)x^+/2} e^{i(\omega_b - q^+)x^-/2} M_{\omega_a}(x^-) M_{\omega_b}(x^+) M_s(x^-, x^+) = \int \frac{dk^+}{2\pi} \frac{dk^-}{2\pi}$$
$$\frac{dk_s^+ dk_s^-}{(2\pi)^2} \tilde{M}_{\omega_a}(k^+) \tilde{M}_{\omega_b}(k^-) \tilde{M}_s(k^+, k^-) \delta(\omega_a - q^- + k^- + k_s^-) \delta(\omega_b - q^+ + k^+ + k_s^+)$$
$$= \delta(\omega_a - q^-) \delta(\omega_b - q_a^+) M_{\omega_a}(0) M_{\omega_b}(0) M_{\omega_s}(0) \, . \tag{4.100}$$

In the last step, we use $q^\pm - k^\pm - k_s^\pm = q^\pm[1 + O(\lambda^2)]$. The collinear matrix element now reduces to the gluon beam function given by,

$$\omega_a \theta(\omega_a) \langle p_{n_a} | \, \mathcal{B}^{\mu c}_{n_a \perp}(0) \delta(b_a^+ - n_a \cdot \hat{p}_{n_a}) \delta(\omega - \overline{P}_{n_a}) \mathcal{B}^{\mu' c'}_{n_a \perp}(0) \, | p_{n_a} \rangle = \frac{g_\perp^{\mu\mu'}}{2} \frac{\delta^{cc'}}{N_c^2 - 1} \omega_a (-\theta(\omega_a))$$
$$\int \frac{dy^-}{4\pi} e^{ib_a^+ y^-/2} \langle p_{n_a} | \, e^{-i\hat{p}^+_{n_a} y^-/2} e^{i\hat{p}^+_{n_a} y^-/2} \mathcal{B}^c_{n_a \perp \mu}(0) e^{-i\hat{p}^+_{n_a} y^-/2} \delta(\omega - \overline{P}_{n_a}) \mathcal{B}^{\mu c}_{n_a \perp}(0) \, | p_{n_a} \rangle$$
$$= \frac{g_\perp^{\mu\mu'}}{2} \frac{\delta^{cc'}}{N_c^2 - 1} \omega_a B_g \Big[\omega_a b_a^+, \frac{\omega_a}{P_a^-} \Big] \tag{4.101}$$

where $\hat{p}^+_{n_a} = n_a \cdot \hat{p}_{n_a}$ and with $e^{i\hat{p}^+_{n_a} y^-/2} \mathcal{B}^c_{n_a \perp \mu}(0) e^{-i\hat{p}^+_{n_a} y^-/2} = \mathcal{B}^c_{n_a \perp \mu}(y^- n_a/2)$. The gluon beam function is defined as

$$B_g \Big[\omega_a b_a^+, \frac{\omega_a}{P_a^-} \Big] = -\theta(\omega_a) \int \frac{dy^-}{4\pi} e^{ib_a^+ y^-/2} \langle p_{n_a} | \, e^{-i\hat{p}^+_{n_a} y^-/2} \mathcal{B}^c_{n_a \perp \mu} \Big(\frac{y^- n}{2} \Big) \delta(\omega - \overline{P}_{n_a}) \mathcal{B}^{\mu c}_{n_a \perp}(0) \, | p_{n_a} \rangle \tag{4.102}$$

and similarly the soft matrix elements define the gluon hemisphere soft function given by

$$S^{gg}_{\text{ihemi}}(k_a^+, k_b^+) = \frac{1}{N_c^2 - 1} \langle 0 | \, \{ tr_{\text{color}} \overline{T}[\mathcal{Y}^\dagger_{n_a}(0) \mathcal{Y}_{n_b}(0)] \delta(k_a^+ - n_a \cdot \hat{P}_{a,s}) \delta(k_b^+ - n_b \cdot \hat{P}_{b,s})$$
$$\overline{T}[\mathcal{Y}^\dagger_{n_b} \mathcal{Y}_{n_a}(0)] \} \, | 0 \rangle \ . \tag{4.103}$$

Putting all the pieces together, the hadronic tensor for the gluon initial state is given by

$$W_{JJ'gg}(q^2, Y, B_a^+, B_b^+) = H_{JJ'gg}(\tilde{b}_a, \tilde{b}_b) \int dk_a^+ dk_b^+ q^2 B_g[x_a E_{\text{cm}}(B_a - k_a^+), x_a]$$
$$B_g[x_b E_{\text{cm}}(B_b - k_b^+), x_b] \times S^{gg}_{\text{ihemi}}(k_a^+, k_b^+) \tag{4.104}$$

where the hard function contains the color structure and the Wilson coefficients. For simplicity, we only considered gluonic initial states, however for the full hadronic tensor

and the hard function, we also need the contributions from $O_{q\bar{q}}$ and the expression can be found in [64]. Adding the contributions from different quark flavors and gluons, the hadronic tensor becomes

$$W_{JJ'}(q^2, Y, B_a^+, B_b^+) = \sum_q W_{JJ'q\bar{q}}(q^2, Y, B_a^+, B_b^+) + W_{JJ'gg}(q^2, Y, B_a^+, B_b^+)\,, \tag{4.105}$$

where the hadronic tensor for the quark contributions can be found in [64].

Inserting back all the components, the differential cross section reads

$$\frac{d\sigma}{dq^2 dY\, dB_a^+ dB_b^+} = \sum_{ij} H_{ij}(q^2, Y) \int dk_a^+ dk_b^+ q^2 B_i[x_a E_{\rm cm}(B_a - k_a^+), x_a] B_j[x_b E_{\rm cm}(B_b - k_b^+), x_b] \times S^{ij}_{\rm ihemi}(k_a^+, k_b^+)\,, \tag{4.106}$$

where the hard function is given by

$$H_{ij}(q^2, Y) = \frac{1}{2E_{\rm cm}^2} \sum_{JJ'} L_{JJ'}(q^2, Y) \times H_{JJ'ij}\Big(x_a E_{\rm cm}\frac{n_a}{2}, x_b E_{\rm cm}\frac{n_b}{2}\Big)\,. \tag{4.107}$$

Eq. (4.106) is the factorization formula for the process $pp \to XL$.

The initial state physics is characterized by three distinct scales $\mu_\Lambda \ll \mu_B \ll \mu_H$. At μ_Λ, the incoming proton contains partons of type k described by the PDFs $f_k(\xi', \mu_\Lambda)$. Evolving μ_Λ to higher scales sums up single logarithms with the DGLAP evolution and changes the type k and momentum fraction ξ' of the partons. At the scale μ_B the measurement probes the proton, breaking it apart identifying a parton j with momentum fraction ξ according to $f_b(\xi, \mu_B)$. The radiation emitted by the parton builds up an incoming jet described by the function $\mathcal{I}_{ij}$ (which are calculable perturbatively and are given in App. A.2) forming the beam function,

$$B_i(t, x, \mu_B) = \sum_j \int_x^1 \frac{dz}{z} \mathcal{I}_{ij}(t, z, \mu_B) f_b(\frac{x}{z}, \mu_B)\Big[1 + O\Big(\frac{\Lambda^2}{t}\Big)\Big]\,, \tag{4.108}$$

where $z = x/\xi$ and $t_{a,b} = \omega_{a,b} b_{a,b}^+ = x_{a,b} E_{\rm cm} b_{a,b}^+$ is the transverse virtuality. By measuring beam thrust, we measure the virtuality of the hard parton in the initial state.

The factorization formula in Eq. (4.106) also applies to Higgs production via gluon fusion, the only difference being in the hard function, which must be changed accordingly. The structure of the factorization formula for $pp \to HX$ with no additional hard jets, and

differential in inclusive beam thrust is,

$$\frac{d^2\sigma}{d\mathcal{T}_{B\mathrm{cm}}dY} = \sigma_0 H_{gg}(m_t, m_H^2, \mu) \int dt_a dt_b B_g(t_a, x_a, \mu) B_g(t_b, x_b, \mu) \times S_{gg}\Big(\mathcal{T}_{B\mathrm{cm}} - \frac{e^{-Y}t_a + e^{Y}t_b}{m_H}, \mu\Big) \tag{4.109}$$

where

$$x_{a,b} = \frac{m_H}{E_{\mathrm{cm}}} e^{\pm Y}\,, \quad \sigma_B = \frac{\sqrt{2}G_F\, m_H^2}{576\pi E_{\mathrm{cm}}^2}\,. \tag{4.110}$$

The hard function is determined by matching QCD currents onto SCET, and can be obtained from the IR-finite part of the $\overline{MS}$ renormalized ggH form factor. It is the same as for threshold Higgs, and is given by

$$H_{gg}(m_t, m_H^2, \mu) = |C_{ggH}(m_t, m_H^2, \mu)|^2\,. \tag{4.111}$$

where C_{ggH}, given in Eq. (A.2).

4.6.3 Application to jet-based observables

In order to obtain a similar factorization formula for the rapidity-dependent jet observables $\mathcal{T}_B^{\mathrm{jet}}$ and $\mathcal{T}_C^{\mathrm{jet}}$, the inclusive beam thrust measurement in the proof sketched for Drell-Yan (and for Higgs production in Eq. (4.109)) needs to be generalized to jet-based observables as well. As we saw in Eq. (4.97), the measurement factorized into collinear and soft components that act independently on the soft and collinear sectors. This must hold true for jet-based observables too so that the matrix elements can be factorized into independent beam and soft functions. Schematically, it was shown in [70], that any generic measurement function $\mathcal{M}$ can be separated into collinear and soft sectors as follows,

$$\mathcal{M} = \mathcal{M}_a \times \mathcal{M}_b \times \mathcal{M}_s + \delta\mathcal{M}\,. \tag{4.112}$$

The operators $\mathcal{M}_a$, $\mathcal{M}_b$ and $\mathcal{M}_s$ act only on n_a-collinear, n_b-collinear, and soft fields respectively assuming that the mixing between the sectors is taken care of by the correction term $\delta\mathcal{M}$. These mixing terms are $O(R^2)$ and are small for small jet radii currently used in experiments, so that the factorization formula holds at leading order. For inclusive observables like beam thrust, $\delta\mathcal{M} = 0$. The measurement function reads (referring to Eq. (4.35))

$$\mathcal{M}(\mathcal{T}_B) = \delta\Big(\mathcal{T}_B - \sum_i |\vec{p}_{Ti}| e^{-|y_i - Y|}\Big)\,. \tag{4.113}$$

Since the inclusive observables sum over all particles, the full $\mathcal{T}_B$ can be written as a sum of collinear and soft contributions $\mathcal{T}_B = \mathcal{T}_{Ba} + \mathcal{T}_{Bb} + \mathcal{T}_S$ (as in Eq. (4.97)), so that the measurement function can also be factorized into measurement acting on each sector as follows

$$\mathcal{M}_a = \delta(\mathcal{T}_{Ba} - p^+ e^Y) \ , \ \mathcal{M}_b = \delta(\mathcal{T}_{Bb} - p^- e^{-Y}) \ , \ \mathcal{M}_S = \delta(\mathcal{T}_{BS} - \sum_{m \in soft} \min\{p^+ e^Y, p^- e^{-Y}\}) \, . \tag{4.114}$$

Let us now consider jet-based observables like $p_T^{\rm jet}$ $\mathcal{T}_B^{\rm jet}$ and $\mathcal{T}_C^{\rm jet}$ defined before. The measurement function for such observables involve more subtleties due to the jet algorithm effects that need to be understood well. The measurement function for such observables is a product of theta functions so that the maximum condition in Eq. (4.5) is satisfied,

$$\begin{aligned}
\mathcal{M}(p_T^{\rm jet}) &= \prod_{j \in \rm jets} \theta\Big(|\vec{p}_{Tj}| < p_T^{\rm cut}\Big) \, , \\
\mathcal{M}(\mathcal{T}_B^{\rm jet}) &= \prod_{j \in \rm jets} \theta\Big(|\vec{p}_{Tj}| e^{-|y_j - Y|} < \mathcal{T}^{\rm cut}\Big) \, , \\
\mathcal{M}(\mathcal{T}_C^{\rm jet}) &= \prod_{j \in \rm jets} \theta\Big(\frac{|\vec{p}_{Tj}|}{2\cosh(y_j - Y)} < \mathcal{T}^{\rm cut}\Big) \, .
\end{aligned} \tag{4.115}$$

Separating into independent collinear and soft sectors, the measurement function for a general $k^{\rm cut}$ is given by

$$\mathcal{M}(k^{\rm cut}) = \mathcal{M}_a^{\rm jet}(k^{\rm cut}) \mathcal{M}_b^{\rm jet}(k^{\rm cut}) \mathcal{M}_S^{\rm jet}(k^{\rm cut}) + \delta\mathcal{M}^{\rm jet}(k^{\rm cut}) \, . \tag{4.116}$$

The functions $\mathcal{M}_i^{\rm jet}$ contain the independent contraint on the collinear and soft sectors, while the left over contribution takes into account the case where there is a mixing between the collinear and soft sectors. A contribution such as $|k_c + k_s < k^{\rm cut}|$ which is a part of this correction term must however be power suppressed in order that the factorization of the cross section into collinear and soft components still hold. It has been shown in [70] that for a jet radius $R \sim \lambda$, $\delta\mathcal{M}^{\rm jet}$ is indeed proportional to R^2 and therefore power suppressed for $R \ll 1$. To understand these jet-algorithm dependent contributions to the measurement, it is useful to express the measurement function as

$$\mathcal{M}^{\rm jet} = (\mathcal{M}_a + \Delta\mathcal{M}_a^{\rm jet})(\mathcal{M}_b + \Delta\mathcal{M}_b^{\rm jet})(\mathcal{M}_S + \Delta\mathcal{M}_S^{\rm jet}) + \delta\mathcal{M}^{\rm jet} \, . \tag{4.117}$$

Here $\Delta\mathcal{M}_i^{\rm jet}$ is defined to contain the jet-algorithm effects within the same sector i.e. clustering of two collinear or soft emissions into one jet. These typically have the form $\alpha_s^N \log^{N-1} R$ and are important at small values of the jet radius R. These arise from correlated emissions as shown in the right side of Fig. 4.7. $\delta\mathcal{M}^{\rm jet}$ is a mixing term which arises due to a soft particle clustering with an n_a or n_b-collinear particle as shown by the left panel of Fig. 4.7 and is proportional to R^2. These corrections become important for

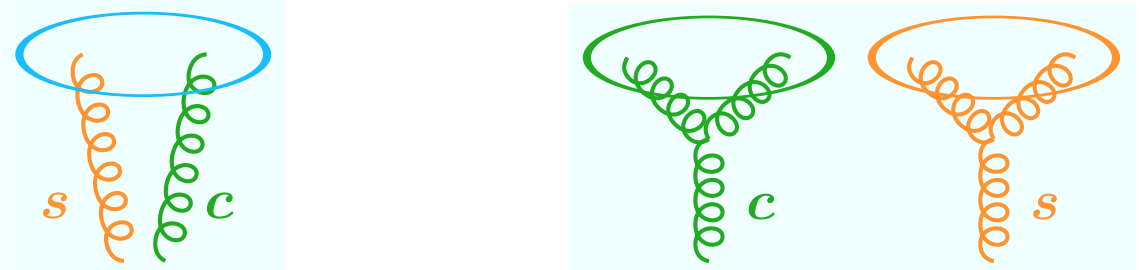

Figure 4.7: *Left: soft and collinear particles clustering into one jet contributing to* $\delta\mathcal{M}^{\text{jet}}$*. Right: clustering within the collinear and soft sectors contributing to* $\Delta\mathcal{M}^{\text{jet}}$*.*

$R \gg \lambda$. At $\mathcal{O}(\alpha_s)$ there are no jet algorithm effects as there is only a single emission, either soft or collinear. A detailed calculation of the clustering effects for the beam and soft function will appear in the next chapter. Let us now discuss in detail the factorization and resummation properties of jet-based observables.

The factorization formula for the jet-based observables is a simple product of the different functions, instead of the convolution in case of inclusive observables. If $R^2 \ll 1$, the resummed contribution for the case of a veto $\mathcal{T}^{\text{jet}}_{B,C} < \mathcal{T}^{\text{cut}}$ can be factorized to all orders in perturbation theory as

$$\frac{\mathrm{d}\sigma_0^{\text{resum}}}{\mathrm{d}Y}(\mathcal{T}^{\text{jet}}_{B,C} < \mathcal{T}^{\text{cut}}) = \sigma_B H_{gg}(m_t, m_H, \mu)\, B_g(m_H \mathcal{T}^{\text{cut}}, x_a, R, \mu) \times B_g(m_H \mathcal{T}^{\text{cut}}, x_b, R, \mu)$$
$$S^{B,C}_{gg}(\mathcal{T}^{\text{cut}}, R, \mu) + \frac{\mathrm{d}\sigma_0^{\text{Rsub}}}{\mathrm{d}Y}(\mathcal{T}^{\text{jet}}_{B,C} < \mathcal{T}^{\text{cut}}, R)\,, \tag{4.118}$$

The only difference between $\mathcal{T}^{\text{jet}}_B$ and $\mathcal{T}^{\text{jet}}_C$ to all orders is their dependence on different soft functions, $S^{B,C}_{gg}$. The beam functions B_i are the same for both observables, because they describe the effects of collinear initial-state radiation, i.e. emissions with forward rapidities, where the $\mathcal{T}^{\text{jet}}_B$ and $\mathcal{T}^{\text{jet}}_C$ measurements are equal up to power corrections (cf. left panel in Fig. 4.1). This can be seen explicitly by expressing the variables $\mathcal{T}_{B,C}$ in terms of plus and minus momenta in one of the two collinear sectors,

$$\mathcal{T}_{Bj} = p_j^+\,, \qquad \mathcal{T}_{Cj} = \frac{p_j^+ p_j^-}{p_j^+ + p_j^-}\,, \tag{4.119}$$

with $p_j^- \gg p_j^+$ and therefore $\mathcal{T}_{Cj} = \mathcal{T}_{Bj} + \mathrm{O}(p_j^+/p_j^-)$, where $p_j^+/p_j^- \sim \mathcal{T}/m_H$ is a power correction. The $\mathrm{O}(R^2)$ corrections from $\delta\mathcal{M}^{\text{jet}}_f$ are collected in the $\mathrm{d}\sigma_0^{\text{Rsub}}$ piece in Eq. (4.118). They start contributing at $\mathrm{O}(\alpha_s^2)$ and so are not yet needed for now. Note that another source of possibly factorization-violating contributions for hadronic observables is related to the interaction between spectator particles mediated by Glauber modes. Usually, these are not considered in perturbative predictions of jet cross sections. As argued in [79], for

jet-based observables these effects are suppressed at least as $\mathrm{O}(R^2)$, and we therefore also neglect them here.

For $\mathcal{T}^{\text{jet}}_{B\text{cm}}$ and $\mathcal{T}^{\text{jet}}_{C\text{cm}}$, the resummed contribution obeys a similar factorization of the form

$$\frac{\mathrm{d}\sigma_0^{\text{resum}}}{\mathrm{d}Y}(\mathcal{T}^{\text{jet}}_{B\text{cm},C\text{cm}} < \mathcal{T}^{\text{cut}}) = \sigma_B H_{gg}(m_t, m_H^2, \mu)\, B_g(m_H \mathcal{T}^{\text{cut}} e^{Y}, x_a, R, \mu) \\ \times B_g(m_H \mathcal{T}^{\text{cut}} e^{-Y}, x_b, R, \mu)\, S_{gg}^{B,C}(\mathcal{T}^{\text{cut}}, R, \mu) + \frac{\mathrm{d}\sigma_0^{\text{Rsub}}}{\mathrm{d}Y}(\mathcal{T}^{\text{jet}}_{B\text{cm},C\text{cm}} < \mathcal{T}^{\text{cut}}, R)\,. \quad (4.120)$$

Here, the hard, beam, and soft functions are the same as in Eq. (4.118), the only difference is that the beam functions are evaluated at different arguments. The soft function $S_{gg}^{B,C}$ is precisely the same as in Eq. (4.118) because it is a vacuum matrix element and, unlike the beam functions that involve the incoming proton states, has no reference to the frame other than through the measurement function itself. By a change (boost) of the soft integration momenta, the soft measurement function for $\mathcal{T}^{\text{jet}}_{B\text{cm},C\text{cm}}$ can therefore always be transformed into that for $\mathcal{T}^{\text{jet}}_{B,C}$, respectively. (Technically, this is a consequence of the RPI-III invariance [80, 81] of the soft function.) The beam functions on the other hand are related to the ones in Eq. (4.118) by a simple rescaling of $\mathcal{T}^{\text{cut}}$. This is because for jets made of $n_a(n_b)$-collinear particles we have $y_j > 0$ ($y_j < 0$) in the $Y = 0$ frame and correspondingly $y_j > Y$ ($y_j < Y$) in the lab frame. According to Eqs. (4.7)-(4.10) for $n_{a,b}$-collinear jets we therefore have $\mathcal{T}_{C\text{cm}} = \mathcal{T}_{B\text{cm}} = \mathcal{T}_B e^{\mp Y}$, respectively. A detailed discussion of the analogous frame-dependence for inclusive beam thrust can be found in [64].

4.7 Resummation of large logarithms in SCET

By implementing a jet veto cut $\mathcal{T}_{B\text{cm}} < \mathcal{T}^{\text{cut}}$, the resulting 0-jet cross section contains large double logarithms of the form $\alpha_s^N \ln^M \mathcal{T}^{\text{cut}}/m_H$ with $M \leq 2N$. The factorization formula above allows to resum these logarithms in SCET. These logarithms are split up as follows

$$\ln^2 \frac{\mathcal{T}^{\text{cut}}}{m_H} = 2\ln^2 \frac{m_H}{\mu} - \ln^2 \frac{\mathcal{T}^{\text{cut}} m_H}{\mu^2} + 2\ln^2 \frac{\mathcal{T}^{\text{cut}}}{\mu} \quad (4.121)$$

where the first, second and third term on the right-side are contained in the hard, beam and soft functions respectively. The singular cross section with these logarithms has the following structure

$$\ln \sigma_0(\mathcal{T}^{\text{cut}}) \sim \Big[L \sum_m c_m^{LL} (\alpha_s L)^m + \sum_m c_m^{NLL} (\alpha_s L)^m + \alpha_s \sum_m c_m^{NNLL} (\alpha_s L)^m + \cdots \Big] \quad (4.122)$$

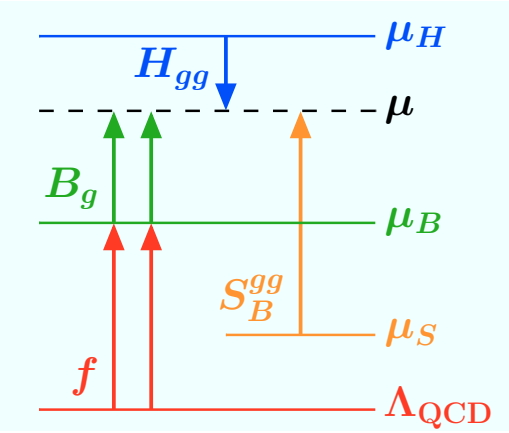

Figure 4.8: *RG evolution of the beam, soft and hard scale to a common scale μ.*

where LL, NLL and NNLL corresponds to leading logarithm, next-to-leading log and next-to-next-to leading log respectively. A resummed cross section is accurate upto LL, NLL or NNLL order if it includes the tower of logarithms upto the first, second and third term respectively. The summation happens in the exponent of the cross section as was shown in Eq. (2.57). These logarithms can be resummed by evaluating all functions at their natural scales i.e. hard function at $\mu_H = m_H$, soft function at $\mu_S = \mathcal{T}^{\rm cut}$ and beam functions at $\mu_B = t^{\rm cut} \sim \sqrt{\mathcal{T}^{\rm cut} m_H}$ and then RG evolving them to the common scale μ as shown in Fig. 4.8 which resums the logarithms. The common choice of the scale μ is $\{m_H, 2m_H, m_H/2\}$.

Table 3.1 shows the various orders in resummed perturbation theory and the corresponding accuracy needed for the matching (to the fixed-order cross section), and the anomalous dimensions that enter the singular corrections.

Log counting:	Fixed-order corrections matching	nonsingular	Resummation input $\gamma^\mu_{H,B,S}$	$\Gamma_{\rm cusp}$	β	PDF
LL	LO	-	-	1-loop	1-loop	LO
NLL	LO	-	1-loop	2-loop	2-loop	LO
NLL′	NLO	-	1-loop	2-loop	2-loop	NLO
NLL′+ NLO	NLO	NLO	1-loop	2-loop	2-loop	NLO
NNLL′+NNLO	NNLO	NNLO	2-loop	3-loop	3-loop	NNLO

As shown in Fig. 4.8, there are three separated scales in the process $\mu_\Lambda \ll \mu_B \ll \mu_H$. At the hadronic scale μ_Λ, the incoming parton is described by the PDFs, and the evolution from μ_Λ to μ_B is the standard DGLAP evolution summing single logarithms. The evolution for $\mu > \mu_B$ sums up the double logarithms of the ratio of μ_B and μ and is given by the

RGE

$$\mu\frac{d}{d\mu}\ln[B_g(t^{\rm cut},x,\mu,R)] = \gamma_B^g(t^{\rm cut},\mu,R) \tag{4.123}$$

Note that, the RGE for jet-based observables takes a product form, as a consequence of the simple multiplicative structure of the factorized cross section. Like the beam function, the evolution for the soft function from μ_S to μ and for the hard function from μ_H to μ is given by a similar RGE

$$\begin{aligned}\mu\frac{\rm d}{{\rm d}\mu}\ln\bigl[C_{ggH}(m_t,m_H^2,\mu)\bigr] &= \gamma_H^g(m_H^2,\mu)\,,\\ \mu\frac{\rm d}{{\rm d}\mu}\ln\bigl[S_g^{B,C}(\mathcal{T}^{\rm cut},R,\mu)\bigr] &= \gamma_S^g(\mathcal{T}^{\rm cut},R,\mu)\,,\end{aligned} \tag{4.124}$$

The generic all-order structure of the anomalous dimensions, as the sum of a noncusp part and an explicitly μ-dependent cusp part, is fixed by RG invariance of the cross section and the well-known Sudakov form of the hard function, which is completely independent of the specific observable. Specifically, we have

$$\begin{aligned}\gamma_H^g(m_H^2,\mu) &= \Gamma^g_{\rm cusp}[\alpha_s(\mu)]\ln\frac{-m_H^2-{\rm i}0}{\mu^2} + \gamma_H^g[\alpha_s(\mu)]\,,\\ \gamma_B^g(t^{\rm cut},R,\mu) &= -2\Gamma^g_{\rm cusp}[\alpha_s(\mu)]\ln\frac{t^{\rm cut}}{\mu^2} + \gamma_B^g[\alpha_s(\mu),R]\,,\\ \gamma_S^g(\mathcal{T}^{\rm cut},R,\mu) &= 4\Gamma^g_{\rm cusp}[\alpha_s(\mu)]\ln\frac{\mathcal{T}^{\rm cut}}{\mu} + \gamma_S^g[\alpha_s(\mu),R]\,.\end{aligned} \tag{4.125}$$

The RG invariance of the cross section moreover requires that the soft anomalous dimension of S_{gg}^B and S_{gg}^C is the same to all orders in perturbation theory, and hence it is the same for all four observables we consider. Integrating Eq. (4.123) from μ_0 to μ by changing the variables to α_s with $d\ln\mu = d\alpha_s/\beta[\alpha_s]$ gives

$$\ln\frac{B(t^{\rm cut},x,\mu,R)}{B(t^{\rm cut},x,\mu_0,R)} = \eta_B(\mu_0,\mu)\ln\left(t^{\rm cut}\mu_0^{-2}\right) + K_B(\mu,\mu_0) \tag{4.126}$$

Solving further yields

$$B_g(t^{\rm cut},x,R,\mu) = U_B(t^{\rm cut},\mu_B,\mu)\,B_g(t^{\rm cut},x,R,\mu_B) \tag{4.127}$$

with the evolution factor given by

$$U_B(t^{\rm cut},\mu_B,\mu) = e^{K_B(\mu_B,\mu)}\left(\frac{t^{\rm cut}}{\mu_B^2}\right)^{\eta_B(\mu_B,\mu)}. \tag{4.128}$$

with

$$K_B(\mu_B,\mu) = +4K_\Gamma^g(\mu_B,\mu) + K_{\gamma_B^g}(\mu_B,\mu) \;\;,\;\; \eta_B(\mu_B,\mu) = -2\eta_\Gamma^g(\mu_B,\mu) \tag{4.129}$$

and

$$\begin{aligned} K_\Gamma^g(\mu_0,\mu) &= \int_{\alpha_s(\mu_B)}^{\alpha_s(\mu)} \frac{d\alpha}{\beta[\alpha]} \Gamma^g_{\text{cusp}}[\alpha] \int_{\alpha_s(\mu_B)}^{\alpha} \frac{d\alpha}{\beta[\alpha]} \;,\; K_{\gamma_i^g}(\mu_0,\mu) = \int_{\alpha_s(\mu_B)}^{\alpha_s(\mu)} \frac{d\alpha}{\beta[\alpha]} \gamma_i^g[\alpha], \\ \eta_\Gamma^g(\mu_0,\mu) &= \int_{\alpha_s(\mu_B)}^{\alpha_s(\mu)} \frac{d\alpha}{\beta[\alpha]} \Gamma^g_{\text{cusp}}[\alpha] \,. \end{aligned} \tag{4.130}$$

Analogous to the RG-evolved beam function, we can write the RG-evolved hard and soft functions as

$$H_{gg}(m_t, q^2, \mu) = U_H(q^2, \mu_H, \mu)\, H_{gg}(m_t, q^2, \mu_H)\,, \tag{4.131}$$

$$S^B_{gg}(\mathcal{T}^{\text{cut}}, \mu) = U_S(\mathcal{T}^{\text{cut}}, \mu_S, \mu)\, S^B_{gg}(\mathcal{T}^{\text{cut}}, \mu_S)\,, \tag{4.132}$$

with the corresponding RG evolution factors given by

$$U_S(\mathcal{T}^{\text{cut}}, \mu_S, \mu) = e^{K_S(\mu_S,\mu)} \Big(\frac{\mathcal{T}^{\text{cut}}}{\mu_S}\Big)^{\eta_S(\mu_S,\mu)}\,, \tag{4.133}$$

$$U_H(q^2, \mu_H, \mu) = \Big| e^{K_H(\mu_H,\mu)} \Big(\frac{-q^2 - i0}{\mu_H^2}\Big)^{\eta_H(\mu_H,\mu)} \Big|^2. \tag{4.134}$$

and

$$\begin{aligned} K_S(\mu_S,\mu) &= -4K_\Gamma^g(\mu_S,\mu) + K_{\gamma_s^g}(\mu_S,\mu)\,, \\ K_H(\mu_H,\mu) &= -2K_\Gamma^g(\mu_H,\mu) + K_{\Gamma_H^g}(\mu_H,\mu)\,, \\ \eta_S(\mu_S,\mu) &= +4\eta_\Gamma^g(\mu_S,\mu) \;\;,\;\; \eta_H(\mu_H,\mu) = +\eta_\Gamma^g(\mu_H,\mu)\,, \end{aligned} \tag{4.135}$$

Explicit analytic expressions for the K_Γ^g, $K_{\gamma_i^g}$ and η_i^g as well as the anomalous dimensions and beta functions relevant for NLL resummation can be found in Ref. [23].

Writing out the evolution factors explicitly, the resummed cross section with a veto on $\mathcal{T}^{\text{jet}}_{B,C}$ reads

$$\begin{aligned} \frac{\mathrm{d}\sigma_0^{\text{resum}}}{\mathrm{d}Y}(\mathcal{T}^{\text{jet}}_{B,C} < \mathcal{T}^{\text{cut}}) = \sigma_B H_{gg}(m_t, m_H^2, \mu_H)\, B_g(m_H \mathcal{T}^{\text{cut}}, x_a, R, \mu_B) \times B_g(m_H \mathcal{T}^{\text{cut}}, x_b, R, \mu_B) \\ S^{B,C}_{gg}(\mathcal{T}^{\text{cut}}, R, \mu_S) \times U_0(m_H, \mathcal{T}^{\text{cut}}, \mu_H, \mu_B, \mu_S) \\ + \frac{\mathrm{d}\sigma_0^{\text{Rsub}}}{\mathrm{d}Y}(\mathcal{T}^{\text{jet}}_{B,C} < \mathcal{T}^{\text{cut}}, R)\,, \end{aligned} \tag{4.136}$$

and for a veto on $\mathcal{T}^{\text{jet}}_{B\text{cm},C\text{cm}}$, we have

$$\begin{aligned}\frac{\mathrm{d}\sigma_0^{\text{resum}}}{\mathrm{d}Y}(\mathcal{T}^{\text{jet}}_{B\text{cm},C\text{cm}} < \mathcal{T}^{\text{cut}}) = \sigma_B H_{gg}(m_t, m_H^2, \mu_H)\, B_g(m_H \mathcal{T}^{\text{cut}} e^{Y}, x_a, R, \mu_B) \\ \times B_g(m_H \mathcal{T}^{\text{cut}} e^{-Y}, x_b, R, \mu_B) S_{gg}^{B,C}(\mathcal{T}^{\text{cut}}, R, \mu_S) \times \\ U_0(m_H, \mathcal{T}^{\text{cut}}, \mu_H, \mu_B, \mu_S) + \frac{\mathrm{d}\sigma_0^{\text{Rsub}}}{\mathrm{d}Y}(\mathcal{T}^{\text{jet}}_{B\text{cm},C\text{cm}} < \mathcal{T}^{\text{cut}}, R)\,.\end{aligned} \tag{4.137}$$

Here, the total evolution factor, combining the individual hard, beam, and soft ones, is

$$U_0(m_H, \mathcal{T}^{\text{cut}}, \mu_H, \mu_B, \mu_S) = U_H(m_H^2, \mu_H, \mu)\, U_B^2(m_H \mathcal{T}^{\text{cut}}, \mu_B, \mu)\, U_S(\mathcal{T}^{\text{cut}}, \mu_S, \mu)\,.$$

The dependence on the common arbitrary scale μ cancels exactly between the individual U_i due to RG consistency. Note that the U_{tot} is the same in Eqs. (4.136) and (4.137), because according to Eq. (4.128)

$$U_B(m_H \mathcal{T}^{\text{cut}} e^{Y}, \mu_B, \mu)\, U_B(m_H \mathcal{T}^{\text{cut}} e^{-Y}, \mu_B, \mu) = U_B^2(m_H \mathcal{T}^{\text{cut}}, \mu_B, \mu)\,. \tag{4.138}$$

Hence, the only difference between the $\mathcal{T}^{\text{jet}}_{B,C}$ and $\mathcal{T}^{\text{jet}}_{B\text{cm},C\text{cm}}$ cross sections is the Y-dependence in the arguments of the fixed-order beam functions in Eqs. (4.136) and (4.137).

In the next section we will provide the different ingredients for predicting the full differential cross section at NLL′+ NLO i.e. the beam, soft and hard functions at NLL′ and the non-singular corrections for matching the resummed cross section to fixed-order.

4.8 Ingredients at NLL′

The resummation at the NLL′ level includes the NLL RG evolution and in addition the fixed order one-loop expressions for the hard, beam and soft functions. The latter provide the exact $\mathrm{O}(\alpha_s)$ boundary conditions for the RGEs, which are formally a NNLL effect, but are important for matching to the full NLO cross section. The $\mathrm{O}(\alpha_s)$ hard function can be taken directly from [23] and is given in App. A.1.

At fixed $\mathrm{O}(\alpha_s)$, the $B_i(t^{\text{cut}}, x, R, \mu_B)$ can be obtained by integrating the one-loop differential t-dependent beam function [23, 82], because the $\mathcal{T}^{\text{jet}}_{B,C}$ measurement function for a veto on the emission of only one gluon is simply a theta function, $\theta(t < t^{\text{cut}})$, of the virtuality t. Therefore, the one-loop gluon matching coefficient is

$$\mathcal{I}_{gj}^{(1)}(t^{\text{cut}}, z, R, \mu_B) = \int_0^{t^{\text{cut}}} \mathrm{d}t\, \mathcal{I}_{gj}^{(1)}(t, z, \mu_B)\,, \tag{4.139}$$

which is given in App. A.2. We stress that this only holds for the one-loop fixed-order contributions. The resummed beam function in Eq. (4.127) is different from integrating the resummed differential t-dependent beam function already at NLL due to the different renormalization structure. At two loops (and beyond) an explicitly R-dependent jet clustering correction term must be added to the integrated bare t-dependent beam functions [83, 84] to obtain the correct bare results for the $\mathcal{T}_{B,C}^{\text{jet}}$-type observables. Since these R-dependent jet clustering corrections affect the UV divergences, the two-loop anomalous dimension of the beam function as well as its NNLL evolution explicitly depend on R. We will compute the R-dependent correction to the 2-loop anomalous dimension in chapter 5.

Similarly, the one-loop soft function for $\mathcal{T}_B^{\text{jet}} < \mathcal{T}^{\text{cut}}$ can be obtained by integrating the one-loop soft function differential in beam thrust [23], see App. A.3.1. The one-loop soft function for $\mathcal{T}_C^{\text{jet}} < \mathcal{T}^{\text{cut}}$ is explicitly calculated in App. A.3.2. (It is directly related to the integrated one-loop soft function for the C-parameter event shape in e^+e^- collisions.)

For the RG evolution at NLL, we require the cusp anomalous dimension to two loops [85], and the noncusp anomalous dimensions to one loop. The one-loop coefficients of the noncusp anomalous dimensions in Eq. (4.125) are the same as for the corresponding beam thrust results [23]. To see this, note that at $\mathrm{O}(\alpha_s)$

$$\gamma_B^{g(1)} = -\mu \frac{\mathrm{d}}{\mathrm{d}\mu} Z_B^{g(1)}\,, \quad \gamma_S^{g(1)} = -\mu \frac{\mathrm{d}}{\mathrm{d}\mu} Z_S^{g(1)}\,, \tag{4.140}$$

and the one-loop $\overline{\text{MS}}$ counterterms, $Z_i^{g(1)}$, for $\mathcal{T}_{B,C}^{\text{jet}} < \mathcal{T}^{\text{cut}}$ and inclusive beam thrust are also simply related by integration.

4.9 NLO Nonsingular with subtraction method

In the previous section we have discussed the ingredients for the resummed part of the $\mathcal{T}_f^{\text{jet}}$-veto cross section to NLL′ order. To incorporate the full $\mathrm{O}(\alpha_s)$ corrections of the fixed-order (FO) cross section at NLO, we must add the $\mathrm{O}(\alpha_s)$ nonsingular contribution in Eq. (4.13), which is particularly relevant for large $\mathcal{T}^{\text{cut}}$. The FO nonsingular contribution differential in $\mathcal{T}_f^{\text{jet}}$ is defined by the difference of the differential FO result in full QCD and the corresponding FO singular contribution,

$$\frac{\mathrm{d}\sigma_0^{\text{nons}}}{\mathrm{d}\mathcal{T}_f^{\text{jet}}\mathrm{d}Y} = \frac{\mathrm{d}\sigma_0^{\text{FO}}}{\mathrm{d}\mathcal{T}_f^{\text{jet}}\mathrm{d}Y} - \frac{\mathrm{d}\sigma_0^{\text{sing}}}{\mathrm{d}\mathcal{T}_f^{\text{jet}}\mathrm{d}Y}\,. \tag{4.141}$$

The FO singular terms in turn are given by a strict expansion of the resummed part of the cross section to a given fixed order in $\alpha_s(\mu_{\text{FO}})$, where $\mu_{\text{FO}} \equiv \mu_r = \mu_f \sim m_H$

is the renormalization and factorization scale of the FO cross section. Suppressing the dependence on $\mathcal{T}_f^{\text{jet}}$ and Y, we thus have

$$\mathrm{d}\sigma_0^{\text{sing}}(\mu_{\text{FO}}) \equiv \mathrm{d}\sigma_0^{\text{resum}}(\mu_H, \mu_B, \mu_S)\Big|_{\text{FO in } \alpha_s(\mu_{\text{FO}})} = \mathrm{d}\sigma_0^{\text{resum}}(\mu_H = \mu_B = \mu_S = \mu_{\text{FO}})\,. \tag{4.142}$$

A priori, Eq. (4.142) is only true up to higher orders in $\alpha_s(\mu_{\text{FO}})$. However, we always reexpand the product of fixed-order contributions to the hard, beam, and soft functions entering in $\mathrm{d}\sigma_0^{\text{resum}}$ in Eqs. (4.136) and (4.137), such that Eq. (4.142) holds exactly. For the NLO singular this means that

$$\begin{aligned}\mathrm{d}\sigma_0^{\text{resum}} \propto\; & H^{(0)} B_a^{(0)} B_b^{(0)} S^{(0)} + H^{(1)} B_a^{(0)} B_b^{(0)} S^{(0)} + H^{(0)} B_a^{(1)} B_b^{(0)} S^{(0)} + H^{(0)} B_a^{(0)} B_b^{(1)} S^{(0)} \\ & + H^{(0)} B_a^{(0)} B_b^{(0)} S^{(1)}\,,\end{aligned} \tag{4.143}$$

where the superscripts (0) and (1) indicate the LO and NLO fixed-order contributions to $H(\mu_H)$, $B(\mu_B)$, and $S(\mu_S)$, respectively. In this way we ensure that when turning off the resummation in the NLL′ result by setting $\mu_H = \mu_B = \mu_S = \mu_{\text{FO}}$, we exactly reproduce the NLO singular cross section. The resummed result differential in $\mathcal{T}_f^{\text{jet}}$ and evaluated at μ_{FO} can be obtained by taking the derivative of the resummed cumulant cross sections in Eqs. (4.136) and (4.137) with respect to $\mathcal{T}^{\text{cut}}$.

We can get the non-singular corrections to the full differential cross section by performing subtractions at NLO, i.e. subtracting the right singular contributions from the full cross section to obtain finite correction. The singular terms in the $\mathcal{T}^{\text{jet}}$ spectrum are proportional to $\delta(\mathcal{T}^{\text{jet}})$ and $\ln \mathcal{T}^{\text{jet}}/\mathcal{T}^{\text{jet}}$ for $\mathcal{T}^{\text{jet}} \to 0$. Once the non-singular contribution is defined as

$$\frac{\mathrm{d}\sigma_0^{\text{nons}}}{\mathrm{d}\mathcal{T}_f^{\text{jet}}\mathrm{d}Y}(\mu_{\text{FO}}) = \frac{\mathrm{d}\sigma_0^{\text{FO}}}{\mathrm{d}\mathcal{T}_f^{\text{jet}}\mathrm{d}Y}(\mu_{\text{FO}}) - \frac{\mathrm{d}\sigma_0^{\text{resum}}}{\mathrm{d}\mathcal{T}_f^{\text{jet}}\mathrm{d}Y}(\mu_H = \mu_B = \mu_S = \mu_{\text{FO}})\,, \tag{4.144}$$

we can integrate this subtraction from $\mathcal{T}_\delta$ upto some $\mathcal{T}^{\text{cut}}$ to obtain the cumulant as follows

$$\frac{\mathrm{d}\sigma_0^{\text{nonsing}}}{dY}(\mathcal{T}^{\text{cut}}) = \int_{\mathcal{T}_\delta}^{\mathcal{T}^{\text{cut}}} \frac{\mathrm{d}\sigma_0^{\text{nons}}}{\mathrm{d}\mathcal{T}_f^{\text{jet}}\mathrm{d}Y}(\mu_{\text{FO}}) \tag{4.145}$$

where $\mathcal{T}_\delta \sim 0.01$. The differential fixed-order cross section $\mathrm{d}\sigma_0^{\text{FO}}/\mathrm{d}\mathcal{T}_f^{\text{jet}}\mathrm{d}Y$ is computed for the four observables in Eq. (4.44), Eq. (B.16), Eq. (B.8) and Eq. (B.22). The integral is cut off by $\mathcal{T}_\delta$, since the integrand is given by the difference of two diverging integrands and this cut-off is the error we make in determining the nonsingular. The numerical integral of the subtraction only encounters an integrable singularity for $\mathcal{T}^{\text{cut}} \to 0$. To check that the subtraction works, and the nonsingular does not contain any $1/\mathcal{T}^{\text{jet}}$ we plot $d\sigma^{\text{nonsing}}/d\ln\mathcal{T}^{\text{jet}} = \mathcal{T}^{\text{jet}} d\sigma^{\text{nonsing}}/d\mathcal{T}^{\text{jet}}$ which goes to 0 for $\mathcal{T}^{\text{cut}} \to 0$ in Fig. 4.9 as expected. Fig. 4.9 shows that for small values of $\mathcal{T}^{\text{cut}}$, the singular contribution dominates

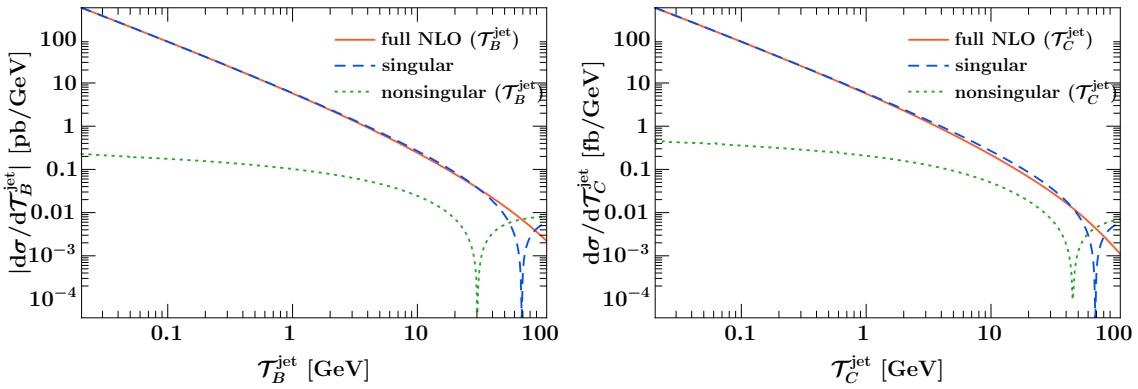

Figure 4.9: *The absolute value of the full, singular and nonsingular constributions to the $\mathcal{T}_B^{\rm jet}$ and $\mathcal{T}_C^{\rm jet}$ spectrum for H+0-jet.*

the full cross section, while at larger $\mathcal{T}^{\rm cut}$ the non-singular corrections become significant. These non-singular terms must be added to the resummed cumulant in each bin of $\mathcal{T}^{\rm cut}$ to get the right inclusive cross section for $\mathcal{T}^{\rm cut} \to \infty$. This type of subtraction has been recently generalized to full NNLO in [86].

The resummed contribution is evolved to an imaginary hard scale, which avoids large corrections in the hard function when evaluated at a timelike argument $q^2 = m_H^2$ [87–90]. For consistency, we have to include the same evolution also in the nonsingular contributions [23, 25], which at NLO simply amounts to multiplying it by the hard evolution factor. The final NLO nonsingular contribution is then given by

$$\frac{\mathrm{d}\sigma_0^{\rm nons}}{\mathrm{d}Y}(\mathcal{T}_f^{\rm jet} < \mathcal{T}^{\rm cut}) = \frac{H_{gg}^{(0)}(-i\mu_{ns})}{H_{gg}^{(0)}(\mu_{\rm ns})} U_H(-i\mu_{ns}, \mu_{ns}) \times \frac{\mathrm{d}\sigma_0^{\rm nons(1)}}{\mathrm{d}Y}(\mathcal{T}_f^{\rm jet} < \mathcal{T}^{\rm cut}, \mu_{ns})\,, \tag{4.146}$$

where we introduced $\mu_{\rm ns}$ to denote the scale at which the nonsingular contributions are evaluated. Combined with the resummed contribution according to Eq. (4.13), this yields the complete cross section for a $\mathcal{T}_f^{\rm jet}$ veto at NLL′+NLO. We have also compared our inclusive NLO cross section for $\mathcal{T}^{\rm cut} \to \infty$ with MCFM and found agreement for all the four observables.

4.10 Scale choices

In this section, we will discuss how to choose appropriate beam and soft scales as a function of $\mathcal{T}^{\rm cut}$. For this purpose, we have to compare the relative size of the singular and nonsingular contributions in relation to the full FO cross section in different regions of $\mathcal{T}_f^{\rm jet}$. For this comparison, we integrate over the full Y-range. The two plots in the first row of

Fig. 4.10 show the magnitude of the differential singular, nonsingular, and full FO cross sections for $\mathcal{T}_{B(\mathrm{cm})}^{\mathrm{jet}}$ and $\mathcal{T}_{C(\mathrm{cm})}^{\mathrm{jet}}$. The curves for $\mathcal{T}_{B\mathrm{cm}}^{\mathrm{jet}}$, $\mathcal{T}_{C\mathrm{cm}}^{\mathrm{jet}}$ are displayed in light colors and for $\mathcal{T}_{B}^{\mathrm{jet}}$, $\mathcal{T}_{C}^{\mathrm{jet}}$ in darker colors. In the second row of Fig. 4.10, we plot the magnitude of the ratio of the singular and nonsingular contributions to the full NLO cross section for both $\mathcal{T}_{B}^{\mathrm{jet}}$ and $\mathcal{T}_{C}^{\mathrm{jet}}$.

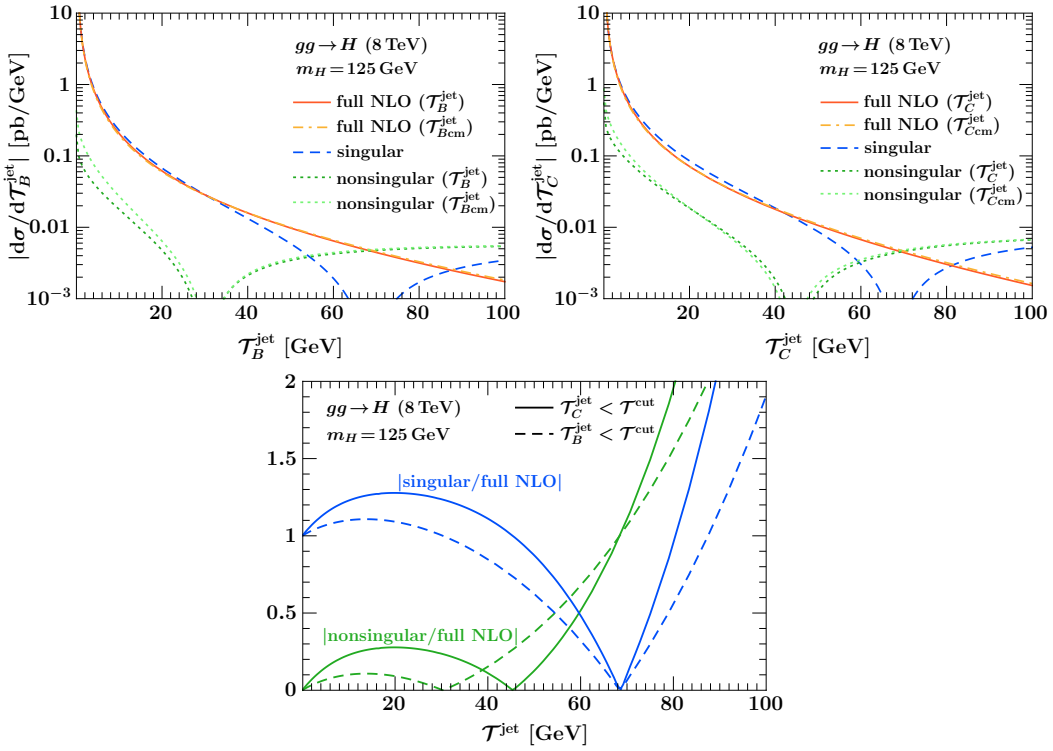

Figure 4.10: *Comparison of the singular, nonsingular, and full NLO cross sections differential in $\mathcal{T}_f^{\mathrm{jet}}$ and integrated over all of Y. The two plots in the first row show the magnitude of the differential cross sections for $\mathcal{T}_B^{\mathrm{jet}}$ and $\mathcal{T}_C^{\mathrm{jet}}$ on a logarithmic scale. The plot in the second row shows the ratios of nonsingular and singular contributions to the full NLO cross section for both $\mathcal{T}_B^{\mathrm{jet}}$ and $\mathcal{T}_C^{\mathrm{jet}}$.*

Note that the singular differential contribution is identical for all four $\mathcal{T}_f^{\mathrm{jet}}$ variables, because the difference between $\mathcal{T}_{B(\mathrm{cm})}^{\mathrm{jet}}$ and $\mathcal{T}_{C(\mathrm{cm})}^{\mathrm{jet}}$ only appears as a constant ($\mathcal{T}_f^{\mathrm{jet}}$-independent) term in the soft function and does not affect the singular spectrum. Also the (explicit) total Y dependence resides in the $\mathcal{T}^{\mathrm{cut}}$-independent part of the NLO singular contribution of the $\mathcal{T}_{B\mathrm{cm}}^{\mathrm{jet}}$ and $\mathcal{T}_{C\mathrm{cm}}^{\mathrm{jet}}$ vetoed cross section and drops out in the spectrum [which can be seen from Eq. (4.137) together with Eqs. (A.8) and (A.9)]. The full FO cross section, however, depends on the specific measurement function and is different for all four observables. We therefore observe significant differences when comparing the nonsingular contributions for $\mathcal{T}_B^{\mathrm{jet}}$ and $\mathcal{T}_C^{\mathrm{jet}}$ in Fig. 4.10. The nonsingular contributions for $\mathcal{T}_{B\mathrm{cm}}^{\mathrm{jet}}$ and $\mathcal{T}_{C\mathrm{cm}}^{\mathrm{jet}}$ (light green dotted lines) are slightly larger than the corresponding ones for $\mathcal{T}_B^{\mathrm{jet}}$ and $\mathcal{T}_C^{\mathrm{jet}}$. This is due to Y-dependent terms that are not captured by the resummed singular contributions and are thus part of the nonsingular contributions in Eq. (4.144).

The plots show that the nonsingular contributions are power suppressed for small values of $\mathcal{T}_f^{\text{jet}}$, become comparable to the singular contributions around $\mathcal{T}_f^{\text{jet}} \sim 60\,\text{GeV}$, and exceed the FO cross section beyond $\mathcal{T}_f^{\text{jet}} \gtrsim 70\,\text{GeV}$. Based on these observations, we can distinguish three different regions according to the relative size of the singular and nonsingular contribution to the full FO cross section at increasing $\mathcal{T}_f^{\text{jet}}$: resummation, transition, and fixed-order regions. (In principle, there is a fourth nonperturbative regime $\mathcal{T}_f^{\text{jet}} \lesssim \Lambda_{\text{QCD}}$, which is however not relevant for our discussion.)

In the resummation region, i.e. at low values $\mathcal{T}_f^{\text{jet}} \ll m_H$, the singular contribution dominates and must be resummed while the nonsingular contributions are power corrections suppressed by $\mathcal{T}_f^{\text{jet}}/m_H$. To correctly resum the large logarithms in this region, the scales should follow their canonical relations as dictated by the factorization of the jet-vetoed cross section,

$$\mu_H = -im_H\,, \quad \mu_B = \sqrt{m_H \mu_S}\,, \quad \mu_S = \mathcal{T}^{\text{cut}}\,. \tag{4.147}$$

At large values of $\mathcal{T}^{\text{cut}} \gtrsim m_H/2$, the singular and nonsingular contributions are equally important and there are large cancellations between the two, which would be spoiled if the resummation is kept on. Hence, in this region the resummation must be turned off, which is achieved by letting all scales approach a common FO scale,

$$|\mu_H| = \mu_B = \mu_S = \mu_{ns} = \mu_{\text{FO}}\,, \tag{4.148}$$

which then ensures that the result correctly reproduces the total cross section [cf. Eqs. (4.144) and (4.146)]. By keeping the hard scale at an imaginary value, this becomes the π^2-improved FO cross section, which exhibits an improved perturbative convergence.

In the transition between the resummation and fixed-order regions, both the resummed logarithmic corrections as well as the nonsingular FO contributions are numerically important. To optimally describe this region, which is often also the experimentally most relevant one, we employ profile scales [91,92] that incorporate the constraints in Eq. (4.147), towards small values of $\mathcal{T}_f^{\text{jet}}$ and provide a smooth interpolation to μ_{FO} at large values of $\mathcal{T}_f^{\text{jet}}$. For our choice of profile scales and the related estimation of perturbative uncertainties we adapt the discussion of the p_T^{jet}-veto in [25] to our present case, where we have virtuality-like (SCET-I) as opposed to p_T-like (SCET-II) scale relations.

For the central profiles we take

$$\begin{aligned} \mu_H &= -i\mu_{\text{FO}} \quad , \quad \mu_{ns} = \mu_{\text{FO}} \\ \mu_S(\mathcal{T}^{\text{cut}}) &= \mu_{\text{FO}} f_{\text{run}}(\mathcal{T}^{\text{cut}}/m_H)\,, \\ \mu_B(\mathcal{T}^{\text{cut}}) &= \sqrt{\mu_S(\mathcal{T}^{\text{cut}})\mu_{\text{FO}}} = \mu_{\text{FO}}\sqrt{f_{\text{run}}(\mathcal{T}^{\text{cut}}/m_H)}\,, \,, \end{aligned} \tag{4.149}$$

where the common profile function $f_{\rm run}(x)$ is as in [25],

$$f_{\rm run}(x) = \begin{cases} x_0\big[1+(x/x_0)^2/4\big] & x \le 2x_0\,, \\ x & 2x_0 \le x \le x_1\,, \\ x + \frac{(2-x_2-x_3)(x-x_1)^2}{2(x_2-x_1)(x_3-x_1)} & x_1 \le x \le x_2\,, \\ 1 - \frac{(2-x_1-x_2)(x-x_3)^2}{2(x_3-x_1)(x_3-x_2)} & x_2 \le x \le x_3\,, \\ 1 & x_3 \le x\,. \end{cases} \tag{4.150}$$

The first regime in Eq. (4.150) for $x \le 2x_0$ is the nonperturbative regime, where we let the scales μ_B and μ_S approach fixed values $\sqrt{x_0}\mu_{\rm FO} > \Lambda_{\rm QCD}$ and $x_0\mu_{\rm FO} > \Lambda_{\rm QCD}$ respectively as $x \to 0$. For $x \sim \Lambda_{\rm QCD}/m_H$, corresponding to $\mathcal{T}_f^{\rm jet} \sim \Lambda_{\rm QCD}$, our purely perturbative predictions are insufficient to correctly describe the cross sections, since here nonperturbative corrections can become of O(1). In practice, this region is irrelevant and has no effect on the cumulant jet-vetoed cross sections that we are interested in.

The second line in Eq. (4.150) corresponds to the resummation region and yields the canonical scaling in Eq. (4.147). The third and fourth lines describe the transition region. They provide a quadratic scaling for a smooth transition to the FO region (last line), where all the scales are equal and the resummation is turned off.

To fix the profile parameters x_i in Eq. (4.150) we first choose a value for x_3, where the resummation is turned off completely. This should happen roughly after the point, where the singular spectrum vanishes (the singular cumulant has a maximum) so the nonsingular spectrum is equal to the full result. In addition, it should certainly happen before the point, where the singular spectrum has the same magnitude but opposite sign as the full and the nonsingular becomes twice the size of the full result, since at this point there is clearly an O(1) cancellation between singular and nonsingular. Hence, for $\mathcal{T}_B^{\rm jet}$ we choose $x_3 = 0.6$ corresponding to $\mathcal{T}_B^{\rm jet} = 75\,\text{GeV}$. For $\mathcal{T}_C^{\rm jet}$ we choose $x_3 = 0.55$, since here the singular-nonsingular cancellations set in a bit earlier. For $x = \mathcal{T}_f^{\rm jet}/m_H \lesssim 0.1$ the physical scales are separated by an order of magnitude (and the nonsingular are suppressed by an order of magnitude). Hence, a natural choice for x_1 is of O(0.1). We use $x_1 = 0.15$ for $\mathcal{T}_B^{\rm jet}$ and $x_1 = 0.1$ for $\mathcal{T}_C^{\rm jet}$, which ensures that the size of the transition region, $x_3 - x_1$, is the same for both and also long enough for the scales to smoothly transit to the FO region. The midpoint of the transition region, x_2, is then fixed by setting $x_2 = (x_3 - x_1)/2$. Note that although the strict canonical scaling stops at x_1, the resummation is still important all the way through the transition region, at least until x_2, and starts to get turned off beyond. To summarize, our central profile parameters for $\mathcal{T}_{B(\rm cm)}^{\rm jet}$ are

$$\begin{aligned} \mu_{\rm FO} &= m_H\,, \qquad x_0 = 2.5\,\text{GeV}/\mu_{\rm FO}\,, \\ \{x_1, x_2, x_3\} &= \{0.15, 0.375, 0.6\}\,, \end{aligned} \tag{4.151}$$

and for $\mathcal{T}^{\text{jet}}_{C(\text{cm})}$ they are

$$\begin{aligned} \mu_{\text{FO}} &= m_H\,, \qquad x_0 = 2.5\,\text{GeV}/\mu_{\text{FO}}\,, \\ \{x_1, x_2, x_3\} &= \{0.1, 0.325, 0.55\}\,. \end{aligned} \tag{4.152}$$

The resulting central profiles for μ_B and μ_S are shown in the first row of Fig. 4.11 by the green and orange solid lines.

4.10.1 Fixed-order and resummation uncertainties

A key aspect of precision cross section predictions is to reliably estimate the perturbative uncertainties. A convenient and physically motivated way to parametrize the theoretical uncertainties in jet-vetoed cross sections is in terms of fully correlated (yield) and fully anticorrelated (migration) components [11,23,25,41], as we have already discussed in Sec. 3.2. We will apply the same procedure here.

First, the resummation uncertainty Δ_{resum} corresponds to the intrinsic uncertainty in the resummed logarithmic series induced by the jet veto (or jet binning) cut. It must be anticorrelated between the cross section that survives the jet veto (the 0-jet bin) and the cross section that is vetoed (the $\geq$ 1-jet bin), such that it cancels in the total inclusive cross section given by their sum. Hence, we can identify Δ_{resum} with the migration uncertainty. Second, the fixed-order uncertainty, Δ_{FO}, comes from scale variations in the FO contributions of the full resummed cross section, such that for large $\mathcal{T}^{\text{cut}}$ it reproduces the FO scale variation uncertainty of the total cross section. It is identified with the yield uncertainty, and effectively probes the size of higher-order nonlogarithmic terms at any value of $\mathcal{T}^{\text{cut}}$. Note that despite its naming, at small $\mathcal{T}^{\text{cut}}$ it does so *within* the resummed prediction. The total uncertainty in the Higgs+0-jet cross section is then given by

$$\Delta_0^2(\mathcal{T}^{\text{cut}}) = \Delta^2_{\text{FO}}(\mathcal{T}^{\text{cut}}) + \Delta^2_{\text{resum}}(\mathcal{T}^{\text{cut}})\,. \tag{4.153}$$

To evaluate Δ_{FO}, we take the collective variation of all scales μ_i up and down by a factor of 2, as shown in the second row of Fig. 4.11. This is done by setting $\mu_{\text{FO}} = \{2m_H, m_H/2\}$ in Eq. (4.149). At large $\mathcal{T}^{\text{cut}}$ values, this yields the standard scale variation of the (π^2-improved) FO cross section. By varying μ_{FO}, all the ratios between the scales μ_H, μ_B, and μ_S are kept fixed, so that the arguments of the logarithms that are resummed in the evolution factors U_i remain unchanged. We stress that the scales do not represent physical input quantities. Rather, the changes observed in the cross section resulting from the scale variations are simply an indicator of the possible size of higher-order corrections.

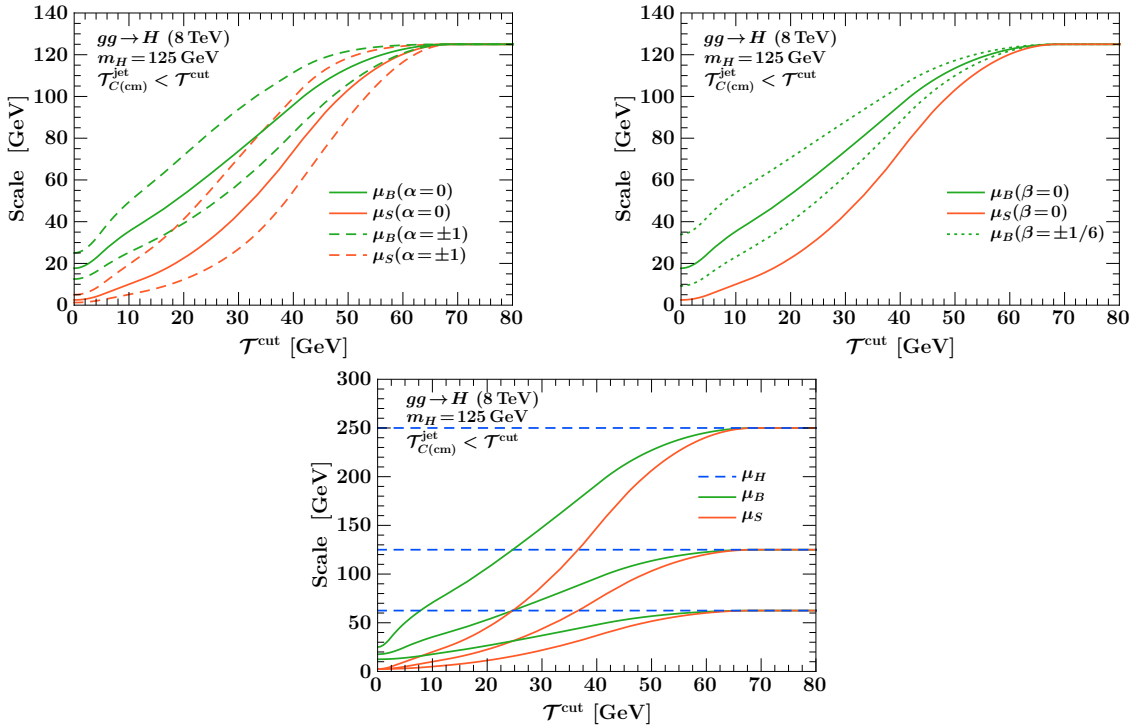

Figure 4.11: *Profile scale variations as described in the text. The two plots in the first line show the variations of the beam and soft scales used to estimate the resummation uncertainty. The plot in the second row shows the collective variation of all scales by a factor of two, which is used to estimate the FO uncertainty.*

In particular, one should not attribute any meaning to possibly asymmetric up/down variations in the cross section. Instead, we take the maximal observed deviation from the central value as our perturbative uncertainty estimate. Thus, we adopt

$$\Delta_{\text{FO}}(\mathcal{T}^{\text{cut}}) = \max_{v \in V_{\text{FO}}} |\sigma_0^v(\mathcal{T}^{\text{cut}}) - \sigma_0^{\text{central}}(\mathcal{T}^{\text{cut}})| \tag{4.154}$$

for the FO uncertainty in Eq. (4.153), where V_{FO} denotes the variations $\mu_{\text{FO}} = \{2m_H, m_H/2\}$.

Next, to estimate the resummation uncertainty, Δ_{resum}, we vary the profile scales for μ_B and μ_S defined in the previous section about their central profile while keeping $|\mu_H| = \mu_{\text{FO}} = m_H$ fixed. The aim is to vary the logarithms in the resummation factors U_i, in order to estimate the potential size of higher-order corrections in the resummed logarithmic series. At the same time, the scales must retain the natural scale hierarchy in the resummation region (as obeyed by the central scales),

$$\mu_{\text{FO}} \sim \mu_H \gg \mu_B \sim \sqrt{\mu_H \mu_S} \gg \mu_S \,, \tag{4.155}$$

for all variations.

First, we define a multiplicative factor

$$f_{\rm vary}(x) = \begin{cases} 2(1-x^2/x_3^2) & 0 \le x \le x_3/2 \\ 1+2(1-x/x_3)^2 & x_3/2 \le x \le x_3 \\ 1 & x_3 \le x \end{cases}, \tag{4.156}$$

which approaches 2 for $\mathcal{T}^{\rm cut} \to 0$ and 1 for $\mathcal{T}^{\rm cut} \to x_3 m_H$, where the resummation is turned off. The up and down variations of μ_S are then parametrized as

$$\mu_S^{\rm vary}(x,\alpha) = f_{\rm vary}^{\alpha}(x)\,\mu_S(x) = \mu_{\rm FO}\, f_{\rm vary}^{\alpha}(x)\, f_{\rm run}(x)\,. \tag{4.157}$$

For the μ_B variations we define

$$\mu_B^{\rm vary}(x,\alpha,\beta) = \mu_S^{\rm vary}(x,\alpha)^{1/2-\beta}\mu_{\rm FO}^{1/2+\beta} = \mu_{\rm FO}\big[f_{\rm vary}^{\alpha}(x)\, f_{\rm run}(x)\big]^{1/2-\beta}, \tag{4.158}$$

where the parameter β modifies the exact canonical relation of the beam and soft scales in Eq. (4.147), to allow for a variation of μ_B independent of μ_S. The central scales in Eq. (4.149) correspond to setting $\alpha = \beta = 0$. The μ_B and μ_S variations we will perform are illustrated in the first row of Fig. 4.11, and are discussed in detail in the following. Note that all μ_B and μ_S variations turn off at large $\mathcal{T}^{\rm cut}$ (beyond x_3), such that the resummation uncertainty vanishes by construction when the resummation itself is turned off.

The arguments of the logarithms resummed in the overall evolution factor, Eq. (4.138), are given by the ratios of the three scales μ_H, μ_B, and μ_S. Because of cancellations due to RG consistency the two relevant independent scale ratios entering the resummed logarithms are

$$\frac{\mu_B^2}{\mu_H^2} \sim \frac{\mathcal{T}^{\rm cut}}{m_H}\,, \qquad \frac{\mu_S^2}{\mu_B^2} \sim \frac{\mathcal{T}^{\rm cut}}{m_H}\,. \tag{4.159}$$

This can be seen best by setting the arbitrary common renormalization scale $\mu = \mu_B$, such that $U_B = 1$ and we are left with only two independent evolution factors U_H and U_S, which resum logarithms of the scale ratios in Eq. (4.159). (The third possible scale ratio $\mu_S/\mu_H \sim \mathcal{T}^{\rm cut}/m_H$ is not independent as it can never appear alone in the evolution.)

We use the same α for both μ_B and μ_S, which ensures that we never violate the parametric scaling $\mu_B^2 \sim \mu_S\mu_H$ when changing μ_S. Varying α while keeping β fixed in this setup then induces equal changes to the logarithms of the scale ratios in Eq. (4.159) of the form

$$\begin{aligned} \ln\frac{\mu_B^2}{\mu_H^2} &\to \ln f_{\rm vary}^{\alpha} + \ln\frac{\mu_B^2}{\mu_H^2}\,, \\ \ln\frac{\mu_S^2}{\mu_B^2} &\to \ln f_{\rm vary}^{\alpha} + \ln\frac{\mu_S^2}{\mu_B^2}\,. \end{aligned} \tag{4.160}$$

On the other hand, varying β with α fixed induces changes in the logarithms of equal magnitude but opposite sign,

$$\begin{aligned} \ln \frac{\mu_B^2}{\mu_H^2} &\to (1-2\beta) \ln \frac{\mu_B^2}{\mu_H^2} \,, \\ \ln \frac{\mu_S^2}{\mu_B^2} &\to (1+2\beta) \ln \frac{\mu_S^2}{\mu_B^2} \,. \end{aligned} \tag{4.161}$$

Hence, separate variations of α and β independently probe the resummation of both types of logarithms. (Changing them together, would effectively double-count the variation for one or the other set of logarithms.)

The precise range of α and β values is to some extent arbitrary. For our analysis of the resummation uncertainty Δ_{resum} we choose the four parameter sets

$$(\alpha, \beta) = \{(+1, 0),\, (-1, 0),\, (0, -1/6),\, (0, +1/6)\} \,, \tag{4.162}$$

which fulfill the requirements in Eq. (4.155). The α variation is shown by the dashed curves in the first plot of Fig. 4.11. It yields the typical factor of 2 variation in the soft scale for $\mathcal{T}^{\text{cut}} \to 0$, and a corresponding factor $\sqrt{2}$ in μ_B. The β variation modifies the canonical relation between μ_B and μ_S "half-way" from $\mu_B^2 = \mu_S^{1/3} \mu_H^{2/3}$ to $\mu_B^2 = \mu_S^{2/3} \mu_H^{1/3}$, and is shown by the dotted lines in the right plot of Fig. 4.11. For most of the relevant $\mathcal{T}^{\text{cut}}$ range, all four variations have an effect of similar size on the scale ratios in Eq. (4.159). For $\mathcal{T}^{\text{cut}} \to 0$, the β variation generates roughly a factor of 2 variation in μ_B, while keeping μ_S fixed. (Since for small $\mathcal{T}^{\text{cut}}$ the scales μ_H, μ_B, and μ_S are widely separated, this still maintains the required scale hierarchy.)

We then define the overall resummation uncertainty as the maximum absolute deviation from the cross section evaluated with central profiles when performing the μ_B and μ_S profile scale variations,

$$\Delta_{\text{resum}}(\mathcal{T}^{\text{cut}}) = \max_{v \in V_{\text{resum}}} |\sigma_0^v(\mathcal{T}^{\text{cut}}) - \sigma_0^{\text{central}}(\mathcal{T}^{\text{cut}})| \,, \tag{4.163}$$

where V_{resum} denotes the set of four variations in Eq. (4.162). This resummation uncertainty together with the fixed-order uncertainty in Eq. (4.154) then determines the total uncertainty of the 0-jet cross section as given in Eq. (4.153).

Finally, we should mention that in principle one should also vary the other profile parameters x_0 and $\{x_1, x_2, x_3\}$ in Eqs. (4.151) and (4.152). However, at the NLL′+NLO order we are working, the resulting cross section variations are much smaller than those from varying μ_{FO}, α, β. This could change at higher orders, at which point these additional profile parameter variations should be included.

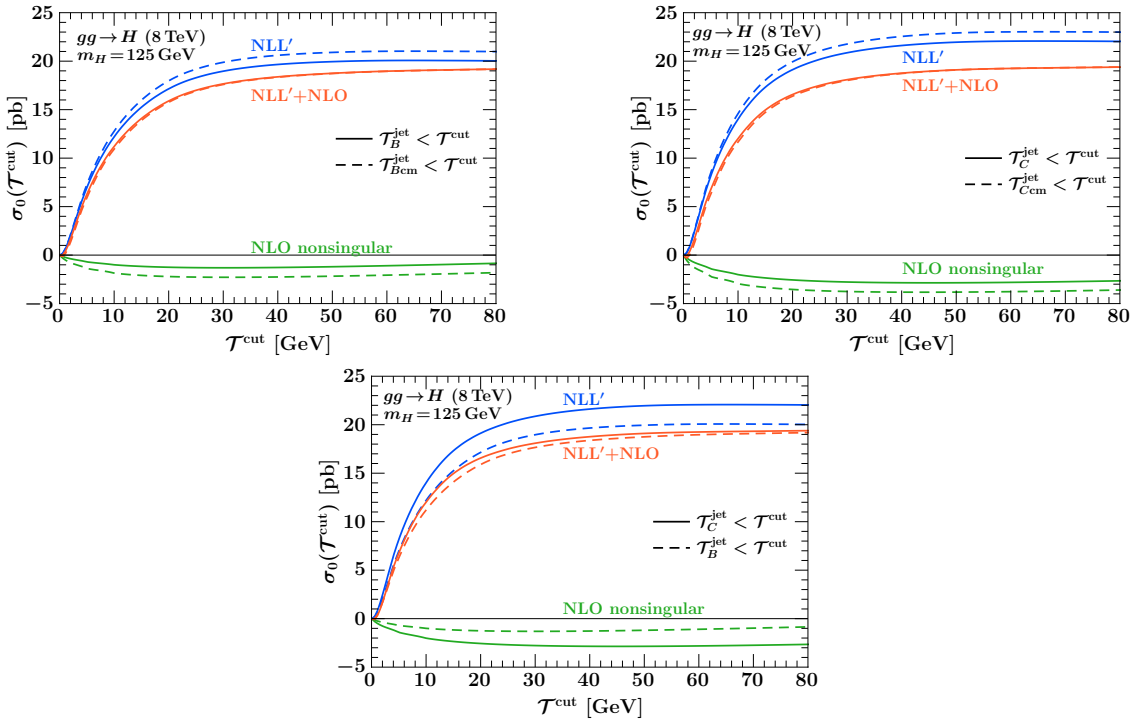

Figure 4.12: *Cumulant NLL′ resummed and NLO nonsingular cross sections as a function of $\mathcal{T}^{\text{cut}}$. The two plots in the first row show the comparison between the two variants of $\mathcal{T}_B$-type and $\mathcal{T}_C$-type veto cross sections, respectively. The last plot shows the comparison between the corresponding contributions to $\mathcal{T}_C$ and $\mathcal{T}_B$-veto cross sections. The resummation/FO scales in the cross sections displayed here are given by the central profiles.*

4.11 Results

In this section, we present numerical results for the Higgs+0-jet gluon-fusion cross sections, $\sigma_0(\mathcal{T}_f^{\text{jet}} < \mathcal{T}^{\text{cut}})$, using the four rapidity-weighted observables $\mathcal{T}_f^{\text{jet}} = \mathcal{T}_B^{\text{jet}}, \mathcal{T}_{B\text{cm}}^{\text{jet}}, \mathcal{T}_C^{\text{jet}}, \mathcal{T}_{C\text{cm}}^{\text{jet}}$ for the jet veto. For all our cross section predictions we employ the MSTW 2008 PDFs [93] together with their corresponding default value of $\alpha_s(m_Z)$. We use LO PDFs at NLL and NLO PDFs at NLL′+NLO, such that the PDF order agrees with the perturbative order of the FO cross section components. For all our results, we set $m_H = 125\,\text{GeV}$ and $E_{\text{cm}} = 8\,\text{TeV}$, except for the comparison of the $\mathcal{T}_C^{\text{jet}}$-binned cross section to the ATLAS data, where we use $m_H = 125.4\,\text{GeV}$ as in the measurement.

We first display the resummed NLL′ and nonsingular NLO contributions separately and the full NLL′+NLO results given by their sum for the jet-vetoed (cumulant) cross sections as a function of $\mathcal{T}^{\text{cut}}$ in Fig. 4.12. In the first row we compare the two observables of $\mathcal{T}_{B,C}^{\text{jet}}$ type, respectively. In the second row of Fig. 4.12 we compare the same results for $\mathcal{T}_B^{\text{jet}}$ and $\mathcal{T}_C^{\text{jet}}$ with each other.

The NLL′ resummed contribution to the $\mathcal{T}_{B\mathrm{cm}}^{\mathrm{jet}}$ cumulant cross section (blue dashed curve) is larger than the one to the $\mathcal{T}_{B}^{\mathrm{jet}}$ veto cross section (blue solid curve). This is due to the additional Y-dependent terms present in the factorization formula for $\mathcal{T}_{B\mathrm{cm}}^{\mathrm{jet}}$ in Eq. (4.137) (which with the resummation switched on also depend on $\mathcal{T}^{\mathrm{cut}}$). As a consequence, the nonsingular contribution to the $\mathcal{T}_{B\mathrm{cm}}^{\mathrm{jet}}$ cumulant (green dashed curve) is slightly more negative than the one for $\mathcal{T}_{B}^{\mathrm{jet}}$ (green solid curve), so that the sum of resummed and nonsingular contributions for each observable reproduces the same total cross section for $\mathcal{T}^{\mathrm{cut}} \to \infty$. This can be seen directly from the combined NLL′+NLO cross section in solid and dashed dark orange curves that approach the same constant value for large $\mathcal{T}^{\mathrm{cut}}$. For $\mathcal{T}^{\mathrm{cut}} \to 0$ on the other hand the Sudakov resummation forces the NLL′+NLO cross section to vanish. Note that for the cross sections integrated over the full Y range shown in Fig. 4.12 the difference between the resummed NLL′+NLO predictions with a $\mathcal{T}_{B\mathrm{cm}}^{\mathrm{jet}}$ and a $\mathcal{T}_{B}^{\mathrm{jet}}$ veto is hardly visible. The same discussion holds for the comparison between $\mathcal{T}_{C\mathrm{cm}}^{\mathrm{jet}}$ and $\mathcal{T}_{C}^{\mathrm{jet}}$ shown in the second plot of Fig. 4.12.

In the second row of Fig. 4.12, we see that the NLL′+NLO cross section for $\mathcal{T}_{C}^{\mathrm{jet}} < \mathcal{T}^{\mathrm{cut}}$ is larger and approaches the total cross section sooner than the one for $\mathcal{T}_{B}^{\mathrm{jet}} < \mathcal{T}^{\mathrm{cut}}$. This difference in the shape of the cumulants arises due to the larger constant term in the NLO soft function S_{gg}^{C} than in S_{gg}^{B} [cf. Eqs. (A.14) and (A.20)], which enters as part of the resummed NLL′ contribution to the cross section, Eq. (4.136). Since the total cross section at large $\mathcal{T}^{\mathrm{cut}}$ has to be the same for both observables, the larger singular contribution for $\mathcal{T}_{C}^{\mathrm{jet}}$ must eventually be compensated for by its nonsingular contribution when integrated over a large enough range of $\mathcal{T}_{C}^{\mathrm{jet}} < \mathcal{T}^{\mathrm{cut}}$, which is indeed more negative than for $\mathcal{T}_{B}^{\mathrm{jet}} < \mathcal{T}^{\mathrm{cut}}$.

To analyze the differences between the two versions of the $\mathcal{T}_{B,C}^{\mathrm{jet}}$-type variables in more detail, we compare in Fig. 4.13, the $\mathcal{T}_{B}^{\mathrm{jet}}$ and $\mathcal{T}_{B\mathrm{cm}}^{\mathrm{jet}}$ cross sections integrated over different $|Y|$ ranges (bins). The plots in the first row of Fig. 4.13 show the spectrum and cumulant cross sections for $\mathcal{T}_{B(\mathrm{cm})}^{\mathrm{jet}}$ in the $|Y| \leq 2$ bin, respectively. Qualitatively they look very similar to the corresponding plots for $|Y| \leq \ln(E_{\mathrm{cm}}/m_H)$ (i.e. the full Y range), except for the somewhat reduced total cross section in the right panel of Fig. 4.13 due to the reduced Y range. In particular, the $\mathcal{T}_{B}^{\mathrm{jet}} < \mathcal{T}^{\mathrm{cut}}$ and $\mathcal{T}_{B\mathrm{cm}}^{\mathrm{jet}} < \mathcal{T}^{\mathrm{cut}}$ vetoes again yield practically the same NLL′+NLO cross sections.

The differences between $\mathcal{T}_{B}^{\mathrm{jet}}$ and $\mathcal{T}_{B\mathrm{cm}}^{\mathrm{jet}}$ get more pronounced at larger Higgs rapidity Y. (The decrease in the overall normalization of all cross sections in the right panels of Fig. 4.13 for larger Y is due to the PDF suppression.) The $\mathcal{T}_{B(\mathrm{cm})}^{\mathrm{jet}}$ spectra in the left panels of Fig. 4.13 show that the singular-nonsingular cancellations happen at lower $\mathcal{T}_{B}^{\mathrm{jet}}$ now, which means that following the discussion in Sec. 4.10, the parameters in the profile scales have to change accordingly. For the resummed cross sections in the $2 \leq |Y| \leq 3$ and $|Y| \geq 3$

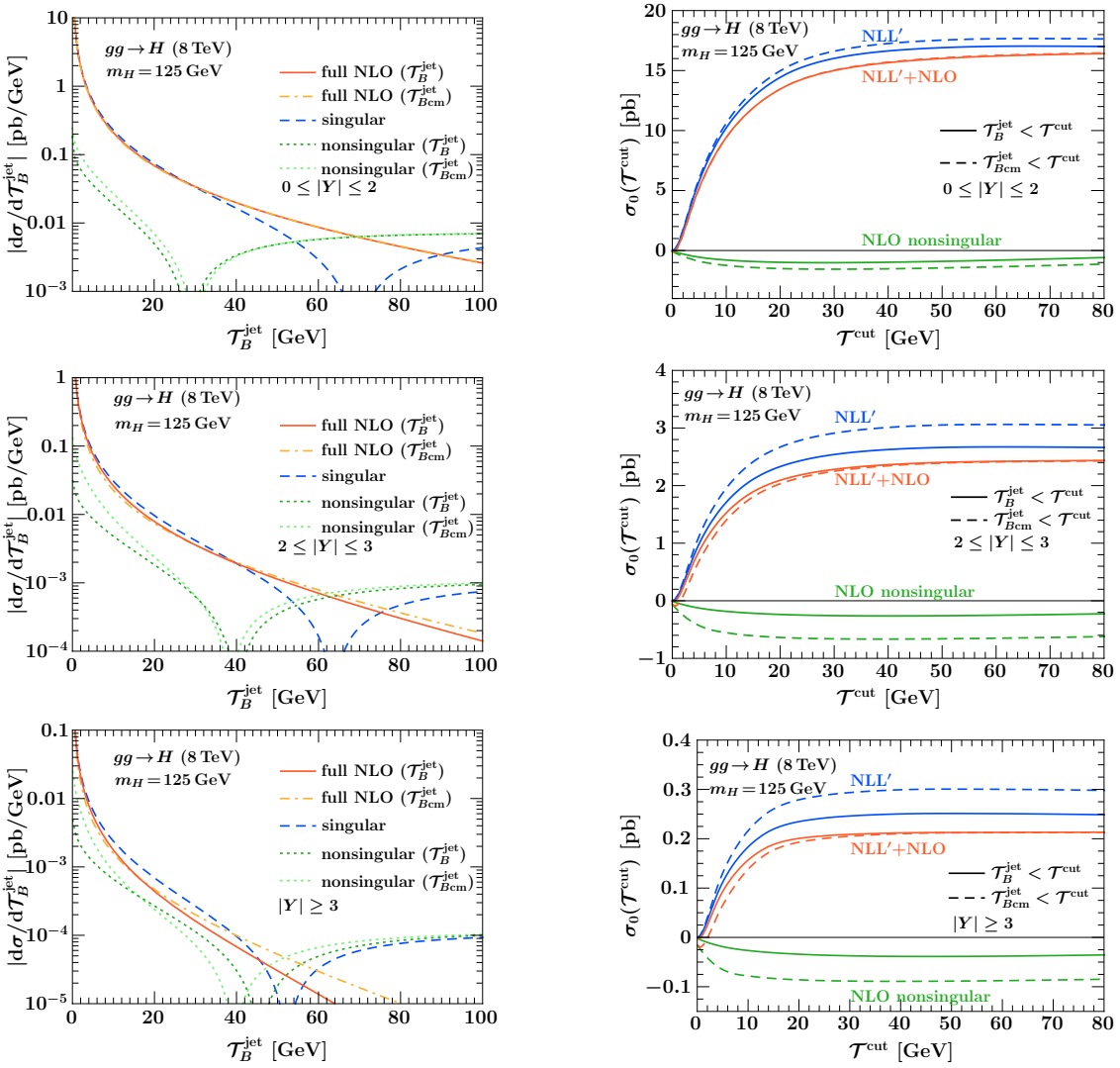

Figure 4.13: *The plots on the left show the differential distributions for $\mathcal{T}_{B(\rm cm)}^{\rm jet}$ for the $|Y| \le 2$ (first line), $2 \le |Y| \le 3$ (middle), and $|Y| \ge 3$ bins (last line) to be compared with the first plot in Fig. 4.10, where the cross sections have been integrated over the full Y range. The plots on the right show the integrated $\mathcal{T}_{B(\rm cm)}^{\rm jet}$ cumulants for the $|Y| \le 2$ (first line), $2 \le |Y| \le 3$ (middle), and $|Y| \ge 3$ bins (last line) to be compared with the first plot in Fig. 4.12, where the cross sections have been integrated over the full Y range.*

bins shown in the middle and last row of Fig. 4.13, we therefore set our profile parameters to $\{x_1, x_2, x_3\} = \{0.1, 0.325, 0.55\}$ and $\{x_1, x_2, x_3\} = \{0.1, 0.275, 0.45\}$, respectively. As observed in the right panels of the second and third row of Fig. 4.13, the $\mathcal{T}_B^{\rm jet}$ and $\mathcal{T}_{B\rm cm}^{\rm jet}$ cumulants for the $2 \le |Y| \le 3$ bin start to differ in their shape: the separation between the respective resummed and nonsingular contributions is increased and the NLL′+NLO $\mathcal{T}_{B\rm cm}^{\rm jet}$ result considerably deviates from the one for $\mathcal{T}_B^{\rm jet}$ at small $\mathcal{T}^{\rm cut}$ values. These effects are even more enhanced for the $|Y| \ge 3$ bin. For very small values of $\mathcal{T}^{\rm cut}$ ($\lesssim 2\,\mathrm{GeV}$) the NLL′+NLO $\mathcal{T}_{B\rm cm}^{\rm jet}$ cumulants in the higher Y bins turn slightly negative. This unphysical effect is formally higher-order and due to a lack of Sudakov suppression of the large non-

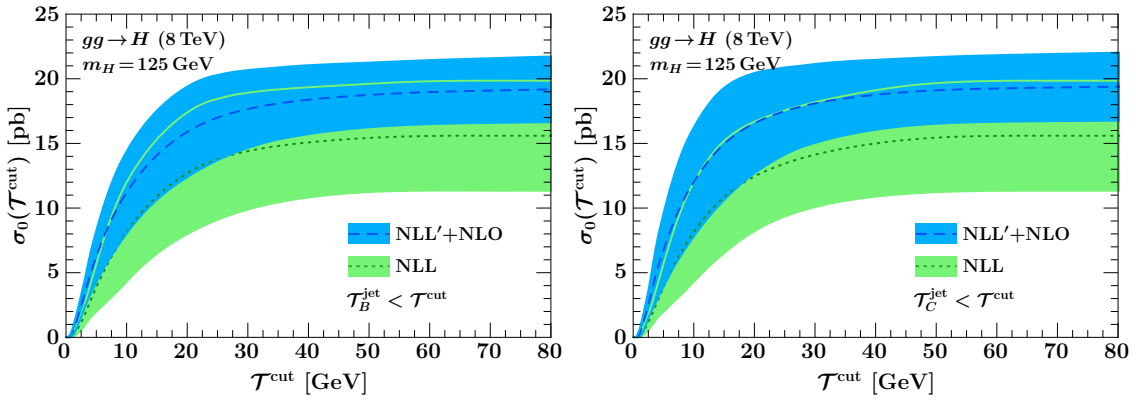

Figure 4.14: *Cumulant cross sections for $\mathcal{T}_B^{\rm jet} < \mathcal{T}^{\rm cut}$ (left panel) and $\mathcal{T}_C^{\rm jet} < \mathcal{T}^{\rm cut}$ (right panel). The (overlapping) green and blue bands represent the NLL and NLL′+NLO predictions with the corresponding uncertainty ($\pm\Delta_0$) from scale variations according to Sec. 4.10.1, respectively. The dashed and dotted lines indicate the respective default predictions using our central profiles for the resummation/FO scales as explained in Sec. 4.10.*

singular corrections meaning that the resummation for $\mathcal{T}_{B\rm cm}^{\rm jet}$ is less effective than for $\mathcal{T}_B^{\rm jet}$. The above conclusions from the analysis of the Y-binned cross sections likewise hold for the $\mathcal{T}_{C(\rm cm)}^{\rm jet}$ observables.

In Fig. 4.14, we finally present the resummed Higgs+0-jet cross section predictions along with their perturbative uncertainty bands ($\pm\Delta_0$) obtained by the scale variations defined before. To study the convergence of our resummed predictions and validate out uncertainty estimates, we show the NLL bands in green color and the NLL′+NLO bands in blue color for $\mathcal{T}_B^{\rm jet} < \mathcal{T}^{\rm cut}$ (left panel) and $\mathcal{T}_C^{\rm jet} < \mathcal{T}^{\rm cut}$ (right panel).

We observe a substantial decrease in uncertainties going from NLL to NLL′+NLO, which is mostly due to NLO singular matching corrections, which partly cancel the scale variation from the NLL resummation factors. Both NLL′+NLO bands have an overlap with their NLL pendants that is consistent with our uncertainty estimates. We emphasize however that more solid conclusions about the order-by-order convergence of the perturbative predictions can be drawn once also the next higher order, i.e. NNLL′+NNLO, is known, which is left for future work.

At $\mathcal{T}^{\rm cut} \sim 25\,\text{GeV}$, we find a perturbative uncertainty of about 20% for our NLL′+NLO predictions, which is largely driven by the sizable FO uncertainties. It is also comparable with the precision obtained for the $p_T^{\rm jet}$-vetoed cross section at the same order in [25]. Similar to the case of $p_T^{\rm jet}$, we also expect a substantial improvement in the precision for $\mathcal{T}_{B,C}^{\rm jet}$ when eventually going to NNLL′+NNLO. For $\mathcal{T}^{\rm cut} \sim 100\,\text{GeV}$, we find a perturbative error of about 13%, which effectively equals the scale variation uncertainty of the total π^2-improved NLO cross section.

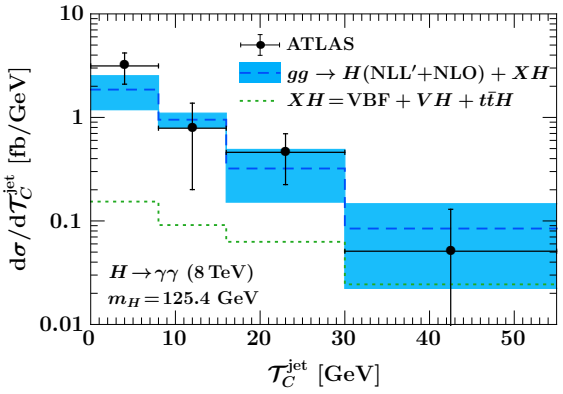

Figure 4.15: *Comparison of the $gg \to H \to \gamma\gamma$ cross section at NLL′+NLO in bins of $\mathcal{T}_C^{\mathrm{jet}}$ to the ATLAS $H \to \gamma\gamma$ measurements [38]. See the text for further details on the applied corrections.*

Last but not least, in Fig. 4.15 we compare our prediction at NLL′+NLO in bins of $\mathcal{T}_C^{\mathrm{jet}}$ with the recent ATLAS measurement in the $H \to \gamma\gamma$ channel [38]. Currently, the measurement has an underlying technical cut on reconstructed jets of $p_{Tj} \geq 25\,\mathrm{GeV}$, which effectively moves events between the first two bins. We correct for this effect by applying an extrapolation factor from Monte Carlo simulation.To directly compare with the measurements, we multiply our predictions by the $H \to \gamma\gamma$ branching ratio of 0.228 ± 0.011 [53] and apply several correction factors as given in [38]: The diphoton kinematic acceptance and photon isolation efficiency are essentially independent of $\mathcal{T}_C^{\mathrm{jet}}$, while nonperturbative corrections due to hadronization and underlying event are practically irrelevant. Finally, we also add the contributions from other production channels as estimated in [38], and which are shown by the green dotted lines. For the uncertainties in our NLL′+NLO predictions we propagate the Δ_{FO} and Δ_{resum} uncertainties by taking the differences of our cumulant predictions at the two bin edges separately for each profile variation. We also add in quadrature an 8% uncertainty for PDF+α_s uncertainties (which we take to be the same as for the total cross section since they are mostly independent of $\mathcal{T}_{Cj}$). [5]

4.12 Conclusions

In this chapter, we briefly discussed different types of jet-veto obseravables and introduced the rapidity-dependent jet-vetoes $\mathcal{T}_{B(\mathrm{cm})}^{\mathrm{jet}}$ and $\mathcal{T}_{C(\mathrm{cm})}^{\mathrm{jet}}$ which have two different types of rapidity weighting and related resummation properties. We gave a brief overview of the SCET Lagrangian, factorization and resummation in the framework of SCET in particular

[5] At present this extrapolation introduces a nonnegligible MC model dependence. To minimize this in the future, it would be advantageous to try to reduce the lower cut on reconstructed jets as much as possible and/or slightly increase the lowest $\mathcal{T}_{Cj}$ bin edge.

we sketched the proof of factorization formula for Drell-Yan cross section differential in inclusive beam thrust. We extended it to predict factorized cross section for Higgs production differential in the rapidity-dependent observables $\mathcal{T}_B^{\text{jet}}$ and $\mathcal{T}_C^{\text{jet}}$. We also discussed the resummation of these cross section with a veto $\mathcal{T}_f^{\text{jet}} < \mathcal{T}^{\text{cut}}$. Since their resummation structure is notably different than for the p_T^{jet} observable, rapidity-weighted $\mathcal{T}_f^{\text{jet}}$-binned cross sections yield valuable complementary information on the properties of additional jet production in a given hard process. Experimentally, such generalized jet vetoes have the advantage to provide efficient methods to veto central jets, while relaxing the phase space constraints (and therefore the requirements on the measurement) for jets with increasingly forward rapidities.

As a concrete example we considered Higgs+0-jet production through gluon fusion at the LHC, and presented cross section predictions at the NLL′+NLO level for all four jet-veto variables. We computed the NLO cross section differential in rapidity Y and the four $\mathcal{T}_f^{\text{jet}}$ observables, and used subtraction method to obtain the nonsingular corrections to the H+0-jet cross section. We analyzed the theoretical uncertainties in the NLL′+NLO cross section via combined scale variations of the different involved resummation and FO scales. We find that the level of theoretical precision that can be reached for such rapidity-weighted jet-veto observables is comparable to what is currently possible for p_T^{jet} vetoes. Comparing our analytic predictions for the $\mathcal{T}_C^{\text{jet}}$-binned cross section with a recent ATLAS measurement in the $H \to \gamma\gamma$ channel [38] we find good agreement. Hence, there are strong motivations that rapidity-dependent jet-vetoes, like the $\mathcal{T}_{B(\text{cm})}^{\text{jet}}$ and $\mathcal{T}_{C(\text{cm})}^{\text{jet}}$ variables discussed here, should be measured in other hadron collider processes such as Drell-Yan, diphoton, and weak diboson production at different invariant masses and rapidities of the produced color-singlet state. This will provide stringent tests of our understanding of jet-veto resummations and jet production in general. In turn, such generalized jet vetoes can be utilized to optimize signal selections in experimental analyses that rely on jet-binning, such as Higgs property measurements or new-physics searches.

As mentioned in Sec. 4.6.3, at $O(\alpha_s^2)$, there are corrections to the factorization formula due to clustering and soft-collinear mixing effects. These corrections were absent at NLL′ when there was a single emission. However going to NNLL′+ NNLO requires us to take into account these corrections. We particularly consider corrections due to the clustering of two soft or collinear particles into a single jet which contributes to ΔM^{jet} in Eq. (4.117) and give rise to terms like $\alpha_s^n \ln^{n-1} R$. These are important for small jet radii typically used in current experiments. In the next chapter we will compute these clustering corrections in the soft and the beam functions at NNLO.

Chapter 5

Clustering corrections in the beam and soft functions

In this chapter, we will compute the leading jet clustering corrections in the soft function and partly in the beam function (for one color structure) at $O(\alpha_s^2)$ for the two jet-based observables $\mathcal{T}_B^{\rm jet}$ and $\mathcal{T}_C^{\rm jet}$. These give rise to logarithms of the jet radius R in the cross section predictions at NNLL′+ NNLO, and are important for the typical jet radii currently used in the experiments.

5.1 Introduction

As discussed in the previous chapter, for jet-based observables at $O(\alpha_s^2)$, a non-trivial clustering can take place between two emitted partons leading to some dependence on the jet radius R. This dependence on the jet algorithm can arise due to the clustering of two particles within the same (soft or collinear) sector or the mixing between the soft and collinear sectors. The correction to the measurement function is given by (as in the previous chapter)

$$\mathcal{M}^{\rm jet} = (\mathcal{M}_a + \Delta\mathcal{M}_a^{\rm jet})(\mathcal{M}_b + \Delta\mathcal{M}_b^{\rm jet})(\mathcal{M}_S + \Delta\mathcal{M}_S^{\rm jet}) + \delta\mathcal{M}_{SC}^{\rm jet}\,, \tag{5.1}$$

where, $\delta\mathcal{M}_{SC}^{\rm jet}$ arises from the clustering of a soft and collinear particle into a single jet, and is an $O(R^2)$ effect. $\Delta\mathcal{M}^{\rm jet}$ contains two contributions: first arising from the correlated emissions which give rise to logarithms of R and are remnants of a collinear divergence (for $R \to 0$) between the two particles. Second arising from the independent (uncorrelated) emissions within each sector which are of $O(R^2)$ like the soft-collinear mixing. The

measurement function for the clustering arising from two independent emissions has the form

$$\Delta\mathcal{M}^{\rm indep} = \Delta\mathcal{M}^{\rm indep}_{CC} + \Delta\mathcal{M}^{\rm indep}_{SS} + \delta\mathcal{M}_{SC} \sim O(R^2)\,, \tag{5.2}$$

where SS, CC denote the independent emissions from soft and collinear sectors respectively and SC denotes the soft-collinear mixing. The factorization formula holds only upto the soft-collinear mixing terms, therefore they should be small and this is true if $R \sim \lambda \ll 1$. For the current experimental analyses, $R = \{0.4, 0.5\}$, so the correction due to $\Delta\mathcal{M}^{\rm indep}$ including the soft-collinear mixing are indeed power suppressed. In this limit however, the corrections due to correlated emissions giving rise to logarithms of R become important, which we will compute for the beam and soft functions in this chapter. These corrections are relative to the global jet-algorithm independent measurement function, so one natural choice is to define the global measurement as the inclusive beam thrust one which is independent of jet algorithm effects. Such a measurement is given by

$$\mathcal{M}_i(\mathcal{T}^{\rm cut}) = \theta\Big(\sum_{m\in {\rm i^{th}sector}} \mathcal{T}_{fm} < \mathcal{T}^{\rm cut}\Big)\,, \tag{5.3}$$

where i denotes the collinear or soft sectors. We choose the inclusive measurement as the global one because the soft and beam functions are known upto NNLO [84, 94]. The measurement function for the clustering correction relative to this inclusive measurement is

$$\begin{aligned}\Delta\mathcal{M}^{\rm jet}_i(\mathcal{T}^{\rm cut}) = {}& \theta(\Delta R_{12} < R)\theta(\mathcal{T}^{\rm jet}_f < \mathcal{T}^{\rm cut}) + \theta(\Delta R_{12} > R)\theta(\mathcal{T}_{f1} < \mathcal{T}^{\rm cut})\theta(\mathcal{T}_{f2} < \mathcal{T}^{\rm cut}) \\ & - \theta(\mathcal{T}_{f1} + \mathcal{T}_{f2} < \mathcal{T}^{\rm cut})\,.\end{aligned} \tag{5.4}$$

Here if the two particles are within a jet radius R, i.e. $\Delta R_{12} < R$, then they are clustered into a jet and $\mathcal{T}^{\rm jet}_f$ which is the observable for the clustered pair, is contrained to be less than $\mathcal{T}^{\rm cut}$. If the particles are more than R apart, the constraint is imposed on the $\mathcal{T}_f$ of each particle. The last term is the inclusive measurement which is subtracted so that $\mathcal{M}_i + \Delta\mathcal{M}^{\rm jet}_i$ is equivalent to the full measurement. This measurement can be simplified further, with the relation $\mathcal{T}^{\rm jet}_f = \mathcal{T}_{f1} + \mathcal{T}_{f2}$, except for the case where the two particles are in the opposite hemispheres and still cluster which is an $O(R^4)$ effect. Neglecting such higher order effects, the measurement function becomes

$$\Delta\mathcal{M}^{\rm jet}_i(\mathcal{T}^{\rm cut}) = \theta(\Delta R_{12} > R)\Big[\theta(\mathcal{T}_{f1} < \mathcal{T}^{\rm cut})\theta(\mathcal{T}_{f2} < \mathcal{T}^{\rm cut}) - \theta(\mathcal{T}_{f1} + \mathcal{T}_{f2} < \mathcal{T}^{\rm cut})\Big]\,. \tag{5.5}$$

This measurement function holds for both soft and beam functions.

The bare clustering corrections are UV-divergent and contribute to the two-loop beam

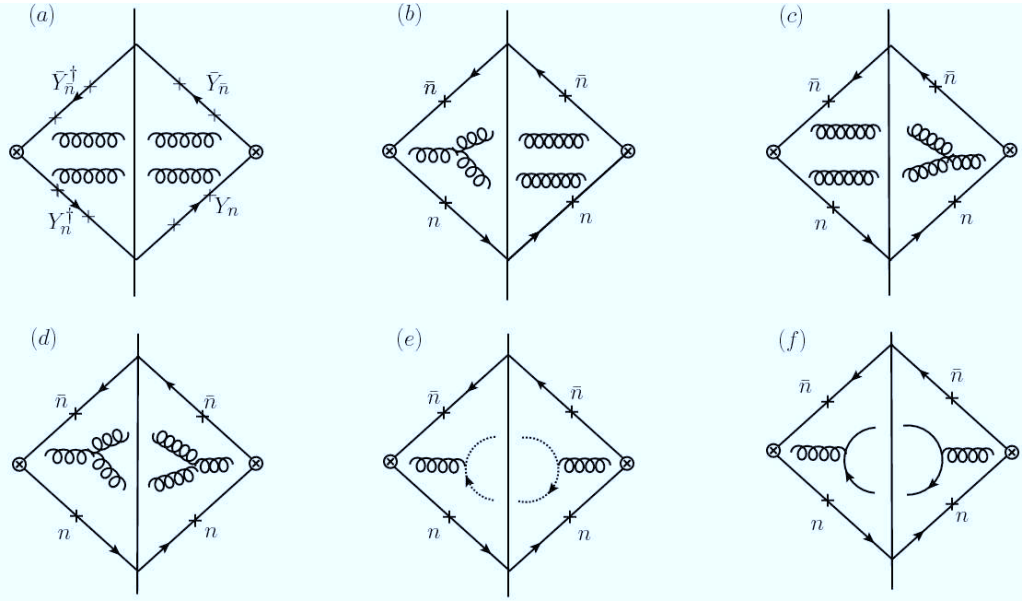

Figure 5.1: *At $O(\alpha_s^2)$, there are 5 classes of diagrams. Here the endpoints of the gluons can be attached to the points on the Wilson lines labeled by a '$\times$' in any order. Diagram (a) contains a correlated contribution when the gluons attach to two different Wilson lines and an independent (uncorrelated) emission contribution with both the gluons attaching the same Wilson line (which we don't consider). Diagrams (b), (c) have a three-gluon vertex, and diagrams (d), (e) and (f) correspond to vaccum polarization with gluon loop, quark loop and a ghost loop respectively.*

and soft anomalous dimension. For the soft function, we need to compute the clustering corrections separately for the two observables $\mathcal{T}_B^{\text{jet}}$ and $\mathcal{T}_C^{\text{jet}}$ because the measurement function is different. The beam function being the same for both $\mathcal{T}_B^{\text{jet}}$ and $\mathcal{T}_C^{\text{jet}}$ (the measurement function for $\mathcal{T}_C^{\text{jet}}$ being equal to $\mathcal{T}_B^{\text{jet}}$ at forward rapidities as discussed in subsec. 4.6.3), the clustering corrections are exactly the same and so it is sufficient to compute them only for $\mathcal{T}_B^{\text{jet}}$. Because the beam function clustering correction is the same for $\mathcal{T}_B^{\text{jet}}$ and $\mathcal{T}_C^{\text{jet}}$, from RG consistency, the $1/\epsilon$ coefficient of the clustering correction in the soft function should be the same for both the observables and this will serve as a cross check of our results. However the non-divergent constant terms can be different for $\mathcal{T}_C^{\text{jet}}$ and $\mathcal{T}_B^{\text{jet}}$. Let us first start with the clustering corrections in the soft function.

5.2 Clustering corrections in the Soft function

We obtain the non-Abelian matrix elements for the bare 2-loop soft function from [94]. To compute the clustering corrections from correlated emissions, we consider all the diagrams shown in Fig. 5.1 except a part of the first diagram which has two independent (uncorrelated) emissions. This part with two independent (uncorrelated) emissions contributes to the $\Delta\mathcal{M}_{SS}^{\text{indep}}$ and is of $O(R^2)$. We don't include these independent emission diagrams in

our calculation as they give rise to corrections that are $O(R^2)$ suppressed for small values of the jet radius R. These have been computed in Ref. [70] and combined with $\Delta\sigma_{CC}^{\text{indep}}$ and $\Delta\sigma_{SC}^{\text{indep}}$ in order to obtain a finite contribution proportional to R^2.

In order to compute the clustering corrections from correlated emissions, we use the measurement function defined in Eq. (5.5). The clustering correction in the soft function is given by

$$\Delta S^{(2)}(k_1,k_2) = \frac{d^dk_1}{(2\pi)^d}\frac{d^dk_2}{(2\pi)^d} A_j(k_1,k_2)\Delta\mathcal{M}^{\text{jet}}(k_1,k_2)C(k_1)C(k_2)\,, \tag{5.6}$$

where k_1 and k_2 are the momenta of emitted gluons, $C(k) = 2\pi\delta(k^2)\theta(k^0)$ is the cut propagator and the amplitude obtained by adding all the non-Abelian diagrams is given by [94]

$$\begin{aligned}
A_A(k_1,k_2) = \frac{C_A^2 g^4\mu^{4\epsilon}}{k_1^-k_1^+k_2^-k_2^+(k_1.k_2)^2(k_1^-+k_2^-)^2(k_1^++k_2^+)^2}\big[&-(-1+\epsilon)k_1^-k_1^+k_2^-k_2^+(k_1^+k_2^- - k_1^-k_2^+)^2\\
&-2(k_1.k_2)^2(k_1^-+k_2^-)(k_1^++k_2^+)(k_1^-(2k_1^++k_2^+)+k_2^-(k_1^++2k_2^+))+k_1.k_2(k_1^-+k_2^-)\\
&(k_1^++k_2^+)((k_1^-)^2k_2^+(2k_1^++k_2^+)+k_1^+(k_2^-)^2(k_1^++2k_2^+)+2k_1^-k_2^-((k_1^+)^2-k_1^+k_2^++(k_2^+)^2))\big]\\
A_f(k_1,k_2) = \frac{2C_AT_fn_fg^4\mu^{4\epsilon}}{(k_1.k_2)^2(k_1^-+k_2^-)^2(k_1^++k_2^+)^2}&\left[2k_1.k_2(k_1^-+k_2^-)(k_1^++k_2^+)-(k_1^+k_2^- - k_1^-k_2^+)^2\right].
\end{aligned} \tag{5.7}$$

Rewriting the d-dimensional phase-space integral in terms of different light-cone components, we get

$$\begin{aligned}
\frac{d^dk_1}{(2\pi)^d}\frac{d^dk_2}{(2\pi)^d}C(k_1)C(k_2) = \frac{1}{(16\pi^2)^2}\frac{e^{\gamma_E 2\epsilon}}{\Gamma(1-\epsilon)^2}\left(\frac{\pi^{1/2}\Gamma(1/2-\epsilon)}{\Gamma(1-\epsilon)}\right)^{-1}\int_0^\infty dk_1^+dk_2^+dk_1^-dk_2^-\\
\times(k_1^+k_1^-k_2^+k_2^-)^{-\epsilon}\int_0^\pi d\Delta\phi\sin\Delta\phi^{-2\epsilon}\,.
\end{aligned} \tag{5.8}$$

Plugging this back into Eq. (5.6), the clustering correction in the soft function is given by

$$\begin{aligned}
\Delta S^{(2)}(k_1,k_2) = \frac{1}{(16\pi^2)^2}\frac{e^{\gamma_E 2\epsilon}}{\Gamma(1-\epsilon)^2}\left(\frac{\pi^{1/2}\Gamma(1/2-\epsilon)}{\Gamma(1-\epsilon)}\right)^{-1}\int_0^\infty dk_1^+dk_2^+dk_1^-dk_2^-(k_1^+k_1^-k_2^+k_2^-)^{-\epsilon}\\
\times\int_0^\pi d\Delta\phi\sin\Delta\phi^{-2\epsilon}A_j(k_1,k_2)\Delta\mathcal{M}^{\text{jet}}(k_1,k_2)\,.
\end{aligned} \tag{5.9}$$

The above equation gives the soft function correction in terms of the momenta k_1 and k_2 of the emitted gluons. It can be re-expressed in terms of the observables $\mathcal{T}_B^{\text{jet}}$ or $\mathcal{T}_C^{\text{jet}}$ and a suitable set of coordinates which can be related to the jet radius dependence in the measurement function. We will first compute the clustering corrections for $\mathcal{T}_B^{\text{jet}}$.

5.2.1 Clustering for $\mathcal{T}_B^{\rm jet}$

The constraints from the measurement function given in Eq. (5.5) depend on ΔR which is defined as $\Delta R = \sqrt{\Delta y^2 + \Delta\phi^2}$, where y is the rapidity and ϕ is the azimuthal angle. In order to express the amplitude and phase space in terms of these, the coordinates we use for $\mathcal{T}_B^{\rm jet}$ are

$$\begin{aligned} y_1 = \frac{1}{2}\log\frac{k_1^-}{k_1^+} \quad , \quad y_2 = \frac{1}{2}\log\frac{k_2^-}{k_2^+} \quad , \quad y_t = \frac{1}{2}(y_1+y_2) \quad , \quad \Delta y = y_1 - y_2 \\ z = \frac{k_1^+}{(k_1^+ + k_2^+)} = \frac{\mathcal{T}_{B1}}{\mathcal{T}_{B1}+\mathcal{T}_{B2}} \quad , \quad \mathcal{T}_T = k_1^+ + k_2^+ = \mathcal{T}_{B1} + \mathcal{T}_{B2} \\ \cos\Delta\phi = \frac{k_1^\perp . k_2^\perp}{|k_1^\perp||k_2^\perp|} = \frac{1/2(k_1^+k_2^- + k_2^+k_1^-) - k_1.k_2}{\sqrt{k_1^+k_1^-k_2^+k_2^-}} \,. \end{aligned} \tag{5.10}$$

In terms of these coordinates, the amplitude becomes

$$\begin{aligned} A_A^{\mathcal{T}_B} &= 4g^4 C_A^2 \mu^{4\epsilon} \frac{1}{(\cosh\Delta y - \cos\Delta\phi)(\cosh\Delta y - (1-2z)\sinh\Delta y)} \\ &\Big[(1-z+z^2)\cos\Delta\phi\cosh\Delta y - (1-2z)\cos\Delta\phi\sinh\Delta y - z(1-z) + \\ &\frac{(1-\epsilon)z^2(1-z)^2\sinh\Delta y^2}{(\cosh\Delta y - \cos\Delta\phi)(\cosh\Delta y - (1-2z)\sinh\Delta y)}\Big] , \\ A_f^{\mathcal{T}_B} &= 4g^4 C_A T_f n_f \mu^{4\epsilon}\Big[\frac{1}{(\cosh\Delta y - \cos\Delta\phi)(\cosh\Delta y - (1-2z)\sinh\Delta y)}\Big]^2 \frac{z(1-z)}{2} \\ &\Big[1 - 2\cos\Delta\phi\cosh\Delta y + 2(1-2z)\cos\Delta\phi\sinh\Delta y + (\cosh\Delta y - (1-2z)\sinh\Delta y)^2\Big] . \end{aligned} \tag{5.11}$$

The measurement function can be expressed in terms of the variables $\mathcal{T}_T$ and z as

$$\begin{aligned} \Delta\mathcal{M}^{\rm jet}(\mathcal{T}^{\rm cut}) &= 2\theta(\Delta R_{12} > R)\Big[\theta(\mathcal{T}_{B1} < \mathcal{T}^{\rm cut})\theta(\mathcal{T}_{B2} < \mathcal{T}^{\rm cut}) - \theta(\mathcal{T}_{B1}+\mathcal{T}_{B2} < \mathcal{T}^{cut})\Big] \\ &= 2\theta(\Delta R_{12} > R)\theta\Big[\mathcal{T}^{\rm cut} < \mathcal{T}_T < \mathcal{T}^{\rm cut}\frac{1}{\max(z,1-z)}\Big] . \end{aligned} \tag{5.12}$$

We have multiplied by 2 to account for the case where both the gluons are in the other hemisphere (i.e. $\mathcal{T}_B$ is equal to the minus component of momenta). Finally the soft function correction for the $\mathcal{T}_B^{\rm jet}$ veto in terms of the variables defined in Eq. (5.10) is

$$\begin{aligned} \Delta S^{(2)}(\mathcal{T}^{\rm cut}) = \frac{4}{(16\pi^2)^2}\frac{e^{\gamma_E 2\epsilon}}{\Gamma(1-\epsilon)^2}\Big(\frac{\pi^{1/2}\Gamma(1/2-\epsilon)}{\Gamma(1-\epsilon)}\Big)^{-1}\int_0^\infty d\mathcal{T}_T\int_0^1 dz\int_0^\infty dy_t \\ \int_{-\infty}^\infty d\Delta y\int_0^\pi d\Delta\phi\frac{\mathcal{T}_T^{-1-4\epsilon}}{z(1-z)}(z^2(1-z)^2)^{-\epsilon}e^{-4\epsilon y_t}A_j^{\mathcal{T}_B}\Delta\mathcal{M}^{\rm jet}\sin\Delta\phi^{-2\epsilon} . \end{aligned} \tag{5.13}$$

The only dependence on $\mathcal{T}_T$ is in the measurement functions. Integration over $\mathcal{T}_T$ gives

$$\int_0^\infty d\mathcal{T}_T \mathcal{T}_T^{-1-4\epsilon}\theta\Big[\mathcal{T}^{\rm cut} < \mathcal{T}_T < \mathcal{T}^{\rm cut}\frac{1}{\max(z,1-z)}\Big] = (\mathcal{T}^{\rm cut})^{-4\epsilon}\frac{(1-\max[z,1-z]^{4\epsilon})}{4\epsilon}$$
$$= (\mathcal{T}^{\rm cut})^{-4\epsilon}(-\log[\max(z,1-z)] - 2\log^2[\max(z,1-z)]\epsilon)\,. \tag{5.14}$$

The integral over y_t can also be performed as the matrix element and measurement function are independent of y_t. This integral yields,

$$\int_0^\infty e^{-4\epsilon y_t} dy_t = \frac{1}{4\epsilon}\,. \tag{5.15}$$

With the remaining integrals, the soft function correction is given by

$$\Delta S^{(2)}(\mathcal{T}^{\rm cut}) = \frac{8}{(16\pi^2)^2}\frac{e^{\gamma_E 2\epsilon}}{\Gamma(1-\epsilon)^2}\Big(\frac{\pi^{1/2}\Gamma(1/2-\epsilon)}{\Gamma(1-\epsilon)}\Big)^{-1}\frac{1}{4\epsilon}\int_0^1 dz\int_{-\infty}^{\infty} d\Delta y\int_0^\pi d\Delta\phi$$
$$\frac{1}{z(1-z)}(z^2(1-z)^2)^{-\epsilon}A_j^{\mathcal{T}_B}\theta(\Delta y^2+\Delta\phi^2>R^2)(\mathcal{T}^{\rm cut})^{-4\epsilon}$$
$$(-\log[\max(z,1-z)] - \log^2[\max(z,1-z)]\epsilon)\sin\Delta\phi^{-2\epsilon}\,. \tag{5.16}$$

We evaluated the integrals in Eq. (5.16) and obtained

$$\Delta S^{(2)}(\mathcal{T}^{\rm cut}) = \Big(\frac{\alpha_s}{\pi}\Big)^2\Big(\frac{\mu}{\mathcal{T}^{\rm cut}}\Big)^{4\epsilon}\Big\{\frac{1}{4\epsilon}\Big[C_A^2\Big(B_1\log R + f_1(R)\Big) + C_A T_f n_f\Big(B_2\log R + f_2(R)\Big)\Big]$$
$$+ C_A^2\Big(C_1\log R + C_2\log^2 R + f_3(R)\Big) + C_A T_f n_f\Big(C_3\log R + C_4\log^2 R + f_4(R)\Big)\Big\}\,, \tag{5.17}$$

where the coeffficients B_1, B_2, C_1, C_2, C_3, C_4 and the functions $f_{1-4}(R)$ are computed below.

In order to extract the $\log R$ coefficients B_1, B_2 and the functions $f_1(R)$, $f_2(R)$, we can simplify the above integral by expanding in the $\epsilon\to 0$ limit,

$$\Delta S^{(2)}(\mathcal{T}^{\rm cut}) = \frac{8}{(16\pi^2)^2}\frac{1}{4\epsilon}\frac{1}{\pi}(\mathcal{T}^{\rm cut})^{-4\epsilon}\int_0^1 dz\int_{-\infty}^{\infty} d\Delta y\int_0^\pi d\Delta\phi\frac{1}{z(1-z)}$$
$$A_j^{\mathcal{T}_B}(-\log[\max(z,1-z)])\theta(\Delta y^2+\Delta\phi^2>R^2)\,. \tag{5.18}$$

The left over integrals are finite and the result is of the form $a\log R + c + O(R^2)$. To extract the coefficients B_1 and B_2 of the leading $\log R$ terms, we can expand the amplitudes in the small R limit, which implies we expand in the small ΔR limit. This allows us to obtain B_1 and B_2 analytically, though the constant terms we get are not right (because we neglect higher R effects). Expanding the amplitudes in Eq. (5.11) in the small ΔR limit, by keeping only the $O(1/\Delta R^2)$ terms, and dropping the higher $O(\Delta R^2)$ dependence, we

get

$$A_{fR}^{\mathcal{T}_B} = 4g^4 C_A T_f n_f \mu^{4\epsilon} \frac{4}{\Delta R^4}\Big[\frac{z(1-z)}{2}\big(\Delta R^2 - 4z(1-z)\Delta y^2\big)\Big]\,,$$
$$A_{AR}^{\mathcal{T}_B} = 4g^4 C_A^2 \mu^{4\epsilon} \frac{2}{\Delta R^2}\Big[(1-z+z^2) - z(1-z) + \frac{2z^2(1-z)^2\Delta y^2(1-\epsilon)}{\Delta R^2}\Big]\,. \tag{5.19}$$

These amplitudes can be integrated over $d\Delta y$ and $d\Delta\phi$ using the master integrals,

$$\int_{-\infty}^{\infty} d\Delta y \int_0^{\pi} \frac{d\Delta\phi}{\pi}\frac{1}{\Delta R^2}\theta(\Delta R > R) = -\log R + \log 2\pi\,,$$
$$\int_{-\infty}^{\infty} d\Delta y \int_0^{\pi} \frac{d\Delta\phi}{\pi}\frac{2\Delta y^2}{\Delta R^4}\theta(\Delta R > R) = -\log R + \log 2\pi + \frac{1}{2}\,. \tag{5.20}$$

Carrying through the integrals we get

$$\int_0^1 dz \int_{-\infty}^{\infty} d\Delta y \int_0^{\pi} \frac{d\Delta\phi}{\pi}\frac{\log[\max(z,1-z)]}{z(1-z)}\theta(\Delta R_{12} > R) A_{AR}^{\mathcal{T}_B} = 4g^4 C_A^2$$
$$\mu^{4\epsilon}\Big[\frac{-1}{36}(131 - 12\pi^2 - 132\log 2)\log\Big(\frac{R}{2\pi}\Big) + \frac{1}{72}(-13 + 12\log 2)\Big]\,,$$
$$\int_0^1 dz \int_{-\infty}^{\infty} d\Delta y \int_0^{\pi} \frac{d\Delta\phi}{\pi}\frac{\log[\max(z,1-z)]}{z(1-z)}\theta(\Delta R_{12} > R) A_{fR}^{\mathcal{T}_B} =$$
$$4g^4 C_A T_f n_f \mu^{4\epsilon}\Big[\frac{1}{18}(23 - 24\log 2)\log\Big(\frac{R}{2\pi}\Big) + \frac{1}{36}(13 - 12\log 2)\Big]\,. \tag{5.21}$$

The above analytic result gives

$$B_1 = \frac{1}{18}(131 - 12\pi^2 - 132\log 2)\ ,\ B_2 = \frac{-1}{9}(23 - 24\log 2)\,. \tag{5.22}$$

To obtain the right constants and the R-dependence, we consider the full amplitudes as given in Eq. (5.11) and perform the integrals in Eq. (5.18) numerically at different values of the jet radius R to get the constant and R-dependent functions $F_1(R)$ and $F_2(R)$ from fitting the result.

For the non-divergent ϵ^0 terms, we can extract the coefficients C_{1-4} analytically in the small R limit as before. Considering Eq. (5.16), the master integrals for Δy and $\Delta\phi$ are

given by,

$$\int_{-\infty}^{\infty} d\Delta y \int_0^{\pi} d\Delta\phi \frac{\Delta\phi^{-2\epsilon}}{\Delta\phi^2+\Delta y^2}\theta(\Delta\phi^2+\Delta y^2 > R^2) = \frac{1}{2}\pi\log 4\pi^2 - \pi\log R + \epsilon\Big(\frac{\pi^3}{12} + \frac{1}{4}\pi\log^2 4 - \pi\log^2\pi - \pi\log 4\log R + \pi\log^2 R\Big) + O(\epsilon^2)\,,$$
$$\int_{-\infty}^{\infty} d\Delta y \int_0^{\pi} d\Delta\phi \frac{2\Delta y^2\Delta\phi^{-2\epsilon}}{(\Delta\phi^2+\Delta y^2)^2}\theta(\Delta\phi^2+\Delta y^2 > R^2) = \frac{\pi}{2} + \pi\log 2 + \pi\log\pi - \pi\log R + \epsilon\Big(\frac{\pi}{2} + \frac{\pi^3}{12} + \pi\log^2 2 + \pi\log 2 - \pi\log^2\pi - \pi\log R - \pi\log 4\log R + \pi\log^2 R\Big) + O(\epsilon^2)\,. \tag{5.23}$$

Here, in order to simplify the result, we have kept only the leading terms in ϵ. The integrals for $\Delta\phi$ and Δy in Eq. (5.16) with $(A_j^{\mathcal{T}_B} \to A_{jR}^{\mathcal{T}_B})$ are performed using the above formulae and then the left over z integral is trivial. We then expand Eq. (5.16) to ϵ^0 considering the full amplitudes from Eq. (5.11), and integrate the expression numerically at different values of R in order to obtain the R-dependent functions $F_3(R)$ and $F_4(R)$ from fitting.

Thus the final result for the clustering corrections in the soft function for $\mathcal{T}_B^{\rm jet}$ is

$$\Delta S^{(2)}(\mathcal{T}^{\rm cut}) = \Big(\frac{\alpha_s}{\pi}\Big)^2\Big(\frac{\mu}{\mathcal{T}^{\rm cut}}\Big)^{4\epsilon}\Big\{\frac{1}{4\epsilon}\Big[C_A^2\Big\{\frac{1}{18}(131-12\pi^2-132\log 2)\log R + f_1(R)\Big\} + C_A T_f n_f\Big\{\frac{-1}{9}(23-24\log 2)\log R + f_2(R)\Big\}\Big] + C_A^2\Big(C_1\log R + C_2\log^2 R + f_3(R)\Big) + C_A T_f n_f\Big(C_3\log R + C_4\log^2 R + f_4(R)\Big)\Big\}\,, \tag{5.24}$$

where

$$C_1 = \frac{1}{216}[1580 - 132\pi^2 - 864\zeta[3]] \;\;,\;\; C_2 = \frac{1}{72}[131 + 12\pi^2 + 132\log 2]\;,$$
$$C_3 = \frac{1}{108}[-245 + 24\pi^2 - 36\log 2] \;\;,\;\; C_4 = \frac{1}{36}[23 - 24\log 2]\,. \tag{5.25}$$

and the R-dependent functions $f_1(R)$, $f_2(R)$, $f_3(R)$ and $f_4(R)$ are defined as

$$f_1(R) = F_1(R) - B_1\log R \;\;,\;\; f_2(R) = F_2(R) - B_2\log R$$
$$f_3(R) = F_3(R) - C_1\log R - C_2\log^2 R \;\;,\;\; f_4(R) = F_4(R) - C_3\log R - C_4\log^2 R \tag{5.26}$$

where $F_{1-4}(R)$ are the best fit curves as shown in Fig. 5.2. The data points in the top panel of Fig. 5.2 are obtained by performing the integrals in Eq. (5.18) numerically at different values of the jet radius R for the two color structures C_A^2 (in orange) and $C_A T_f n_f$ (in blue). The orange (C_A^2) and the blue ($C_A T_f n_f$) solid curves in Fig. 5.2 are the best fit curves ($F_1(R)$ and $F_2(R)$ respectively) with the parametric form,

$$F(R) = a\log R + b\log^2 R + f(R) \tag{5.27}$$

Table 5.1: *Coefficients for the fitting functions $F_1(R)$, $F_2(R)$, $F_3(R)$, $F_4(R)$, $F_5(R)$ and $F_6(R)$ for the soft function and $G_1(1,R)$, $G_2(z,R)$ for the beam function. Each $F_i(R)$ is plotted in Fig. 5.2 and Fig. 5.3 and $G_1(1,R)$, $G_2(z,R)$ is plotted in Fig. 5.5.*

Observable	function	a	b	c	d	e	f	g
$\mathcal{T}^{\rm jet}_{B,C}$	$F_1(R)$	-4.385	0	-0.937	0.653	-0.011	0.0002	0.0013
$\mathcal{T}^{\rm jet}_{B,C}$	$F_2(R)$	-0.707	0	0.747	0.019	-0.0004	-0.0001	-0.0008
$\mathcal{T}^{\rm jet}_{B}$	$F_3(R)$	-3.525	1.096	-0.549	0.813	-0.340	-0.064	0.496
$\mathcal{T}^{\rm jet}_{B}$	$F_4(R)$	-0.306	0.1767	0.363	0.003	-0.001	-0.0097	-0.00002
$\mathcal{T}^{\rm jet}_{C}$	$F_5(R)$	-3.525	1.096	-0.479	6.675	-6.29	5.35	8.59
$\mathcal{T}^{\rm jet}_{C}$	$F_6(R)$	-0.306	0.1767	0.382	-0.020	0.023	-0.030	-0.035
$\mathcal{T}^{\rm jet}_{B,C}$	$G_1(1,R)$	-0.189	0.0883	0.273	-0.0076	0.00015	-0.0043	0.00036
$\mathcal{T}^{\rm jet}_{B,C}$	$G_2(0.1,R)$	-1.464	0	-3.092	-17.059	19.68	-21.98	-22.478
$\mathcal{T}^{\rm jet}_{B,C}$	$G_2(0.5,R)$	-0.198	0	-0.306	-2.139	2.461	-2.753	-2.802

where

$$f(R) = c + dR^2 + eR^4 + fR^2 \log R + gR^4 \log R\,.$$

where $a = \{B_1, B_2\}$ and $b = 0$ for the $1/\epsilon$ terms, $a = \{C_1, C_2\}$ and $b = \{C_3, C_4\}$ for the ϵ^0 terms. The other coefficients obtained from fitting are as shown in the Table. 5.1. We have also cross-checked that we obtain the right coefficients B_1, B_2 and C_{1-4} by letting them float free in the fit.

The plots in the lower panel of Fig. 5.2 similarly show the data points obtained by expanding Eq. (5.16) to $O(\epsilon^0)$ and integrating it at different values of R. The corresponding best fit curves are represented by functions $F_3(R)$ and $F_4(R)$ respectively, having the same parametric form as in Eq. (5.27), with $a = C_1$ or C_3 and $b = C_2$ or C_4 and the other coefficients as given in Table. 5.1.

The correction to the two loop soft anomalous dimension is given by

$$\Delta\gamma_S^{(2)}(\mathcal{T}^{\rm cut}, \mu) = \left(\frac{\alpha_s^2(\mu)}{\pi}\right)^2 C_{\mathcal{T}}^{(2)}\,, \tag{5.28}$$

where

$$C_{\mathcal{T}}^{(2)} = \left(\frac{\mu}{\mathcal{T}^{\rm cut}}\right)^{4\epsilon}\Big[C_A^2\Big\{\frac{1}{18}(131 - 12\pi^2 - 132\log 2)\log R + f_1(R)\Big\} + C_A T_f n_f\Big\{\frac{-1}{9}(23 - 24\log 2)\log R + f_2(R)\Big\}\Big]\,. \tag{5.29}$$

The soft anomalous dimension from these clustering effects is cancelled by the anomalous dimensions of the beam function leaving a fixed-order contribution that has a logarithm of the ratio of the beam and soft scales.

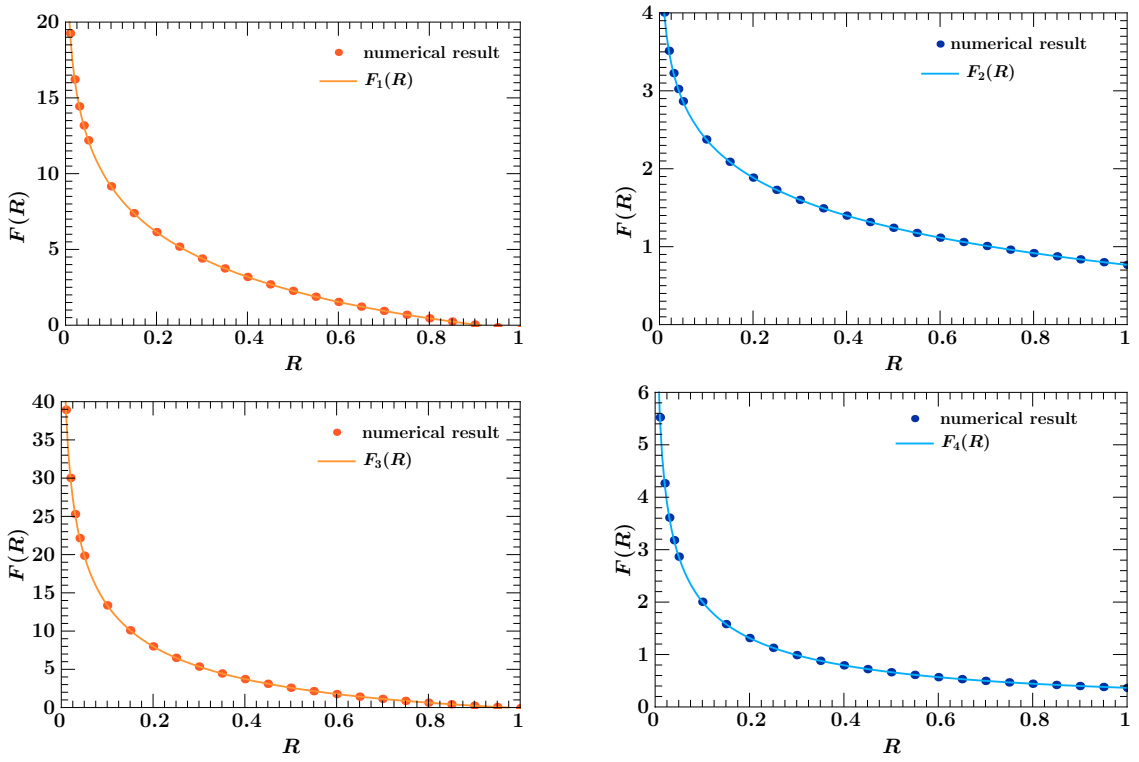

Figure 5.2: *Top panel: Plot for the $1/\epsilon$ terms in Eq. (5.24) as a function of the jet radius R for C_A^2 and $C_A T_f n_f$ color structures, showing both data points and the corresponding best fit curves $F_1(R)$ and $F_2(R)$. Bottom panel: Plot for the ϵ^0 terms in Eq. (5.24) as a function of R for C_A^2 and $C_A T_f n_f$ color structures, showing both data points and the corresponding best fit curves $F_3(R)$ and $F_4(R)$.*

5.2.2 Clustering for $\mathcal{T}_C^{\text{jet}}$

Let us now compute the clustering corrections for $\mathcal{T}_C^{\text{jet}}$, the steps being analogous to $\mathcal{T}_B^{\text{jet}}$ though more tedious. The measurement function for $\mathcal{T}_C^{\text{jet}}$ is analogous to Eq. (5.5) and is given by

$$\begin{aligned}\Delta M^{\text{jet}}(\mathcal{T}^{\text{cut}}) &= \theta(\Delta R_{12} > R)\Big[\theta(\mathcal{T}_{C1} < \mathcal{T}^{\text{cut}})\theta(\mathcal{T}_{C2} < \mathcal{T}^{\text{cut}}) - \theta(\mathcal{T}_{C1} + \mathcal{T}_{C2} < \mathcal{T}^{\text{cut}})\Big] \\ &= \theta(\Delta R_{12} > R)\theta\Big[\mathcal{T}^{\text{cut}} < \mathcal{T}_T' < \mathcal{T}^{\text{cut}}\frac{1}{\max(z', 1-z')}\Big]\,, \end{aligned} \tag{5.30}$$

where

$$\mathcal{T}_T' = \mathcal{T}_{C1} + \mathcal{T}_{C2} \quad , \quad z' = \frac{\mathcal{T}_{C1}}{\mathcal{T}_{C1} + \mathcal{T}_{C2}}\,. \tag{5.31}$$

In place of $\mathcal{T}_T$ and z defined earlier, we have for $\mathcal{T}_C^{\text{jet}}$, $\mathcal{T}_T'$ and z' while the other variables Δy, $\Delta\phi$ and y_t remain the same as defined in Eq. (5.10). In order to express the correction in the soft function given by Eq. (5.9) in terms of these new variables, we have from the

definition of $\mathcal{T}_C^{\rm jet}$,

$$\mathcal{T}_{C1} = \frac{k_1^+ k_1^-}{k_1^+ + k_1^-} \quad , \quad \mathcal{T}_{C2} = \frac{k_2^+ k_2^-}{k_2^+ + k_2^-} \,, \tag{5.32}$$

which implies we can express k_1^+ and k_2^+ as

$$\begin{aligned} k_1^+ &= \mathcal{T}_{C1}(e^{-2y_1}+1) = z'\mathcal{T}_T'(e^{-(2y_t+\Delta y)}+1) \\ k_2^+ &= \mathcal{T}_{C2}(e^{-2y_2}+1) = (1-z')\mathcal{T}_T'(e^{-(2y_t-\Delta y)}+1)\,. \end{aligned} \tag{5.33}$$

The amplitudes in Eq. (5.7) can be expressed in terms of these new set of variables as,

$$\begin{aligned} A_A^{\mathcal{T}_C} &= 4g^4 C_A^2 \mu^{4\epsilon} \frac{1}{(\cosh\Delta y - \cos\Delta\phi)(\cosh\Delta y - (1-2\tilde{z})\sinh\Delta y)} \\ &\Big[(1-\tilde{z}+\tilde{z}^2)\cos\Delta\phi\cosh\Delta y - (1-2\tilde{z})\cos\Delta\phi\sinh\Delta y - \tilde{z}(1-\tilde{z}) + \\ &\frac{(1-\epsilon)\tilde{z}^2(1-\tilde{z})^2\sinh\Delta y^2}{(\cosh\Delta y - \cos\Delta\phi)(\cosh\Delta y - (1-2\tilde{z})\sinh\Delta y)}\Big]\,, \\ A_f^{\mathcal{T}_C} &= 4g^4 C_A T_f n_f \mu^{4\epsilon}\Big[\frac{1}{(\cosh\Delta y - \cos\Delta\phi)(\cosh\Delta y - (1-2\tilde{z})\sinh\Delta y)}\Big]^2 \frac{\tilde{z}(1-\tilde{z})}{2} \\ &\Big[1 - 2\cos\Delta\phi\cosh\Delta y + 2(1-2\tilde{z})\cos\Delta\phi\sinh\Delta y + (\cosh\Delta y - (1-2\tilde{z})\sinh\Delta y)^2\Big]\,, \end{aligned} \tag{5.34}$$

where $\tilde{z}$ is given by

$$\tilde{z} = \frac{z'[(\cosh\Delta y - \sinh\Delta y)^2 e^{\Delta y} + e^{2y_t}]}{e^{2y_t} + e^{\Delta y}(1 + z'[-1 + (\cosh\Delta y - \sinh\Delta y)^2])}\,, \tag{5.35}$$

The phase space factor from Eq. (5.9) in terms of these variables is given by

$$\begin{aligned} \Phi &= \frac{e^{\gamma_E 2\epsilon}}{\Gamma(1-\epsilon)^2}\Big(\frac{\pi^{1/2}\Gamma(1/2-\epsilon)}{\Gamma(1-\epsilon)}\Big)^{-1}\int dk_1^+ dk_1^- dk_2^+ dk_2^- (k_1^+ k_1^- k_2^+ k_2^-)^{-\epsilon}\sin\Delta\phi^{-2\epsilon} d\Delta\phi = \\ &\frac{e^{\gamma_E 2\epsilon}}{\Gamma(1-\epsilon)^2}\Big(\frac{\pi^{1/2}\Gamma(1/2-\epsilon)}{\Gamma(1-\epsilon)}\Big)^{-1}\frac{-4}{\mathcal{T}_T'(-1+z')z'}\{e^{-2(\Delta y+2y_t)}(e^{\Delta y}+e^{2y_t})^2(1+e^{\Delta y+2y_t})^2 \\ &\mathcal{T}_T'^4(-1+z')^2 z'^2)\}^{-\epsilon}\sin\Delta\phi^{-2\epsilon} d\mathcal{T}_T' dz' d\Delta y dy_t d\Delta\phi\,. \end{aligned} \tag{5.36}$$

Combining the above phase space factor with the amplitude and measurement function, the full correction to the soft function for $\mathcal{T}_C^{\rm jet}$ is given by

$$\begin{aligned} \Delta S^{(2)}(\mathcal{T}^{\rm cut}) = \frac{4}{(16\pi^2)^2}\frac{e^{\gamma_E 2\epsilon}}{\Gamma(1-\epsilon)^2}\Big(\frac{\pi^{1/2}\Gamma(1/2-\epsilon)}{\Gamma(1-\epsilon)}\Big)^{-1}\int_0^1 dz' \int_{-\infty}^{\infty} d\Delta y \int_{-\infty}^{\infty} dy_t \int_0^{\pi} d\Delta\phi \\ \frac{1}{z'(1-z')}(z'^2(1-z')^2)^{-\epsilon}\{e^{-2(\Delta y+2y_t)}(e^{\Delta y}+e^{2y_t})^2(1+e^{\Delta y+2y_t})^2\}^{-\epsilon}\sin\Delta\phi^{-2\epsilon} \\ A_j^{\mathcal{T}_C}\theta(\Delta R^2 > R^2)(\mathcal{T}^{\rm cut})^{-4\epsilon}(-\log[\max(z',1-z')] - 2\log^2[\max(z',1-z')]\epsilon)\,. \end{aligned} \tag{5.37}$$

The result of performing these integrals is the same as given in Eq. (5.17), with different coefficients which we will compute below.

In order to extract the $1/\epsilon$ terms, we can expand the phase-space factor in the $\epsilon \to 0$ limit. For the $\log R$ coefficients B_1 and B_2, we also expand the amplitude and phase space in the small ΔR limit. This simplifies the phase space factor to

$$\lim_{\epsilon\to 0,\Delta y\to 0} \Phi = \Phi_0 = \frac{-4(e^{-4y_t}(1+e^{2y_t})^4 \mathcal{T}_T'^4(-1+z')^2 z'^2)^{-\epsilon}}{\mathcal{T}_T'(-1+z')z'}\,. \tag{5.38}$$

Expanding the amplitudes in Eq. (5.34) in the small ΔR limit, we obtain the same expressions as for $\mathcal{T}_B^{\text{jet}}$ in Eq. (5.19),

$$\begin{aligned} A_{fR}^{\mathcal{T}_C} &= 4g^4 C_A T_f n_f \mu^{4\epsilon} \frac{4}{\Delta R^4}\Big[\frac{z'(1-z')}{2}\big(\Delta R^2 - 4z'(1-z')\Delta y^2\big)\Big]\,, \\ A_{AR}^{\mathcal{T}_C} &= 4g^4 C_A^2 \mu^{4\epsilon} \frac{2}{\Delta R^2}\Big[(1-z'+z'^2) - z'(1-z') + \frac{2z'^2(1-z')^2\Delta y^2(1-\epsilon)}{\Delta R^2}\Big]\,. \end{aligned} \tag{5.39}$$

This is as expected, because the $1/\epsilon$ coefficients which contribute to the anomalous dimensions for $\mathcal{T}_C^{\text{jet}}$ should be the same as $\mathcal{T}_B^{\text{jet}}$, because the beam functions are the same. As for $\mathcal{T}_B^{\text{jet}}$, the y_t dependence in the small ΔR limit occurs only in the phase space factor Φ_0. Integrating over y_t we get,

$$\int_{-\infty}^{\infty} -\frac{4(e^{-4y_t}(1+e^{2y_t})^4)^{-\epsilon}\mathcal{T}_T'^{-1-4\epsilon}}{(-1+z')z'}dy_t = -\frac{4\mathcal{T}_T'^{-1-4\epsilon}}{(-1+z')z'}\Big(\frac{1}{2\epsilon} - \frac{\pi^2}{3}\epsilon + O(\epsilon^2)\Big)\,. \tag{5.40}$$

The $\mathcal{T}_T'$ integral can also be performed over the measurement function as in the case of $\mathcal{T}_B^{\text{jet}}$. The soft function correction for $\mathcal{T}_C^{\text{jet}}$ after the y_t and $\mathcal{T}_T'$ integrals in the limit of $(\epsilon, \Delta R) \to 0$ is given by

$$\begin{aligned} \Delta S^{(2)}(\mathcal{T}^{\text{cut}}) = \frac{4}{(16\pi^2)^2}\int_0^1 dz' \int_{-\infty}^{\infty} d\Delta y \int_0^g \pi \frac{d\Delta\phi}{\pi}\Big(\frac{1}{2\epsilon}\Big)\frac{1}{z'(1-z')} \\ A_{jR}^{\mathcal{T}_C}\theta(\Delta y^2+\Delta\phi^2 > R^2)(\mathcal{T}^{\text{cut}})^{-4\epsilon}(-\log[\max(z', 1-z')])\,. \end{aligned} \tag{5.41}$$

These integrals are again finite and of the form $a\log R + c + O(R^2)$. The integrals over Δy and $\Delta\phi$ can be performed using the master formulae given in Eq. (5.20) and we checked that we obtain the same coefficients as for $\mathcal{T}_B^{\text{jet}}$ in Eq. (5.22). To determine the constant, we can consider the integral over the full amplitude,

$$\int A_j^{\mathcal{T}_C} = \int (A_j^{\mathcal{T}_C} - A_{jR}^{\mathcal{T}_C}) + \int A_{jR}^{\mathcal{T}_C} \tag{5.42}$$

where the integral over the difference is given by

$$\Delta S^{\rm sub}(R) = \Big(\frac{\alpha_s}{\pi}\Big)^2 \Big(\frac{\mu}{\mathcal{T}^{\rm cut}}\Big)^{4\epsilon} 4j \int_0^1 dz' \int_0^\infty d\Delta y \int_0^\infty dy_t \int_0^\pi \frac{d\Delta\phi}{\pi} \frac{(-\log[\max(z', 1-z')])}{z'(1-z')}$$
$$\theta(\Delta R^2 > R^2) \Big[\frac{A_j^{\mathcal{T}_C}}{4g^4 j\mu^{4\epsilon}} \{e^{-2(\Delta y+2y_t)}(e^{\Delta y}+e^{2y_t})^2(1+e^{\Delta y+2y_t})^2\}^{-\epsilon}$$
$$- \frac{A_{jR}^{\mathcal{T}_C}}{4g^4 j\mu^{4\epsilon}} \Big(e^{-4y_t}(1+e^{2y_t})^4\Big)^{-\epsilon}\Big] . \tag{5.43}$$

and where $j = C_A^2$ or $C_A T_f n_f$, $\epsilon \sim 10^{-5}$. We use a subtraction method here because the y_t integral cannot be performed analytically when we consider the full amplitude and the phase space (i.e. we cannot factor out the $1/\epsilon$ divergence). The difference $A - A_R$ gives a finite result in the limit $R \to 0$. To obtain the right constant, the known result of the integral over A_R needs to be added back. We found that this constant and the R-dependent functions (given by $F_1(R)$ and $F_2(R)$ in Fig. 5.2) obtained in this way agree with $\mathcal{T}_B^{\rm jet}$ as expected.

For the non-divergent ϵ^0 contribution, the $\log R$ coefficients $C_{1-4}(R)$ can be computed as for $\mathcal{T}_B^{\rm jet}$ using the master integrals in Eq. (5.23) and the amplitudes in Eq. (5.39). We know from Eq. (5.40), that there is no ϵ^0 coefficient from the phase space. The $\log R$ and $\log^2 R$ coefficients that we obtain analytically for $\mathcal{T}_C^{\rm jet}$ happen to be the same as given in Eq. (5.25). For the constant, we perform the subtraction integral, $A_{\mathcal{T}_C} - A_{\mathcal{T}_B}$ given by,

$$\Delta S_{\mathcal{T}_C}(R) = \Big(\frac{\alpha_s}{\pi}\Big)^2 \Big(\frac{\mu}{\mathcal{T}^{cut}}\Big)^{4\epsilon} 4j \int_0^1 dz' \int_0^\infty d\Delta y \int_0^\infty dy_t \int_0^\pi d\Delta\phi \frac{1}{z'(1-z')} (z'^2(1-z')^2)^{-\epsilon}$$
$$\theta(\Delta R^2 > R^2) \Big[\frac{A_j^{\mathcal{T}_C}}{4g^4 j\mu^{4\epsilon}} \Big\{ e^{-2(\Delta y+2y_t)}(e^{\Delta y}+e^{2y_t})^2(1+e^{\Delta y+2y_t})^2 \Big\}^{-\epsilon} \frac{e^{\gamma_E 2\epsilon}}{\Gamma(1-\epsilon)^2}$$
$$\Big(\frac{\pi^{1/2}\Gamma(1/2-\epsilon)}{\Gamma(1-\epsilon)}\Big)^{-1} (-\log[\max(z', 1-z')] - 2\epsilon \log^2[\max(z', 1-z')]) \sin\Delta\phi^{-2\epsilon}$$
$$- \int dz \delta(z-z') \frac{1}{\pi} \frac{A_j^{\mathcal{T}_B}}{4g^4 j\mu^{4\epsilon}} e^{-4y_t} (-\log[\max(z, 1-z)])\Big] , \tag{5.44}$$

where $j = C_A^2$ or $C_A T_f n_f$ and $\epsilon \sim 10^{-5}$. Here the subtracted term $A_j^{\mathcal{T}_B}$ only contains the right $1/\epsilon$ terms which cancel with $\mathcal{T}_C^{\rm jet}$ and the remaining finite $O(\epsilon^0)$ result can be plotted at different values of R to obtain an R-dependent function. The result of Eq. (5.44) is plotted in Fig. 5.3, where the orange and blue data points are for the color structures C_A^2 and $C_A T_f n_f$ respectively. Functions $F_5(R)$ and $F_6(R)$ parameterized by Eq. (5.27) are the corresponding best fit curves indicated by the orange and blue solid lines in Fig. 5.3. Thus

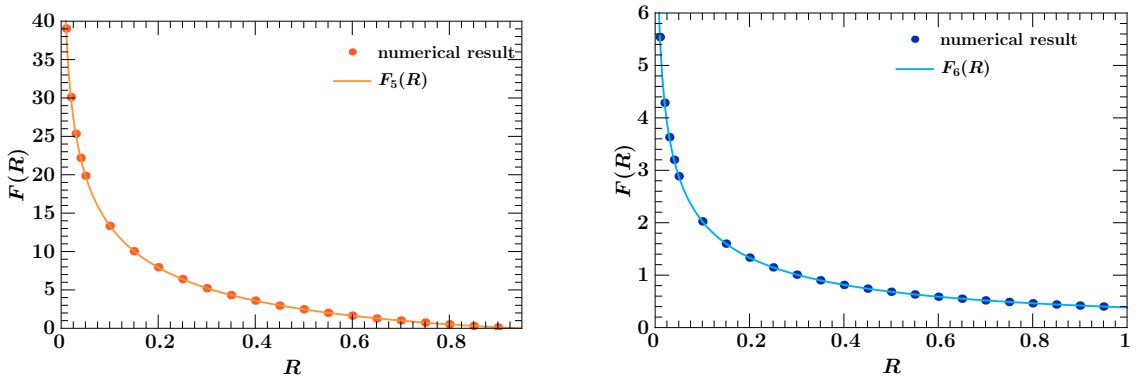

Figure 5.3: *The plots show the numerical result of the integrals in Eq. (5.44) for C_A^2 and $C_A T_f n_f$ color structures plotted as a function of the jet radius R and the corresponding best fit curves $F_5(R)$ and $F_6(R)$.*

the final result for the clustering corrections in the soft function for $\mathcal{T}_C^{\text{jet}}$ is

$$\begin{aligned}\Delta S_C^{(2)}(\mathcal{T}^{\text{cut}}) = \left(\frac{\alpha_s}{\pi}\right)^2 \left(\frac{\mu}{\mathcal{T}^{\text{cut}}}\right)^{4\epsilon} \Big\{ \frac{1}{4\epsilon} \Big[C_A^2 \Big\{ \frac{1}{18}(131 - 12\pi^2 - 132\log 2)\log R + f_1(R) \Big\} \\ + C_A T_f n_f \Big\{ \frac{-1}{9}(23 - 24\log 2)\log R + f_2(R) \Big\} \Big] + C_A^2 \Big(C_1 \log R + \\ C_2 \log R^2 + f_5(R) \Big) + C_A T_f n_f \Big(C_3 \log R + C_4 \log R^2 + f_6(R) \Big) \Big\}, \end{aligned} \tag{5.45}$$

where C_1, C_2, C_3 and C_4 are as defined for $\mathcal{T}_B^{\text{jet}}$ in Eq. (5.25) and the functions $f_{1,2}(R)$ are as defined in Eq. (5.26) and

$$f_5(R) = F_5(R) - C_1 \log R - C_2 \log^2 R \ , \quad f_6(R) = F_6(R) - C_3 \log R - C_4 \log^2 R \, . \tag{5.46}$$

The correction to the soft anomalous dimension from clustering for $\mathcal{T}_C^{\text{jet}}$ is the same as $\mathcal{T}_B^{\text{jet}}$ given in Eq. (5.28).

5.3 Clustering corrections in the Beam function

For the clustering corrections in the beam function, we will only consider here the $C_A T_f n_f$ contribution from the diagrams in Fig. 5.4 which allows us to check the consistency while the full calculation including the C_A^2 color structure is analogous and is left for future.

The general setup for computing the clustering corrections in the beam function is similar to the soft function with the measurement function given by Eq. (5.5). Because we defined the clustering corrections relative to the inclusive beam thrust measurement, we can follow the approach used in computing the partonic gluon beam functions at $O(\alpha_s^2)$ in [84] to obtain the amplitudes for the Feynman diagrams given in Fig. 5.4. The On-Shell diagram

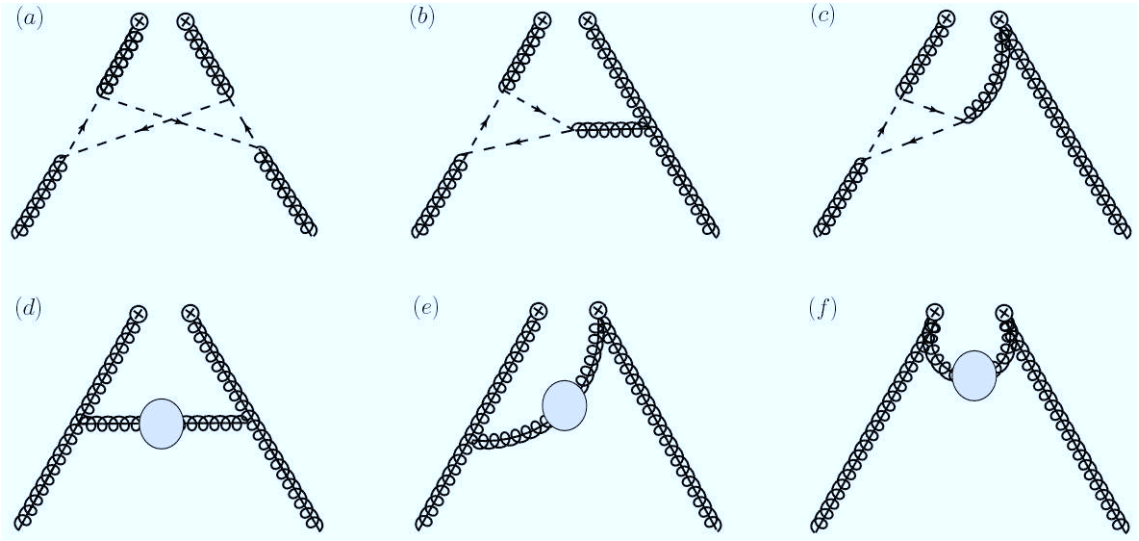

Figure 5.4: *Diagrams contributing to the calculation of $C_A T_f n_f$ color structure in the clustering correction for the beam functions at $O(\alpha_s^2)$. The full amplitude is obtained by adding the contribution from all these graphs including the mirror graphs for (b), (c) and (e).*

method as discussed in [84] is used to compute these diagrams in which all possible cuts are evaluated by putting the particles crossing the cut on shell. For the beam functions, there is an additional measurement delta function, $\delta(\omega - \bar{\mathcal{P}}_n)$, as we saw in Eq. (4.102) which fixes the sum of the minus momenta of all particles in each hemisphere to be equal to $\omega = zp^-$. With this constraint, the correction in the gluon beam function in terms of the momenta k_1 and k_2 of the emitted gluons is given by,

$$\Delta B_{g/g}^{\rm bare}(k_1,k_2,z) = \Big(\frac{\pi^{1/2-\epsilon}}{\Gamma[1/2-\epsilon]}\Big)\Big(\frac{\pi^{1-\epsilon}}{\Gamma[1-\epsilon]}\Big)\int_0^\infty (k_1^+k_1^-k_2^+k_2^-)^{-\epsilon}\delta(k_1^- + k_2^- - (1-z)p^-)$$
$$dk_1^+dk_2^+dk_1^-dk_2^- \times \int_0^\pi (1-\cos^2\Delta\phi)^{-\epsilon} A_{B,nf}\Delta\mathcal{M}^{\rm jet}(k_1,k_2)d\Delta\phi\,, \quad (5.47)$$

where $A_{B,nf}$ is the amplitude for the diagrams given in Fig. 5.4 taken from Ref. [84] and p^- is the total partonic n-collinear momentum. We use the coordinates defined for $\mathcal{T}_B^{\rm jet}$ in Eq. (5.10) to express Eq. (5.47) in terms of z, $\mathcal{T}_T$, Δy, y_t and $\Delta\phi$. To avoid confusion, we rename the variable z defined in Eq. (5.10) by z_1. The clustering correction in terms of these variables is

$$\Delta B_{g/g}^{\rm bare}(\mathcal{T}^{\rm cut},z) = \Big(\frac{\pi^{1/2-\epsilon}}{\Gamma[1/2-\epsilon]}\Big)\Big(\frac{\pi^{1-\epsilon}}{\Gamma[1-\epsilon]}\Big)\int_0^\infty d\mathcal{T}_T\int_0^1 dz_1\int_{-\infty}^\infty dy_t\int_{-\infty}^\infty d\Delta y\int_0^\pi d\Delta\phi$$
$$(e^{4y_t}\mathcal{T}_T^4 z_1^2(1-z_1)^2)^{-\epsilon} 4\mathcal{T}_T^3 z_1(1-z_1)e^{4y_t}(1-\cos^2\Delta\phi)^{-\epsilon}$$
$$\delta\Big(z_1\mathcal{T}_T e^{2y_t+\Delta y} + (1-z_1)\mathcal{T}_T e^{2y_t-\Delta y} - (1-z)p^-\Big) A_{B,nf}\Delta\mathcal{M}^{\rm jet}(\mathcal{T}^{\rm cut})\,. \quad (5.48)$$

The $\mathcal{T}_T$ dependence can be factored out and the integral over $\mathcal{T}_T$ can be performed over

the measurement function as in the case of the soft function (Eq. (5.14)). Performing the y_t integral using the delta function in z we get

$$\Delta B_{g/g}^{\rm bare}(\mathcal{T}^{\rm cut}, z) = \Big(\frac{\pi^{1/2-\epsilon}}{\Gamma[1/2-\epsilon]}\Big)\Big(\frac{\pi^{1-\epsilon}}{\Gamma[1-\epsilon]}\Big)\int_0^1 dz_1 \int_{-\infty}^{\infty} d\Delta y \int_0^{\pi} d\Delta\phi (e^{4y_t'}\mathcal{T}_T^4 z_1^2(1-z_1)^2)^{-\epsilon}$$
$$4e^{4y_t'}\mathcal{T}_T^3 z_1(1-z_1)(1-\cos^2\Delta\phi)^{-\epsilon} A_{B,nf}\frac{1}{2p^-(1-z)}\,, \tag{5.49}$$

where

$$y_t' = \frac{1}{2}\log\Big(\frac{(1-z)p^-}{\mathcal{T}_T(z_1 e^{\Delta y}+(1-z_1)e^{-\Delta y})}\Big)\,. \tag{5.50}$$

The integral in Eq. (5.49) is proportional to $(1-z)^{-1-2\epsilon}$ which can be expressed in terms of the plus distribution identity as,

$$\frac{1}{(1-z)^{1+2\epsilon}} = \frac{-1}{2\epsilon}\delta(1-z) + \mathcal{L}_0(1-z) + O(\epsilon)\,. \tag{5.51}$$

To compute the $\delta(1-z)$ coefficients, we can take the $z\to 1$ limit which simplifies the amplitude $A_{B,nf}$ to a great extent. In order to extract the $\log R$ coefficients analytically, we expand the amplitude in the small ΔR limit as for the soft function. As before, the integrals over $\Delta\phi$ and Δy can be performed using the master integrals in Eq. (5.20) and the left over z_1 integral is trivial. To obtain the constant and an R-dependent function, we perform the integrals in Eq. (5.49) numerically at different values of R, after expanding the integrand in the $\epsilon\to 0$ limit. The $1/\epsilon$ term thus obtained in Eq. (5.52) is $-1/2$ times that for the soft function in Eq. (5.24). From the factorization formula, the consistency relation for the anomalous dimensions is given by $2\gamma_B^g+\gamma_H^g+\gamma_S^g=0$. Because the hard function has no R-dependence, the divergence in the soft function due to clustering effects is exactly cancelled by that in the beam functions for $\Delta B_{g/g} = (-1/2)\Delta S_g$ which is the result we obtained for the $C_A T_f n_f$ color structure.

For the $O(\epsilon^0)$ terms, we follow the same procedure as in the soft function to obtain the coefficients of $\log R$ and $\log^2 R$ analytically and the function $g_1(z=1,R)$ from fitting. For the $\mathcal{L}_0(1-z)$ terms, we need to keep the full z dependence in the amplitude, but we can consider the amplitude in the small ΔR limit to compute the $\log R$ coefficient analytically. To obtain the constant and the R-dependence, for each value of z, the integrals in Eq. (5.49) are performed numerically at different values of R and an R-dependent function $g_2(z,R)$ is obtained by fitting the data for each value of z.

The final result for the corrections due to clustering in the bare partonic gluon beam

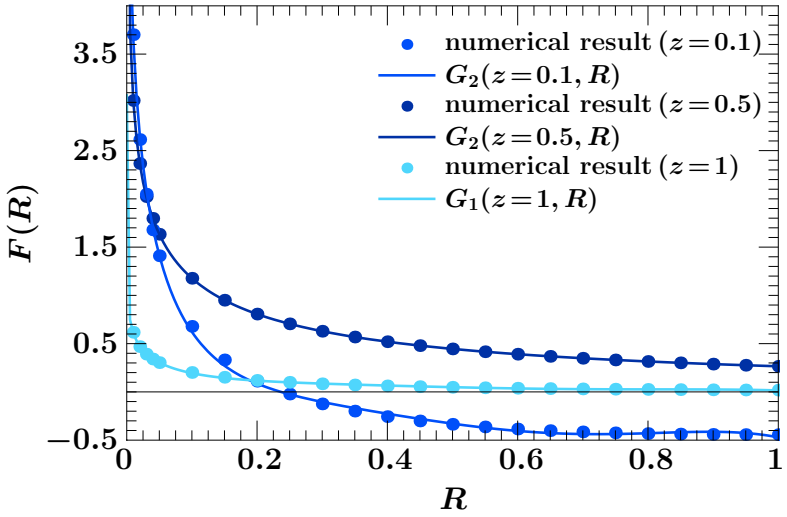

Figure 5.5: *Plot for the coefficient of $\mathcal{L}_0(1-z)$ and $\delta(1-z)\epsilon^0$ terms in Eq. (5.52) as a function of the jet radius R and the corresponding best fit curves $g_1(1,R)$ and $g_2(z,R)$ for $z = \{0.1, 0.5\}$.*

function for $C_A n_f T_f$ contribution is given by

$$\begin{aligned}\Delta B^{\rm bare}_{g/g}(t^{\rm cut},z) = -\Big(\frac{\alpha_s}{\pi}\Big)^2\Big(\frac{\mu^2}{t^{\rm cut}}\Big)^{2\epsilon} C_A T_f n_f \Big[\delta(1-z)\Big\{\frac{1}{4\epsilon}\Big[\frac{1}{18}(-23+24\log 2)\log R + f_2(R)\Big] \\ + \frac{2}{72}\Big(-68+4\pi^2+23\log 2+12\log^2 2\Big)\log R + \frac{1}{72}\Big(-23+24\log 2\Big)\log^2 R \\ + g_1(z=1,R)\Big\} + \mathcal{L}_0(1-z)\Big\{\frac{-2}{72}(-23+24\log 2)P_{gg}(z)(1-z)\log R \\ + g_2(z,R)\Big\}\Big] \qquad (5.52)\end{aligned}$$

where $t^{\rm cut} = zp^-\mathcal{T}^{\rm cut}$, $f_2(R)$ is the best fit curve as given in Eq. (5.26) and

$$g_1(1,R) = G_1(1,R) - A_1\log R - A_2\log^2 R \;\;,\;\; g_2(z,R) = G_2(z,R) - A_3\log R\,. \qquad (5.53)$$

with

$$\begin{aligned}A_1 &= \frac{2}{72}\Big(-68+4\pi^2+23\log 2+12\log^2 2\Big) \;\;,\;\; A_2 = \frac{1}{72}\Big(-23+24\log 2\Big)\,, \\ A_3 &= \frac{-2}{72}(-23+24\log 2)P_{gg}(z)(1-z)\,. \qquad (5.54)\end{aligned}$$

$G_1(1,R)$ and $G_2(z,R)$ are the best fit curves as shown in Fig. 5.5 with the parametric form given in Eq. (5.27). We have chosen $z = \{0.5, 0.1\}$ for illustration. We find that the coefficient of the $\log R$ term in Eq. (5.52) is proportional to the gluon-gluon splitting function as was shown in the case of clustering corrections for $p_T^{\rm jet}$ in Ref. [25].

5.4 Conclusions and Outlook

In this chapter, we computed the clustering logarithms in the soft function and partially in the beam function at $O(\alpha_s^2)$ for the jet-based observables $\mathcal{T}_B^{\text{jet}}$ and $\mathcal{T}_C^{\text{jet}}$. At one-loop when there is a single emission, there are no clustering and jet algorithm effects. At $O(\alpha_s^2)$, jet algorithm dependent corrections can arise due to the clustering of two collinear or soft particles into a single jet. These corrections give rise to logarithms of the jet radius R and are UV-divergent thus contributing to the 2-loop anomalous dimensions for the soft and beam functions. This divergence is cancelled between the soft and beam functions, leaving a logarithm of the ratio of the beam and soft scales in the cross section. For the soft function, we calculated these corrections and found that $\mathcal{T}_B^{\text{jet}}$ and $\mathcal{T}_C^{\text{jet}}$ have the same anomalous dimensions while the non-logarithmic constants differ between the two. For the beam function, we computed the corrections considering the $O(\alpha_s^2)$ diagrams which contribute to $C_A T_f n_f$ color structure and checked that this result correctly cancels the divergence in the soft function for the same color structure. The clustering corrections for the C_A^2 contribution in the beam function is left for future work.

Considering the H+0-jet cross section at NNLL′+ NNLO, the clustering corrections contribute to the two loop non-cusp anomalous dimensions and the 2-loop constants for the beam and soft functions. After cancellation of the divergence, the left over term has a logarithm of the ratio of the beam and soft scales and because for the $\mathcal{T}_f^{\text{jet}}$ veto, $\mu_B \sim \sqrt{m_H \mathcal{T}^{\text{cut}}}$ and $\mu_S = \mathcal{T}^{\text{cut}}$, the clustering effect in the cross section has the form

$$\Delta\sigma(\mathcal{T}^{\text{cut}}) = \sigma_B \left(\frac{\alpha_s}{\pi}\right)^2 \left[\frac{1}{2} \ln\left(\frac{m_H}{\mathcal{T}^{\text{cut}}}\right) C_{\mathcal{T}}^{(2)}(\ln R) + \Delta C(R)\right]. \tag{5.55}$$

where $C_{\mathcal{T}}^{(2)}$ contains the logarithms of R that contribute to the anomalous dimension (e.g. Eq. (5.28)) and $\Delta C(R)$ is the 2-loop constant. At each order, there is a contribution from the clustering correction which multiplies the resummed cross section and has the form,

$$\Delta U^{(n)}(R, \mathcal{T}^{\text{cut}}) = \exp\left[\left(\frac{\alpha_s}{\pi}\right)^n C_n(R) \frac{1}{2} \log\left(\frac{m_H}{\mathcal{T}^{\text{cut}}}\right)\right]. \tag{5.56}$$

where $C_n(R) \sim C_n^{(n-1)} \ln^{n-1} R + C_n^{(n-2)} \ln^{n-2} R + \cdots + C_n^{(1)} \ln R + C_n^{(0)}(R)$. $C_n^{(0)}(R)$ are the finite non-logarithmic terms. If one considers $R \sim m_H/\mathcal{T}^{\text{cut}}$, then these logarithms are large and need to be resummed. For p_T^{jet}, the leading α_s^3 coefficients were computed in [95] and found to be small. It is unknown if these coefficients are related or one needs to calculate them at each order which can make resummation challenging.

The resummation for the H+0-jet cross section at NNLL′ requires determining the hard, beam and soft functions upto $O(\alpha_s^2)$, the anomalous dimensions of each upto $O(\alpha_s^2)$ and the cusp anomalous dimension upto $O(\alpha_s^3)$. The NNLO result for the hard function, the

two-loop result for the non-cusp hard anomalous dimension and the three-loop result for the gluon cusp anomalous dimension are known. The two-loop soft function was partially known without the jet-algorithm effects. We have calculated these jet clustering effects and the 2-loop soft anomalous dimension for both $\mathcal{T}_B^{\text{jet}}$ and $\mathcal{T}_C^{\text{jet}}$ in this chapter. The anomalous dimension for the beam function can be determined from the soft function using RG consistency. The $O(\alpha_s^2)$ matching kernels for the gluon beam functions were calculated in [84] for inclusive beam thrust which can be used to obtain the beam functions for $\mathcal{T}_B^{\text{jet}}$. However the full $O(\alpha_s^2)$ result for the $\mathcal{T}_B^{\text{jet}}$ beam functions requires the clustering corrections and the 2-loop constants. We have computed these corrections for diagrams contributing to $C_A T_f n_f$ color structure in this chapter. The only remaining input requires extending this general setup and implementing it for the other color structure which is left for future work. With all these inputs and extracting the NNLO nonsingular contributions, we can obtain the numerical results for the full NNLL′+ NNLO resummed H+0-jet cross section with a veto $\mathcal{T}_f^{\text{jet}} < \mathcal{T}^{\text{cut}}$.

Chapter 6

Conclusions

In this thesis, we have studied perturbative uncertainties in the fixed-order predictions of exclusive jet cross sections relevant for Higgs measurements at the LHC and obtained resummed cross section predictions for new types of rapidity-dependent jet veto observables in the framework of Soft Collinear Effective theory (SCET). In particular, we studied and generalised the techniques to estimate theoretical uncertainties induced due to non-trivial jet binning and jet veto cuts and applied them to estimate the perturbative uncertainties in the NLO predictions for $pp \to H+$ 2 jets cross section via gluon gluon fusion (ggF), implementing the vector boson fusion (VBF) selection cuts used by ATLAS and CMS. We introduced and discussed a new class of jet veto observables for which the transverse momentum of a jet is weighted by a smooth function of the jet rapidity and provided resummed predictions for the H+0-jet cross section at NLL′+ NLO order. To extend these predictions to NNLL′+NNLO, we also computed the corrections due to jet clustering effects in the soft functions and partly in the beam functions at $O(\alpha_s^2)$. More details of the work presented in this thesis is summarised in the following.

NLO Uncertainties in H+2-jets

Jets are relevant in multiple contexts in the Higgs measurements at the LHC. Separating data into "jet bins" and measuring cross sections with a specific number of jets in the final state, is useful to enhance the Higgs signal from backgrounds. Cuts on the kinematics of jets help in discriminating between the different Higgs production mechanisms in particular between VBF, which is accompanied by two forward jets, from ggF. With the typical experimental selection cuts used by ATLAS and CMS, the VBF sample is contaminated by a 25% fraction from H+2-jet production via ggF, which has large perturbative uncertainties. In the first part of this thesis, we performed a detailed study of these uncertainties. We gave a general discussion of jet binning uncertainties, reviewing and extending the so-called ST procedure of estimating fixed-order uncertainties in exclusive jet cross sections. A jet

binning (veto) cut introduces Sudakov logarithms in the cross section and it is important to take into account the possible sizable effects of the higher-order logarithms in the cross section predictions. Such a jet binning cut divides the total inclusive cross section ($\sigma_{\geq 0}$) into an exclusive 0-jet cross section (σ_0) and an inclusive 1-jet cross section ($\sigma_{\geq 1}$). The uncertainties induced by such a binning can be parametrized in terms of fully correlated and fully anti-correlated components of a covariance matrix. The correlated component corresponds to the overall yield uncertainty for all bins and the anti-correlated component is the migration uncertainty introduced by the binning cut which drops out in the sum over the bins ($\sigma_0 + \sigma_{\geq 1}$). Using this method, we estimated the perturbative uncertainties in the exclusive cross section for H+2 jets via ggF, by implementing the VBF selection cuts used by ATLAS and CMS in their $H \to \gamma\gamma$ analyses. Our method can be applied to all decay channels which use similar VBF selection criteria. We used MCFM to compute the NLO H+2-jets cross section as a function of two kinematic variables p_{THjj} and $\Delta\phi_{H\text{–}jj}$. We observed that the uncertainties in the exclusive 2-jet cross section for $p^{\text{cut}}_{THjj} < 30\,\text{GeV}$ are about 44% and 49% for ATLAS and CMS tight which is substantially larger than the 21% uncertainty in the inclusive cross section. Similarly for $\Delta\phi_{H\text{–}jj} > 2.6$, we see a moderate increase in uncertainty to 26% for ATLAS and CMS tight. As an illustration to the application of our procedure for more complicated cut-based or multivariate analyses (MVA), we also considered a combination of cuts on both $\Delta\phi_{H\text{–}jj}$ and p_{THjj}, and found that the uncertainties can get larger than 50%. These uncertainties should be carefully taken into account in the theoretical predictions of cross section as well as in experiments which impose indirect restrictions or jet veto cuts on additional emissions.

In order to estimate the uncertainties in separating the ggF-VBF cross sections, we also studied the uncertainties in the ggF cross section measured relative to the expected VBF cross section i.e. $\Delta\sigma_2^{ggF}/\sigma_2^{VBF}$. We found that the relative uncertainty coming from the ggF contribution quickly increases below $p_{THjj} < 30\,\text{GeV}$ and $\pi - \Delta\phi_{H\text{–}jj} < 0.4$, which means that tighter selection cuts are not always beneficial as the reduction in the ggF contamination can be easily overwhelmed by the increasing perturbative uncertainties. Together with the ATLAS experimentalists, we also applied our method to construct a covariance matrix for estimating uncertainties in cross sections with arbitrary number of selection cuts. We compared the uncertainties in the exclusive $pp \to H + 2$-jet cross section via ggF from MCFM, with the uncertainties obtained by applying our covariance matrix to the H+0-jet cross section prediction from POWHEG+PYTHIA8 as a function of $\pi - \Delta\phi^{\text{cut}}_{H\text{–}jj}$ and found good agreement. We devised a method to propagate the uncertainties into a multivariate selection and found that harder cuts on the MVA classifier impose tighter constraints on the $\Delta\phi_{H\text{–}jj}$ phase space leading to increased theoretical uncertainties.

Rapidity dependent jet vetoes

Jet selection cuts and jet vetoes typically lead to Sudakov logarithms and larger uncer-

tainties in the fixed-order cross section predictions. In the first part of the thesis, we studied a method to explicitly take into account these logarithmic corrections in the fixed-order uncertainty estimates. However, as the vetoes get tighter, these logarithms become larger and dominate the perturbative series eventually leading to the breakdown of the fixed-order predictions, in which case a systematic resummation of these logarithms is necessary. In the second part of this thesis, we considered the resummation of the H+0-jet cross section with a veto on a new class of rapidity-dependent observables using SCET. We introduced two types of jet-based observables, $\mathcal{T}_B^{\rm jet}$ and $\mathcal{T}_C^{\rm jet}$, for which the transverse momentum of a jet is weighted by a smooth function of the jet rapidity, the weighting function being different for each. Each of the two $\mathcal{T}_B$ and $\mathcal{T}_C$-type observables were further classified into two observables, depending on the frame they were defined in, as $\mathcal{T}_{(B,C)\,\rm cm}$ defined in the hadronic center-of-mass frame i.e. lab frame and $\mathcal{T}_{B,C}$ as the one defined in a frame boosted with respect to the lab frame. These observables are useful both from experimental and theoretical point of view. With a jet veto observable like $p_T^{\rm jet}$ commonly used in current experiments, the jets can be reconstructed down to some minimum p_T, which ristricts how low one can go in the veto cut. Furthermore, low p_T jets are hard to identify at forward rapidities in harsh pile-up conditions. A better and cleaner way is to use rapidity dependent jet vetoes for which the rapidity weighting function can be chosen such that the veto gets tighter at central rapidities and looser at forward rapidities. Such jet vetoes are theoretically well motivated as they can also provide complementary ways to divide the phase space into exclusive jet bins.

The full H+0-jet cross section with a veto $\mathcal{T}_{B,C} < \mathcal{T}^{\rm cut}$ consist of two components, the resummed logarithmic contribution which is dominant at small values of $\mathcal{T}^{\rm cut}$ and the nonsingular corrections which are suppressed by $O(\mathcal{T}^{\rm cut}/m_H)$ and become important at large $\mathcal{T}^{\rm cut}$ to obtain the full inclusive cross section. We computed the $pp \to HX$ cross section differential in the $\mathcal{T}_{B,B\rm cm}$ and $\mathcal{T}_{C,C\rm cm}$ observables at NLO and used NLO subtraction method where we used the singular cross section as the "subtraction term" to cancel the divergences in the full NLO predictions and obtain the finite non singular corrections. We studied the factorization of the H+0-jet cross section into hard, beam and soft functions for $\mathcal{T}_{B,C}$-type observables in the framework of SCET and obtained resummed predictions for the H+0-jet cross section at full NLL$'$+NLO. To evaluate the uncertainties in our resummed predictions, we considered the covariance matrix as before and associated the resummation uncertainty with the migration uncertainty and the fixed-order uncertainty with the overall yield uncertainty. We obtained the fixed-order uncertainties by collectively varying the fixed-order scale by a factor of two, keeping the scale ratios in the logarithms fixed. For the resummation uncertainty, we vary the profile scales for the beam and soft functions in order to estimate the size of higher-order corrections in the logarithmic series. The resummation uncertainty corresponds to the intrinsic uncertainty in the resummed logarithmic series caused by the jet veto cut and vanishes at large $\mathcal{T}^{\rm cut}$ where the resum-

mation of logarithms become unimportant. The resummation uncertainty together with the fixed-order uncertainty then determines the total uncertainty in the resummed H+0-jet cross section. At NLL′+NLO, we find an uncertainty of about 20% at $\mathcal{T}^{\rm cut} \sim 25\,\text{GeV}$ which is comparable to $p_T^{\rm jet}$ at the same order, but we expect reduced uncertainties going to NNLL′+ NNLO. We also compared our NLL′+NLO numerical results in bins of $\mathcal{T}_C^{\rm jet}$ with the recent ATLAS measurements in the $H \to \gamma\gamma$ channel and found good agreement.

Clustering corrections

At $O(\alpha_s^2)$, for the jet-based observables we considered, there are corrections arising due to the clustering of two soft or collinear particles into a single jet or due to the mixing between the soft and collinear sectors. The soft-collinear mixing gives rise to corrections of $O(R^2)$ in the cross section and for large values of the jet radius ($R \sim 1$), these become $O(1)$ contributions which inhibit the soft-collinear factorization. The standard jet radii used in the Higgs analyses are $R = 0.4$ for ATLAS and $R = 0.5$ for CMS. With these values the soft-collinear mixing contributions are power suppressed while the corrections arising due to the clustering of two soft or collinear particles that introduce terms of the form $\alpha_s^N \log^{N-1} R$, are numerically important. In the last part of this thesis, we computed these clustering corrections in the soft function and partly (only for the $C_A T_f n_f$ color structure) in the beam functions at $O(\alpha_s^2)$. Our calculation of the clustering corrections in the soft function for $\mathcal{T}_B^{\rm jet}$ and $\mathcal{T}_C^{\rm jet}$, resulted in the same anomalous dimensions for the two, as expected (the beam functions being the same for $\mathcal{T}_B^{\rm jet}$ and $\mathcal{T}_C^{\rm jet}$), but different non-logarithmic constants. The bare corrections due to clustering are UV-divergent and we checked for one color structure ($C_A T_f n_f$) that this divergence cancels between the soft and the beam functions. The calculation for the remaining color structures in the beam function is left for the future. With these clustering corrections, we can compute the $O(\alpha_s^2)$ beam and soft functions for $\mathcal{T}_B^{\rm jet}$ and $\mathcal{T}_C^{\rm jet}$ and can extend the resummation to NNLL′ order. Including the NNLO nonsingular contribution, we can obtain the full NNLL′+NNLO resummed result for H+0-jet cross section with $\mathcal{T}_{B,C}$-type jet vetoes.

The Run 2 of the LHC is the beginning of the precision phase where precise predictions of fixed-order cross sections which take into account the effects of jet binning and jet veto cuts and resummed predictions for different jet veto observables and processes is of prime importance. Our work aimed at providing methods to estimate uncertainties in the fixed-order cross section predictions and obtaining resummed predictions for new class of jet veto observables using SCET. These methods of estimating uncertainties have been used in the ATLAS VBF analyses for different channels and in the theory predictions of cross sections. The new class of rapidity dependent observables can prove to be good central jet vetoes, and we propose that they should be measured and tested against theory predictions in other SM processes such as Drell-Yan, diphoton and weak diboson production.

Appendix A

Hard, beam and soft functions

A.1 Hard Function

The hard function is defined as

$$H_{gg}(m_t, q^2, \mu) = |C_{ggH}(m_t, q^2, \mu)|^2 \,, \tag{A.1}$$

where C_{ggH} is the Wilson coefficient from matching the full ggH form factor in the SM onto the ggH current in SCET. For on-shell Higgs production it is evaluated at $q^2 = m_H^2$. At one loop,

$$C_{ggH}(m_t, q^2, \mu) = \alpha_s(\mu) F^{(0)}\Big(\frac{q^2}{4m_t^2}\Big)\Big\{1 + \frac{\alpha_s(\mu)}{4\pi}\Big[C^{(1)}\Big(\frac{-q^2 - i0}{\mu^2}\Big) + F^{(1)}\Big(\frac{q^2}{4m_t^2}\Big)\Big]\Big\}, \tag{A.2}$$

where the coefficients $C^{(i)}$ and $F^{(i)}$ up to $i = 2$ can be found in [23]. For our NLL′ resummed predictions we need the NLO coefficient

$$C^{(1)}(x) = C_A\Big(-\ln^2 x + \frac{\pi^2}{6}\Big) \,, \tag{A.3}$$

and we used

$$F^{(0)}(z) = \frac{3}{2z} - \frac{3}{2z}\Big|1 - \frac{1}{z}\Big| \arcsin^2(\sqrt{z}) \,, \tag{A.4}$$

$$F^{(1)}(z) = 5C_A - 3C_F + \mathrm{O}(z) \,, \tag{A.5}$$

where the terms neglected in Eq. (A.5) have a numerically very small effect as $m_H^2 \ll 4m_t^2$.

A.2 Beam function

We expand the beam function matching coefficients in Eq. (4.108) as

$$\mathcal{I}_{ij}(t^{\rm cut}, z, R, \mu) = \sum_{n=0}^{\infty} \Big[\frac{\alpha_s(\mu)}{4\pi}\Big]^n \mathcal{I}_{ij}^{(n)}(t^{\rm cut}, z, R, \mu)\,. \tag{A.6}$$

At tree level we have

$$\mathcal{I}_{ij}^{(0)}(t^{\rm cut}, z, R, \mu) = \delta_{ij}\,\delta(1-z)\,. \tag{A.7}$$

We can obtain the one-loop matching coefficients for the gluon beam function by integrating the beam thrust matching coefficients $\mathcal{I}_{gj}(t, z, \mu)$ in [23] over t from 0 to $t^{\rm cut}$. The results read

$$\mathcal{I}_{gg}^{(1)}(t^{\rm cut}, z, R, \mu) = 2C_A\theta(z)\Big[\ln^2\frac{t^{\rm cut}}{\mu^2}\,\delta(1-z) + P_{gg}(z)\ln\frac{t^{\rm cut}}{\mu^2} + I_{gg}(z)\Big] \tag{A.8}$$

and

$$\mathcal{I}_{gq}^{(1)}(t^{\rm cut}, z, R, \mu) = 2C_F\theta(z)\Big[P_{gq}(z)\ln\frac{t^{\rm cut}}{\mu^2} + I_{gq}(z)\Big], \tag{A.9}$$

where

$$I_{gg}(z) = \mathcal{L}_1(1-z)\,\frac{2(1-z+z^2)^2}{z} - \frac{\pi^2}{6}\delta(1-z) - P_{gg}(z)\ln z\,, \tag{A.10}$$

$$I_{gq}(z) = P_{gq}(z)\ln\frac{1-z}{z} + \theta(1-z)z\,. \tag{A.11}$$

The LO gluon splitting functions are defined as

$$\begin{aligned} P_{gg}(z) &= 2\mathcal{L}_0(1-z)\frac{(1-z+z^2)^2}{z}\,,\\ P_{gq}(z) &= \theta(1-z)\,\frac{1+(1-z)^2}{z}\,, \end{aligned} \tag{A.12}$$

and

$$\mathcal{L}_n(x) = \bigg[\frac{\theta(x)\ln^n x}{x}\bigg]_+ = \lim_{\epsilon\to 0}\frac{\rm d}{{\rm d}x}\bigg[\theta(x-\epsilon)\frac{\ln^{n+1}x}{n+1}\bigg] \tag{A.13}$$

denotes the usual plus distributions.

A.3 Soft functions

A.3.1 Soft function for $\mathcal{T}^{\text{jet}}_{B(\text{cm})}$

The soft function for $\mathcal{T}^{\text{jet}}_{B(\text{cm})}$ can be obtained by integrating the beam thrust soft function $S_{gg}(k,\mu)$ in [23] over $0 < k < \mathcal{T}^{\text{cut}}$. Through NLO this yields

$$S^B_{gg}(\mathcal{T}^{\text{cut}},\mu) = 1 + \frac{\alpha_s(\mu)C_A}{\pi}\left(-2\ln^2\frac{\mathcal{T}^{\text{cut}}}{\mu} + \frac{\pi^2}{12}\right). \tag{A.14}$$

A.3.2 Soft function for $\mathcal{T}^{\text{jet}}_{C(\text{cm})}$

In this appendix we calculate the soft function S^C_{gg} at one loop. The bare one-loop soft function for a generic (differential) measurement function $\mathcal{M}(\mathcal{T})$ and two (incoming) gluons is given by [96]

$$S^{\text{bare}(1)}_{gg}(\mathcal{T}) = 4C_A\, g^2\left(\frac{e^{\gamma_E}\mu^2}{4\pi}\right)^{\epsilon}\int\frac{d^dp}{(2\pi)^d}(p^+p^-)^{-1}\times 2\pi\delta(p^2)\theta(p_0)\,\mathcal{M}(\mathcal{T},p^+,p^-)\,, \tag{A.15}$$

where p is the momentum of the emitted soft gluon.

At one loop the soft measurement function for $\mathcal{T}^{\text{jet}}_C$ according to Eq. (4.9) reads

$$\mathcal{M}(\mathcal{T}^{\text{jet}}_C,p^+,p^-) = \delta\Big(\mathcal{T}^{\text{jet}}_C - \frac{|\vec{p}_T|}{e^Y+e^{-Y}}\Big) = \delta\Big(\mathcal{T}^{\text{jet}}_C - \frac{p^+p^-}{p^++p^-}\Big)\,. \tag{A.16}$$

Inserting this in Eq. (A.15) and simplifying we get

$$S^{\text{bare}(1)}_{gg}(\mathcal{T}^{\text{jet}}_C) = \frac{\alpha_sC_A}{\pi}\frac{(e^{\gamma_E}\mu^2)^{\epsilon}}{\Gamma(1-\epsilon)}\int dp^+dp^-\frac{\theta(p^+)\theta(p^-)}{(p^+p^-)^{1+\epsilon}}\times\delta\Big(\mathcal{T}^{\text{jet}}_C - \frac{p^+p^-}{p^++p^-}\Big)\,. \tag{A.17}$$

Integration over p^+ and p^- yields

$$S^{\text{bare}(1)}_{gg}(\mathcal{T}^{\text{jet}}_C) = -\frac{\alpha_sC_A}{\pi}\frac{(e^{\gamma_E}\mu^2)^{\epsilon}}{\Gamma(1-\epsilon)}\frac{\Gamma(\epsilon)^2}{\Gamma(2\epsilon)}(\mathcal{T}^{\text{jet}}_C)^{-1-2\epsilon}\,. \tag{A.18}$$

Expanding $(\mathcal{T}^{\text{jet}}_C)^{-1-2\epsilon}$ in terms of plus distributions and subtracting the $1/\epsilon$ divergence, the $\overline{\text{MS}}$ renormalized one-loop piece of the differential soft function reads

$$S^{(1)}_{gg}(\mathcal{T}^{\text{jet}}_C) = \frac{\alpha_sC_A}{\pi}\left[-\frac{4}{\mu}\mathcal{L}_1\Big(\frac{\mathcal{T}^{\text{jet}}_C}{\mu}\Big) + \frac{\pi^2}{4}\delta(\mathcal{T}^{\text{jet}}_C)\right]. \tag{A.19}$$

As expected, replacing $C_A \to C_F$, this result agrees with the one-loop soft function for the

C-parameter event shape in $e^+e^- \to q\bar{q}$ [76]. For the $\mathcal{T}_C^{\text{jet}}$-veto we integrate over $\mathcal{T}_C^{\text{jet}}$ and find

$$S_{gg}^C(\mathcal{T}^{\text{cut}}, \mu) = 1 + \frac{\alpha_s(\mu) C_A}{\pi} \left(-2 \ln^2 \frac{\mathcal{T}^{\text{cut}}}{\mu} + \frac{\pi^2}{4} \right), \tag{A.20}$$

where we also added the trivial tree-level contribution.

This result only differs from the one in Eq. (A.14) for $\mathcal{T}_B^{\text{jet}}$ in the $\mathcal{T}^{\text{cut}}$-independent constant, while the logarithmic term is dictated by the RG structure and is the same for all four observables we consider.

Appendix B

NLO H+0-jet crosss section

B.1 H+0-jet cross section differential in $\mathcal{T}_B^{\text{jet}}$

The measurement function for $\mathcal{T}_B^{\text{jet}}$ is

$$1 = \int d\mathcal{T}_B [\delta(\mathcal{T}_B - e^Y p^+)\theta(e^{-Y}p^- - e^Y p^+) + \delta(\mathcal{T}_B - e^{-Y}p^-)\theta(e^Y p^+ - e^{-Y}p^-)] \,. \quad \text{(B.1)}$$

Inserting the measurement function for $\mathcal{T}_B^{\text{jet}}$ in Eq. (4.32) we have

$$\begin{aligned}\frac{d\sigma}{d\mathcal{T}_B} = \frac{1}{16\pi E_{\text{cm}}^2} \int \frac{dz_a}{z_a}\frac{dz_b}{z_b} f_a\Big(\frac{\tilde{x}_a}{z_a}\Big) f_b\Big(\frac{\tilde{x}_b}{z_b}\Big) \frac{|\overline{M}_{ab}|^2}{E_{\text{cm}}^2} \delta\Big(\frac{\tilde{x}_b}{z_b} - \tilde{x}_b - \frac{p^+}{E_{\text{cm}}}\Big)\delta\Big(\frac{\tilde{x}_a}{z_a} - \tilde{x}_a - \frac{p^-}{E_{\text{cm}}}\Big) \\ \delta\Big(\tilde{x}_b\tilde{x}_a - \frac{p^+p^-}{E_{\text{cm}}^2} - \frac{m_H^2}{E_{\text{cm}}^2}\Big)\Big[\delta(\mathcal{T}_B - e^Y p^+)\theta(e^{-Y}p^- - e^Y p^+) + \delta(\mathcal{T}_B - e^{-Y}p^-) \\ \theta(e^Y p^+ - e^{-Y}p^-)\Big]\delta\Big(e^{2Y} - \frac{\tilde{x}_a}{\tilde{x}_b}\Big) d\tilde{x}_a d\tilde{x}_b dp^+ dp^- \,. \end{aligned} \quad \text{(B.2)}$$

Changing variables to

$$p^+ = \tilde{p}^+ e^Y \quad p^- = \tilde{p}^- e^{-Y} \quad \tilde{x}_a = x_a e^Y \quad \tilde{x}_b = x_b e^{-Y} \,, \quad \text{(B.3)}$$

the differential cross section becomes

$$\begin{aligned}\frac{d\sigma}{d\mathcal{T}_B} = \frac{1}{16\pi E_{\text{cm}}^2}\Big[\int \frac{dz_a}{z_a}\frac{dz_b}{z_b} f_a\Big(\frac{x_a e^Y}{z_a}\Big) f_b\Big(\frac{x_b e^{-Y}}{z_b}\Big) \frac{|\overline{M}_{ab}|^2}{E_{\text{cm}}^2} \delta\Big(\frac{x_b}{z_b} - x_b - \frac{\mathcal{T}_B}{E_{\text{cm}}}\Big)\delta\Big(\frac{x_a}{z_a} - x_a - \frac{\tilde{p}^-}{E_{\text{cm}}}\Big) \\ \delta\Big(x_b x_a - \frac{\mathcal{T}_B\tilde{p}^-}{E_{\text{cm}}^2} - \frac{m_H^2}{E_{\text{cm}}^2}\Big)\theta\Big(\tilde{p}^- - \mathcal{T}_B\Big) d\tilde{p}^- + \frac{dz_a}{z_a}\frac{dz_b}{z_b} f_a\Big(\frac{x_b e^{-Y}}{z_b}\Big) f_b\Big(\frac{x_a e^Y}{z_a}\Big) \frac{|\overline{M}_{ab}|^2}{E_{\text{cm}}^2} \\ \Big(\frac{x_a}{z_a} - x_a - \frac{\mathcal{T}_B}{E_{\text{cm}}}\Big)\delta\Big(\frac{x_b}{z_b} - x_b - \frac{\tilde{p}^+}{E_{\text{cm}}}\Big)\delta\Big(x_b x_a - \frac{\mathcal{T}_B\tilde{p}^+}{E_{\text{cm}}^2} - \frac{m_H^2}{E_{\text{cm}}^2}\Big)\theta\Big(\tilde{p}^+ - \mathcal{T}_B\Big) d\tilde{p}^+\Big] \\ \delta\Big(e^{2Y} - e^{2Y}\frac{x_a}{x_b}\Big) dx_a dx_b de^{2Y} \,. \end{aligned} \quad \text{(B.4)}$$

Doing the $\tilde{p}^-$ ($\tilde{p}^+$ for the other branch) and the $z_b(z_a)$ integrals using the delta function we have

$$\frac{d\sigma}{d\mathcal{T}_B} = \frac{1}{16\pi E_{\rm cm}^2}\Big[\int \frac{dz_a}{z_a} f_a\Big(\frac{x_a e^Y}{z_a}\Big) f_b\Big(\frac{(E_{\rm cm}x_b + \mathcal{T}_B)e^{-Y}}{E_{\rm cm}}\Big)|\overline{M}_{ab}|^2 \delta\Big(x_b x_a - \frac{\mathcal{T}_B p_0^-}{E_{\rm cm}^2} - \frac{m_H^2}{E_{\rm cm}^2}\Big)$$
$$\theta\Big(p_0^- - \mathcal{T}_B\Big)\frac{z_b'}{E_{\rm cm} + \mathcal{T}_B} + \{a \leftrightarrow b, p_0^- \to p_0^+\}\Big]\delta\Big(1 - \frac{x_a}{x_b}\Big) dx_a dx_b 2dY\,, \tag{B.5}$$

where

$$p_0^- = \frac{x_a E_{\rm cm}(1-z_a)}{z_a}\ ,\ p_0^+ = \frac{x_b E_{\rm cm}(1-z_b')}{z_b'}\ ,\ z_b' = \frac{E_{\rm cm}x_b}{E_{\rm cm} + \mathcal{T}_B} \tag{B.6}$$

Now performing one of the x integrals using the delta functions we get

$$\frac{d\sigma}{d\mathcal{T}_B} = \frac{2}{16\pi E_{\rm cm}^2}\Big[\int \frac{dz_a}{z_a} f_a\Big(\frac{x e^Y}{z_a}\Big) f_b\Big(\frac{(E_{\rm cm}x + \mathcal{T}_B)e^{-Y}}{E_{\rm cm}}\Big)\frac{|\overline{M}_{ab}|^2}{E_{\rm cm}} \delta\Big(x^2 - \frac{\mathcal{T}_B x(1-z_a)}{z_a E_{\rm cm}} - \frac{m_H^2}{E_{\rm cm}^2}\Big)$$
$$\theta\Big(\frac{x(1-z_a)E_{\rm cm}}{z_a} - \mathcal{T}_B\Big) + \{a \leftrightarrow b\}\Big] x dx dY\,. \tag{B.7}$$

Performing the z integral using the delta functions we get

$$\frac{d\sigma}{d\mathcal{T}_B dY} = \frac{2}{16\pi E_{\rm cm}^2}\Big[\int f_a\Big(\frac{x e^Y}{z_a'}\Big) f_b\Big(\frac{(E_{\rm cm}x + \mathcal{T}_B)e^{-Y}}{E_{\rm cm}}\Big)\frac{|\overline{M}_{ab}|^2}{E_{\rm cm}} \theta\Big(\frac{x(1-z_a')E_{\rm cm}}{z_a'} - \mathcal{T}_B\Big)$$
$$\frac{E_{\rm cm}^2 z_a'}{x^2 E_{\rm cm}^2 - \mathcal{T}_B x E_{\rm cm} - m_H^2} + \{a \leftrightarrow b\}\Big] dx\,, \tag{B.8}$$

where

$$z_a' = \frac{E_{\rm cm}\mathcal{T}_B x}{-m_H^2 + E_{\rm cm}^2 x^2 + E_{\rm cm}\mathcal{T}_B x}\,. \tag{B.9}$$

As for the case of $\mathcal{T}_{B\rm cm}$ the x integral can be performed numerically over the PDFs to get the final cross section differential in Y and $\mathcal{T}_B$.

B.2 Differential cross section for $\mathcal{T}_C^{\rm jet}$

The measurement function for $\mathcal{T}_C^{\rm jet}$ is given by

$$1 = \int d\mathcal{T}_C\, \delta\Big(\mathcal{T}_C - \frac{p^+ p^-}{p^+ e^Y + p^- e^{-Y}}\Big)\,. \tag{B.10}$$

Inserting the measurement function in Eq. (4.32),

$$\begin{aligned}\frac{d^4\sigma}{d\tilde{x}_a d\tilde{x}_b dp^+ dp^-} =& \frac{1}{16\pi E_{cm}^2}\int \frac{dz_a}{z_a}\frac{dz_b}{z_b} f_a\Big(\frac{\tilde{x}_a}{z_a}\Big) f_b\Big(\frac{\tilde{x}_b}{z_b}\Big)\frac{|\overline{M}_{ab}|^2}{E_{\text{cm}}^2}\delta\Big(\frac{\tilde{x}_b}{z_b}-\tilde{x}_b-\frac{p^+}{E_{\text{cm}}}\Big)\\ &\delta\Big(\frac{\tilde{x}_a}{z_a}-\tilde{x}_a-\frac{p^-}{E_{\text{cm}}}\Big)\delta\Big(\tilde{x}_b\tilde{x}_a-\frac{p^+p^-}{E_{\text{cm}}^2}-\frac{m_H^2}{E_{\text{cm}}^2}\Big)\delta\Big(\mathcal{T}_C-\frac{p^+p^-}{p^+e^Y+p^-e^{-Y}}\Big)\\ &\delta\Big(e^{2Y}-\frac{\tilde{x}_a}{\tilde{x}_b}\Big)d\mathcal{T}_C de^{2Y}\,. \end{aligned} \tag{B.11}$$

Rescaling p^- to p^-e^{2Y} and doing the $\tilde{x}_a$, p^+ and p^- integrals using the delta functions we get

$$\begin{aligned}\frac{d\sigma}{d\mathcal{T}_C} =& \frac{1}{16\pi E_{cm}^2}\int \frac{dz_a}{z_a}\frac{dz_b}{z_b} f_a\Big(\frac{\tilde{x}_b e^{2Y}}{z_a}\Big) f_b\Big(\frac{\tilde{x}_b}{z_b}\Big)\frac{|\overline{M}_{ab}|^2}{E_{\text{cm}}^2}\delta\Big(\tilde{x}_b^2 e^{2Y}-\frac{p_0^+p_0^-e^{2Y}}{E_{\text{cm}}^2}-\frac{m_H^2}{E_{\text{cm}}^2}\Big)\\ &\delta\Big(\mathcal{T}_C-\frac{p_0^+p_0^-e^{2Y}}{p_0^+e^Y+p_0^-e^Y}\Big)E_{\text{cm}}^2\tilde{x}_b d\tilde{x}_b de^{2Y}\,, \end{aligned} \tag{B.12}$$

where,

$$\tilde{x}_a=\tilde{x}_b e^{2Y}\;\;,\;\; p_0^+=\tilde{x}_b\Big(\frac{1-z_b}{z_b}\Big)E_{\text{cm}}\;\;,\;\; p_0^-=\tilde{x}_b\Big(\frac{1-z_a}{z_a}\Big)E_{\text{cm}}\,. \tag{B.13}$$

Defining $\tilde{x}_b=e^{-Y}x_b$ the differential cross section becomes

$$\begin{aligned}\frac{d\sigma}{d\mathcal{T}_C} =& \frac{2}{16\pi E_{cm}^2}\int \frac{dz_a}{z_a}\frac{dz_b}{z_b} f_a\Big(\frac{x_b e^{Y}}{z_a}\Big) f_b\Big(\frac{x_b e^{-Y}}{z_b}\Big)|\overline{M}_{ab}|^2\delta\Big(x_b^2\Big(\frac{-1+z_a+z_b}{z_a z_b}\Big)-\frac{m_H^2}{E_{\text{cm}}^2}\Big)\\ &\delta\Big(\frac{E_{\text{cm}}x_b(-1+z_b)(-1+z_a)+\mathcal{T}_C(-z_b+z_a(-1+2z_b)}{-z_b+z_a(-1+2z_b)}\Big)x_b dx_b dY\,. \end{aligned} \tag{B.14}$$

Performing the x_b integral using the delta function we get

$$\begin{aligned}\frac{d\sigma}{d\mathcal{T}_C} =& \frac{1}{16\pi E_{cm}^2}\int \frac{dz_a}{z_a}\frac{dz_b}{z_b} f_a\Big(\frac{x_b' e^{Y}}{z_a}\Big) f_b\Big(\frac{x_b' e^{-Y}}{z_b}\Big)|\overline{M}_{ab}|^2\Big|\frac{z_a z_b}{-1+z_a+z_b}\Big|\\ &\delta\Big(\frac{E_{\text{cm}}x_b'(-1+z_b)(-1+z_a)+\mathcal{T}_C(-z_b+z_a(-1+2z_b)}{-z_b+z_a(-1+2z_b)}\Big)dY\,, \end{aligned} \tag{B.15}$$

where $x_b'=m_H/E_{\text{cm}}\sqrt{z_a z_b/(-1+z_a+z_b)}$. To simplify the z_a integral, we transform the variables z_a, z_b as $z_a=1/(1+z_1)$ and $z_b=1/(1+z_2)$ which results in

$$\begin{aligned}\frac{d\sigma}{d\mathcal{T}_C dY} =& \frac{1}{16\pi E_{cm}^2}\int \frac{dz_1}{1+z_1}\frac{dz_2}{1+z_2}\frac{1}{|1-z_1z_2|} f_a\Big(\frac{e^Y m_H(1+z_1)\sqrt{1/(1-z_1z_2)}}{E_{\text{cm}}}\Big)\\ &f_b\Big(\frac{e^{-Y}m_H(1+z_2)\sqrt{1/(1-z_1z_2)}}{E_{\text{cm}}}\Big)\delta\Big(\frac{\mathcal{T}_C(z_1+z_2)-m_H z_1 z_2\sqrt{\frac{1}{1-z_1z_2}}}{z_1+z_2}\Big)\,. \end{aligned} \tag{B.16}$$

where one of the z_1 or z_2 integrals is performed using the delta function, and the other one is used to integrate over the PDFs numerically.

B.3 Differential cross section for $\mathcal{T}_{C\mathrm{cm}}^{\mathrm{jet}}$

The measurement function of $\mathcal{T}_{C\mathrm{cm}}$ is

$$1 = \int d\mathcal{T}_{C\mathrm{cm}} \delta\Big(\mathcal{T}_{C\mathrm{cm}} - \frac{p^+p^-}{p^+ + p^-}\Big) \,. \tag{B.17}$$

Inserting the measurement function in Eq. (4.32)

$$\begin{aligned}\frac{d^4\sigma}{d\tilde{x}_a d\tilde{x}_b dp^+ dp^-} =& \frac{1}{16\pi E_{cm}^2} \int \frac{dz_a}{z_a}\frac{dz_b}{z_b} f_a\Big(\frac{\tilde{x}_a}{z_a}\Big) f_b\Big(\frac{\tilde{x}_b}{z_b}\Big) \frac{|\overline{M}_{ab}|^2}{E_{\mathrm{cm}}^2} \delta\big(\frac{x_b}{z_b} - \tilde{x}_b - \frac{p^+}{E_{\mathrm{cm}}}\big) \\ & \delta\big(\frac{\tilde{x}_a}{z_a} - \tilde{x}_a - \frac{p^-}{E_{\mathrm{cm}}}\big) \delta\Big(\tilde{x}_b\tilde{x}_a - \frac{p^+p^-}{E_{\mathrm{cm}}^2} - \frac{m_H^2}{E_{\mathrm{cm}}^2}\Big) \delta\Big(\mathcal{T}_{C\mathrm{cm}} - \frac{p^+p^-}{p^+ + p^-}\Big) d\mathcal{T}_{C\mathrm{cm}} \,.\end{aligned} \tag{B.18}$$

Rescaling $p^+ = \tilde{p}^+ e^{-Y}$, $p^- = \tilde{p}^- e^{Y}$, $\tilde{x}_b = x_b e^{-Y}$ and $\tilde{x}_a = x_a e^{Y}$

$$\begin{aligned}\frac{d^4\sigma}{dx_a dx_b d\tilde{p}^+ d\tilde{p}^-} =& \frac{1}{16\pi E_{cm}^2} \int \frac{dz_a}{z_a}\frac{dz_b}{z_b} f_a\Big(\frac{x_a e^{Y}}{z_a}\Big) f_b\Big(\frac{x_b e^{-Y}}{z_b}\Big) \frac{|\overline{M}_{ab}|^2}{E_{\mathrm{cm}}^2} \delta\big(\frac{x_b}{z_b} - x_b - \frac{\tilde{p}^+}{E_{\mathrm{cm}}}\big) \\ & \delta\big(\frac{x_a}{z_a} - x_a - \frac{\tilde{p}^-}{E_{\mathrm{cm}}}\big) \delta\Big(x_b x_a - \frac{\tilde{p}^+\tilde{p}^-}{E_{\mathrm{cm}}^2} - \frac{m_H^2}{E_{\mathrm{cm}}^2}\Big) \delta\Big(\mathcal{T}_{C\mathrm{cm}} - \frac{\tilde{p}^+\tilde{p}^-}{\tilde{p}^+ e^{-Y} + \tilde{p}^- e^{Y}}\Big) \\ & \delta\Big(e^{2Y} - e^{2Y}\frac{x_a}{x_b}\Big) d\mathcal{T}_{C\mathrm{cm}} de^{2Y} \,.\end{aligned} \tag{B.19}$$

Doing the x_a, $\tilde{p}^-$ and $\tilde{p}^+$ integrals we get

$$\begin{aligned}\frac{d\sigma}{d\mathcal{T}_{C\mathrm{cm}}} =& \frac{1}{16\pi E_{cm}^2} \int \frac{dz_a}{z_a}\frac{dz_b}{z_b} f_a\Big(\frac{x_b e^{Y}}{z_a}\Big) f_b\Big(\frac{x_b e^{-Y}}{z_b}\Big) \frac{|\overline{M}_{ab}|^2}{E_{\mathrm{cm}}^2} \delta\Big(x_b^2 - \frac{\tilde{p}_0^+\tilde{p}_0^-}{E_{\mathrm{cm}}^2} - \frac{m_H^2}{E_{\mathrm{cm}}^2}\Big) \\ & \delta\Big(\mathcal{T}_{C\mathrm{cm}} - \frac{\tilde{p}_0^+\tilde{p}_0^-}{\tilde{p}_0^+ e^{-Y} + \tilde{p}_0^- e^{Y}}\Big) x_b dx_b 2dY \,,\end{aligned} \tag{B.20}$$

where

$$x_a = x_b e^{2Y} \;,\; \tilde{p}_0^+ = x_b\Big(\frac{1-z_b}{z_b}\Big) E_{\mathrm{cm}} \;,\; \tilde{p}_0^- = x_b\Big(\frac{1-z_a}{z_a}\Big) E_{\mathrm{cm}} \,. \tag{B.21}$$

Now performing the x_b integral we get

$$\begin{aligned}\frac{d\sigma}{d\mathcal{T}_{C\mathrm{cm}} dY} =& \frac{1}{16\pi E_{cm}^2} \int \frac{dz_a}{z_a}\frac{dz_b}{z_b} f_a\Big(\frac{e^{Y} m_H \sqrt{z_a z_b/(-1+z_a+z_b)}}{E_{\mathrm{cm}} z_a}\Big) f_b\Big(\frac{e^{-Y} m_H \sqrt{z_a z_b/(-1+z_a+z_b)}}{E_{\mathrm{cm}} z_b}\Big) \\ & \delta\Big(\frac{\mathcal{T}_{C\mathrm{cm}} + e^{Y} m_H (-1+z_a)(-1+z_b)\sqrt{z_a z_b/(-1+z_a+z_b)}}{e^{2Y} z_b + z_a(-1+z_b+e^{2Y} z_b)}\Big) \Big|\frac{z_a z_b}{-1+z_a+z_b}\Big| \,.\end{aligned} \tag{B.22}$$

The z_a and z_b integral can be performed as in the $\mathcal{T}_C^{\mathrm{jet}}$ case shown before.

Bibliography

[1] F. Englert and R. Brout, *Broken Symmetry and the Mass of Gauge Vector Mesons*, *Phys.Rev.Lett.* **13** (1964) 321–323.

[2] P. W. Higgs, *Broken Symmetries and the Masses of Gauge Bosons*, *Phys.Rev.Lett.* **13** (1964) 508–509.

[3] P. W. Higgs, *Broken symmetries, massless particles and gauge fields*, *Phys.Lett.* **12** (1964) 132–133.

[4] G. Guralnik, C. Hagen, and T. Kibble, *Global Conservation Laws and Massless Particles*, *Phys.Rev.Lett.* **13** (1964) 585–587.

[5] **The ATLAS**, *Observation of an excess of events in the search for the Standard Model Higgs boson in the gamma-gamma channel with the ATLAS detector*, *ATLAS-CONF-2012-091, ATLAS-COM-CONF-2012-109* (2012).

[6] **The CMS**, *Evidence for a new state decaying into two photons in the search for the standard model Higgs boson in pp collisions*, *CMS-PAS-HIG-12-015* (2012).

[7] C. W. Bauer, S. Fleming, and M. E. Luke, *Summing Sudakov logarithms in $B \to X_s\gamma$ in effective field theory*, *Phys. Rev. D* **63** (2000) 014006, [hep-ph/0005275].

[8] C. W. Bauer, S. Fleming, D. Pirjol, and I. W. Stewart, *An Effective field theory for collinear and soft gluons: Heavy to light decays*, *Phys. Rev. D* **63** (2001) 114020, [hep-ph/0011336].

[9] C. W. Bauer and I. W. Stewart, *Invariant operators in collinear effective theory*, *Phys. Lett. B* **516** (2001) 134–142, [hep-ph/0107001].

[10] C. W. Bauer, D. Pirjol, and I. W. Stewart, *Soft collinear factorization in effective field theory*, *Phys. Rev. D* **65** (2002) 054022, [hep-ph/0109045].

[11] S. Gangal and F. J. Tackmann, *Next-to-leading-order uncertainties in Higgs+2 jets from gluon fusion*, *Phys.Rev.* **D87** (2013), no. 9 093008, [arXiv:1302.5437].

[12] S. Gangal, M. Stahlhofen, and F. J. Tackmann, *Rapidity-Dependent Jet Vetoes*, *Phys. Rev.* **D91** (2015), no. 5 054023, [arXiv:1412.4792].

[13] G. Altarelli and G. Parisi, *Asymptotic Freedom in Parton Language*, *Nucl. Phys.* **B126** (1977) 298.

[14] S. I. T. Yu. L. Dokshitzer, D. I. Dyakonov *Phys. Rep. 58* **269** (1980).

[15] J. Collins and D. Soper, *Back to back jets in qcd: Comparison with experiment*, *Phys. Rev. Lett.* **48** (1982).

[16] G. S. J.C. Collins, D.E. Soper *Nucl. Phys.* **B250** (1985).

[17] M. S. D. Graudenz and P. Zerwas, *QCD corrections to Higgs Boson production at proton-proton colliders*, *Phys. Rev. Lett.* (1993), no. 1372.

[18] D. G. P. Z. M. Spira, A. Djouadi, *Higgs Boson production at the LHC*, *Nucl. Phys.* **B453** (1995).

[19] R. V. Harlander and W. B. Kilgore, *Next-to-next-to-leading order Higgs production at hadron colliders*, *Phys. Rev. Lett.* **88** (2002) 201801, [hep-ph/0201206].

[20] C. Anastasiou and K. Melnikov, *Higgs boson production at hadron colliders in NNLO QCD*, *Nucl. Phys.* **B646** (2002) 220–256, [hep-ph/0207004].

[21] R. D. Ball, M. Bonvini, S. Forte, S. Marzani, and G. Ridolfi, *Higgs production in gluon fusion beyond NNLO*, *Nucl. Phys.* **B874** (2013) 746–772, [arXiv:1303.3590].

[22] M. Bonvini, R. D. Ball, S. Forte, S. Marzani, and G. Ridolfi, *Updated Higgs cross section at approximate N^3LO*, *J. Phys.* **G41** (2014) 095002, [arXiv:1404.3204].

[23] C. F. Berger, C. Marcantonini, I. W. Stewart, F. J. Tackmann, and W. J. Waalewijn, *Higgs Production with a Central Jet Veto at NNLL+NNLO*, *JHEP* **1104** (2011) 092, [arXiv:1012.4480].

[24] A. Banfi, G. P. Salam, and G. Zanderighi, *NLL+NNLO predictions for jet-veto efficiencies in Higgs-boson and Drell-Yan production*, *JHEP* **1206** (2012) 159, [arXiv:1203.5773].

[25] I. W. Stewart, F. J. Tackmann, J. R. Walsh, and S. Zuberi, *Jet p_T Resummation in Higgs Production at NNLL′+NNLO*, *Phys. Rev. D* **89** (2014) 054001, [arXiv:1307.1808].

[26] T. T. Jouttenus, I. W. Stewart, F. J. Tackmann, and W. J. Waalewijn, *Jet Mass Spectra in Higgs + One Jet at NNLL*, *Phys. Rev. D* **88** (2013) 054031, [arXiv:1302.0846].

[27] R. Boughezal, F. Caola, K. Melnikov, F. Petriello, and M. Schulze, *Higgs boson production in association with a jet at next-to-next-to-leading order in perturbative QCD*, *JHEP* **1306** (2013) 072, [arXiv:1302.6216].

[28] J. M. Campbell, R. K. Ellis, and G. Zanderighi, *Next-to-Leading order Higgs + 2 jet production via gluon fusion*, *JHEP* **0610** (2006) 028, [hep-ph/0608194].

[29] R. Frederix and S. Frixione, *Merging meets matching in MC@NLO*, *JHEP* **1212** (2012) 061, [1209.6215].

[30] J. M. Campbell, R. K. Ellis, R. Frederix, P. Nason, C. Oleari, et al., *NLO Higgs Boson Production Plus One and Two Jets Using the POWHEG BOX, MadGraph4 and MCFM*, *JHEP* **1207** (2012) 092, [1202.5475].

[31] J. R. Forshaw and M. Sjodahl, *Soft gluons in Higgs plus two jet production*, *JHEP* **0709** (2007) 119, [arXiv:0705.1504].

[32] N. Kidonakis, G. Oderda, and G. F. Sterman, *Evolution of color exchange in QCD hard scattering*, *Nucl. Phys.* **B531** (1998) 365–402, [hep-ph/9803241].

[33] P. Bolzoni, F. Maltoni, S.-O. Moch, and M. Zaro, *Higgs production via vector-boson fusion at NNLO in QCD*, *Phys.Rev.Lett.* **105** (2010) 011801, [arXiv:1003.4451].

[34] F. Maltoni, K. Mawatari, and M. Zaro, *Higgs characterisation via vector-boson fusion and associated production: NLO and parton-shower effects*, *Eur.Phys.J.* **C74** (2014), no. 1 2710, [arXiv:1311.1829].

[35] P. Nason and C. Oleari, *NLO Higgs boson production via vector-boson fusion matched with shower in POWHEG*, *JHEP* **1002** (2010) 037, [arXiv:0911.5299].

[36] S. Frixione, P. Torrielli, and M. Zaro, *Higgs production through vector-boson fusion at the NLO matched with parton showers*, *Phys.Lett.* **B726** (2013) 273–282, [arXiv:1304.7927].

[37] **ATLAS, CMS**, G. Aad et al., *Combined Measurement of the Higgs Boson Mass in pp Collisions at $\sqrt{s} = 7$ and 8 TeV with the ATLAS and CMS Experiments*, *Phys.Rev.Lett.* **114** (2015) 191803, [arXiv:1503.07589].

[38] **ATLAS**, G. Aad et al., *Measurements of fiducial and differential cross sections for Higgs boson production in the diphoton decay channel at $\sqrt{s} = 8$ TeV with ATLAS*, *JHEP* **1409** (2014) 112, [arXiv:1407.4222].

[39] **ATLAS**, G. Aad et al., *Measurements of the Total and Differential Higgs Boson Production Cross Sections Combining the $H \to \gamma\gamma$ and $H \to ZZ^* \to 4\ell$ Decay Channels at $\sqrt{s} = 8$ TeV with the ATLAS Detector*, arXiv:1504.05833.

[40] **ATLAS**, *Measurements of the Higgs boson production and decay rates and coupling strengths using pp collision data at $\sqrt{s}$ = 7 and 8 TeV in the ATLAS experiment*, arXiv:1507.04548.

[41] I. W. Stewart and F. J. Tackmann, *Theory Uncertainties for Higgs and Other Searches Using Jet Bins*, *Phys. Rev. D* **85** (2012) 034011, [arXiv:1107.2117].

[42] The ATLAS and CMS collaborations, *Procedure for the LHC Higgs boson search combination in summer 2011*, *ATL-PHYS-PUB-2011-011, CMS-NOTE-2011-005* (2011).

[43] S. Dittmaier, S. Dittmaier, C. Mariotti, G. Passarino, R. Tanaka, et al., *Handbook of LHC Higgs Cross Sections: 2. Differential Distributions*, 1201.3084.

[44] J. M. Campbell, R. K. Ellis, and C. Williams, *Hadronic production of a Higgs boson and two jets at next-to-leading order*, *Phys. Rev. D* **81** (2010) 074023, [1001.4495].

[45] **The ATLAS**, *Observation and study of the higgs boson candidate in the two photon decay channel with the atlas detector at the lhc*, *ATLAS-CONF-2012-168* (2012).

[46] J. M. Campbell and R. K. Ellis, *An Update on vector boson pair production at hadron colliders*, *Phys. Rev. D* **60** (1999) 113006, [hep-ph/9905386].

[47] A. Martin, W. Stirling, R. Thorne, and G. Watt, *Uncertainties on alpha(S) in global PDF analyses and implications for predicted hadronic cross sections*, *Eur. Phys. J. C* **64** (2009) 653–680, [0905.3531].

[48] **The ATLAS**, *Update of the $\boldsymbol{H \to WW^{(*)} \to e\nu\mu\nu}$ analysis with 13 fb^{-1} of $\sqrt{s} = 8$ tev data collected with the atlas detector*, *ATLAS-CONF-2012-158* (Nov, 2012).

[49] **The ATLAS**, *Search for the standard model higgs boson in $h \to \tau\tau$ decays in proton-proton collisions with the atlas detector*, *ATLAS-CONF-2012-160* (Nov, 2012).

[50] **The CMS**, *Evidence for a particle decaying to w+w- in the fully leptonic final state in a standard model higgs boson search in pp collisions at the lhc*, *CMS-PAS-HIG-12-042* (2012).

[51] **The CMS**, *Higgs to tau tau (sm) (hcp)*, *CMS-PAS-HIG-12-043* (2012).

[52] **SM AND NLO MULTILEG and SM MC Working Groups**, J. Alcaraz Maestre et al., *The SM and NLO Multileg and SM MC Working Groups: Summary Report*, 1203.6803.

[53] **LHC Higgs Cross Section Working Group**, S. Heinemeyer et al., *Handbook of LHC Higgs Cross Sections: 3. Higgs Properties*, arXiv:1307.1347.

[54] P. Nason, *A New method for combining NLO QCD with shower Monte Carlo algorithms*, *JHEP* **0411** (2004) 040, [hep-ph/0409146].

[55] S. Frixione, P. Nason, and C. Oleari, *Matching NLO QCD computations with Parton Shower simulations: the POWHEG method*, *JHEP* **0711** (2007) 070, [arXiv:0709.2092].

[56] S. Alioli, P. Nason, C. Oleari, and E. Re, *A general framework for implementing NLO calculations in shower Monte Carlo programs: the POWHEG BOX*, *JHEP* **1006** (2010) 043, [arXiv:1002.2581].

[57] T. Sjostrand, S. Mrenna, and P. Z. Skands, *A Brief Introduction to PYTHIA 8.1*, *Comput.Phys.Commun.* **178** (2008) 852–867, [arXiv:0710.3820].

[58] *Measurements of the properties of the higgs-like boson in the two photon decay channel with the atlas detector using 25* fb^{-1} *of proton-proton collision data*, Tech. Rep. ATLAS-CONF-2013-012, CERN, Geneva, Mar, 2013.

[59] **CMS**, *Updated measurements of the Higgs boson at 125 GeV in the two photon decay channel*, .

[60] **ATLAS**, G. Aad et al., *Search for an additional, heavy Higgs boson in the* $H \to ZZ$ *decay channel at* $\sqrt{s} = 8$ *TeV in pp collision data with the ATLAS detector*, arXiv:1507.05930.

[61] **ATLAS**, G. Aad et al., *Measurement of Higgs boson production in the diphoton decay channel in pp collisions at center-of-mass energies of 7 and 8 TeV with the ATLAS detector*, *Phys. Rev.* **D90** (2014), no. 11 112015, [arXiv:1408.7084].

[62] **ATLAS**, G. Aad et al., *Measurements of Higgs boson production and couplings in diboson final states with the ATLAS detector at the LHC*, *Phys.Lett.* **B726** (2013) 88–119, [arXiv:1307.1427].

[63] **ATLAS**, *Measurements of the properties of the Higgs-like boson in the two photon decay channel with the ATLAS detector using 25* fb^{-1} *of proton-proton collision data*.

[64] I. W. Stewart, F. J. Tackmann, and W. J. Waalewijn, *Factorization at the LHC: From PDFs to Initial State Jets*, *Phys. Rev. D* **81** (2010) 094035, [arXiv:0910.0467].

[65] I. W. Stewart, F. J. Tackmann, and W. J. Waalewijn, *N-Jettiness: An Inclusive Event Shape to Veto Jets*, *Phys. Rev. Lett.* **105** (2010) 092002, [arXiv:1004.2489].

[66] S. D. Ellis and D. E. Soper, *Successive combination jet algorithm for hadron collisions*, *Phys. Rev.* **D48** (1993) 3160–3166, [hep-ph/9305266].

[67] Y. L. Dokshitzer, G. D. Leder, S. Moretti, and B. R. Webber, *Better jet clustering algorithms*, *JHEP* **08** (1997) 001, [hep-ph/9707323].

[68] M. Cacciari, G. P. Salam, and G. Soyez, *The Anti-k(t) jet clustering algorithm*, *JHEP* **04** (2008) 063, [arXiv:0802.1189].

[69] T. Becher and M. Neubert, *Factorization and NNLL Resummation for Higgs Production with a Jet Veto*, *JHEP* **1207** (2012) 108, [arXiv:1205.3806].

[70] F. J. Tackmann, J. R. Walsh, and S. Zuberi, *Resummation Properties of Jet Vetoes at the LHC*, *Phys. Rev. D* **86** (2012) 053011, [arXiv:1206.4312].

[71] A. Banfi, P. F. Monni, G. P. Salam, and G. Zanderighi, *Higgs and Z-boson production with a jet veto*, *Phys. Rev. Lett.* **109** (2012) 202001, [arXiv:1206.4998].

[72] X. Liu and F. Petriello, *Resummation of jet-veto logarithms in hadronic processes containing jets*, *Phys. Rev. D* **87** (2013) 014018, [arXiv:1210.1906].

[73] X. Liu and F. Petriello, *Reducing theoretical uncertainties for exclusive Higgs-boson plus one-jet production at the LHC*, *Phys. Rev. D* **87** (2013), no. 9 094027, [arXiv:1303.4405].

[74] T. Becher, M. Neubert, and L. Rothen, *Factorization and N^3LL_p+NNLO predictions for the Higgs cross section with a jet veto*, *JHEP* **1310** (2013) 125, [arXiv:1307.0025].

[75] R. Boughezal, X. Liu, F. Petriello, F. J. Tackmann, and J. R. Walsh, *Combining Resummed Higgs Predictions Across Jet Bins*, *Phys. Rev. D* **89** (2014) 074044, [arXiv:1312.4535].

[76] S. Alioli, C. W. Bauer, C. J. Berggren, A. Hornig, F. J. Tackmann, et al., *Combining Higher-Order Resummation with Multiple NLO Calculations and Parton Showers in GENEVA*, *JHEP* **1309** (2013) 120, [arXiv:1211.7049].

[77] C. W. Bauer and I. W. Stewart, *SCET Lecture Notes TASI 2013*, .

[78] M. Zeng, *Drell-Yan process with jet vetoes: breaking of generalized factorization*, arXiv:1507.0165.

[79] J. R. Gaunt, *Glauber Gluons and Multiple Parton Interactions*, *JHEP* **1407** (2014) 110, [arXiv:1405.2080].

[80] J. Chay and C. Kim, *Collinear effective theory at subleading order and its application to heavy - light currents*, *Phys.Rev.* **D65** (2002) 114016, [hep-ph/0201197].

[81] A. V. Manohar, T. Mehen, D. Pirjol, and I. W. Stewart, *Reparameterization invariance for collinear operators*, *Phys.Lett.* **B539** (2002) 59–66, [hep-ph/0204229].

[82] I. W. Stewart, F. J. Tackmann, and W. J. Waalewijn, *The Quark Beam Function at NNLL*, *JHEP* **1009** (2010) 005, [arXiv:1002.2213].

[83] J. R. Gaunt, M. Stahlhofen, and F. J. Tackmann, *The Quark Beam Function at Two Loops*, *JHEP* **1404** (2014) 113, [arXiv:1401.5478].

[84] J. Gaunt, M. Stahlhofen, and F. J. Tackmann, *The Gluon Beam Function at Two Loops*, *JHEP* **1408** (2014) 020, [arXiv:1405.1044].

[85] G. Korchemsky and A. Radyushkin, *Renormalization of the Wilson Loops Beyond the Leading Order*, *Nucl. Phys.* **B283** (1987) 342–364.

[86] J. Gaunt, M. Stahlhofen, F. J. Tackmann, and J. R. Walsh, *N-jettiness Subtractions for NNLO QCD Calculations*, arXiv:1505.0479.

[87] G. Parisi *Phys. Lett. B* **90,295** (1980).

[88] G. F. Sterman *Nucl. Phys.* **B281, 310** (1987).

[89] L. Magnea and G. F. Sterman *Phys. Rev. D* **42, 4222** (1990).

[90] V. Ahrens, T. Becher, M. Neubert, and L. L. Yang, *Origin of the Large Perturbative Corrections to Higgs Production at Hadron Colliders*, *Phys. Rev.* **D79** (2009) 033013, [arXiv:0808.3008].

[91] Z. Ligeti, I. W. Stewart, and F. J. Tackmann, *Treating the b quark distribution function with reliable uncertainties*, *Phys. Rev. D* **78** (2008) 114014, [arXiv:0807.1926].

[92] R. Abbate, M. Fickinger, A. H. Hoang, V. Mateu, and I. W. Stewart, *Thrust at N^3LL with Power Corrections and a Precision Global Fit for $\alpha_s(m_Z)$*, *Phys. Rev. D* **83** (2011) 074021, [arXiv:1006.3080].

[93] A. Martin, W. Stirling, R. Thorne, and G. Watt, *Parton distributions for the LHC*, *Eur. Phys. J. C* **63** (2009) 189–285, [arXiv:0901.0002].

[94] A. Hornig, C. Lee, I. W. Stewart, J. R. Walsh, and S. Zuberi, *Non-global Structure of the $O(alpha_s^2)$ Dijet Soft Function*, *JHEP* **08** (2011) 054, [arXiv:1105.4628].

[95] S. Alioli and J. R. Walsh, *Jet Veto Clustering Logarithms Beyond Leading Order*, *JHEP* **03** (2014) 119, [arXiv:1311.5234].

[96] T. T. Jouttenus, I. W. Stewart, F. J. Tackmann, and W. J. Waalewijn, *The Soft Function for Exclusive N-Jet Production at Hadron Colliders*, *Phys. Rev. D* **83** (2011) 114030, [arXiv:1102.4344].